

Exploring Advanced Topological Metamaterials for Elastic Wave Manipulation

by

Patrick A. Dorin

A dissertation submitted in partial fulfillment
of the requirements for the degree of
Doctor of Philosophy
(Mechanical Engineering)
in the University of Michigan
2023

Doctoral Committee:

Professor Kon-Well Wang, Chair
Professor Daniel J. Inman
Assistant Professor Bogdan-Ioan Popa
Professor Kai Sun
Assistant Professor Serife Tol

Patrick A. Dorin

pdorin@umich.edu

ORCID iD: 0000-0002-2280-2851

© Patrick Dorin 2023

Dedication

To Sarah and my grandparents: Karen, Patrick C., Elba, and Antonio

Acknowledgements

I owe a profound debt of gratitude to the numerous mentors, colleagues, friends, and family members whose contributions were instrumental in bringing this dissertation to fruition. First and foremost, I would like to express my deepest appreciation to my advisor, Prof. Kon-Well Wang. His unwavering encouragement, support, and guidance have played a pivotal role in my development as a researcher and scholar. I am immensely grateful to have had the opportunity to work with and learn from him during my time at the University of Michigan. I would also like to thank the members of my doctoral committee, Prof. Daniel J. Inman, Prof. Bogdan-Ioan Popa, Prof. Kai Sun, and Prof. Serife Tol, for their insightful feedback and support throughout this dissertation journey. I would also like to acknowledge funding support from the organizations and institutions that helped make this research possible: the National Science Foundation, the Air Force Office of Scientific Research, and the University of Michigan.

I am extremely grateful to my colleagues (both past and present) at the Structural Dynamics and Controls lab, who not only provided me with endless inspiration and insight but also made my experience within the lab truly enjoyable. I would like to express special thanks to Megan Hathcock for her support at every step of my doctoral experience, Prof. Jinki Kim for his outstanding mentorship and belief in me during the first year of my Ph.D. studies, and Dr. Xiang Liu for his valuable input and fruitful discussions regarding my dissertation research (including helping to formulate the design concept for one of my dissertation chapters). Furthermore, I would be remiss in not mentioning the excellent undergraduate and master's student researchers that I had the pleasure of directly working with: Mustafa Khan, whose innovative experimental ideas and hard work contributed to one of my dissertation chapters, along with Tao Wang and Qing Yin. I would also like to thank Osama Jameel and Polytec, Inc. for their dedicated assistance with experimental measurements and the use of their laser Doppler vibrometry equipment in my dissertation research.

During my time in the University of Michigan Department of Mechanical Engineering, I had the privilege of engaging with countless graduate student colleagues who not only helped to enrich

my research but also provided empathy during the challenging phases of the Ph.D. process, for which I am deeply grateful. Moreover, I cannot overstate how responsive and helpful the entire Mechanical Engineering Department staff was throughout my entire time at Michigan, making my life easier and greatly aiding my progression toward my degree. During my time in Ann Arbor, I had the privilege of serving alongside wonderful colleagues and leaders in the Mechanical Engineering Graduate Council and the student organization Service Learning and Trans-disciplinary Education. I am deeply grateful to the individuals who influenced my journey within these student groups, as they facilitated the successful achievement of my goals within these organizations and gave me a vital perspective on the profound significance of service, not only within the academic research community but also within the broader surrounding community.

This dissertation would not have been possible without the invaluable guidance I received throughout my academic and professional journey leading up to my studies at the University of Michigan. I would like to extend a sincere thanks to the mentors who encouraged my pursuit of academic research during my undergraduate education at the University of Notre Dame. I have particular gratitude for Prof. Steven Schmid, who provided me with valuable tutelage as my undergraduate research advisor, along with Prof. David Hoelzle and Prof. Glen Niebur, whose exceptional teaching and mentorship helped steer me toward the path of doctoral education. I owe my fascination with structural dynamics and vibrations to my memorable tenure at Honeywell Aerospace. I am deeply indebted to Lori Armon, Todd Braman, Owen Grossman, Tom Rolfer, and Matthew Schlager, among many others, for teaching me how to be a professional engineer and igniting my passion for structural dynamics. I would also like to thank Mark Wendlandt for supporting my technical development and providing me with every opportunity to thrive at Honeywell.

I could not have undertaken this journey without the unyielding support and encouragement of my friends and family. Without you I would not be where I am today. Brian B., Brian M., Jonathan, Nate, and Nick, I will never forget our many memorable conversations on graduate school, research, and life in general, as well as the countless shared meals, hangouts, and runs that provided a needed respite from the rigors of the doctoral experience. I am also incredibly grateful to my friends from Michigan, “The Hassen,” and “Squad”; you provided me with so much joy throughout my Ph.D. years. Looking forward to our get-togethers provided me with the extra motivation I needed to push through difficult obstacles in my research. I would also like to express my deepest

gratitude to my family, including the Skurlas, Dorins, and Cajas-Rojas spread throughout the world. Thank you, Dr. Patrick C. Dorin, for showing me the positive impact that education can have on the world; Karen, for showing me the meaning of unconditional love; Tito, for instilling wonder in me and teaching me the value of hard work; and Meme, el hilo de mi corazón. Mom and Dad, thank you for your unending support, sacrifice, and love, your perfect example of positivity and perseverance, and the countless opportunities you have made possible for me.

Most importantly, thank you Sarah, for being the love of my life and the most incredible wife and life partner a person could ask for. Thank you for being my rock during the most difficult of times, my biggest supporter, and for being the reason I wake up excited to face each day, no matter the challenges that lay ahead. Finally, thank you Chiquito Banano, for granting me with the “kick” I needed to push through the finish line.

Table of Contents

Dedication	ii
Acknowledgements	iii
List of Tables	x
List of Figures	xi
List of Appendices	xxvi
List of Abbreviations	xxvii
Abstract	xxviii
Chapter 1. Introduction.....	1
1.1 Background	1
1.1.1 Elastic metamaterials.....	1
1.1.2 Topological metamaterials	7
1.2 Current state of the art and research gap.....	10
1.2.1 First-order topological metamaterials.....	10
1.2.2 Higher-order topological metamaterials.....	13
1.2.3 Research gaps	14
1.3 Research statement	16
1.4 Outline of dissertation chapters and addressing the research gaps	17
Chapter 2. 2D Piezoelectric Metamaterial.....	19
2.1 Introduction	19
2.2 Concept and theoretical model.....	22
2.2.1 System description.....	22

2.2.2	Governing equations.....	23
2.2.3	Dispersion relation.....	24
2.2.4	Negative capacitance circuitry	27
2.3	Working principle - obtainment of tunable topological wave propagation.....	28
2.3.1	Unit cell dispersion analysis.....	29
2.3.2	Topological interface states	34
2.3.3	Path tunable topological wave propagation.....	36
2.4	Parametric study – frequency and mode shape tunability.....	38
2.4.1	Frequency tunability of the Dirac point.....	38
2.4.2	Achievable operating region for topological interface states	41
2.4.3	Influence of electromechanical coupling on topological wave tunability	44
2.4.4	Finite element evaluation of frequency and mode shape tunable topological waves...	46
2.5	Lattice reconfiguration	48
2.5.1	Formation of additional Dirac point through lattice reconfiguration	48
2.5.2	High-frequency interface state from Dirac 2.....	49
2.5.3	Boundary states from Dirac 2.....	50
2.6	Conclusions and discussion.....	53
Chapter 3.	3D Metastable Metamaterial.....	55
3.1	Introduction	55
3.2	Concept and theoretical model	57
3.2.1	Proposed EM overview	57
3.2.2	Theoretical model.....	57
3.2.3	3D EM design methodology.....	58
3.3	Unit cell analysis for 2D surface states using the elastic analog of the QVHE	61
3.3.1	Methodology for a full topological bandgap	62

3.3.2 Band inversion and topological invariant calculations for the QVHE:	65
3.4 On-demand reconfigurable 2D topological surface states	68
3.4.1 Supercell dispersion analysis.....	68
3.4.2 Full-scale numerical simulations of on-demand tunable 2D topological surface states	68
3.5 Layer-polarized topological states	72
3.5.1 Unit cell dispersion analysis for layer-polarized topological states	72
3.5.2 Supercell dispersion analysis for layer-polarized topological states.....	74
3.5.3 Full-scale numerical simulations for layer-polarized topological wave propagation in a 3D metastructure	76
3.6 Bilayer-locked topological states	77
3.7 Advanced 3D elastic wave networks	78
3.8 Conclusions and discussion.....	79
Chapter 4. 3D Multimodal Locally Resonant Metamaterial	82
4.1 Introduction	82
4.2 Concept and theoretical model	83
4.3 Unit cell dispersion and multimodal resonance effect	84
4.4 Supercell analysis for 2D topological states.....	89
4.5 Topological waveguides in full-scale 3D metastructures	92
4.6 Experimental realization	94
4.7 Conclusions and discussion.....	98
Chapter 5. 2D Higher-Order Locally Resonant Metamaterial	100
5.1 Introduction	100
5.2 2D higher-order topological metamaterial description	101
5.3 Unit cell band structure and multimodal resonance effect	103
5.4 Supercell analysis for multiband 1D topological states	107

5.5 Emergence of multiband topological corner states	108
5.6 Multiband corner states for multifunctional wave-based computing.....	115
5.7 Higher-order topological states in a fractal TM	117
5.8 Conclusions and discussion.....	124
Chapter 6. Scholarly Contributions, Broader Impacts, and Future Opportunities	126
6.1 Summary of scholarly contributions	126
6.2 Broader impacts and opportunities for future research	130
6.2.1 Advanced elastic wave control in contemporary engineering applications	130
6.2.2 Innovative topological physics for mechanics (elastic wave), acoustics, photonics/ electromagnetics, and condensed matter physics	133
6.2.3 Next-generation mechanical structures and systems with physical intelligence	135
Appendices.....	138
Bibliography	180

List of Tables

Table 2.1. Definition of geometric and material properties.	30
Table 3.1. Geometric dimensions.....	58
Table 3.2. Material properties	59
Appendix Table C.1. Valley Chern numbers calculated for D2, D3, and D4.....	160
Appendix Table D.1. C_n rotation eigenvalues at high-symmetry points of Type A and Type B lattice configurations for the 2D HOTM	173
Appendix Table D.2. The topological indices, bulk polarizations, and corner charges for the 2D HOTM.	174
Appendix Table D.3. Summary of the corner state eigenmode characteristics.	177

List of Figures

Fig 1.1. Vibrations and elastic waves are nearly ubiquitous in mechanical structures. Structures are exposed to ambient vibrations from the external environment (e.g., wind loading, seismic events) and operational vibrations caused by the active operation of mechanical systems (e.g., aircraft or automotive engine, CNC turning)..... 2

Fig 1.2. (a) Simplified model of local resonance in a 1D spring-mass lattice. Local resonators have mass mr and stiffness kr ; spring-mass lattice has mass $m1$ and stiffness $k1$. (b) Band structures for a locally resonant EM with resonators that are decoupled from a generic mechanical medium (left panel) and resonators attached to a generic mechanical medium (right panel). The locally resonant bandgap is designated by the orange shading and the Bragg bandgap is designated by the gray shading. 4

Fig 1.3. Local resonance in EMs. (a) Simplified local resonators attached to a 1D rotating rod, a 1D beam, and a 2D thin plate (figure reused from [65] with written permission from the publisher). (b) Beam and tip-mass resonators attached to a 1D beam (figure reused from [65] with written permission from the publisher). (c) Bolt resonators attached to a 2D thin plate (figure reused from [66] under license CC BY 3.0). (d) Electromechanical resonators coupled to a 1D beam (figure reused from [67] with written permission from the publisher)..... 5

Fig 1.4. Elastic waveguides formed from inclusions in periodic lattices. Upon excitation, a confined elastic wave will propagate through the inclusion. (a) is an example of successful waveguiding (figure reused from [74] with written permission from the publishers). (b) is an example of how unwanted scattering or localization can inhibit successful propagation around sharp bends of a waveguide (figure reused from [75] under license CC BY 4.0). 6

Fig 1.5. (a) Diagrams of a TI. The top panel is a TI composed of bulk crystal and exhibiting a topologically protected boundary state (represented by the orange arrows). The bottom panel shows a TI comprised of two bulk crystals connected at an interface, where a topologically protected interface state preferentially localizes (represented by the orange arrow). (b) The crystal band structure for the TI. The orange band represents the topological boundary (or interface) state, which emerges in the bulk energy bandgap. (c) Summary of the analogy between quantum materials and EMs that is employed to create TMs. 8

Fig 1.6. (a) Schematic of topological states in 1D, 2D, and 3D first-order TMs. Topological states are confined to the paths that are shown in orange. “Type A” and “Type B” represent topologically distinct bulk crystals (i.e., at their interface, there is a topological transition). These crystals are insulating in the bulk. (b) 1D first-order TM (beam with a varying cross-section) hosting a 0D topological point state (figure reused from [130] under license CC BY 4.0). (c) 2D first-order TM (thin plate with circular inclusions) hosting a 1D topological edge state (figure reused from [27] under license CC BY 4.0). (d) 3D first-order TM (cubic lattice) hosting 2D

topological surface state (top) and layer-selective topological state (bottom) (figure reused from [131] with written permission from the publisher). 11

Fig 1.7. (a) Schematics of (from left to right) second-order 2D HOTI, second-order 3D HOTI, and third-order 3D HOTI. (b) 2D HOTM with corner states generated from quantized multipole moments (figure reused from [198] with written permission from the publisher). (c) 2D HOTM with corner states generated from a Cn -symmetric mechanism (figure reused from [110] with written permission from the publisher). 14

Fig 2.1. (a) Isometric view of piezoelectric metamaterial, with unit cell enclosed in dashed lines. (b) Cross-section and (c) top view of metamaterial unit cell. Blue indicates electrode geometry connected to circuit 1, red indicates electrode geometry connected to circuit 2. 25

Fig 2.2. $\Omega(k)$ Dispersion diagram for unit cell with $\beta = 0$ and $\Omega t - eff = 16.0$. The red lines represent results from PWE method, and the open black circles represent results from FE simulations. Band structure for bare bimorph plate is shown as gray dashed lines. For all results in this figure, the three bands with the lowest frequency (i.e., the first three bands) are displayed. The Dirac point is enclosed in the black box. Inset contains schematic of reciprocal lattice and IBZ (blue triangle). 29

Fig 2.3. (a) Dispersion curves (specifically, the first and second bands) for $\beta = 0$ (solid lines) and $\beta = \pm 0.04$ (dotted lines) with $\Omega t - eff = 16.0$. The bandgap $\Omega bandgap$ opened from the Dirac point when $\beta = \pm 0.04$ is indicated by the shaded region. (b) Schematic of unit cells for Type A ($\beta > 0$) and Type B ($\beta < 0$) lattices. The smaller inductance (LI) is connected to the red electrode and the larger inductance (LII) is connected to the blue electrode. (c) Mode shapes evaluated at the K point for the first band (\blacktriangle) and second band (\blacksquare), revealing a band inversion between Type A ($\beta = 0.04$) and Type B ($\beta = -0.04$) unit cells. 33

Fig 2.4. (a) Band structure for a finite strip ($|\beta| = 0.04$, $\Omega t - eff = 16.0$, $\vartheta eff = 2$, and all parameters from Table 2.1) with a Type I interface. The colormap indicates the localization of the flexural displacement at the interface through the localization parameter Λ , with darker red shading indicating localized interface states ($\Lambda \approx 1$). The rectangular gray shaded region represents a frequency range where no bulk modes exist and corresponds to the topological bandgap. The diagram of the finite strip is shown below the band structure, with the interface used for Λ calculations enclosed in a dashed black box. A symmetric mode shape that is calculated from the interface state at $\Omega = 8.5$ with a localized displacement ($\Lambda m = 0.92$) is also shown. (b) Band structure and schematic for a finite strip with a Type II interface. At the bottom, an antisymmetric mode shape that is calculated from the interface state at $\Omega = 8.7$ (with $\Lambda m = 0.72$). 36

Fig 2.5. Schematics (left column) and steady-state response (right column) for guided wave propagation along (a) straight, (b) sharp corner, (c) shallow corner, and (d) ‘Z-shape with defect’ interfaces. In the schematics, R1, R2, and R3 represent output signal receivers and black lines enclose the interface between Type A and Type B lattices. Circuit parameters are defined as: $\beta = \pm 0.04$, $\Omega t - eff = 16.0$, and $\xi = 0.79$, resulting in $\Omega Dirac = 8.9$ and $\vartheta eff = 2$. A harmonic out-of-plane point excitation ($\Omega e = 8.7$) is applied where indicated by the black arrow. For steady-state response, the out-of-plane displacement amplitude is indicated by the color intensity. The

steady-state displacement fields illustrate the path tunability and topological protection of the proposed metamaterial. 39

Fig 2.6. (a) Dirac frequency Ω_{Dirac} as a function of circuit tuning frequency $\Omega t - eff$ for various ϑ_{eff} . The upper limiting frequency (Ω_{limit}) of 17.55 is indicated by a dotted black line. (b) Evolution of the first and second bands (all bands are shown as black lines) with increasing $\Omega t - eff$ (indicated by arrow) for $\Omega t - eff$ specified between 2 and 150 ($\beta = 0$ and $\vartheta_{eff} = 2$). Ω_{limit} is indicated by dashed red lines. (c) Evolution of third band for same set of parameters. (d) Band structure comparison for proposed metamaterial with high tuning frequency ($\Omega t - eff = 131$, indicated by solid red lines) and bare bimorph plate (indicated by dashed black line)..... 40

Fig 2.7. (a) Valley Chern magnitude $|Cv|$ calculated as a function of Dirac frequency Ω_{Dirac} and inductance perturbation magnitude $|\beta|$ with $\vartheta_{eff} = 0.42$. Increasing $|Cv|$ indicated by increasing brightness. (b) Relative bandgap $\Omega_{bandgap} - relative$ as a function of Dirac frequency Ω_{Dirac} and inductance perturbation magnitude $|\beta|$ with $\vartheta_{eff} = 0.42$. Increasing $\Omega_{bandgap} - relative$ indicated by increasing brightness. The achievable operating region is enclosed by the dashed black line. (c) Schematic for finite strip with Type I interface that is used to generate interface modes. Interface mode shapes for finite strip with unit cell parameters indicated by \bullet , \blacksquare , \blacktriangle , \star , and \blacklozenge markings in (b). 43

Fig 2.8. (a) Relative bandgap $\Omega_{bandgap} - relative$ as a function of Dirac frequency Ω_{Dirac} and inductance perturbation magnitude $|\beta|$ for PNN-PZT piezoelectric layers ($\vartheta_{eff} = 0.56$). Increasing $\Omega_{bandgap} - relative$ indicated by increasing brightness. The achievable operating region is enclosed by the dashed black lines. (c) Schematic for finite strip with Type I interface that is used to generate interface modes. Interface mode shapes for finite strip with unit cell parameters indicated by \bullet , \star , \blacklozenge , and markings in (a). (b) and (d) report the same results as (a) and (c), respectively, for PZT-5H with negative capacitance circuitry ($\vartheta_{eff} = 2$). Findings illustrate how the size of the achievable operating region, and thus tunability of the topological interface state, increases with larger ϑ_{eff} 45

Fig 2.9. (a) Schematics for thin plate metastructures with straight and Z-shaped Type I lattice interfaces (enclosed in black lines). A harmonic out-of-plane point excitation is applied where indicated by the arrow. Negative capacitance circuitry is connected such that $\vartheta_{eff} = 2$ in all cases. (b) Steady-state displacement fields for $|\beta| = 0.050$, $\Omega_{Dirac} = 10.4$, and $\Omega_e = 10.2$. (c) Steady-state displacement fields for $|\beta| = 0.032$, $\Omega_{Dirac} = 5.9$, and $\Omega_e = 5.9$. For steady-state response, the out-of-plane displacement amplitude is indicated by the color intensity. The results illuminate how tunable topological interface states can be harnessed to achieve topological wave propagation with adjustable levels of displacement localization over a large frequency range... 47

Fig 2.10. (a) Schematics for three lattice configurations attainable through circuit tailoring in the proposed metamaterial. Circuits are connected to electrodes that are represented by blue and red circles. For Configuration 3, electrodes pertaining to shorted circuits are omitted for clarity. Unit cell (enclosed in dashed black lines) circuit parameter details and lattice symmetries are listed below each schematic. (b) Dispersion diagrams corresponding to lattice Configurations 1-3 calculated using the PWE method with $\Omega t - eff = 28$ and $\vartheta_{eff} = 2$. Dirac 1, topological

bandgaps, and Dirac 2 are all highlighted for Configuration 1, Configuration 2, and Configuration 3, respectively. 49

Fig 2.11. (a) Band structure for a finite strip ($|\beta| = 0.70$, $\Omega t - eff = 28.0$, $\vartheta eff = 2$) with a Type I interface. Dark red shading indicates localized interface states ($\Lambda \approx 1$) and white shading indicates boundary states ($\Lambda \approx 0$). The rectangular gray shaded region represents a frequency range where no bulk modes exist. (b) A symmetric mode shape that is calculated from the interface state at $\Omega = 16.3$ with a localized displacement ($\Lambda m = 0.96$) is shown. Two boundary mode shapes that are calculated from the degenerate boundary states at $\Omega = 16.8$ ($\Lambda = 0$) are also shown. (c) (top row) Schematics for thin plate metastructures with straight and Z-shaped Type I lattice interfaces (enclosed in black lines). A harmonic ($\Omega e = 16.8$) out-of-plane point excitation is applied where indicated by ‘Src’. (bottom row) Steady-state displacement fields illustrating guided wave propagation for the high-frequency interface states. 51

Fig 2.12. (a) Band structure for a finite strip ($|\beta| = 0.70$, $\Omega t - eff = 28.0$, $\vartheta eff = 2$) comprised of Type B unit cells (no interface, see schematic). Dark red shading indicates localized boundary states ($\psi \approx 1$). The rectangular gray shaded region indicates a frequency range where no bulk modes exist. Left and right boundary mode shapes are shown. (b) (top) Schematic for thin plate metastructure with fixed and free boundaries selected to attain boundary states. A harmonic ($\Omega e = 16.5$) out-of-plane point excitation is applied where indicated by ‘Src’. (bottom) Steady-state displacement field illustrating flexural displacement confinement along plate boundaries. 52

Fig 3.1. (a) Schematic of the proposed 3D EM, a dashed black box encloses the unit cell. (b) Schematic of the proposed 3D EM unit cell comprised of an aluminum thin plate (gray), two silicone rubber interconnecting rods (purple), and 12 point masses (orange). A blacked dashed box encloses a single bistable element, with a detail view provided. 56

Fig 3.2. Normalized force-displacement ($F-d$) relation for the bistable internal elements. Stars mark stable states at $d = 0$ (stable state 1) and $d = 1.97$ (stable state 2). Circles mark intersections of $F1$ and $F3$ at $d1 = 0.06$ and $d2 = 1.94$ 60

Fig 3.3. (a) Direct lattice for the Type 0 switching configuration of the proposed 3D EM. The reciprocal unit cell is shown to the right, with the IBZ outlined in light blue. (b) Type A and Type B switching configurations, and their corresponding mode shapes at the K point for the bands that border the bandgap (where marked by \blacksquare and \blacktriangle). (c) Band structure for the 3D EM in the Type 0 configuration. The two-fold Dirac nodal line is enclosed in a dotted red box. Colormap indicates the mode polarization using the metric Π . Blue modes are primarily in-plane modes; black modes are primarily out-of-plane modes. $kx - ky$ and $ky - kz$ projections are shown below, with the Dirac degeneracy marked by an orange dot and line, respectively. (d) Band structure for the 3D EM in the Type A or B configuration (identical for both). The full topological bandgap is marked by gray shading, while the blue arrows mark the partial bandgap for in-plane modes. The inset contains a mode shape evaluated at the K point at the lower boundary of the partial bandgap (see \star). 62

Fig 3.4. Band structure for the proposed 3D EM with various $mratio$ values: (a) $mratio = 2$, (b) $mratio = 1.5$, (c) $mratio = 1$, and (d) $mratio = 0.75$ showing in-plane partial bandgaps of 2.5 kHz to 4.3 kHz, 2.8 kHz to 4.3 kHz, 3.2 kHz to 4.3 kHz, and 3.9 kHz to 4.4 kHz, respectively

(in-plane bandgaps are indicated by blue arrows and grey shading). The two-fold Dirac nodal line is enclosed in a dotted red box. Colormap indicates the mode polarization using the metric Π . Blue modes are primarily in-plane modes; black modes are primarily out-of-plane polarized.

..... 65

Fig 3.5. (a) Band structures for the Type 0 (left column) and Type A/B (right column) switching configurations for $Er = 50$ MPa. The degenerate eigenmodes at the K and H points are indicated with orange circles (left). The full topological bandgap is indicated by the gray shading (right). The band structures for the Type 0 (left) and Type A/B (right) configurations are shown for (b) $Er = 100$ MPa and (c) $Er = 1000$ MPa. Note that in (b) and (c), the increased Er prevents the opening of a full topological bandgap from the Dirac degeneracy..... 66

Fig 3.6. Berry Curvature Bpk for the Type A lattice: (a) band 1 ($B1Type A$) and (b) band 2 ($B2Type A$). Bpk for the Type B lattice: (c) band 1 ($B1Type B$) and (d) band 2 ($B2Type B$). The colormaps indicate the magnitude of Bpk 69

Fig 3.7. (a) Schematic of the supercell used for band structure calculations, with periodic and low-reflecting boundary conditions applied at the surfaces/directions that are indicated. Reciprocal space, where the light blue outline indicates one-half of the surface BZ projected onto the $ky - s - kz - s$ plane. Schematics for the proposed EM for a supercell with a (b) Type I and (c) Type II interfaces. (d) Band structure for supercells (both Type I and Type II interface configurations are superimposed). Topological bandgap is marked by gray shading. Colormap indicates confinement of mode displacement at the interface, with red indicating interface modes ($\Lambda \approx 1$) and black indicating bulk modes (if outside topological bandgap and $\Lambda < 1$) or boundary modes (if inside topological bandgap and $\Lambda \approx 0$). Mode shapes for Type I (purple star) and Type II (purple square) interfaces are at the bottom. (e) Band structure for the entire projected surface BZ for the supercell with a Type I interface. (f) Band structure for the entire projected surface BZ for the supercell with a Type II interface..... 70

Fig 3.8. (a) 3D metastructure built from $8 \times 8 \times 8$ unit cells and a schematic of three waveguide configurations used for full-scale modeling, where the input is marked by a black star. (b) Reconfigurable topological wave propagation illustrated by steady-state displacements for Configurations 1-3. Independent layer responses are marked by L1-L8, with L1 being the bottom layer..... 71

Fig 3.9. (a) Schematic of the bilayer unit cell comprised of two Type 0 monolayer unit cells stacked in the z direction. Band structure for this configuration is shown below, with a four-fold Dirac degeneracy at H enclosed in an orange box. The projection of the band structure over the $kx - ky$ and $ky - kz$ planes near H is shown in (c). (b) Schematic for the bilayer unit cell in the Type D switching configuration (Type A over Type B). Band structure for the 3D EM in Type C or D configuration (identical for both) is shown below. The full topological bandgap is marked by gray shading. The projection of the band structure over the $kx - ky$ and $ky - kz$ planes near H is shown in (d). (e) Diagram of the Type C (left) and Type D (right) bilayer unit cell switching configurations. Below are mode shapes at the H point for the bands that border the bandgap (as marked in (b) by \blacksquare and \blacktriangle), indicating a band inversion between the Type C and Type D lattices. 73

Fig 3.10. (a) Berry Curvature Bpk for the Type D lattice: (a) band 1 near H ($BH - 1Type D$), (b) band 2 near H ($BH - 2Type D$), (c) band 1 near H' ($BH' - 1Type D$), (b) band 2 near H' ($BH' - 2Type D$). The colormaps indicate the magnitude of Bpk 75

Fig 3.11. (a) Schematic of the bilayer supercell in metastable switching configurations with a Type III-1 (top) or Type III-2 (bottom) interface. (b) Band structure for the proposed EM for a supercell with a Type III-1 interface (note: Type III-2 band structure is identical). The colormap indicates the mode localization with metric Λ . Red modes are localized to the interface ($\Lambda \approx 1$), while black modes are bulk modes (if outside topological bandgap and $\Lambda < 1$) or boundary modes (if inside topological bandgap and $\Lambda \approx 0$). Representative mode shapes for the topological interface states (at M) are shown in (c). (d) 3D metastructure built from $8 \times 8 \times 9$ unit cells and a schematic of the waveguide configuration used for full-scale modeling, where the input is marked by a black star. (e) Layer-polarized topological wave propagation illustrated by steady-state displacement that is confined to four specific layers (outlined with dashed black lines). Independent layer responses are marked by L1-L9, with L1 being the bottom layer. 76

Fig 3.12. (a) Schematic (isometric and front views) of an eight-layer stack supercell, consisting of a four-layer Type III-2 interface stacked onto a four-layer Type III-1 interface, creating a Type IV interface. Band structure for the supercell with bilayer-locked and monolayer modes. Topological bandgap is marked by gray shading. Colormap indicates confinement of mode displacement at the interface, with red indicating interface modes ($\Lambda \approx 1$) and black indicating bulk modes (if outside topological bandgap and $\Lambda < 1$) or boundary modes (if inside topological bandgap and $\Lambda \approx 0$). Two bilayer-locked modes and six monolayer modes exist within the topological bandgap. One example of a bilayer-locked mode and two examples of monolayer modes are displayed to the right of the band structure. (b) Adaptive topological wave propagation of bilayer-locked state in 3D metastructure (straight line and sharp corner), calculated from full-scale numerical simulations. 78

Fig 3.13. (a) Layer converter schematic and steady-state displacement (side view and layer views) for excitation located at the star. Type I interfaces are marked in blue and Type II interfaces are marked in red. Steady-state displacement results illustrate layer conversion ($fe = 2920$ Hz) and wave splitting ($fe = 3020$ Hz) behavior (b) Wave-focusing gate schematic and steady-state displacement (side view and layer views) for excitation located at the star. Steady-state displacement results show a wave-focusing behavior that can act as a frequency-dependent ON/OFF gate..... 80

Fig 4.1. (a) A schematic of the 3D TM. (b) Isometric and top views of the metamaterial unit cell. (c) The band structure for the Type 0 lattice ($\alpha = 0$). The four Dirac nodal line degeneracies are indicated by the dotted red boxes. The colorbar indicates the mode polarization quantified by the parameter Π . (d) The band structure for the Type A/B ($\alpha = -0.11/0.11$) lattices. The band structures for Type A and Type B lattices are identical and superimposed. The three split Dirac degeneracies are marked by gray shading. (e) The mode shapes (taken along $K-H$) for the bands that border the four (D1, D2, D3, and D4) topological bandgaps in the $|\alpha|=0.11$ case, illustrating multimodal resonance. 87

Fig 4.2. Parameter study illustrating the effect of the (a) mass height hm and (b) spring ligament width $wl1$ on the Dirac nodal line frequency fd , which is taken at the midpoint between K and

H for each D1-D4 ($fd - D1$, $fd - D2$, $fd - D3$, and $fd - D4$). All presented values are for the Type 0 lattice configuration ($\alpha = 0$). The insets show the unit cell geometries for the minimum and maximum specified values of hm and $wl1$. The vertical dashed black lines indicate the specified hm and $wl1$ for all presented results in this chapter. The dashed red lines indicate the minimum frequency of the ligament/rod modes. 89

Fig 4.3. (a) Schematic of an eight-unit supercell with a Type I interface indicated by the blue planar surface. (b) The reciprocal space, with one-half of the surface BZ projected onto the $ky - s - kz - s$ plane outlined in light blue. (c) The band diagram for the supercell presented in (a). The red bands ($\Lambda i \approx 1$) are interface modes and the black bands ($\Lambda i \approx 0$) are bulk modes. Representative mode shapes for the hybrid torsional (purple star), in-plane torsional (purple circle), and in-plane translational (purple square) topological interface states are shown at the bottom. (d) The schematic and band diagram for a supercell comprised of eight Type B unit cells. The red bands ($\Lambda b \approx 1$) are boundary modes and the black bands ($\Lambda b \approx 0$) are bulk modes. Representative mode shapes for the topological boundary states are shown at the bottom. 91

Fig 4.4. (a) Schematic of a full-scale 3D metastructure constructed from an $8 \times 8 \times 6$ pattern of the metamaterial unit cell (left) and illustrations of V-shaped (middle) and Z-shaped (right) waveguides. The distribution of Type A and Type B unit cells is denoted by the letters “A” and “B.” (b) Steady-state displacement fields illustrating waveguides for all-layer (L1-L6) input excitations of 1.3 kHz (hybrid torsional), 3.6 kHz (in-plane torsional), and 4.9 kHz (in-plane translational). (c) Wave attenuation when an out-of-plane excitation is used in the frequency ranges of the in-plane topological states. (d) Steady-state displacement fields illustrating layer-locked waveguiding for two-layer (L1 and L4) input excitations of 1.4 kHz (hybrid torsional), 3.6 kHz (in-plane torsional), and 4.9 kHz (in-plane translational). For a two-layer input of 1.3 kHz, the hybrid torsional state exhibits wave transmission across all six layers. 93

Fig 4.5. (a) The experimental testbed with an inset showing detail for a unit cell. (b) A topological boundary state with hybrid torsional polarization that is found in the band structure of a four-unit supercell. (c) Experimentally measured out-of-plane velocity field (left) and FE simulated displacement field (right) for the 3D metastructure obtained at $fm1 = 1.3$ kHz. For clarity, both the full-scale and layer views of the simulated displacement field are shown. The schematic of the 3D metastructure testbed is given in the top right, where the blue shading represents the V-shaped waveguide. (d) The experimentally measured out-of-plane velocity (vop) for Point A (solid lines) and Point B (dashed lines) on each of the four layers. The frequency range for effective waveguiding is marked by the gray shading. (e) Experimentally measured out-of-plane velocity fields for L4 that illustrate the topological waveguide across a wide frequency range. A bulk response is demonstrated at 1.54 kHz. 95

Fig 4.6. (a) (top) A schematic of the 3D metastructure testbed where the red shading represents the path of a V-shaped waveguide. (bottom) A topological boundary state with an in-plane torsional polarization that is found in the band structure of a four-unit supercell. (b) Experimentally measured in-plane velocity field and FE simulated displacement field for L4 of the 3D metastructure obtained at $fm2 = 3.7$ kHz. (c) The experimentally measured in-plane velocity (vip) for a Point Inside and a Point Outside the waveguide on L4. The frequency range for effective waveguiding is marked by the gray shading. (d) (top) A schematic of the 3D metastructure testbed where the blue shading represents the path of a V-shaped waveguide.

(bottom) A topological boundary state with an in-plane translational polarization that is found in the band structure of a four-unit supercell. (e) Experimentally measured in-plane velocity field and FE simulated displacement field for L4 of the 3D metastructure obtained at $f_{m3} = 4.4$ kHz. (f) The experimentally measured in-plane velocity (v_{ip}) for a Point Inside and a Point Outside the waveguide on L4. The frequency range for effective waveguiding is marked by the gray shading. See Appendix C.9 for the transmission ratio plots that accompany (c) and (f). (g) Experimentally measured in-plane velocity fields for L4 that illustrate the in-plane topological waveguides across a wide frequency range. A bulk response is demonstrated at 4.12 kHz. 97

Fig 5.1. Description of the 2D HOTM and unit cell analysis. (a) Schematic of the 2D HOTM in a Type B lattice configuration, including a detail view of one resonator site. The aluminum substrate is light gray and the steel masses are dark gray. (b) Schematics and band structures for Type 0 and Type A/B lattices. The colormap indicates the mode polarization per the parameter Π . The four topological bandgaps are marked with gray shading and labeled I, II, III, and IV. (c) The mode shapes taken at M for the bands bordering the four topological bandgaps, illustrating the bending and torsional resonances. The out-of-plane displacement (w) fields are presented. 102

Fig 5.2. Phase profiles of the eigenmodes for bands 1-8, in order of lowest to highest frequency. Bands 1-4 are the lower-frequency bending modes and bands 5-8 are the higher-frequency torsional (about the connector ligaments) modes. The phase profiles are calculated at each of the high-symmetry points (Γ, X, M) for the Type A (left column) and Type B (right column) lattice configurations. The C_n rotation eigenvalues are labeled below each phase profile. 105

Fig 5.3. Supercell analysis for multiband edge states in the 2D HOTM. (a) A schematic of the supercell, where the interface between Type A and Type B sublattices is marked by the dashed black line. Below is the band structure, with the four topological bandgaps (I, II, III, and IV) uncovered in the unit cell analysis shaded in gray. Within the bandgaps, the red bands are topological edge states ($\Lambda \approx 1$) and the black bands are boundary states ($\Lambda \approx 0$). All other bands in the band structure are bulk bands ($0 < \Lambda < 1$). The total displacement (d) fields of the Edge state I, II, III, and IV eigenmodes are also included. (b) The out-of-plane displacement (w) fields for each of the four edge states, illustrating the bending (Edge states I and II) and torsional (Edge states III and IV) eigenmodes. 107

Fig 5.4. Eigenfrequency study for the full-scale structure with monomer corners. (a) Schematic of the full-scale structure with the Type B domain enclosed within the Type A domain, with the inset showing a monomer corner. Eigenfrequency spectra for topological (b) bandgap I, (c) bandgap II, and (d) bandgaps III and IV. The corner states are marked in red, edge states in blue, and bulk states in black. The bandgaps are indicated by the light gray shading. Eigenmodes illustrating the total displacement (d) fields for each of the edge states and corner states are also provided. 109

Fig 5.5. Eigenfrequency study for the full-scale structure with trimer corners. (a) Schematic of the full-scale structure with the Type A domain enclosed within the Type B domain, with the inset showing a trimer corner. Eigenfrequency spectra for topological (b) bandgap I, (c) bandgap II, and (d) bandgaps III and IV. The corner states are marked in red, edge states in blue, and bulk

states in black. The bandgaps are indicated by the light gray shading. Eigenmodes illustrating the total displacement (d) fields for each of the edge states and corner states are also provided. ... 111

Fig 5.6. Schematic of the full-scale plate in the monomer lattice configuration, with locations marked for the excitation (green star) and measurements of the bulk (yellow triangle), edge (purple square), and corner (blue circle) dynamic response. Normalized frequency response for Bandgaps I (b), II (c), III (d), and IV (e), with the insets showing displacement fields of edge, corner, and bulk states at specific frequency values. The displacement is normalized according to the maximum value calculated at the bulk, corner, and edge positions in the respective frequency ranges. 113

Fig 5.7. Schematic of the full-scale plate in the trimer lattice configuration, with locations marked for the excitation (green star) and measurements of the bulk (yellow triangle), edge (purple square), and corner (blue circle) dynamic response. Normalized frequency response for Bandgaps I (b), II (c), III (d), and IV (e), with the insets showing displacement fields of edge, corner, and bulk states at specific frequency values. The displacement is normalized according to the maximum value calculated at the bulk, corner, and edge positions in the respective frequency ranges. 114

Fig 5.8. Wave-based computing with the 2D HOTM. Schematics and normalized $|w|$ as a function of the phase offset θ for the (a) trimer and (b) monomer lattices. The excitations A and B have a baseline phase of θ_0 and are located where indicated by the yellow and purple stars. The displacement response is measured at corner QT or QM , where marked by the blue circles. The insets show the out-of-plane displacement $|w|$ fields calculated for each excitation frequency f , scaled to $Max|w\theta||f$. (c) A frequency-dependent logic gate constructed from the trimer lattice configuration by exciting the T-III A and T-III B corner states. The output threshold delineating 0 and 1 bits is marked by the horizontal dashed line. Truth tables are given for the OR and XOR logic operations. 116

Fig 5.9. An investigation of higher-order topological states in fractal lattices. Schematics and top views of (a) Configuration 1 and (b) Configuration 2 of the fractal HOTM. The two unique configurations of fractal lattices are created by patterning the Type A (orange) and Type B (gray) subdomains to create 1.89D Sierpiński Carpets. The borders (i.e., topological interfaces) between Type A and Type B subdomains are marked by dashed lines. There are eight small square subdomain borders, one medium square subdomain border, and one large square subdomain border. The four edges of the plate that make up the exterior boundary are fixed, as indicated by the slanted lines. The insets show a monomer corner, a dimer resonator pair, and a trimer corner for each lattice configuration. The eigenfrequency spectra for (c) Configuration 1 and (d) Configuration 2. The bulk and boundary states are indicated with black points, the topological edge states with blue points, and the topological corner states with points of various colors.... 119

Fig 5.10. Exemplar bulk, edge, and corner eigenmodes for the fractal HOTM in (a) Configuration 1 and (b) Configuration 2 that illustrate the wave confinement of the topological states. A larger total displacement d is indicated by increasing brightness..... 122

Fig 5.11. Eigenmodes for the corner states of the fractal HOTM in (a) Configuration 1 and (b) Configuration 2. For the full-scale results, a larger total displacement d is indicated by increasing

brightness. Insets of the out-of-plane displacements w are included to elucidate the symmetry characteristics of each mode. 123

Fig 6.1. A summary of the scholarly contributions. (a) The advanced class of novel TMs synthesized in this dissertation. (b) TMs that employ resonant circuit tuning and metastable switching to enable comprehensive on-demand tunability (i.e., responsiveness). (c) TMs that harness innovative realizations of local resonance to achieve broadband, multiband, and subwavelength (i.e., easily integrated) wave control. (d) TMs that exploit the rich dimensionality of 3D mechanical architectures for new wave control functionalities..... 127

Fig 6.2. Broader impacts of the novel class of TMs synthesized in this dissertation. The images of the TMs from this dissertation are enclosed in dashed black lines. (a) Examples of ways the novel TMs can enhance performance in engineering applications, including vibration mitigation, energy harvesting, sensing/NDE, and integrated phononic circuitry. The image of the 3D “stacked-chip” electrical circuit is reused from [310] under license CC BY 4.0. (b) The TMs and fundamental insight gained from this dissertation may inspire future research in the fields of topological mechanics, acoustics, photonics, and condensed matter physics. The quantum material image is reused from [311] with written permission from the publisher. The topological mechanics image is reused from [75] under license CC BY 4.0. The topological photonics image is reused from [312] with written permission from the publisher. The topological acoustics image is reused from [247] under license CC BY 4.0. 132

Appendix Figure A.1. Schematic of a single resonant circuit with negative capacitor connected in series. 140

Appendix Figure A.2. Isometric (a) and top (b) views of COMSOL geometry for unit cell dispersion analysis. All dimensions and materials are specified to match those utilized in the PWE model (see Table 2.1 in Chapter 2). The top view (b) contains distinctions for the different circuit conditions that are specified at the surface of the metamaterial. The gray area is at short circuit ($v = 0$), the orange area is at open circuit ($i=0$), and the purple area is the electrode surfaces that are connected to external circuitry. The open circuit (orange) area is not explicitly included in the PWE derivation, but is included in the COMSOL FE model to prevent the occurrence of a voltage discontinuity. 143

Appendix Figure A.3. Dispersion diagram for unit cell with $\beta = 0$ and $\Omega t - eff = 16.0$ computed from the COMSOL FE model. The colormap indicates the polarization of the modal displacement through the polarization parameter Π . Light yellow shading indicates modes dominated by out-of-plane (flexural) displacement ($\Pi \approx 1$). Dark blue shading indicates modes dominated by in-plane ($\Pi \approx 0$) displacement. 144

Appendix Figure A.4. Dirac frequency $\Omega Dirac$ as a function of circuit tuning frequency $\Omega t - eff$ for extreme ϑeff . The upper limiting frequency ($\Omega limit$) of 17.55 is indicated by a dotted black line. $\Omega limit$ is unchanged, even for extremely small ($\vartheta eff = 0.05$) or large ($\vartheta eff = 422$) effective coupling values. 146

Appendix Figure A.5. (a) Band structure for $\vartheta eff = 0.42$ (solid black lines) and $\vartheta eff = 2$ (dash-dot blue lines) with $\beta = 0$ and $\Omega t - eff$ selected such that $\Omega Dirac = 10.4$. (b) Band

structure for $\vartheta_{eff} = 0.42$ (solid and dashed black lines) and $\vartheta_{eff} = 2$ (dash-dot blue lines) with various inductance perturbations $|\beta|$ to open the Dirac point located at $\Omega_{Dirac} = 10.4$. (c) Band structure for $\vartheta_{eff} = 0.42$ (solid black lines) and $\vartheta_{eff} = 2$ (dash-dot blue lines) with $\beta = 0$ and $\Omega t - eff$ selected such that $\Omega_{Dirac} = 5.9$. (d) Band structure for $\vartheta_{eff} = 0.42$ (solid and dashed black lines) and $\vartheta_{eff} = 2$ (dash-dot blue lines) with various $|\beta|$ to open the Dirac point located at $\Omega_{Dirac} = 5.9$ 147

Appendix Figure A.6. (a) Schematics for thin plate metastructures with straight and Z-shaped Type I lattice interfaces (enclosed in black lines). A harmonic out-of-plane point excitation is applied where indicated by the black arrow. Negative capacitance circuitry is connected such that $\vartheta_{eff} = 2$ in all cases. (b) Steady-state displacement fields for $|\beta| = 0.014$, $\Omega_{Dirac} = 5.9$, and $\Omega e = 5.9$. (c) Steady-state displacement fields for $|\beta| = 0.060$, $\Omega_{Dirac} = 5.9$, and $\Omega e = 5.9$. For steady-state response, the out-of-plane displacement amplitude is indicated by the color intensity. The results illuminate how wave propagation can become delocalized at sharp corners for a $|\beta|$ that is specified as too small or too large. 149

Appendix Figure A.7. Band structure for a finite strip ($|\beta| = 0.70$, $\Omega t - eff = 28.0$, $\vartheta_{eff} = 2$) with a Type II interface. Dark red shading indicates localized interface states ($\Lambda \approx 1$) and white shading indicates boundary states ($\Lambda \approx 0$). The rectangular gray shaded region indicates a frequency range where no bulk modes exist. Below the band structure, an antisymmetric mode shape that is calculated from the interface state at $\Omega = 15.8$ with a localized displacement ($\Lambda = 0.91$) is shown. 151

Appendix Figure B.8. (a) Schematic (isometric and front views) of an eight-layer stack supercell, consisting of a four-layer Type III-2 interface stacked onto a four-layer Type III-1 interface, creating a Type IV interface. (b) Band structure for the eight-layer supercell. Topological bandgap is marked by gray shading. Colormap indicates confinement of mode displacement at the interface, with red indicating interface modes ($\Lambda \approx 1$) and black indicating bulk modes (if outside topological bandgap and $\Lambda < 1$) or boundary modes (if inside topological bandgap and $\Lambda \approx 0$). Two bilayer-locked modes and six monolayer modes exist within the topological bandgap. Displacement is localized at an interface on the layers indicated under the “Disp. Loc.” heading (e.g., for the mode with displacement localized to layer 1, “L1” is indicated to the right of the mode shape). The two L4-L5 modes are the bilayer-locked states, while the other six (L1, L2, L3, L6, L7, and L8) are monolayer states. (c) Schematic, side view, isometric view, and layer view of topological wave propagation of a bilayer-locked state in a 3D metastructure. The excitation location is marked by a black star. 152

Appendix Figure B.9: (a) Schematic of the surface state wave splitter. The excitation location is marked by a black star. (b) Side view, isometric views (From above and below), and layer view of topological wave propagation in the surface state wave splitter. Schematic and steady-state displacement fields for (c-e) reconfigurable layer converter and (f) multi-state wave splitter. In all schematics (left side, a-f), Type I interfaces are indicated by blue shading and Type II interfaces by red shading. S1, S2, and S3 are sections of the 3D metastructure with specified metastable switching configurations. L1-L8 are the eight layers of the metastructure, with L1 being the bottommost layer. For all configurations in this figure (a-f), low-reflecting boundary conditions are applied to the boundaries perpendicular to the x - y plane. 156

Appendix Figure C.10: COMSOL model for the metamaterial unit cell used in FE simulations. 157

Appendix Figure C.11: (a) Evolution of the D1, D2, D3, and D4 partial bandgaps as a function of the mass perturbation magnitude $|\alpha|$. Open circles and crosses denote the lower and upper boundaries of the bandgaps opened from the four Dirac degeneracies. The D1, D2, D3, and D4 bandgaps are represented by the yellow, cyan, purple, and orange shaded regions, respectively. (b) Band structure for the large mass perturbation ($|\alpha| = 0.40$) case. The topological partial bandgap opened from the Dirac degeneracy D1 is marked with gray shading. The mode shapes for the bands bordering the bandgap illustrate the out-of-plane translational displacements of the resonators ($\Pi \approx 1$). (c) An interface mode that emerges within the D1 topological bandgap with displacement confined at the interface between the Type A and Type B segments in an eight-unit supercell. 158

Appendix Figure C.12. Berry Curvature Bpk evaluated for the bands bordering the topological bandgap that emerges from D2. (a) Bpk for band 1 ($B1Type A$) and band 2 ($B2Type A$) of the Type A lattice. (b) Bpk for band 1 ($B1Type B$) and band 2 ($B2Type B$) of the Type B lattice. The colorbars indicate the magnitude of Bpk . The opposite $Bp(k)$ values illustrate the band inversion between Type A and Type B lattices. 160

Appendix Figure C.13. Berry Curvature Bpk evaluated for the bands bordering the topological bandgap that emerges from D3. (a) Bpk for band 1 ($B1Type A$) and band 2 ($B2Type A$) of the Type A lattice. (b) Bpk for band 1 ($B1Type B$) and band 2 ($B2Type B$) of the Type B lattice. The colorbars indicate the magnitude of Bpk . The opposite $Bp(k)$ values illustrate the band inversion between Type A and Type B lattices. 161

Appendix Figure C.14. Berry Curvature Bpk evaluated for the bands bordering the topological bandgap that emerges from D4. (a) Bpk for band 1 ($B1Type A$) and band 2 ($B2Type A$) of the Type A lattice. (b) Bpk for band 1 ($B1Type B$) and band 2 ($B2Type B$) of the Type B lattice. The colorbars indicate the magnitude of Bpk . The opposite $Bp(k)$ values illustrate the band inversion between Type A and Type B lattices. 162

Appendix Figure C.15. Selected mode shapes for the bands bordering the four topological bandgaps that emerge when $|\alpha| = 0.11$, illustrating the four primary resonant modes of the metamaterial: (a) D4: in-plane (x - y) translational at 5.0 kHz ($\Pi \approx 0$), (b) D3: in-plane (x - y) twisting at 3.5 kHz ($\Pi \approx 0$), (c) D2: rocking at 1.5 kHz ($\Pi = 0.6$), and (d) D1: out-of-plane translational at 0.36 kHz ($\Pi \approx 1$). Both isometric and top views are provided. These mode shapes are taken for a wave vector k specified at the midpoint of the K - H line in the reciprocal unit cell. 163

Appendix Figure C.16. Band structure for the $\alpha = 0$ case with (a) $hm = 0$ mm (no mass), (b) $hm = 4$ mm, and (c) $hm = 12$ mm. The Dirac degeneracies are enclosed in dotted red boxes. These plots illustrate how increasing the resonator mass lowers the frequency fd of the D1, D2, D3, and D4 ($fd - D1$, $fd - D2$, $fd - D3$, and $fd - D4$) degeneracies and separates them from the ligament/rod modes that exist above 6.5 kHz. The horizontal red dashed line indicates the frequency (6.5 kHz) where the undesirable ligament/rod modes emerge that may interact with the topological bands and inhibit the successful formation of topological bandgaps and waveguides.

The insets illustrate how these modes are dominated by the displacements of the aluminum ligaments and interconnecting rods. For the $hm = 0$ mm (no mass) scenario in a), only D1 and D2 are visible at frequencies less than 12 kHz, and the band structure is heavily contaminated with modes that would make it difficult to open topological bandgaps. This dense band structure is a common feature of 3D EMs, and makes the realization of low-frequency and multiband topological states in 3D structures challenging. Conversely, for a higher value of $hm = 12$ mm, all four degeneracies D1-D4 are well separated from the ligament/rod modes in the frequency domain (i.e., $fd - D1$, $fd - D2$, $fd - D3$, and $fd - D4$ are all well below the red dashed line) and are thus not susceptible to interactions with them. 164

Appendix Figure C.17. Analysis establishing the design criteria for the out-of-plane lattice constant h_0 , which defines the height of the interconnecting rods. (a) Band structure for $\alpha = 0$ and $h_0 = 20$ mm. The Dirac degeneracies are enclosed in dotted red boxes and the horizontal red dashed line indicates the lowest frequency of the ligament/rod modes. For this case, the ligament/rod modes emerge at 7.20 kHz, well distanced from the D3 and D4 Dirac degeneracies that are located at $fd - D3 = 3.66$ kHz, and $fd - D4 = 4.76$ kHz. (b) The ligament/rod mode frequencies are evaluated as a function of h_0 . As h_0 is increased, the mass of the interconnecting rods increases and the lateral stiffness decreases, leading to a reduction in the ligament/rod mode frequency boundary. For $h_0 \geq 35$ mm, the ligament/rod modes overlap with $fd - D3$ and $fd - D4$. The band structures for $|\alpha| = 0.11$ are calculated with (c) $h_0 = 35$ mm and d) $h_0 = 45$ mm. These band structures provide examples of why overlap of the topological bands with the ligament/rod modes is detrimental to the formation of topological bandgaps. The negative effects of this scenario are twofold: (i) the topological bandgaps are destroyed by the ligament/rod mode band crossing and (ii) the topological properties, as quantified by valley Chern number calculations (see Appendix C.3), are contaminated. An out-of-plane lattice constant of $h_0 = 25$ mm is chosen in Chapter 4 to ensure that no undesired band crossing occurs and provide sufficient mechanical clearance for $|\alpha|$ up to a value of $|\alpha| = 0.50$ 165

Appendix Figure C.18. (a) The band structure for the supercell with a Type I interface presented in Fig 4.3a of Chapter 4. (b) The band structure for the supercell constructed from all Type B unit cells presented in Fig 4.3d of Chapter 4. In a) and b), the blue bands ($\Pi \approx 0$) are in-plane modes, the yellow bands ($\Pi \approx 1$) are out-of-plane modes, and the green bands ($\Pi \approx 0.5$) are modes with mixed polarization. The bulk modes that pass through the D2 (1.3 to 1.5 kHz) and D4 (4.5 to 5.1 kHz) bandgaps contain different polarizations than the respective topological states that exist in each of the bandgaps and do not visibly interact (e.g., veering or modal energy exchange) with them. These characteristics limit the possibility of unwanted mode hybridization or coupling of bulk modes with the topological states. (c) A mode shape taken at Γ (see the purple square in d) that illustrates the quasi-rigid body motion of the interconnecting rods. (d) Demonstration of how the supercell (eight-unit supercell with Type I interface) band structure can be tailored by adjusting the elastic modulus of the interconnecting rods Er . For aluminum rods ($Er = 69$ GPa), wave energy transmission in the z direction is limited to the long wavelength regime for a frequency range of 1.28 to 1.33 kHz. Above 1.33 kHz, the Γ - Z directional bandgap leads to layer-locked wave propagation (e.g., given a 1.4 kHz excitation in Fig 4.4). On the other hand, for rods made from a rubber-like material ($Er = 0.069$ GPa), the frequency range of z direction transmission shrinks to 1.28 to 1.30 kHz and the portion of the band with nonzero group velocity extends beyond the long wavelength regime. (e) A comparison

of the supercell modes for the D2 hybrid torsional, D3 in-plane torsional, and D4 in-plane translational topological states. All mode shapes are evaluated at Γ . The mode shapes illustrate how the D2 hybrid torsional state transmits energy in the z direction by coupling the hybrid torsional resonant mode with the motion of the interconnecting rods. The D3 and D4 in-plane resonances do not couple well with the interconnecting rods (which show negligible displacement in those cases) and as a result do not propagate elastic waves in the z direction, creating layer-dependent behavior. 166

Appendix Figure C.19. Theoretical investigation of the 2D topological metamaterial. (a) Unit cell analysis. (b) Supercell study. (c) Full-scale simulations of topological wave control. 167

Appendix Figure C.20. Experimental investigation of wave control in the 2D topological metamaterial. (a) A schematic of the experimental setup. (b) Experimentally measured out-of-plane velocity magnitudes (v_{op}) for the frequency range of the hybrid torsional 2 topological waveguide. (c) Experimentally measured out-of-plane transmission ratio for the hybrid torsional 2 topological waveguide, where the input location is treated as the reference. (d) Steady-state wave fields illustrating topological waveguiding achieved by activating the hybrid torsional 1 and hybrid torsional 2 topological states illustrated in Appendix Figure C.19b. The experimental results reveal successful confinement of the dynamic response into the designated waveguide and agree with the theoretical predictions displayed in Appendix Figure C.19c. 168

Appendix Figure C.21. (a) Components of the 3D metastructure assembly. (b) The out-of-plane and in-plane piezo-actuators. (c) A schematic of the experimental setup. In-plane measurements require the use of all three lasers, out-of-plane measurements only require the use of one laser. 170

Appendix Figure C.22. Experimentally measured transmission ratio (left column) and out-of-plane velocity magnitude v_{op} (right column) for (a) L4, (b) L3, (c) L2, and (d) L1 of the 3D metastructure. (e) Transmission ratio for the in-plane twisting (left) and in-plane translational (right) experimental measurements. All transmission ratios are defined using the relevant PZT input location as the reference. The frequency ranges where the wave field is trapped in the designated waveguide are indicated by gray shading. 171

Appendix Figure D.23: COMSOL model of the 2D HOTM for FE calculations. 172

Appendix Figure D.24. A description of the band inversion that occurs between the Type A and Type B domains. The left and right panels contain the band structures for the Type A and Type B lattices, with the “+” and “-” labels representing positive and negative eigenmode parities, respectively. The parity exchange at X for both sets of bands (1-4: bending and bands 5-8: torsional) is displayed in the middle panel. 174

Appendix Figure D.25. Corner state out-of-plane (w) wave fields calculated in the eigenfrequency study. (a)-(c) Eigenmodes for the monomer corner lattice configuration. (d)-(h) Eigenmodes for the trimer corner lattice configuration. The inset shows a zoomed-in view of the displacement field for the corner state. The black dashed line in the inset is the angular bisector for the corner that is used for symmetry evaluations. 176

Appendix Figure D.26. An investigation of the effect of damping on the frequency response of the 2D HOTM. The out-of-plane displacement amplitude $|w|$ is normalized according to the maximum value calculated at resonance (746.6 Hz) for the T-IV Corner state in the no damping case ($\eta = 0\%$). Insets show the displacement fields with successful wave confinement for the cases of $\eta = 0.1\%$ and $\eta = 0.01\%$ 178

Appendix Figure D.27. An exemplar boundary mode (735 Hz) and an exemplar in-plane bulk mode (743 Hz) for the fractal HOTM in Configuration 1. These modes do not couple with or inhibit the emergence of topological edge and corner states. The boundary states (left panel, 735 Hz) do not strongly interfere with topological states because they exist in a frequency range (734-740 Hz) with separation from all topological states. The in-plane ($\Pi \approx 0$) bulk state (right panel, 743 Hz) arises because, as mentioned in Section 5.3, in-plane bands do cross through topological bandgaps III and IV. However, these purely in-plane modes not directly interact with the torsional topological states..... 179

List of Appendices

Appendix A: Supplemental Information for Chapter 2	139
Appendix B: Supplemental Information for Chapter 3.....	152
Appendix C: Supplemental Information for Chapter 4.....	157
Appendix D: Supplemental Information for Chapter 5	172

List of Abbreviations

- EM** Elastic metamaterial
TM Topological metamaterial
HOTM Higher-order topological metamaterial
nD n-dimensional (e.g., 1D: one-dimensional)
TI Topological insulator
HOTI Higher-order topological insulator
QHE Quantum Hall effect
QSHE Quantum spin Hall effect
QVHE Quantum valley Hall effect
SIS Space inversion symmetry
TRS Time reversal symmetry
FE Finite element
PWE Plane wave expansion
BZ Brillouin zone
IBZ Irreducible Brillouin zone
DOF Degree-of-freedom
SSH Su–Schrieffer–Heeger
PI Physical intelligence

Abstract

Elastic metamaterials enable control over the propagation of vibrations and elastic waves in mechanical structures, a useful feature that has been employed in numerous applications, such as energy harvesting, seismic mitigation, vibration and noise mitigation, sensing and imaging, and information processing. Recently, researchers have incorporated topological phase theory from condensed matter physics into elastic metamaterials to attain new functionality and robustness. Elastic wave control with these so-called topological metamaterials is immune to unwanted performance degradation in the presence of structural imperfections. Topological metamaterials also facilitate the manipulation of elastic wave energy in nearly arbitrary directions and serve as excellent macroscale platforms to investigate quantum transport physics.

While topological metamaterials have demonstrated extraordinary control over elastic wave propagation, research gaps exist that are hindering their implementation in technical applications and provide opportunities for advancement. Easily integrated (i.e., compact) topological metamaterials that provide comprehensively adaptable wave control have yet to be developed. Furthermore, the topological metamaterials studied to date are often constrained to function over a fixed, singular, and narrow frequency bandwidth. Finally, despite plenty of studies on 1D and 2D topological metamaterials, topological phases in 3D and fractal mechanical systems have yet to be fully explored. To address the research gaps and advance the state of the art, this thesis explores a new class of advanced topological metamaterials that achieve responsive, broadband, easily integrated, and multidimensional elastic wave control and uncover new knowledge in topological and elastic wave physics. To achieve the research vision, the suite of novel topological metamaterials presented in this dissertation is synthesized through the understanding and harnessing of comprehensive on-demand adaptivity, local resonance, higher-order topological phases, and the rich dimensionality of 3D mechanical structures.

Four novel topological metamaterials are created and investigated in this dissertation. First, a 2D topological metamaterial is synthesized that harnesses resonant piezoelectric circuitry for comprehensively tunable elastic wave control. This innovative metamaterial unlocks the capability

to concurrently adjust the path, shape, and frequency of topological states, operates over a broad and subwavelength frequency bandwidth, and facilitates a new understanding of adaptive topological wave control. Next, a 3D topological metamaterial is proposed that can be tuned on-line through metastable elements. By taking advantage of the adaptivity of this 3D metastable metamaterial, the path of 2D topological surface states is on-demand controlled for the first time, a bilayer-locked topological state is discovered, and 3D elastic wave networks with unprecedented dimension-switching, filtering, and splitting capabilities are realized. Taking inspiration from the first two studies, a novel 3D topological metamaterial is created that exploits multimodal local resonance to achieve wave control that is low-frequency, multiband, and polarization-dependent. Outcomes from this work include the first full-field experimental measurements of a 2D topological state and multi-polarized waveguides in a 3D mechanical structure. Finally, higher-order topological phases and multimodal resonance are used to synthesize a 2D topological metamaterial that attains 0D and 1D topological waveguides across multiple frequency bands. The unique capabilities of this novel metamaterial are employed to investigate topological wave control in fractal geometries and realize wave-based mechanical logic gates. Overall, this thesis presents groundbreaking results in elastic wave control, establishing unprecedented capabilities that hold promise for a diverse set of engineering applications. Moreover, this research uncovers new fundamental insights into the interplay between topological and elastic wave physics, with implications across multiple disciplines in the physical sciences.

Chapter 1. Introduction

1.1 Background

1.1.1 Elastic metamaterials

Modern engineering applications (e.g., autonomous electric vehicles, interconnected wireless devices, on-chip transducers, robotic systems, and biomedical implantable devices) often require materials with extraordinary performance and function. The bulk properties of conventional structural materials (e.g., metals, ceramics, plastics) are determined by the composition of their atomic-scale building blocks, which are atoms and molecules. To surpass what is attainable with these conventional materials, researchers have developed *metamaterials* [1,2,11–14,3–10] to control the electromagnetic (e.g., photonic), acoustic, and mechanical properties of advanced structural systems. Metamaterials are constructed from the rational geometric design of internal building blocks that are microscopic to macroscopic in size and fabricated from conventional bulk materials. These internal building blocks are tessellated into periodic (or sometimes quasiperiodic or random) patterns to create the metamaterial architecture. With this unique design methodology, metamaterials can achieve extraordinary properties that are “beyond” what is achievable with the constituent bulk materials (e.g., negative Poisson’s ratio, anomalous refractive index, negative effective mass or modulus, non-reciprocal behaviors [1,2,11–14,3–10]).

The need to manipulate vibrations and elastic waves in mechanical structures poses a formidable technical challenge that has widespread implications across numerous fields, including energy generation [15], manufacturing [16,17], transportation [18], civil infrastructure [19,20], and aerospace/defense [21–24] (Fig 1.1). Metamaterials that are specifically designed to control vibrations and elastic waves in mechanical structures are known as *elastic metamaterials* (EMs) [1–4,7,12]. Apart from addressing the aforementioned need for vibration and elastic wave control in many critical industries, EMs contain intriguing characteristics that have made them the subject of significant research interest, some of which include:

- EMs can be used to create load-bearing structural systems.

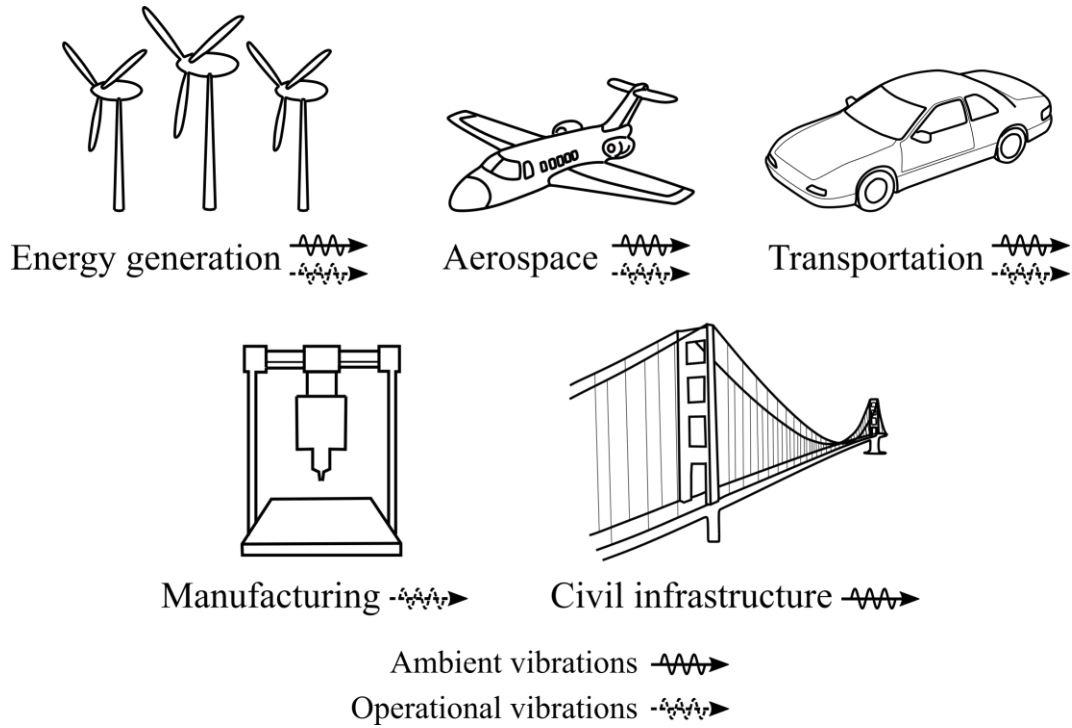


Fig 1.1. Vibrations and elastic waves are nearly ubiquitous in mechanical structures. Structures are exposed to ambient vibrations from the external environment (e.g., wind loading, seismic events) and operational vibrations caused by the active operation of mechanical systems (e.g., aircraft or automotive engine, CNC turning).

- EMs contain a larger set of wave polarizations (three: two quasi-shear and one quasi-longitudinal) than acoustic (one: longitudinal) and electromagnetic/photonic (two: two transverse) metamaterials [25]. This feature of EMs results in both technical challenges and a rich design space.
- Elastic waves can hold a high amount of energy, are scalable, are not easily “jammed,” and generally have low material and radiation losses for frequencies less than 100 kHz [26,27].
- EMs can be designed to operate in a low-frequency regime, which is defined in this thesis as less than 20 kHz (i.e., the audible frequency regime). Functionality in this frequency range is crucial for many structural applications, such as those shown in Fig 1.1.

With these features in mind, EMs have been investigated as a method to improve performance and achieve new functionality in applications that include, but are not limited to, vibration energy harvesting [28–33], seismic mitigation [7,34,35], vibration and noise mitigation [36–43], sensing/imaging [44–47], actuation [12,48,49], and information processing [50–54].

EMs traditionally derive many of their intriguing attributes from the phenomenon of local resonance [2,55–63]. Local resonance in EMs is realized through the embedding or attaching of spring-mass resonators to a mechanical medium, which is typically a continuous or lattice-like

mechanical structure. A model of a one-dimensional (1D; note that “dimension” throughout this dissertation refers to the spatial dimension) locally resonant EM is shown in Fig 1.2a, where local resonators with stiffness k_r and mass m_r are attached to a mechanical medium that is modeled as a spring-mass lattice with stiffness k_1 and mass m_1 . The unit cell, which is the smallest repeated unit of the EM, is periodically tessellated to create the lattice that makes up the EM. The size of the unit cell in an EM is defined by the lattice constant (labeled as a in Fig 1.2a), which represents the characteristic size of the EM. When an EM with local resonance is subjected to a dynamic excitation near the natural frequency of the resonators, $f_r = \frac{1}{2\pi} \sqrt{\frac{k_r}{m_r}}$ (i.e., the resonant frequency), there is energy stored by the resonator masses and then extracted from the system as negative work [57,60]. In other words, there is an energy exchange between the elastic wave and the local resonators that leads to wave attenuation near the frequency f_r . This phenomenon can be analyzed using the dispersion relation (i.e., the band structure) of the EM (Fig 1.2b), which characterizes wave propagation by relating the wave frequency (temporal frequency) f and wavenumber k . The wavenumber refers to the spatial frequency of a wave, is also known as the wave vector, and is related to the spatial wavelength λ of the wave through $k = 1/\lambda$. The vertical dashed lines at $k = \pi/a$ in the band structures of Fig 1.2b signify the border of the first Brillouin zone, which encapsulates the periodic unit cell in reciprocal space. Reciprocal space, or k -space, is the space where the Fourier transform of the lattice in direct/real space is represented and characterizes the periodicity of a system [64]. A system with local resonators that are decoupled from a generic mechanical medium is considered first, as shown at the bottom of the left panel in Fig 1.2b. Assuming the mechanical medium is non-dispersive (meaning all waves have the same phase speed $c_p = 2\pi f/k$) and linear, the wave propagation in it can be represented by a straight line with slope c_g , which is the wave speed in the medium (left panel in Fig 1.2b) [56]. The decoupled local resonators are represented by a flat band at f_r , since there is no wave propagation in the disconnected resonators (i.e., the wave is stationary and the wave speed $c_g = 0$). When the resonators are connected to the mechanical medium (see the bottom of the right panel in Fig 1.2b), they interact with the elastic waves propagating through the medium. This interaction results in an energy exchange and mode hybridization that appears in the band structure as two continuous bands (see the two lowest frequency bands represented by solid lines in the right panel of Fig 1.2b) that are formed from the avoided crossing of the two independent bands shown in the left panel

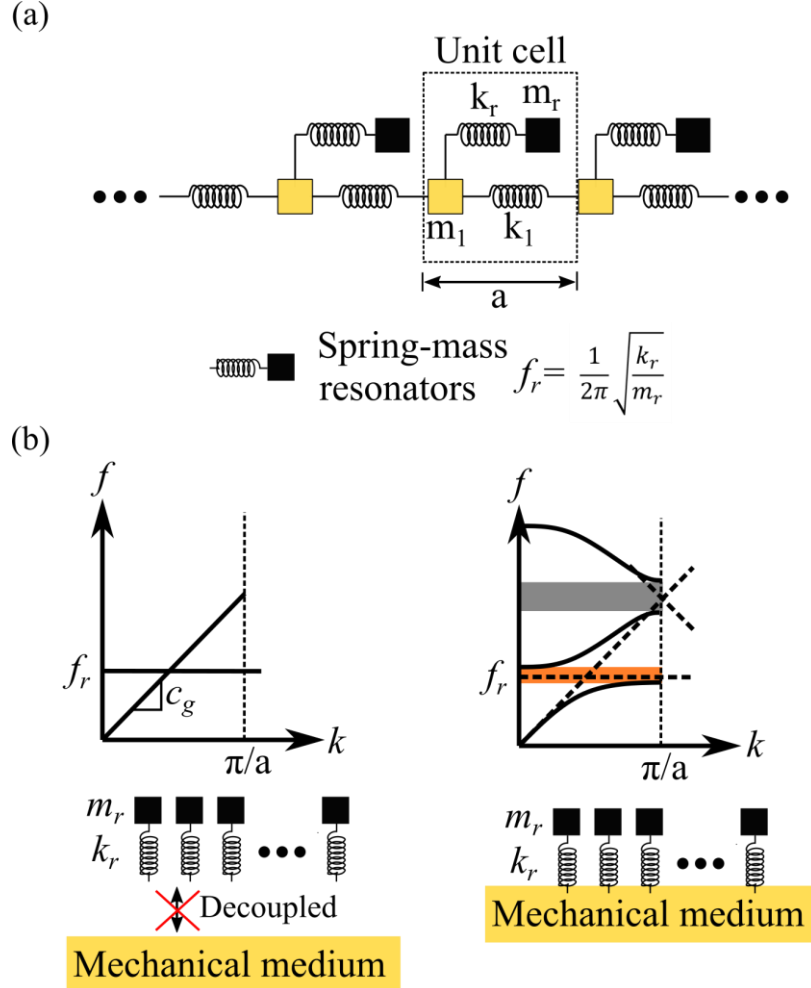


Fig 1.2. (a) Simplified model of local resonance in a 1D spring-mass lattice. Local resonators have mass m_r and stiffness k_r ; spring-mass lattice has mass m_1 and stiffness k_1 . (b) Band structures for a locally resonant EM with resonators that are decoupled from a generic mechanical medium (left panel) and resonators attached to a generic mechanical medium (right panel). The locally resonant bandgap is designated by the orange shading and the Bragg bandgap is designated by the gray shading.

of Fig 1.2b [56]. As illustrated by the orange shading in Fig 1.2b, the resulting two continuous bands are separated by a frequency gap centered near f_r , known as a locally resonant bandgap, where elastic waves do not propagate and there is wave/vibration attenuation. The frequency range of this locally resonant bandgap is dependent on the properties of the resonators, i.e., k_r and m_r , which means that locally resonant bandgaps can be specified at very low frequencies if desired and are not reliant on the spatial periodicity of the lattice (i.e., on the value of the lattice constant a). This lattice size-independent feature distinguishes local resonance from the other physical mechanism that is often used to achieve wave/vibration bandgaps: the Bragg scattering phenomenon. Bragg bandgaps are formed in periodic mechanical structures that are often referred

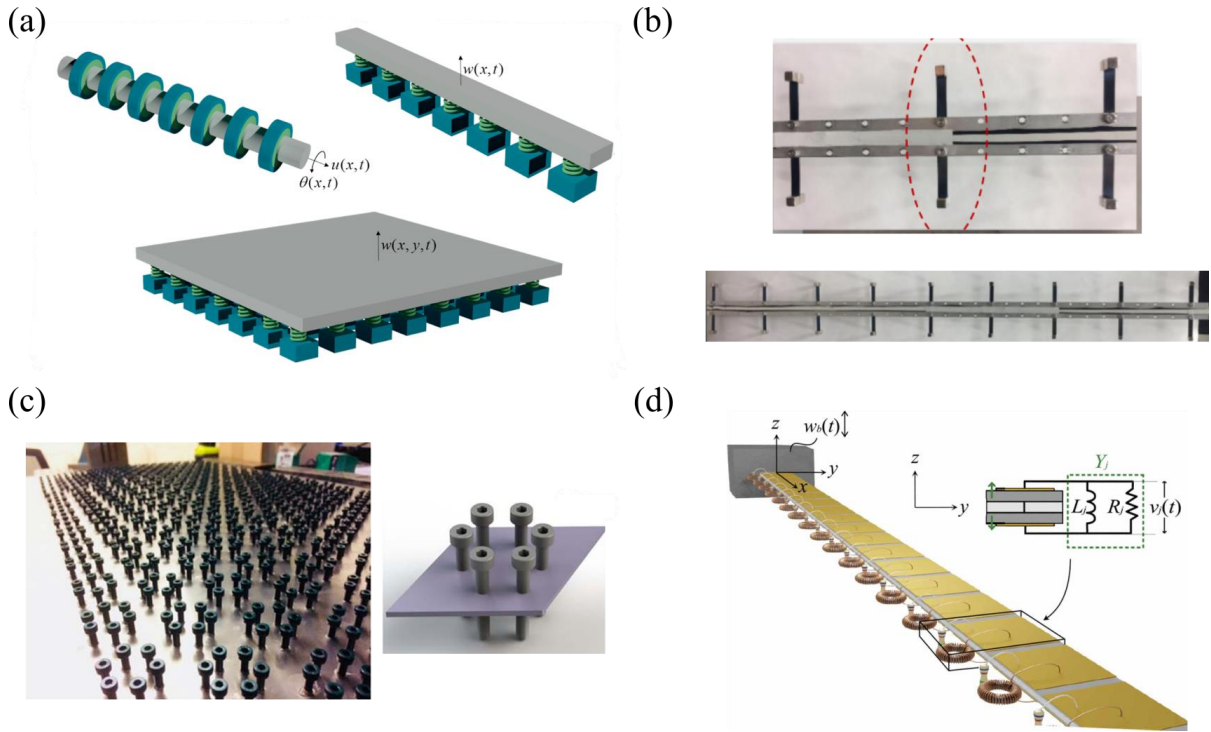


Fig 1.3. Local resonance in EMs. (a) Simplified local resonators attached to a 1D rotating rod, a 1D beam, and a 2D thin plate (figure reused from [65] with written permission from the publisher). (b) Beam and tip-mass resonators attached to a 1D beam (figure reused from [65] with written permission from the publisher). (c) Bolt resonators attached to a 2D thin plate (figure reused from [66] under license [CC BY 3.0](https://creativecommons.org/licenses/by/3.0/)). (d) Electromechanical resonators coupled to a 1D beam (figure reused from [67] with written permission from the publisher).

to as *phononic crystals* [2,56,58]. The Bragg bandgaps in these so-called phononic crystals are formed by the destructive interference of incident and scattered waves at wavelengths λ near the spatial periodicity of the lattice a , according to the Bragg condition $a = n \frac{\lambda}{2}$ for an integer n [2,56,58]. This destructive interference is caused by a periodic impedance mismatch that is engineered into the phononic crystals. The periodic impedance mismatch has been achieved through many different methods, with two primary examples being material periodicity and geometric periodicity (e.g., periodically arranged holes in a thin plate) [2,56,62,68–72]. Per the Bragg condition, the center frequency of Bragg bandgaps is determined by the characteristic size of the lattice (a), and thus large structures are required to achieve large wavelength λ and low-frequency Bragg bandgaps [2,56,58]. In the band structure, Bragg bandgaps emerge from band folding at the edges of the first Brillouin zone near frequencies that are governed by the Bragg condition (e.g., see the gray shading in the right panel of Fig 1.2b). The frequency range of the Bragg bandgap indicated by the gray shading in the right panel of Fig 1.2b can be changed by adjusting the lattice constant a , whereas the frequency range of the locally resonant bandgap

indicated by the orange shading in the right panel of Fig 1.2b can be tailored by adjusting the properties of the local resonators m_r and k_r . The ability to modify the frequency properties of locally resonant EMs without adjusting the lattice constant a is a significant advantage that has been heavily exploited to achieve low-frequency vibration and elastic wave control in compact mechanical structures [2,55–63].

Examples of EMs that are comprised of spring-mass resonators affixed to continuous mechanical structures are given in Fig 1.3a, where resonators are attached to a 1D rotating rod, 1D beam, and 2D thin plate [65]. Beyond the simplified spring-mass resonators depicted in Fig 1.3a, there are a wide variety of practical spring-mass resonator designs that can be physically realized and attached to or embedded within structures. Some examples from previous research include two-phase structures with soft material inclusions in a stiff 2D matrix [73], three-phase structures such as lead spheres coated in silicone rubber embedded into an epoxy matrix [55], beam and tip mass resonators attached to a 1D beam [65] (Fig 1.3b), bolt resonators affixed to a 2D thin plate [66] (Fig 1.3c), cylindrical stubs attached to 2D thin plates [59], and resonant circuits electromechanically coupled to a 1D beam [67] (Fig 1.3d).

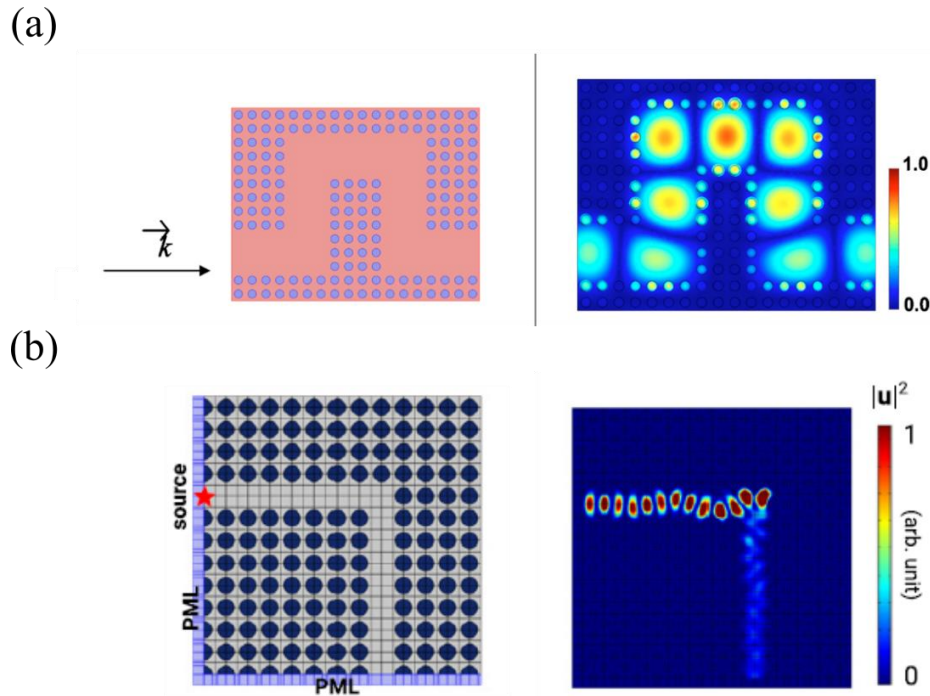


Fig 1.4. Elastic waveguides formed from inclusions in periodic lattices. Upon excitation, a confined elastic wave will propagate through the inclusion. (a) is an example of successful waveguiding (figure reused from [74] with written permission from the publishers). (b) is an example of how unwanted scattering or localization can inhibit successful propagation around sharp bends of a waveguide (figure reused from [75] under license [CC BY 4.0](https://creativecommons.org/licenses/by/4.0/)).

Building upon the wave/vibration attenuation made possible in EMs, an advanced objective that has received significant research attention is the confinement of elastic waves to a specified path or location through the formation of a waveguide. Conventional elastic waveguides obtain wave confinement by creating an inclusion where the wave can preferentially localize within a periodic lattice [74,76–82] (Fig 1.4a). In the periodic lattice, waves are attenuated by a locally resonant or Bragg bandgap. When the inclusion is added to the lattice by removing local resonators or Bragg scattering elements (e.g., left side of Fig 1.4a), defect modes emerge within the bandgap [74]. These defect modes enable the confined propagation of elastic waves and vibrations through the waveguide path (e.g., right side of Fig 1.4a [74]). While these conventional waveguides facilitate useful functionalities for various wave/vibration engineering systems, they can suffer from performance degradation when disorder (e.g., a sharp bend in the waveguide or mistuned elements) or imperfections (e.g., a manufacturing impurity) exist within the periodic lattice [75,76,83–85] (Fig 1.4b).

1.1.2 Topological metamaterials

Discoveries in the field of condensed matter physics have inspired investigations into how topological phases [86–89] can be used to avoid the aforementioned (Sec. 1.1.1) performance degradation and attain exceptional control over wave propagation in elastic [90–96], acoustic [97,98], and photonic [99–102] metamaterials. The mathematical field of *topology* involves the study of quantized properties of geometric objects or spaces [87,89,100]. These quantized properties, known as *topological invariants*, are conserved under continuous deformations (e.g., compressing or stretching). Topologically distinct (equivalent) objects have different (identical) topological invariants. As initially established in quantum electronic systems, the topology of the band structure can be utilized as a tool to obtain protected conducting states at the boundaries of a crystal that is insulating (meaning it contains an energy bandgap) in the bulk (or alternatively, protected states may occur at the interface of two topologically distinct bulk-insulating crystals), creating a phase of matter known as a topological insulator (TI) (see Fig 1.5a,b for a basic schematic of a TI and its band structure) [86–88]. Topological phases, such as TIs, are generally realized and protected by crystal symmetries (most commonly time-reversal symmetry and parity symmetry) [86]. The topology of a bulk crystal band structure can be quantified by a topological

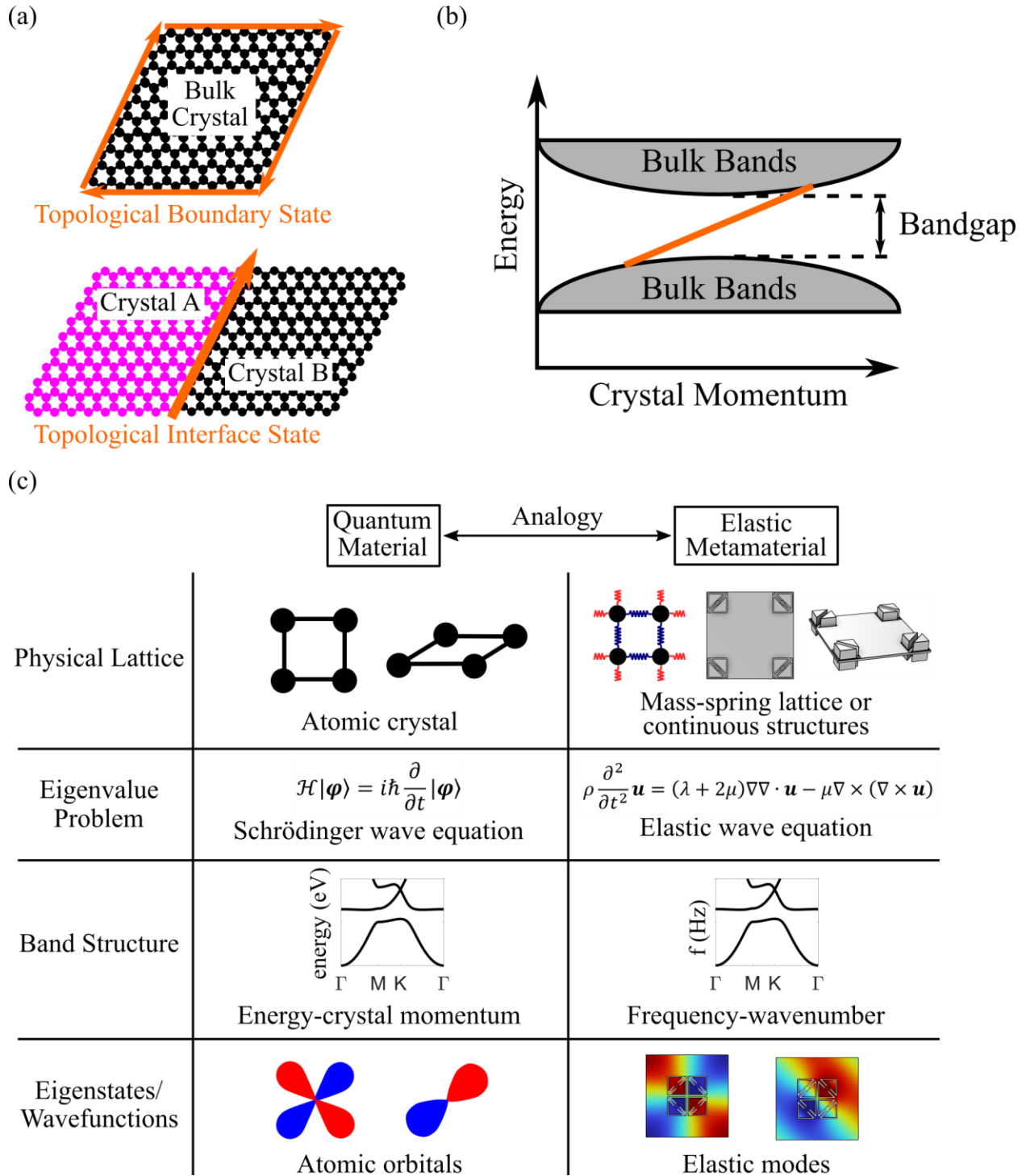


Fig 1.5. (a) Diagrams of a TI. The top panel is a TI composed of bulk crystal and exhibiting a topologically protected boundary state (represented by the orange arrows). The bottom panel shows a TI comprised of two bulk crystals connected at an interface, where a topologically protected interface state preferentially localizes (represented by the orange arrow). (b) The crystal band structure for the TI. The orange band represents the topological boundary (or interface) state, which emerges in the bulk energy bandgap. (c) Summary of the analogy between quantum materials and EMs that is employed to create TMs.

invariant, which is calculated from the winding of the system eigenmodes in reciprocal (i.e., momentum) space [86,87,100]. In an ordinary insulator, the dispersion bands are topologically trivial, and the value of the topological invariant is zero. For a topologically nontrivial insulator (e.g., a TI), the bands have a nonzero topological invariant. A continuous deformation connects two topologically equivalent insulators, where the bulk energy bandgap does not close [86,87,89,100]. On the other hand, two topologically distinct insulators are connected through a discontinuous deformation, where the bandgap must close and reopen (i.e., a cutting of the band structure in reciprocal space) [86,87,89,100]. This discontinuous deformation corresponds to a topological transition. According to the bulk-boundary correspondence principle, gapless boundary states will emerge at the boundary/interface where the topological transition occurs [86,87,91] (Fig 1.5a,b). These topological states contain exotic properties, such as robustness, confinement, and directionality, which are protected against any imperfections that do not alter the bulk topology.

Topological states can be incorporated into mechanical structures by creating analogs of topological quantum materials in EMs. The analogy between quantum electronic materials and EMs is summarized in Fig 1.5c. For quantum materials, the wavelike behavior of electrons in an atomic crystal lattice is modeled using the Schrödinger wave equation [103], which is solved as an eigenvalue problem (left column of Fig 1.5c). Computing the eigensolution results in a band structure that relates energy to crystal momentum (from the eigenvalues) and atomic orbitals that describe the probabilistic locations of electrons in the atoms (from the eigenvectors). When building a macro-scale mechanical analog in EMs (right column of Fig 1.5c), the atomic lattice is replaced by a mass-spring lattice or continuous structures with distinct mass sites and stiffness couplings. In this case, the solution to the elastic wave eigenvalue problem [25] provides a band structure that relates wave frequency to wavenumber (from the eigenvalues) and elastic modes that describe the wave fields (i.e., mechanical displacement fields) of the system (from the eigenvectors). To obtain topological states in quantum materials (mechanical structures/EMs), the band structure is used to identify the energy (frequency) bandgap where the state may emerge and the atomic orbital (elastic eigenmode) wavefunctions are used to evaluate the topological invariants. This analogy facilitates the integration of topological states, which were initially uncovered in quantum materials, into EMs.

When exploited by EMs for the control of elastic waves, topological states provide an avenue to achieving quasi-lossless (i.e., immune to undesirable scattering) transportation of elastic energy along waveguides with sharp bends and structural imperfections. This robust feature of *topological metamaterials* (TMs, as EMs with topological phases will be referred to in this document) makes them a promising choice for a wide variety of practical engineering applications, which often contain imperfections or disorders due to fabrication defects. In addition to alleviating practical concerns, the robustness of TMs adds functionality by enabling the manipulation of elastic wave energy in waveguides that travel in nearly arbitrary directions and/or unidirectional paths. The remarkable functionality and robustness of TMs have been exploited to enhance performance in engineering applications, which include vibration energy harvesting [104–108], on-chip communications [109–112], elastic antennas [113], and mechanical information processing (e.g., mechanical computing and wave splitting) [114–116]. More generally, topological materials (i.e., materials in all quantum and classical wave systems that incorporate topological phases) have also shown great promise for use in sensing/imaging [117–119], communications delay lines [120,121], memory [122], lasing [123–125], quantum computations [126–128], and tweezer manipulation [129]. Moreover, TMs are of particular scientific importance, as they serve as excellent macroscale platforms to investigate topological transport theories developed in condensed matter physics. The mechanical structures made from TMs are often easier to design, build, manipulate (i.e., scientists can explore a large parameter space), and test with (i.e., experimental measurements are more straightforward and atomic-level manipulation is not required), when compared to experimental quantum systems [88,91].

1.2 Current state of the art and research gap

1.2.1 First-order topological metamaterials

TMs have been investigated in 1D, 2D, and 3D mechanical systems that contain the symmetries that are necessary to realize the desired topological phases. According to topological phase theory, a n th order d -dimensional TIs (and therefore, TMs) contain $d - 1, d - 2, \dots, d - n + 1$ dimensional gapped boundary states and $d - n$ dimensional gapless boundary states [88,93,100]. Thus, first-order TMs ($n=1$) contain gapless boundary states that are one dimension lower than the bulk. For first-order TMs, there are 0D “point” states in 1D structures, 1D topological “edge” states in 2D structures, and 2D “surface” states in 3D structures (see a schematic of the topological states

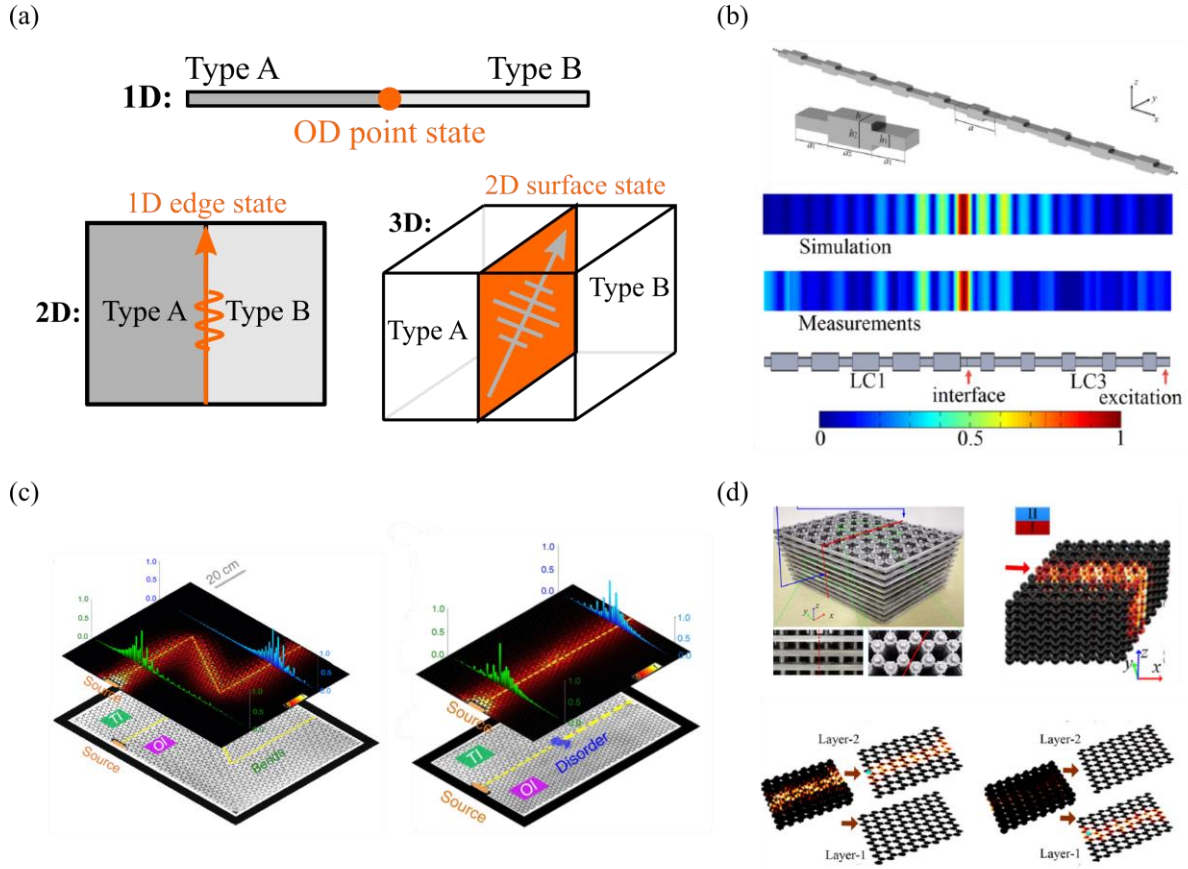


Fig 1.6. (a) Schematic of topological states in 1D, 2D, and 3D first-order TMs. Topological states are confined to the paths that are shown in orange. “Type A” and “Type B” represent topologically distinct bulk crystals (i.e., at their interface, there is a topological transition). These crystals are insulating in the bulk. (b) 1D first-order TM (beam with a varying cross-section) hosting a 0D topological point state (figure reused from [130] under license [CC BY 4.0](https://creativecommons.org/licenses/by/4.0/)). (c) 2D first-order TM (thin plate with circular inclusions) hosting a 1D topological edge state (figure reused from [27] under license [CC BY 4.0](https://creativecommons.org/licenses/by/4.0/)). (d) 3D first-order TM (cubic lattice) hosting 2D topological surface state (top) and layer-selective topological state (bottom) (figure reused from [131] with written permission from the publisher).

of first-order TMs in Fig 1.6a).

1D topological physics have been explored in spring-mass chains [83,132,133], rods [134], and beams [130,135–137]. In 1D TMs, the Zak phase [138,139] is the topological invariant that is calculated to characterize the bulk topology (i.e., it characterizes the topological properties of the bulk). Topologically protected wave localization is obtained by connecting two bulk configurations with dissimilar Zak phases to form a topological transition. By using this methodology, both in-plane (i.e., longitudinal) and out-of-plane (i.e., bending) polarized elastic waves have successfully been localized to 0D locations in 1D structures (see an example in Fig 1.6b [130]). More recently, on-line tunable TMs have been created to maximize performance in the presence of varying external conditions, adapt to changing operating requirements, and enable

new functionality. Tunable 1D TMs have been developed that use active piezoelectric circuit elements [134,135] or externally applied deformations [137] to adjust the frequency of the 0D topological state in an on-demand fashion. This frequency adjustment capability significantly enhances the operating bandwidth of the TM.

To achieve protected wave propagation that is localized to waveguides in first-order 2D TMs, the elastic analogs of the quantum Hall effect (QHE) [140–143], quantum spin Hall effect (QSHE) [144–149], and quantum valley Hall effect (QVHE) [83,150,159–164,151–158] have been extensively investigated (along with other mechanisms, such as finite-frequency Maxwell modes [165]). The mechanical structures used to realize these 2D topological phases include thin plates, 2D reticular designs, and interconnected active or gyroscopic elements that contain the required symmetries for each phase (QHE, QSHE, or QVHE). Researchers have shown in-plane and out-of-plane (i.e., flexural) polarized elastic waves confined within 1D topological edge states (see an example in Fig 1.6c [27]). Like first-order 1D TMs, recent investigations have focused on introducing tunability to first-order 2D TMs. First-order 2D TMs with on-line adjustable spatial path [166–172], mode shape [173], and frequency [174–176] have each been explored. Advanced wave control functions can be attained by tailoring the mode shape or spatial path, such as a versatile elastic wave filter or splitter.

3D TMs offer a pathway to study 3D topological physics and enable unprecedented elastic wave control functionality along multiple planes and spatial directions. 2D topological surface states in first-order 3D TMs are more difficult to realize than topological states in first-order 1D and 2D TMs due to the inherent complexities of manufacturing intricate 3D mechanical structures, computational resource requirements for full-scale 3D modeling, and the frequent presence of undesirable wave coupling and mode conversion that are consequences of the three distinct elastic wave mode polarizations. Recent advances in 3D fabrication methods and high-performance computing resources have prompted the development of 3D EMs (where the focus is on the formation of elastic wave bandgaps) [37,38,43,177–183] and first-order 3D TMs [26,75,131,184–188]. The elastic analog of Weyl semimetals [189,190] (Weyl semimetals are a 3D topological phase) has been harnessed in various theoretical studies to investigate the formation of Weyl points in 3D TMs and achieve unidirectional and topologically protected 2D surface states [26,75,184–187]. The QVHE has also been incorporated into a 3D layered mechanical structure [131], where 2D topological surface states and layer-selective wave control are demonstrated (Fig 1.6d). The

initial studies on first-order 3D TMs illustrate some of the many benefits that comprehensive 3D elastic wave control could provide, extending beyond what is achievable in 1D and 2D systems.

1.2.2 Higher-order topological metamaterials

Higher-order topological insulators (HOTIs) are a new class of topological phases of matter that emerged from TI theory. In n th order d -dimensional HOTIs, there are $d - 1, d - 2, \dots, d - n + 1$ dimensional gapped boundary states and $d - n$ dimensional gapless boundary states, where $d > 1$ and $n > 1$ [88,93,100,191–194]. Therefore, a second-order 2D HOTI has gapped 1D edge states and in-gap boundary states at its 0D corners, a second-order 3D HOTI has gapped 2D surface states and gapless boundary states along its 1D “hinges,” and a third-order 3D HOTI has gapped 2D surface states and 1D hinge states to go along with in-gap boundary states at its 0D corners (see a schematic for HOTIs in Fig 1.7a). HOTIs have distinct topological physics (and distinct topological invariants) when compared to the first-order TI class of topological materials [88]. The topological phase theories used to derive HOTIs are generally separated into two primary categories that reflect their different fundamental mechanisms: (i) HOTIs with quantized multipole moments [193] or (ii) C_n -symmetric HOTIs without quantized multipole moments (but usually do have bulk dipole moments) [195–197]. Noncommutative mirror symmetries that may be difficult to realize in practical settings are required to realize HOTIs in (i), making the methodology in (ii) easier to implement experimentally. In all HOTIs, gapless topological states are found at the “boundaries of boundaries,” unlocking a pathway to multidimensional topological physics. Within this dissertation, *multidimensional* refers to the ability to achieve topological states across a hierarchy of several unique dimensions (e.g., 1D edge states and 0D corner states coexisting in the same 2D system).

Higher-order TMs (HOTMs) have been investigated in 2D mechanical structures. These second-order 2D TMs have an insulating bulk, gapped 1D edge states, and in-gap 0D corner states. 2D HOTMs have been realized using quantized multipole moments [198] (Fig 1.7b) or various C_n -symmetric mechanisms [110,199,208,200–207] (Fig 1.7c). The HOTMs presented thus far display extraordinary elastic wave manipulation along multidimensional boundaries and serve as excellent platforms for investigating novel topological physics. It is anticipated that further research in HOTMs will result in significant advances for various technical applications, such as vibration energy harvesting, quantum computing, imaging, sensing, and signal processing [88].

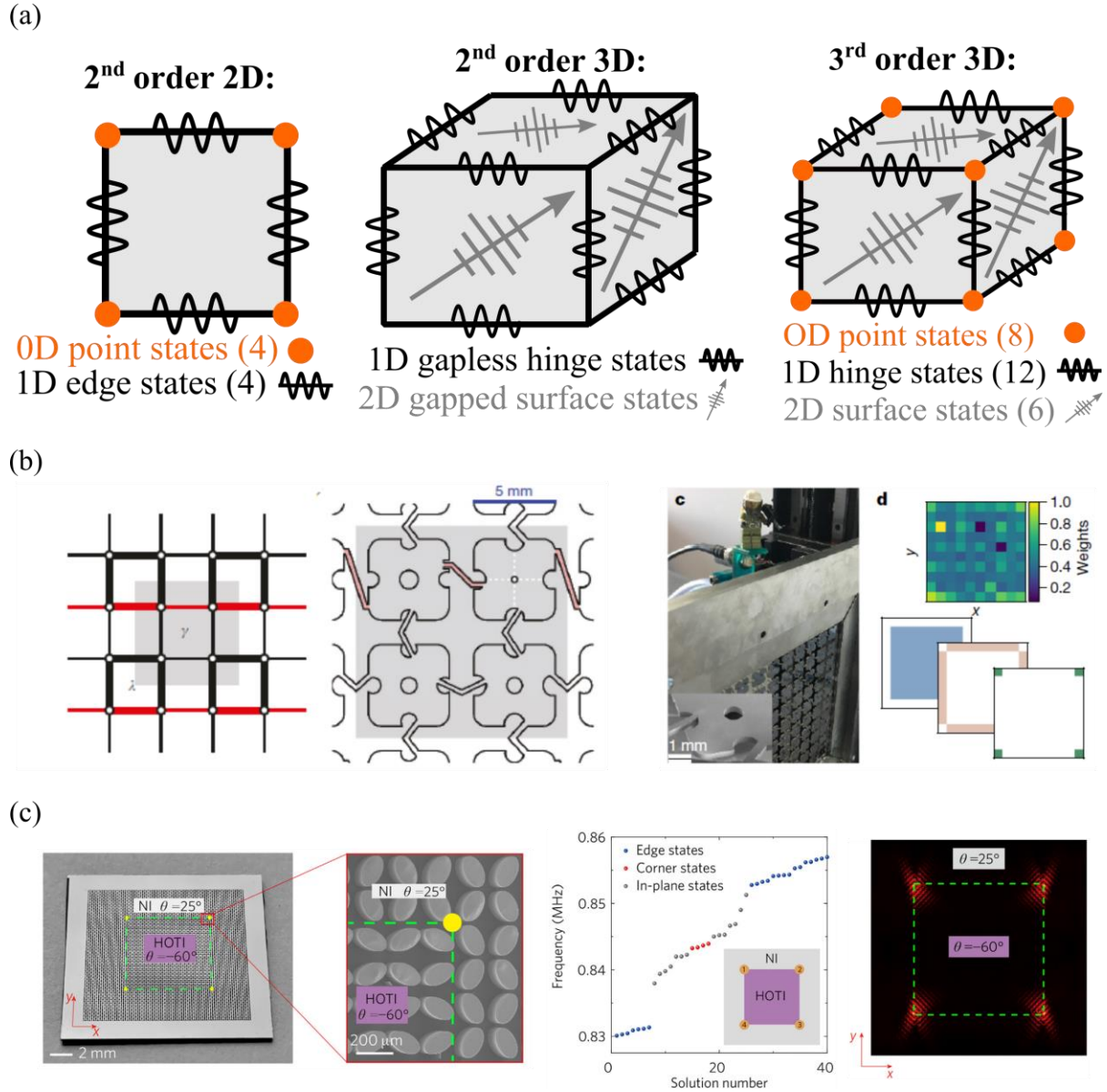


Fig 1.7. (a) Schematics of (from left to right) second-order 2D HOTI, second-order 3D HOTI, and third-order 3D HOTI. (b) 2D HOTM with corner states generated from quantized multipole moments (figure reused from [198] with written permission from the publisher). (c) 2D HOTM with corner states generated from a C_n -symmetric mechanism (figure reused from [110] with written permission from the publisher).

1.2.3 Research gaps

The previous research on TMs has uncovered new knowledge in topological physics and elastic wave transport phenomena. These breakthroughs have been exploited to synthesize platforms with unprecedented wave control capabilities. The most cutting-edge TMs that have been investigated to date employ basic on-demand adaptivity (in first-order 1D and 2D TMs), 3D first-order topological physics (in first-order 3D TMs), or higher-order topological physics (in 2D HOTMs).

However, research gaps exist that are impeding the broad implementation of TMs in practice and offer clear opportunities for advancement. The key gaps in the current state of the art include:

- i. Lack of concurrent and comprehensive adaptivity of path, shape, dimensionality, and frequency of topological states:* The tunable 1D [134,135,137] and 2D TMs [166,167,176,168–175] that have been investigated thus far have each concentrated on tailoring an individual characteristic (e.g., the spatial path) of the elastic waves, and tunable 3D TMs have yet to be realized. As a result, concurrent tunability of the wave path, shape, dimensionality, and frequency characteristics of topological states has yet to be achieved. Moreover, the lack of tunability in 3D TMs has hindered the broad and efficient exploration of topological phases in 3D mechanical structures. To fully explore integrated topological physics in TM platforms and enable robust performance for a broad set of wave control applications, TMs with multiple comprehensively tunable wave transport characteristics must be developed.
- ii. TMs often have an operating frequency range that is singular, narrow, and fixed:* Little attention has been paid to creating TMs that operate over multiple distinct frequency bands, despite studies in photonic metamaterials, acoustic metamaterials, and EMs that illustrate the great promise of multiband lasers [209], filters [210], resonators [211], on-chip circuits [212], and isolators [213,214]. Apart from operating over a sole frequency band, the TMs studied to date predominantly operate over a limited and invariable frequency region. Since the primary focus of tunable TMs has been on the adjustability of the wave path [166–172], TMs that are programmable over a broad frequency bandwidth have yet to be fully explored. There is a lack of insight into the physical mechanisms that could be exploited to tune the frequency of a TM over a wide range, resulting in a bandwidth limitation that is a notable disadvantage in technical applications requiring robust wave control over a wide range of frequencies.
- iii. Large-scale TMs are required for elastic wave control at low frequencies:* The tunable or 3D TMs generated thus far do not exhibit *subwavelength* elastic wave control, and thus must be very large to manipulate waves in a low-frequency regime (audible range of few Hz to 20 kHz). In a subwavelength system, the dimensions (specifically, the lattice constant a) of the structure are less than the wavelength λ of the wave being controlled ($a < \lambda/2$). The frequency bandwidth of such systems can be altered (e.g., moved to a low-frequency

range) by tailoring local properties (e.g., the frequencies of local resonators) without adjusting the lattice constant. The compact characteristic of subwavelength structures makes them easy to integrate within size-constrained applications where low-frequency wave control is desired (e.g., structural elements of vehicles/aircraft/spacecraft).

1.3 Research statement

To address the research gaps and advance the state of the art, this dissertation aims to synthesize and explore a new class of advanced TMs that achieve *responsive, broadband, easily integrated, and multidimensional* elastic wave control and *facilitate the discovery of new knowledge* in topological and elastic wave physics. The research hypothesis is that the understanding and harnessing of *comprehensive adaptivity, local resonance, higher-order topological states*, and the *rich dimensionality of 3D mechanical structures* will enable the achievement of the broad research aims. The research questions that must be addressed to evaluate the hypothesis include:

- I. Can TM design methodologies be uncovered that enable *concurrent on-demand adaptivity* of elastic wave path, shape, dimensionality, and frequency?
- II. How can *local resonance* be strategically incorporated into 2D, 3D, and *higher-order* TMs to attain topological states that operate in multiband and subwavelength frequency regimes?
- III. How can the *rich dimensionality of 3D mechanical architectures* be exploited and physically realized in experimental testbeds to achieve unparalleled elastic wave control functionality and uncover a new understanding of elastic wave propagation in 3D structures?

In this dissertation, new theoretical and experimental approaches are established that harness cutting-edge topological physics, stimuli-responsive materials (e.g., piezoelectric), metastability (metastability is the coexistence of several internal stable states given a constant global topology [215]), multimodal local resonance, and novel 3D geometric architectures to answer the research questions. Through these innovative approaches, unprecedented elastic wave control capabilities are attained and new insight is uncovered into the physics that govern tunable, multidimensional (i.e., across a hierarchy of multiple unique dimensions), and 3D topological phases in mechanical systems. The advanced TMs synthesized herein may have a profound impact on myriad

engineering applications and serve as platforms for future scientific exploration in topological and elastic wave physics.

1.4 Outline of dissertation chapters and addressing the research gaps

This dissertation is outlined as follows:

Chapter 1: Introduction

Introductory chapter that includes a background on EMs and TMs, literature review on the current state of the art, the identified research gaps, and the research statement for this dissertation.

Chapter 2: 2D Piezoelectric Metamaterial (addresses research gaps i, ii, and iii)

Synthesis of a tunable first-order 2D TM that exploits resonant piezoelectric circuitry to concurrently tailor the frequency, path, and shape of topological 1D edge states that are in multiple distinct frequency bands and within a subwavelength frequency regime.

Chapter 3: 3D Metastable Metamaterial (addresses research gap i)

Creation of a tunable first-order 3D TM that can be adjusted via metastability. The adaptive property of the proposed TM is used to adjust the path of 2D topological surface states, uncover a bilayer-locked topological state, and construct advanced 3D elastic wave networks.

Chapter 4: 3D Multimodal Locally Resonant Metamaterial (addresses research gaps ii and iii)

Development and experimental realization of a first-order 3D TM that exploits multimodal local resonance to enable low-frequency (i.e., few Hz to 20 kHz) elastic wave control over multiple distinct frequency bands. A rich set of polarization-, frequency-, and layer-dependent behaviors are uncovered and a comprehensive experimental investigation is undertaken.

Chapter 5: 2D Higher-Order Locally Resonant Metamaterial (addresses research gaps ii and iii)

Synthesis of a 2D HOTM that exploits higher-order topological phases and multimodal resonance to obtain multiband 0D corner states in a low-frequency regime. The proposed metamaterial platform is employed to create multifunctional wave-based logic elements and explore elastic wave control in fractal TMs.

Chapter 6: Summary of Scholarly Contributions and Broader Impact

A summary of the dissertation that includes a discussion on the scholarly contributions, potential broader impacts on science and technology, and promising opportunities for future research.

Appendix A: Supplemental Information for Chapter 2

Appendix B: Supplemental Information for Chapter 3

Appendix C: Supplemental Information for Chapter 4

Appendix D: Supplemental Information for Chapter 5

Bibliography

Chapter 2. 2D Piezoelectric Metamaterial

In this chapter, a 2D piezoelectric metamaterial is introduced with the capability to concurrently tailor the frequency, path, and mode shape of topological 1D edge states using resonant circuitry (i.e., this is a first-order 2D TM). The plane wave expansion method is used to detect a frequency-tunable subwavelength Dirac point in the band structure of the periodic unit cell and discover an operating region over which topological wave propagation can exist. Dispersion analyses for a supercell illuminate how circuit parameters can be utilized to adjust mode shapes corresponding to topological edge states. A further evaluation provides insight into how increased electromechanical coupling and lattice reconfiguration can be exploited to enhance the frequency range for topological wave propagation, increase achievable mode localization, and attain edge states in an additional discrete frequency band. Topological guided wave propagation that is subwavelength in nature and adaptive in path, localization, and frequency is illustrated in numerical simulations of thin plate structures. The outcomes from this chapter indicate that the proposed 2D piezoelectric TM is easily integrable (i.e., it is subwavelength) in low-frequency applications, can operate over an adjustable wide frequency bandwidth that spans multiple discrete bands, and is the most comprehensively tunable 2D TM realized to date.

2.1 Introduction

Protected wave propagation in first-order 2D TMs that is confined to a waveguide is obtained through the activation of localized topological edge states that arise from the QHE, QSHE, and QVHE. Due to the active/moving components that are generally required to break time-reversal symmetry (TRS) for the QHE [140–143] and the complex geometries necessary to achieve a double Dirac cone (a band degeneracy where four cones meet in reciprocal space) in the band structure for the QSHE [144–149], the relatively simpler QVHE has garnered significant attention. The QVHE requires the formation of a single Dirac cone (a degeneracy where two cones meet) in the band structure of the periodic unit cell. This single Dirac cone is opened with a lattice perturbation that breaks space inversion symmetry (SIS), which produces a bandgap that can support 1D topological edge states due to valley-dependent topological properties [150–153].

These valley-dependent topological properties are characterized by the topological invariant known as the valley Chern number. A topological transition can be engineered by connecting lattices with distinct valley Chern values at an interface. This topological transition enables topologically protected 1D edge states with localized displacement at the interface. Topologically protected wave transmission according to the elastic analog of the QVHE has been obtained in 2D reticular structures [154–156] and continuous thin plates with periodically placed masses [157,158] or inclusions [27,159]. These structures emulate the elastic QVHE by exploiting a periodic impedance mismatch (Bragg scattering mechanism), and thus the resulting topological edge states exist at frequencies corresponding to wavelengths that are dependent on (and on the same order of) the lattice constant. The addition of local mass resonators [83,160,162–164] and acoustic black holes [161] to continuous plates has facilitated the achievement of topological edge states at frequencies that are determined by the characteristics of the local element (mass resonator or acoustic black hole). Topological wave propagation at low frequencies corresponding to wavelengths that are larger than the lattice constant has been demonstrated by carefully selecting the properties of these local elements [83,144,162,164]. Subwavelength TMs such as these could be highly valuable for engineering applications that require wave control at low frequencies in size-constrained environments.

To extend beyond the functionalities available in fixed structures and enable adaptivity to varying operating requirements and external conditions, many recent investigations have focused on introducing tunability to first-order 2D TMs. The spatial path of topological wave propagation has been demonstrated to be adjustable by applying an external magnetic field [166], modifying mechanical boundary conditions [167,168], adding an elastic foundation [169], connecting negative capacitance piezoelectric circuitry [170,171], or switching stable states in bistable elements [172]. The shape and localization of topological edge states have been tuned by exploiting an applied strain field [173]. Initial studies involving real-time frequency tuning of topological edge states have shown that an applied temperature [174], strain field [175], or electrical field [176] can increase the frequency range over a limited region that is related to the Bragg mechanism or the magnitude of lattice perturbation.

The tunable TMs that have been investigated thus far have each concentrated on tailoring an individual characteristic of the topological wave to unlock novel functions and enhance performance in devices exhibiting elastic wave control. However, concurrent tunability of the

frequency and spatial characteristics of topological edge states has yet to be fully explored in a singular TM. Such a metamaterial would be of great benefit for devices such as wave filters, multiplexers, and energy harvesters that must route energy over a large frequency bandwidth. Besides primarily focusing on one adaptive characteristic, the currently established tunable TMs generally rely on the Bragg mechanism to generate a Dirac cone. Due to the interaction of platform-specific tuning parameters with the underlying physics of the Bragg mechanism, these metamaterials are either incapable of on-line frequency tuning (e.g., they are path tunable only) or can only practically do so over a limited range. Moreover, structures fabricated from these metamaterials would need to be large to control energy at low frequencies that correspond with fundamental system modes, which can be critical in structural applications. As a result, an easily integrable TM that is capable of subwavelength elastic wave control and programmable over a broad frequency bandwidth has yet to be developed.

The research presented within this chapter proposes a piezoelectric TM harnessing integrated resonant circuitry for comprehensively tunable subwavelength wave control. The goal of this chapter is to uncover insights into critical adaptive parameters and synthesize a framework for the attainment of programmable topological wave propagation using resonant electromechanical metamaterials. In contrast to previous works, the proposed methodology and approach in this chapter has achieved clear advancements: (a) the rich tailorable characteristics of the piezoelectric metamaterial enable the concurrent adaptation of the frequency range, path, and mode shape of topological edge states and the discovery an additional edge state in a separate discrete frequency band and (b) this on-demand tunability of topological properties is achieved for the first time in a subwavelength (i.e., compact) and load-bearing thin plate structure.

To accomplish the research objective, this chapter presents the evaluation of the dispersion relation for the unit cell from the plane wave expansion (PWE) method. The PWE method is selected because of its concise nature and computational efficiency when compared to the often-used finite element (FE) method, since there can be a low (e.g., 50-100) number of degrees of freedom required to achieve an accurate result from PWE calculations for thin plate structures [58,83]. This method is utilized to establish the working principle for the achievement of topological edge states from the QVHE. Beyond establishing a working principle for the attainment of topological edge states for fixed system parameters, the advantages of the PWE method facilitate a comprehensive parameter study through rapid calculations of the metamaterial

dispersion relation. A parametric analysis is performed to identify and explore an achievable operating region for tunable topological wave propagation. Numerical computations of the dispersion relation for a finite strip of connected unit cells (i.e., a supercell) uncover how circuit parameters can enable the adjustment of topological edge states. Further analysis is conducted to investigate how topological edge state adaptivity can be augmented by the connection of negative capacitance to enhance electromechanical coupling and lattice reconfiguration via shorting circuits to obtain an additional Dirac cone. Finally, the activation of topological edge states for the achievement of guided topological wave propagation at lattice interfaces and boundaries is revealed by numerical simulations of a thin plate structure.

2.2 Concept and theoretical model

2.2.1 System description

As shown in Fig 2.1, the proposed piezoelectric metamaterial is comprised of a bimorph thin plate with substrate (gray) and piezoelectric (yellow) layers. The substrate layer has thickness h_s , density ρ_s , elastic modulus E_s , and Poisson's ratio ν_s while the piezoelectric layers have thickness h_p and density ρ_p . The piezoelectric elements are connected to external circuitry through conductive circular electrodes (red and blue in Fig 2.1) with radius r_p and a thickness that is assumed to be negligible [216]. The electrodes are arranged in a honeycomb lattice formation that contains the symmetries required to achieve the elastic analog of the QVHE. The metamaterial unit cell is defined by the basis vectors $\vec{a}_1 = a\hat{i}$ and $\vec{a}_2 = a\left(\cos\frac{\pi}{3}\hat{i} + \sin\frac{\pi}{3}\hat{j}\right)$, where a is the lattice constant, and the resulting unit cell area is $A_c = \frac{\sqrt{3}}{2}a^2$ (Fig 2.1c). This unit cell contains two electrode pairs that form capacitors (capacitor 1 and capacitor 2) that are centered at $\vec{R}_1 = \frac{a}{2\sqrt{3}}\left(\cos\frac{\pi}{6}\hat{i} + \sin\frac{\pi}{6}\hat{j}\right)$ and $\vec{R}_2 = \frac{-a}{2\sqrt{3}}\left(\cos\frac{\pi}{6}\hat{i} + \sin\frac{\pi}{6}\hat{j}\right)$. Each capacitor ($C_{p,1}$ and $C_{p,2}$) is connected to an inductor (L_1 and L_2) to form a resonant LC circuit with a natural frequency of $\omega_{t,j} = \sqrt{\frac{1}{L_j C_{p,j}}}$ for the j th circuit. A negative capacitor with capacitance $C_{N,j}$ (i.e., for a capacitor with capacitance $C = -1$ F, $C_N = 1$ F) is connected in parallel to the j th resonant circuit. Ohmic losses are not considered in the derivation for the dispersion analysis, as all circuit elements are assumed to be ideal. In addition, damping is neglected, and perfect adhesion is assumed to exist between layers.

2.2.2 Governing equations

In the derivation of the theoretical model for the metamaterial, small deflections and a thin structure (in the \bar{z} direction) are assumed. The classical theory of thin plates [25] and the linear theory of piezoelectricity [217,218] are applied. Assuming a transversely isotropic material and plane stress, the elastic, piezoelectric, and permittivity constants for the piezoelectric elements of the bimorph plate are obtained from the reduced (from the full 3D form) piezoelectric constitutive relations for a thin plate [217] as:

$$\begin{aligned}\bar{c}_{11}^E &= \frac{s_{11}^E}{(s_{11}^E + s_{12}^E)(s_{11}^E - s_{12}^E)} \\ \bar{c}_{12}^E &= \frac{-s_{12}^E}{(s_{11}^E + s_{12}^E)(s_{11}^E - s_{12}^E)} \\ \bar{c}_{66}^E &= \frac{1}{s_{66}^E} = \frac{1}{2}(\bar{c}_{11}^E - \bar{c}_{12}^E) \\ \bar{e}_{31} &= \frac{d_{31}}{s_{11}^E + s_{12}^E} \quad \bar{\epsilon}_{33}^S = \epsilon_{33}^T - \frac{2d_{31}^2}{s_{11}^E + s_{12}^E}\end{aligned}\tag{2.1}$$

where \bar{c}_{11}^E , \bar{c}_{12}^E , and \bar{c}_{66}^E are the reduced elastic constants evaluated at a constant electric field, \bar{e}_{31} is the reduced piezoelectric constant, $\bar{\epsilon}_{33}^S$ is the reduced permittivity constant evaluated at a constant strain, s_{11}^E and s_{12}^E are elastic compliance constants, d_{31} is a piezoelectric coefficient, and ϵ_{33}^T is permittivity calculated under constant stress. A uniform electric field is assumed across each electrode. The governing equations for the flexural displacement and voltage response of the metamaterial are derived using the extended Hamilton's principle [219], the integral form of Gauss's law [217], and Kirchoff's laws, and are given as:

$$D_T \bar{\nabla}^4 \bar{w}(\bar{r}, t) + m \frac{\partial^2 \bar{w}(\bar{r}, t)}{\partial t^2} - \theta \sum_{j=1}^{N_e} \bar{\nabla}^2 \bar{v}_j(t) \bar{\chi}_j(\bar{r}) = 0\tag{2.2}$$

$$L_j(C_{p,j} - C_{N,j}) \frac{\partial^2 \bar{v}_j(t)}{\partial t^2} + \bar{v}_j(t) + \theta \iint_{\bar{D}_j} L_j \frac{\partial^2}{\partial t^2} \bar{\nabla}^2 \bar{w}(\bar{r}, t) d^2 \bar{r} = 0, \quad j = 1 \dots N_e \text{ electrode pairs}\tag{2.3}$$

where $\bar{r} = (\bar{x}, \bar{y})$, $\bar{w}(\bar{r}, t)$ is the flexural displacement of the plate, m is the effective mass per unit area of the plate, D_T is the effective flexural rigidity of the plate at short circuit, θ is an electromechanical coupling coefficient, $\bar{v}_j(t)$ is the output voltage across the j th electrode pair, $C_{p,j}$, L_j , and $C_{N,j}$ are the capacitance, connected inductance, and connected negative capacitance corresponding to the j th electrode pair, N_e is the total number of electrode pairs, $\bar{\nabla}^2$ and $\bar{\nabla}^4$ are the

Laplacian and biharmonic operators, respectively, and t is time. Furthermore, $\bar{\chi}_j(\bar{r}) = \begin{cases} 1, & \bar{r} \in \bar{D}_j \\ 0, & \text{otherwise} \end{cases}$, where the value of the step-function $\bar{\chi}_j(\bar{r})$ depends on \bar{D}_j , which represents the subdomain in $\bar{x} - \bar{y}$ space containing the j th electrode pair. The definitions for m , D_T , θ , and $C_{p,j}$ are given by:

$$\begin{aligned} m &= \rho_s h_s + 2\rho_p h_p \\ D_T = D_s + D_p &= \frac{E_s h_s^3}{12(1 - \nu_s^2)} + \tilde{c}_{11}^E \left(\frac{2h_p^3}{3} + h_p^2 h_s + \frac{h_p h_s^2}{2} \right) \\ \theta &= \tilde{e}_{31}(h_p + h_s) \\ C_{p,j} &= \frac{2\tilde{\epsilon}_{33}^S}{h_p} A_{e,j} = \tilde{C}_p A_{e,j} \end{aligned} \quad (2.4)$$

where D_s and D_p are the flexural rigidities of the substrate and the piezoelectric layers, respectively, $A_{e,j}$ is the area within the unit cell that contains the j th electrode pair, and \tilde{C}_p is the capacitance per unit area. A harmonic response is assumed at frequency ω , such that:

$$\bar{w}(\bar{r}, t) = \bar{W}(\bar{r})e^{i\omega t} \quad \bar{v}_j(t) = \bar{V}_j e^{i\omega t} \quad (2.5)$$

To generalize the results, a nondimensionalization scheme is adopted and the resulting equations are:

$$\left(\nabla^4 - \frac{\omega^2 m a^4}{D_T} \right) w(r) - \sum_{j=1}^{N_e} \frac{\theta^2 a^2}{(C_{p,j} - C_{N,j}) D_T} \nabla^2 v_j \chi_j(r) = 0 \quad (2.6)$$

$$(1 - L_j(C_{p,j} - C_{N,j})\omega^2)v_j - \omega^2 L_j(C_{p,j} - C_{N,j}) \iint_{D_j} \nabla^2 w(r) d^2r = 0; \quad j = 1 \dots N_e \text{ electrode pairs} \quad (2.7)$$

where the non-dimensional flexural displacement, voltage, time, and length scales are defined as:

$$w = \frac{\bar{W}}{a}, v_j = \frac{1}{a} \frac{C_{p,j} - C_{N,j}}{\theta} \bar{V}_j, \tau = \sqrt{\frac{1}{L_j(C_{p,j} - C_{N,j})}} t, x = \frac{\bar{x}}{a}, y = \frac{\bar{y}}{a}, \text{ and } z = \frac{\bar{z}}{a}, \text{ respectively, } r = (x, y),$$

∇^2 and ∇^4 are the nondimensional Laplacian and biharmonic operators, respectively, and $\chi_j(r) =$

$$\begin{cases} 1, & r \in D_j \\ 0, & \text{otherwise} \end{cases}, \text{ where } D_j \text{ is the subdomain in } x - y \text{ space containing the } j\text{th electrode pair.}$$

2.2.3 Dispersion relation

To attain the dispersion diagram (i.e., band structure) of the metamaterial, the dispersion relation of the unit cell is analyzed using the PWE method. For this study, the number of electrode pairs (capacitors) in the unit cell is set to $N_e = 2$, as is shown in Fig 2.1. The inductors L_1 and L_2

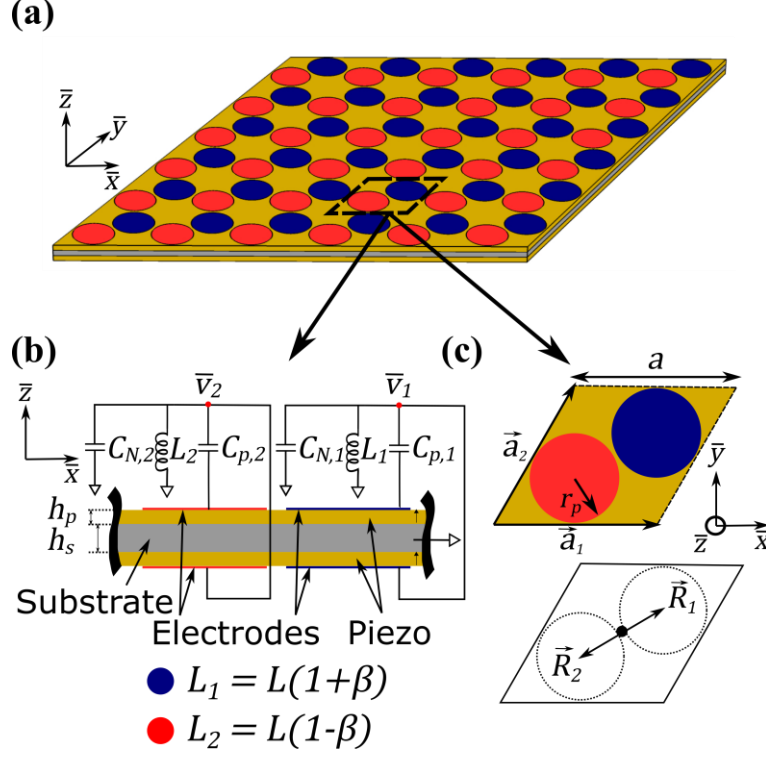


Fig 2.1. (a) Isometric view of piezoelectric metamaterial, with unit cell enclosed in dashed lines. (b) Cross-section and (c) top view of metamaterial unit cell. Blue indicates electrode geometry connected to circuit 1, red indicates electrode geometry connected to circuit 2.

are defined as $L_1 = L(1 + \beta)$ and $L_2 = L(1 - \beta)$, where β is a circuit inductance perturbation parameter. The PWE method is applied following the steps outlined in previous investigations utilizing mechanical resonators [58,83,144], where the nondimensional flexural displacement $w(r)$ of the plate is expressed as a superposition of plane waves:

$$w(r) = \sum_G W(G) e^{-ia(k+G) \cdot r}, \quad G = m\vec{b}_1 + n\vec{b}_2 \quad (2.8)$$

$$m, n \in [-M, M], \quad k = (k_x, k_y)$$

where $\vec{b}_1 = \frac{\pi}{a} \left(2\hat{i}, -\frac{2}{\sqrt{3}}\hat{j} \right)$ and $\vec{b}_2 = \frac{\pi}{a} \left(0\hat{i}, \frac{4}{\sqrt{3}}\hat{j} \right)$ are the reciprocal lattice basis vectors (a diagram of the reciprocal lattice is contained in the inset of Fig 2.2), G is the reciprocal lattice vector, m and n are the plane wave indices, k is the Bloch wave vector, and M is an integer chosen such that $N^2 = (2M + 1)^2$ is the number of plane waves that are included in the calculation. Eq. 2.8 is substituted into Eq. 2.6, the result is multiplied by the complex conjugate $e^{ia(K+G') \cdot r}$, and integrated over the dimensionless unit cell $\iint_{A_{c-ND}} dr$, where $A_{c-ND} = \sqrt{3}/2$ represents the dimensionless area of the unit cell, defined as $A_{c-ND} = A_c/a^2$. Using the property of orthogonality:

$$\iint_{A_{c-ND}} e^{-ia(G-G') \cdot r} dr = \begin{cases} A_{c-ND} & \text{for } G = G' \\ 0 & \text{otherwise} \end{cases} \quad (2.9)$$

Eq. 2.10 is obtained. Similarly, by substituting Eq. 2.8 into Eq. 2.7, Eq. 2.11 is obtained. The following equations define the dispersion relation of the metamaterial unit cell:

$$(a^4|k + G|^4 - \Omega^2)W(G) + \sum_{j=1}^{N_e} \frac{\vartheta}{1 - \xi_j} \frac{a^2}{A_c} \frac{a^2}{A_{e,j}} a^2|k + G|^2 \iint_{D_j} v_j e^{ia(k+G) \cdot r} d^2r = 0 \quad (2.10)$$

$$\left(\frac{\Omega_{t,j}^2}{(1 - (-1)^j \beta)(1 - \xi_j)} - \Omega^2 \right) v_j + \Omega^2 a^2 \sum_G W(G) |k + G|^2 \iint_{D_j} e^{-ia(k+G) \cdot r} d^2r = 0 \quad (2.11)$$

$$j = 1 \dots N_e \text{ electrode pairs}$$

where Ω is nondimensional frequency, ϑ is the nondimensional electromechanical coupling factor, $\Omega_{t,j}$ is the nondimensional circuit tuning frequency, and ξ_j is the negative capacitance ratio for the j th circuit. The derived model is general and allows for unit cells with different electrode shapes and capacitance definitions. However, in this study, these features are selected to be uniform across both electrode pairs, as $C_{N,j} = C_N$, $C_{p,j} = C_p$, and $A_{e,j} = A_e$, such that $\Omega_{t,j} = \Omega_t$ and $\xi_j = \xi$. The equations for Ω , ϑ , Ω_t , and ξ are given as:

$$\begin{aligned} \Omega &= \omega a^2 \sqrt{\frac{m}{D_T}} \\ \vartheta &= \frac{\theta^2}{\tilde{C}_p D_T} \\ \Omega_t &= \sqrt{\frac{1}{LC_p}} a^2 \sqrt{\frac{m}{D_T}} \\ \xi &= \frac{C_N}{C_p} \end{aligned} \quad (2.12)$$

To evaluate the dispersion relation for the system, Eqs. 2.10 and 2.11 are arranged in the form of the classical eigenvalue problem:

$$([\mathbf{K}] - \lambda[\mathbf{M}])[\mathbf{u}] = 0 \quad (2.13)$$

where the eigenvalues λ (defined as $\lambda = \Omega^2$) and eigenvectors $[\mathbf{u}]$ (defined as $[\mathbf{u}] = [\{W_{m,n}\} \ v_1 \ v_2]^T$) can be computed by specifying the Bloch wave vector k . The matrices $[\mathbf{K}]$ and $[\mathbf{M}]$ of the eigenvalue problem are explicitly defined in Appendix A.1. For the given eigenvalue problem with a specified wave vector k , there are $N^2 + 2$ calculated eigenvalues λ that

are used to obtain the band structure in the $\Omega(k)$ format, since the band frequencies Ω can be computed from the eigenvalues as $\Omega = \sqrt{\lambda}$. This is referred to as the $\Omega(k)$ method, since the band frequency Ω is calculated for a prescribed wave vector k . The $\Omega(k)$ method is selected for the band structure calculations because it has been previously demonstrated to effectively identify the bandgaps and Dirac points that are required to achieve topological waves in EMs [58,83,144].

2.2.4 Negative capacitance circuitry

Per Eq. 2.12, Ω_t and ξ are parameters that are directly controllable with circuit elements (e.g., synthetic inductor or negative capacitor), while the electromechanical coupling factor ϑ is dependent on material and geometric properties, and thus cannot be altered after metamaterial fabrication. While ϑ cannot be controlled directly by external circuitry, the addition of a negative capacitor in parallel to resonant circuitry has been shown to effectively (i.e., “synthetically”) enhance the electromechanical coupling of a piezoelectric system. Previous studies have exploited an enhanced electromechanical coupling through negative capacitance circuitry to achieve vibration attenuation over a broad frequency bandwidth [36,220–223]. In this investigation, negative capacitance circuitry is also used to tailor the electromechanical coupling of the system, as can be seen by defining an effective electromechanical coupling factor ϑ_{eff} as:

$$\vartheta_{eff} = \frac{\vartheta}{1 - \xi} \quad (2.14)$$

This term, which is present in Eq. 2.10, measures the level of effective electromechanical coupling when accounting for the connected negative capacitor. Thus, by careful selection of the negative capacitance ratio (e.g., $\xi \approx 1$), the effective electromechanical coupling ϑ_{eff} can be significantly enhanced.

Since C_N is an active component, a stability analysis is necessary. The stability requirement is obtained from the dispersion relation for the metamaterial by evaluating the eigenvalues of Eq. 2.13, per the technique outlined in [224]. For positive eigenvalues ($\lambda = \Omega^2 > 0$), the oscillation frequencies ($\pm\omega$) are purely real, and there is a bounded oscillatory response (see Eq. 2.5). On the other hand, for negative eigenvalues ($\lambda = \Omega^2 < 0$), the result is frequencies with a nonzero imaginary part ($\pm i\omega$) and an unbounded response (Eq. 2.5). For the proposed metamaterial, when $\xi < 1$, all eigenvalues are positive, and the system response is bounded. In contrast, when $\xi > 1$,

negative eigenvalues appear, and the system response is unbounded. Therefore, to maintain stability:

$$C_N < C_p \leftrightarrow \xi < 1 \quad (2.15)$$

There is a physical explanation for the derived stability criterion. The parallel-connected negative capacitor reduces the effect of the inherent capacitance of an electrode pair, causing a reduction in the total capacitance present in the corresponding circuit ($C_T = C_p - C_N$, see Eq. 2.3). C_T must remain positive to maintain stability, since negative total capacitance in a circuit is analogous to negative compliance (stiffness) in a mechanical system, and no additional balancing terms exist in the circuit governing equation (Eq. 2.3).

In addition to changing the effective electromechanical coupling, the inclusion of negative capacitance influences the effective nondimensional tuning frequency of the resonant circuits. Through observation of Eq. 2.11, this influence can be measured as:

$$\Omega_{t-eff}^2 = \frac{\Omega_t^2}{1 - \xi} \quad (2.16)$$

where Ω_{t-eff} is the effective nondimensional tuning frequency. Therefore, as the negative capacitance ratio ξ is increased towards unity and effective coupling is enhanced, the effective tuning frequency is shifted to a higher value. The result indicates that, if ξ is specified to be close to unity, a large inductance would be required to achieve a low-frequency value for Ω_{t-eff} because Ω_t would need to be set to a very low value. If the inductance required to achieve a desired low tuning frequency is too large to be achieved with a standard inductor, a synthetic inductor created from active circuit components [225] or a specially designed large passive inductor [226] could be utilized. If these alternative inductor solutions are deemed impractical due to power or size requirements, an alternative for enhancing the effective electromechanical coupling is to connect the negative capacitor to the resonant circuit in a series configuration [221,222], instead of parallel (see Appendix A.2).

2.3 Working principle - obtainment of tunable topological wave propagation

In this section, the working principle is outlined for the attainment of subwavelength topological wave propagation using the proposed metamaterial. A unit cell dispersion analysis is conducted to identify lattices with nontrivial topological characteristics and define metrics that are indicators of waveguide performance. A finite strip analysis is undertaken to investigate how

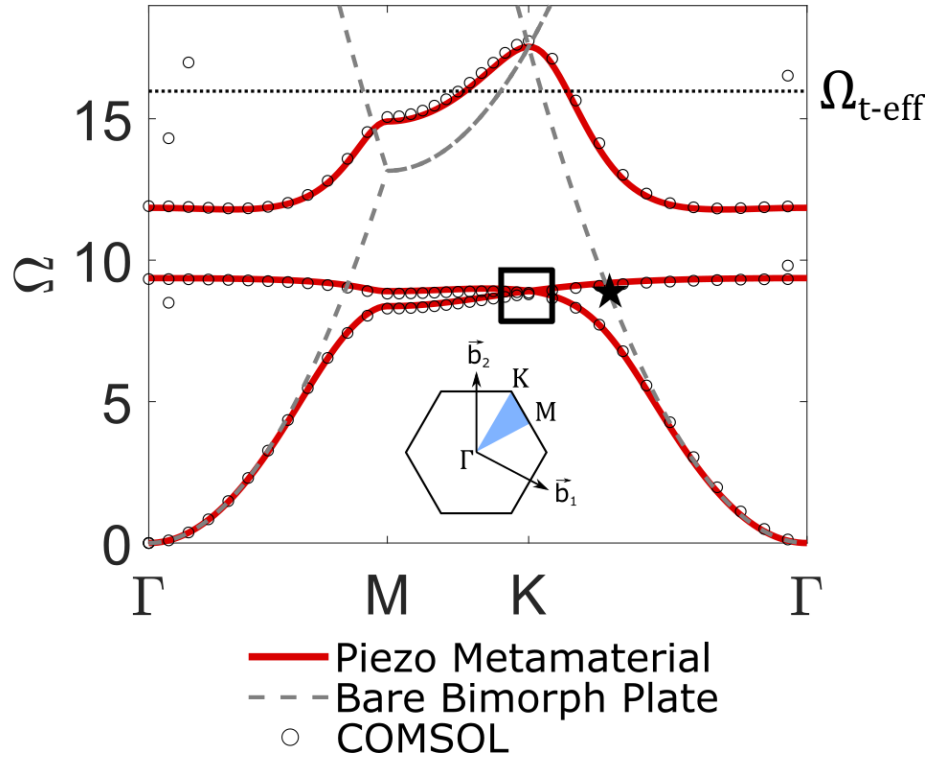


Fig 2.2. $\Omega(k)$ Dispersion diagram for unit cell with $\beta = 0$ and $\Omega_{t\text{-eff}} = 16.0$. The red lines represent results from PWE method, and the open black circles represent results from FE simulations. Band structure for bare bimorph plate is shown as gray dashed lines. For all results in this figure, the three bands with the lowest frequency (i.e., the first three bands) are displayed. The Dirac point is enclosed in the black box. Inset contains schematic of reciprocal lattice and IBZ (blue triangle).

localized topological edge states can be obtained through the connection of topologically distinct lattices. Numerical simulations are performed to illustrate how these edge states can be exploited to achieve guided topological wave propagation that is tunable in both the frequency and spatial domains.

2.3.1 Unit cell dispersion analysis

The band structure of the proposed metamaterial is obtained through a unit cell dispersion analysis. For this study, PZT-5H (a commonly utilized piezoceramic) is selected as the material for the piezoelectric layers and aluminum is selected as the material for the substrate layer. The material properties associated with PZT-5H and aluminum that are used in dispersion calculations are listed in Table 2.1. The geometric dimensions specified for the analysis are also included in Table 2.1. The layer thicknesses h_s and h_p are selected such that the nondimensional

Table 2.1. Definition of geometric and material properties.

Parameter	Value
<i>Geometric Dimensions</i>	
a	40 mm
h_s	1 mm
h_p	1 mm
r_p	10.6 mm
<i>Substrate Layer Material Properties</i>	
ρ_s	2700 kg/m ³
E_s	70 GPa
ν_s	0.3
<i>Piezoelectric Layer Material Properties</i>	
ρ_p	7500 kg/m ³
\bar{c}_{11}^E	66.2 GPa
\bar{e}_{31}	-23.4 C/m ²
$\bar{\epsilon}_{33}^S$	17.3 nF/m

electromechanical coupling factor is maximized for the selected materials ($\vartheta = 0.42$, see Eq. 2.12). The negative capacitance ratio is set to $\xi = 0.79$, such that the effective electromechanical coupling factor ϑ_{eff} is equal to 2. The tuning frequency of the circuit (Ω_t) is selected as 7.3, resulting in an effective tuning frequency (Ω_{t-eff}) of 16.0. The dispersion analysis of the unit cell is performed by solving the eigenvalue problem derived from the PWE method (Eq. 2.13). $M = 3$ is chosen, such that $N^2 = (2M + 1)^2 = 49$ plane waves are considered in the calculation and $N^2 + 2 = 51$ eigenvalues λ are obtained for each selected k . The band (i.e., dispersion curve) frequencies Ω are calculated by specifying the Bloch wave vector k to follow the edges of the irreducible Brillouin zone (IBZ - shown as the blue triangle in the inset of Fig 2.2), solving for the eigenvalues λ , and converting to frequency ($\Omega = \sqrt{\lambda}$), such that the resulting band structure is in the $\Omega(k)$ form. The band structure for the unit cell with both inductance parameters set as identical values (i.e., $\beta = 0$) is displayed as the solid red lines in Fig 2.2. The band structure is also generated using the commercial FE software COMSOL Multiphysics to validate the results derived from the PWE method (see Appendix A.3.1 for more information on the FE model). Comparison of the results (in Fig 2.2) generated from the PWE method (solid red lines) and FE simulations (open black

circles) indicates a close match, despite the solution from the PWE method requiring multiple orders of magnitude fewer degrees of freedom (13348 for FE vs. 51 for PWE). As seen in Fig 2.2, there are FE results located near the Γ point in reciprocal space that do not directly match the PWE predictions. This discrepancy is observed because the additional FE results are modes that are dominated by in-plane (refers to the \bar{x} - \bar{y} plane, perpendicular to the thickness of the plate) displacement, which is not accounted for in the governing equations for flexural (i.e., out-of-plane, \bar{z} direction) plate response (Eqs. 2.2 and 2.3) that are used in the derivation of the PWE solution (Eq. 2.13). As presented in Appendix A.3.2, these in-plane modes do not hybridize with the specific out-of-plane modes that are of interest in this study, and thus do not inhibit the achievement of topologically-protected flexural waves (as will be shown in later sections).

Due to the presence of C_3 lattice symmetry, SIS, and TRS [91], a Dirac point (which is the vertex of a Dirac cone in k_x - k_y space) is formed in the band structure between the first and second bands at the K point in reciprocal space (see black box in Fig 2.2). The Dirac point exists at the Dirac frequency $\Omega_{Dirac} = 8.9$. Per the QVHE, topological wave propagation can be obtained at frequencies near this Dirac point. To determine whether subwavelength topological wave propagation could be obtained at this frequency, the band structure for a bare bimorph plate (defined to be the bimorph plate consisting of the substrate layer, piezoelectric layers, and electrodes, with all of the connected circuits shorted) is calculated using the PWE method (dashed gray curves in Fig 2.2). At the Dirac frequency, the wavelength of propagating waves in the bare plate is 97 mm (marked by a black star in Fig 2.2), which is 2.4 times larger than the lattice constant ($a = 40$ mm). Thus, by connecting resonant circuitry in the proposed metamaterial, the Dirac point is attainable in a subwavelength frequency regime. This subwavelength characteristic could be leveraged in applications that require low frequency (corresponding to large wavelengths) topological wave control in a small package.

To obtain topological edge states per the QVHE, different inductance values are selected for each of the two circuits in the unit cell ($\beta \neq 0$), which breaks SIS. The band structure for $\beta = \pm 0.04$ is shown as the dotted lines in Fig 2.3a (the band structure for $\beta = 0$ is also included as solid lines for reference). Due to the broken SIS when $\beta \neq 0$, a bandgap (i.e., topological bandgap) is opened from the Dirac point, which is indicated by the shaded region ($\Omega_{bandgap}$). To provide a measure of bandgap size that is not skewed toward higher frequencies, a relative bandgap ($\Omega_{bandgap-relative}$) is defined as:

$$\Omega_{bandgap-relative} = \frac{\Omega_{2-min} - \Omega_{1-max}}{\frac{\Omega_{2-min} + \Omega_{1-max}}{2}} = \frac{2|\Omega_{bandgap}|}{\Omega_{2-min} + \Omega_{1-max}} \quad (2.17)$$

where $|\Omega_{bandgap}|$ is the magnitude of $\Omega_{bandgap}$ (shown in Fig 2.3a), and Ω_{p-min} and Ω_{p-max} represent the minima and maxima of the p th band, respectively. A lattice with the inductance perturbation parameter specified as $\beta > 0$ is defined as a Type A lattice, whereas $\beta < 0$ for a Type B lattice (see schematics in Fig 2.3b). While the dispersion diagrams for Type A ($\beta = 0.04$) and Type B ($\beta = -0.04$) lattices are identical (Fig 2.3a), a band inversion exists between the two lattice types. The mode shapes for the first two bands evaluated at the K point are shown in Fig 2.3c for Type A and Type B lattices. These mode shapes illustrate the band inversion, as the eigenvectors $u_p(k)$ for the p th band (where $p = 1$ is marked by a triangle and $p = 2$ is marked by a square) are interchanged for Type A and Type B lattices. This band inversion contributes to different topological characteristics for each lattice type. These topological characteristics are quantified by evaluating the topological invariant for the QVHE, the valley Chern number C_{v-p} , which is defined as [153,157,227]:

$$C_{v-p} = \frac{1}{2\pi} \iint_v B_p(k) d^2k \quad (2.18)$$

$$B_p(k) = -\nabla_k \times \langle u_p(k) | i\nabla_k[\mathbf{M}] | u_p(k) \rangle$$

where C_{v-p} is the topological charge (called the valley Chern number) for the p th band, which is calculated by integration of the Berry curvature ($B_p(k)$) near the K point in reciprocal space. The theoretical values for $C_{v-1}^{Type A}$, $C_{v-2}^{Type A}$, $C_{v-1}^{Type B}$, and $C_{v-2}^{Type B}$ are -0.5, 0.5, 0.5, and -0.5, respectively [157,228]. The opposite signs of the C_{v-p} values for Type A and Type B lattices indicate that they are topologically distinct. A method that is commonly utilized to obtain topological edge states is the connection of two topologically distinct lattices (e.g., Type A and Type B lattices) at an interface. The result is a topological transition and $N_{interface-states}$ (where $N_{interface-states} = |C_{v-p}^{Type A} - C_{v-p}^{Type B}|$) protected edge states with displacement localized at the interface, otherwise referred to as topological interface states [91,228]. Therefore, a topological interface state can be obtained by connecting the Type A and Type B lattices outlined in this analysis ($N_{interface-states} = 1$).

The topological interface state must be excited in a way that does not activate the bulk modes of a given structure to obtain localized topological wave propagation. To achieve this goal, the

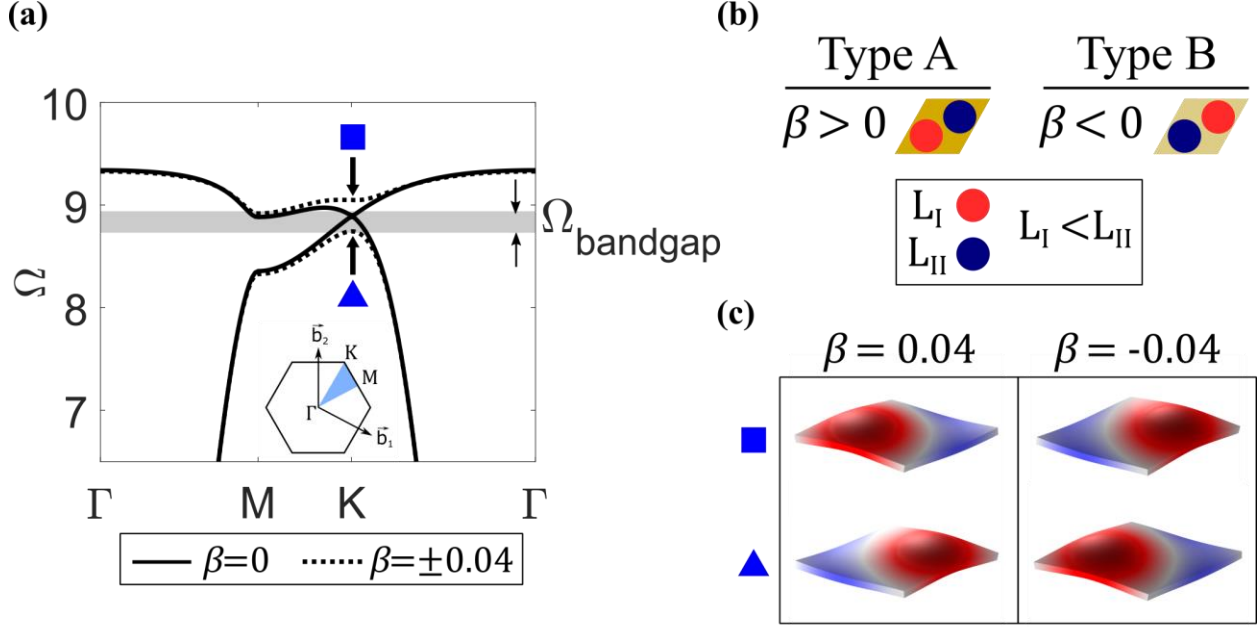


Fig 2.3. (a) Dispersion curves (specifically, the first and second bands) for $\beta = 0$ (solid lines) and $\beta = \pm 0.04$ (dotted lines) with $\Omega_{t-eff} = 16.0$. The bandgap $\Omega_{bandgap}$ opened from the Dirac point when $\beta = \pm 0.04$ is indicated by the shaded region. (b) Schematic of unit cells for Type A ($\beta > 0$) and Type B ($\beta < 0$) lattices. The smaller inductance (L_I) is connected to the red electrode and the larger inductance (L_{II}) is connected to the blue electrode. (c) Mode shapes evaluated at the K point for the first band (▲) and second band (■), revealing a band inversion between Type A ($\beta = 0.04$) and Type B ($\beta = -0.04$) unit cells.

interface state is excited at a frequency within the common topological bandgap that is found in the dispersion diagrams of the Type A and Type B lattices ($\Omega_{bandgap}$, Fig 2.3a). Therefore, the potential operating bandwidth of the topological interface state for a fixed selection of system parameters spans the topological bandgap ($\Omega_{bandgap}$). A nontrivial topological bandgap is required for an easily activated interface state to exist, and the larger the bandgap is, the greater the potential operating bandwidth of the topological waveguide. In addition to a nontrivial operating bandwidth, topological protection from defects and disorder is a required characteristic of the topological interface state. According to the elastic analog of the QVHE, the robustness to defects and disorder is related to the localization of the Berry curvature $B_p(k)$ at the K, K' points in reciprocal space [159,229]. The magnitude of the valley Chern number $|C_{v-p}|$ provides a measure of this localization and thus describes the level of topological protection inherent to the interface state. The closer the value of $|C_{v-p}|$ is to the theoretical value of 0.5, the greater the amount of topological protection. The value of 0.5 is an idealized value for $|C_{v-p}|$, as the lattice perturbation that breaks SIS and opens the topological bandgap reduces its magnitude [175,229].

Previous investigations into the elastic analog of the QVHE have shown that $|C_{v-p}| \geq 0.25$ can provide a sufficient amount of topological protection from disorder and defects in mechanical lattices [157,175].

Based on this discussion, the performance criteria defined for this investigation that are obtainable from the unit cell dispersion analysis are (1) $\Omega_{bandgap-relative} > 0$, such that a nontrivial potential operating bandwidth exists, and (2) $|C_{v-p}| \geq 0.3$ for $p = 1,2$, such that there is a minimum acceptable level of topological protection. The values of $\Omega_{bandgap-relative}$ and $|C_{v-p}|$ are 0.02 and 0.3, respectively, for the parameters specified in this analysis (where $\Omega_{t-eff} = 16.0$ and $\beta = \pm 0.04$). These results indicate that a topologically protected edge state would emerge in a structure containing an interface between the Type A ($\beta = 0.04$) and Type B ($\beta = -0.04$) lattices.

2.3.2 Topological interface states

A dispersion analysis is conducted for a finite strip of unit cells containing an interface between Type A and Type B lattices to demonstrate the emergence of topologically protected interface states. For this finite strip analysis, all parameters are defined identically to the unit cell analysis discussed in the previous section ($\beta = \pm 0.04$, $\Omega_{t-eff} = 16.0$, $\vartheta_{eff} = 2$, and all parameters from Table 2.1). The finite strip is comprised of 18 unit cells, with nine Type A unit cells connected to nine Type B unit cells at an interface (see Fig 2.4 for a schematic). A periodic boundary condition is applied in the $k_{//}$ direction, while the remaining boundaries at the ends of the finite strip are fixed. An interface composed of adjacent smaller inductance values (L_I , marked in red on the schematic) is designated as a Type I interface (Fig 2.4a), while an interface composed of adjacent larger inductance (L_{II} , marked in blue on the schematic) values is designated as a Type II interface (Fig 2.4b). The dispersion diagrams for Type I (Fig 2.4a) and Type II (Fig 2.4b) interfaces are generated using COMSOL Multiphysics. For each band, a localization parameter Λ is defined to measure the amount of flexural displacement that is localized at the interface as:

$$\Lambda = \frac{\iiint_{V_{interface}} |\bar{w}|^2 dV}{\iiint_{V_S} |\bar{w}|^2 dV} \quad (2.19)$$

where $V_{interface}$ is the total volume of the two adjacent unit cells at the interface (enclosed in the dashed black boxes in Fig 2.4) and V_S is the volume of the entire finite strip. This localization parameter is calculated for each band and is represented in the dispersion diagrams as a colormap. For a mode shape with flexural displacement that is highly localized to the interface (i.e., an

interface state), the band is a dark red shade. Lighter shaded bands indicate bulk modes ($\Lambda \ll 1$). The rectangular gray shaded region in both Fig 2.4a and Fig 2.4b separates an acoustic (low-frequency) set of bulk modes from an optical (higher-frequency) set of bulk modes and closely aligns with the topological bandgap ($\Omega_{bandgap}$) calculated in the unit cell dispersion analysis. For the Type I interface (Fig 2.4a), an interface state with highly localized displacement emerges from the optical set of bulk bands and crosses the topological bandgap to the acoustic set of bulk bands. A mode shape corresponding to this interface state at $\Omega = 8.5$ is shown in Fig 2.4a, where symmetric localized displacement exists at the interface. This mode shape contains the maximum localization of flexural displacement at the interface (as measured by $\Lambda_m = 0.92$) when compared to all other interface state modes that reside within the topological bandgap. The mathematical expression for Λ_m is given as:

$$\Lambda_m = \max_{\Omega \in \Omega_{bandgap}} \Lambda(\Omega) \quad (2.20)$$

An additional localized state exists near $\Omega = 9.4$. However, this interface state is difficult to utilize without activating the bulk modes since it is not in the topological bandgap. In contrast to the Type I interface, for a Type II interface, the primary interface state emerges from the acoustic bulk bands and crosses the topological bandgap to approach the optical bulk bands (Fig 2.4b). A mode shape corresponding to this interface state at $\Omega = 8.7$ is shown in Fig 2.4b, where the flexural displacement field is now antisymmetric about the interface, and the resulting maximum displacement localization is somewhat less ($\Lambda_m = 0.72$ compared to $\Lambda_m = 0.92$ for the Type I interface state).

Two observations are gained from the finite strip analysis. First, the proposed metamaterial enables the obtainment of symmetric and antisymmetric topological interface states, which aligns with previous investigations into the QVHE [157]. Due to the tunability of the circuit parameters in the proposed metamaterial, switching between these interface state types (symmetric and antisymmetric) could easily be achieved in practice. Second, the finite strip dispersion analysis supports the performance requirement for a nontrivial topological bandgap ($\Omega_{bandgap-relative} > 0$) derived from the unit cell dispersion analysis. In the finite strip analysis, the potential frequency bandwidth for both interface state types aligns with the topological bandgap, as unwanted hybridization of the interface state with bulk states may occur for frequencies outside of the targeted bandgap range (the rectangular gray shaded regions in Fig 2.4).

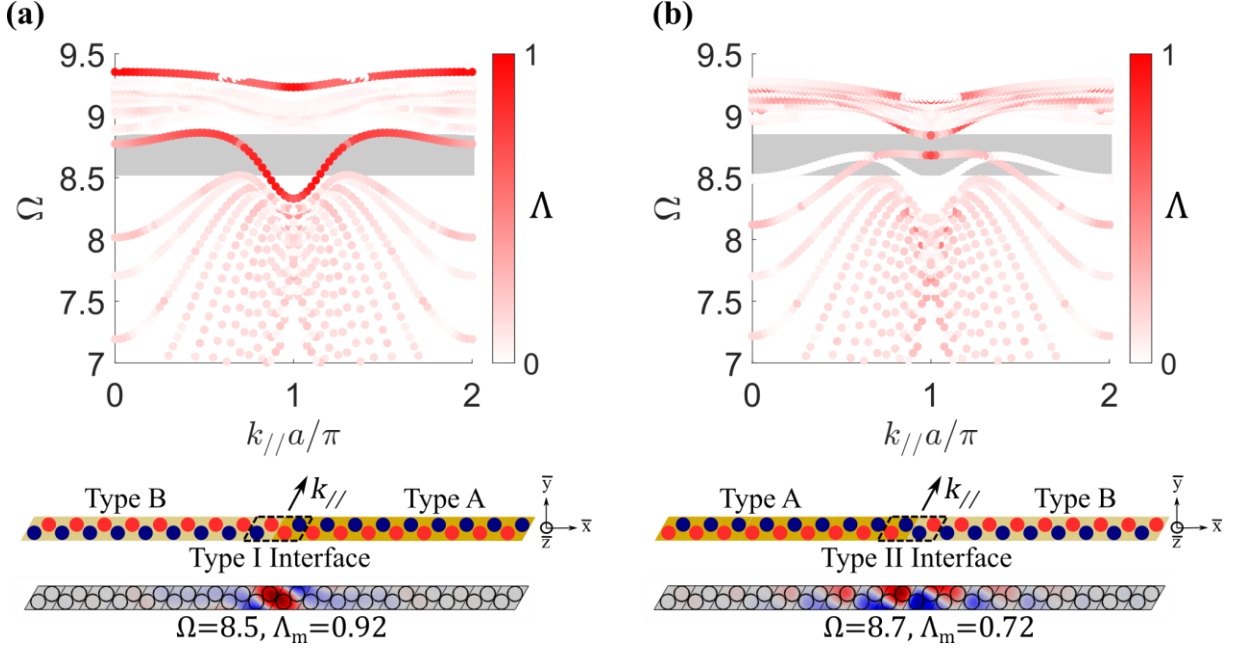


Fig 2.4. (a) Band structure for a finite strip ($|\beta| = 0.04$, $\Omega_{t-eff} = 16.0$, $\vartheta_{eff} = 2$, and all parameters from Table 2.1) with a Type I interface. The colormap indicates the localization of the flexural displacement at the interface through the localization parameter Λ , with darker red shading indicating localized interface states ($\Lambda \approx 1$). The rectangular gray shaded region represents a frequency range where no bulk modes exist and corresponds to the topological bandgap. The diagram of the finite strip is shown below the band structure, with the interface used for Λ calculations enclosed in a dashed black box. A symmetric mode shape that is calculated from the interface state at $\Omega = 8.5$ with a localized displacement ($\Lambda_m = 0.92$) is also shown. (b) Band structure and schematic for a finite strip with a Type II interface. At the bottom, an antisymmetric mode shape that is calculated from the interface state at $\Omega = 8.7$ (with $\Lambda_m = 0.72$).

2.3.3 Path tunable topological wave propagation

The ability to achieve topological wave propagation from the interface states is investigated with FE simulations of a plate constructed from the proposed metamaterial. The proposed metamaterial enables concurrent tunability of the topological wave path, mode shape, and frequency, which advances upon previously developed platforms that are generally narrowband in nature and only focus on one tailorable characteristic. Each of the proposed metamaterial's tailorable properties are investigated separately in this chapter to simplify the analysis. The path tunability of the topologically protected waveguide is examined in this section, while comprehensive analyses on frequency and mode shape tailoring are contained in Section 2.4.

The plate used for FE simulations consists of a 16 by 20 lattice of unit cells, with low-reflecting boundary conditions (see Appendix A.3.1 for more information on the low-reflecting boundary conditions) applied along all outer boundaries to suppress reflections (see left column of Fig 2.5 for plate schematics). The lattice contains an interface between Type A and Type B unit cells,

which is enclosed by the black lines in Fig 2.5a, Fig 2.5b, Fig 2.5c, and Fig 2.5d. A resistance (R) of 10Ω is applied to each individual circuit to account for minor circuit losses that may arise in practical implementation. The plate is excited harmonically at a frequency that is within the topological bandgap ($\Omega_e = 8.7$), thus corresponding to a subwavelength regime (since the Dirac point at $\Omega_{\text{Dirac}} = 8.9$ contains the subwavelength characteristic). The excitation is applied as an out-of-plane point excitation at the location indicated by the arrow. FE simulations using COMSOL Multiphysics are conducted to obtain the steady-state displacement field. Fig 2.5a shows a displacement field with flexural response that is guided along a Type I interface, which supports a symmetric interface state. This specific case shows a straight line of wave propagation that is localized at the interface and is guided to a receiver indicated in Fig 2.5a as “R1”. In Fig 2.5b and Fig 2.5c, the interface is changed using circuit parameters such that flexural response under the same excitation is guided to receivers “R2” or “R3”. In Fig 2.5b, guided transmission is demonstrated along a Type I interface with a sharp (120°) corner, indicating that the nontrivial topological property of the interface state provides protection from disorder. In Fig 2.5c, a Type I interface and a Type II interface are concatenated to achieve topological wave propagation around a shallow (60°) corner. It can be seen that the flexural displacement is symmetric along the Type I interface segment and antisymmetric along the Type II segment, revealing that the two edge state types are compatible and can be used in series to achieve a variety of interface paths. The results in Fig 2.5a, Fig 2.5b, and Fig 2.5c illustrate the path tunability of the proposed TM. As shown in the presented example, an input can be guided to three different receivers by using circuit elements (e.g., a synthetic inductor that can tune β) to vary the interface properties and location. For each of these cases, the wave amplitude (as indicated by the color intensity) is nearly identical from the input location to the designated output receiver, while the energy present at the other output receivers is negligible (e.g., in Fig 2.5a, there is a trivial amount of flexural displacement present near R2 and R3). This realization of nearly lossless transmission to the desired location(s) is obtainable due to the robustness of the topological interface state and the presence of the topological bandgap, which minimizes energy leakage into the bulk. Finally, to demonstrate the robustness of the topological interface state in the presence of both disorder and defects, a lattice is constructed with two sharp corners and a defect (one unit cell with both circuits shorted) in the interface path (Fig 2.5d). The steady-state response of the plate reveals flexural displacement that is guided along the Z-shaped interface path without undesirable localization or amplitude reduction

at defects or sharp corners. This result indicates that guided transmission through more complicated wave paths (e.g., having multiple corners) can be obtainable from the proposed metamaterial, even in the presence of imperfections (e.g., malfunctioning/shorted circuits) that are commonly found in practical applications.

2.4 Parametric study – frequency and mode shape tunability

In this section, a parametric study is undertaken to extensively explore the adaptive characteristics of the proposed metamaterial and develop a detailed understanding of system parameters that govern performance. A framework is developed to assess the frequency and interface mode shape tunability of the metamaterial and uncover insights into the impact of electromechanical coupling on topological elastic wave control.

2.4.1 Frequency tunability of the Dirac point

Since topological wave propagation occurs at a frequency near the Dirac frequency (Ω_{Dirac}), the tunability of the Dirac point is investigated. The eigenvalue problem derived from the PWE method (Eq. 2.13) is utilized to calculate Ω_{Dirac} as a function of the effective circuit tuning frequency Ω_{t-eff} . Calculations are conducted with $\beta = 0$ for three different effective negative capacitance is implemented with PZT-5H ($\xi = 0.79$, $\vartheta_{eff} = 2$). Fig 2.6a illustrates how Ω_{Dirac} can be continuously tuned through a large frequency range (Ω_{Dirac} exists between 0 and 17.55) by tailoring the effective tuning frequency Ω_{t-eff} of the resonant circuits. Alterations to the lattice constant a , which can be difficult or impractical to achieve in mechanical structures after they have been fabricated, are not required to tune the Dirac frequency, since the proposed metamaterial relies on locally resonant circuits instead of a Bragg scattering mechanism. Further observation of Fig 2.6a indicates that the Dirac frequency Ω_{Dirac} is always less than the effective tuning frequency Ω_{t-eff} of the resonant circuits (regardless of ϑ_{eff}), which can facilitate the achievement of Dirac points in a deep subwavelength regime ($\Omega_{Dirac} \rightarrow 0$ for $\Omega_{t-eff} \rightarrow 0$) and aligns with results that have been previously reported for thin plate metamaterials with spring-mass resonators [162,163]. In contrast to previous studies that have used mechanical resonators, the frequency of the Dirac point (Ω_{Dirac}) in the proposed metamaterial can easily be adjusted on-line by using tunable circuit parameters (Ω_{t-eff}). Therefore, the tunability of the proposed

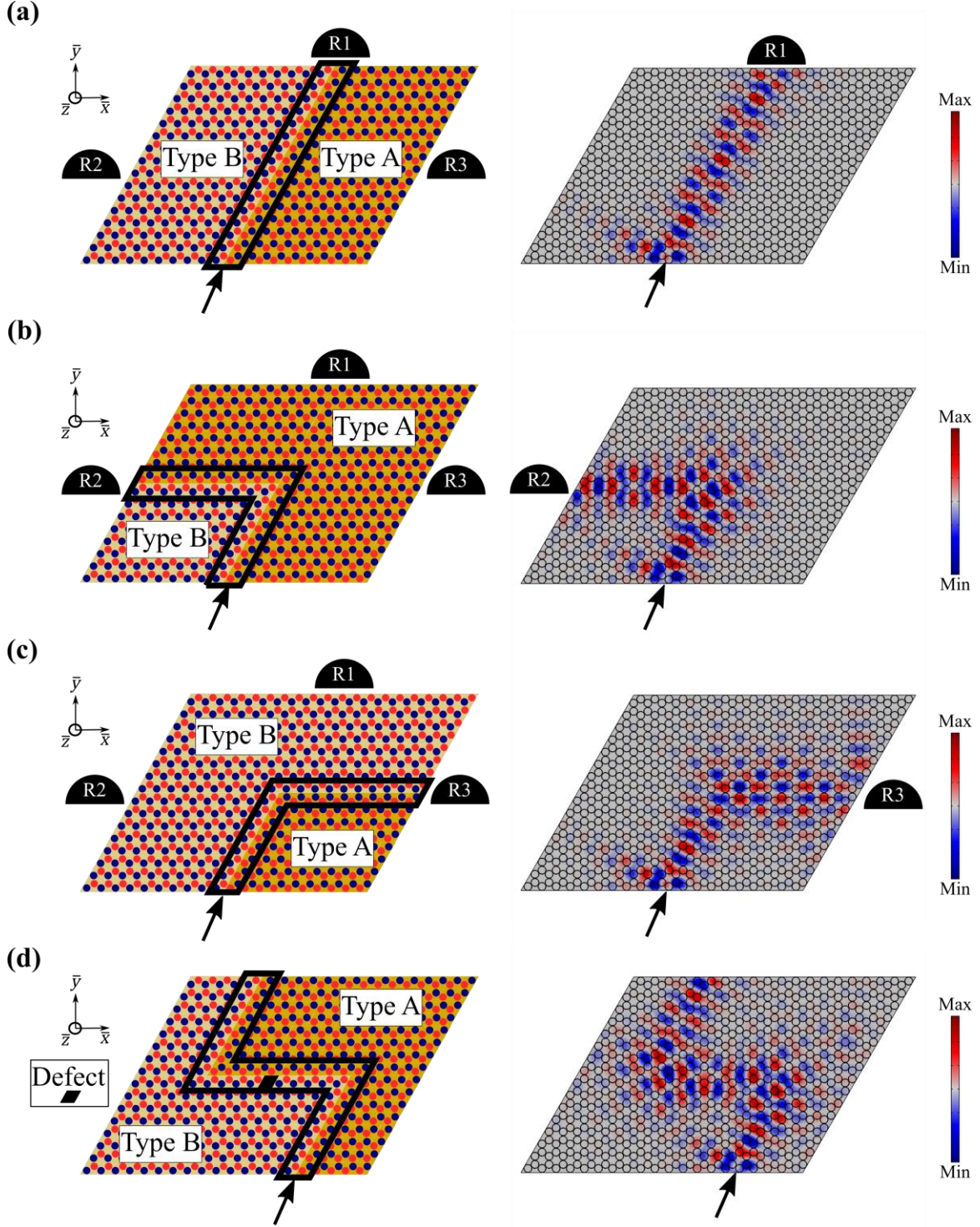


Fig 2.5. Schematics (left column) and steady-state response (right column) for guided wave propagation along (a) straight, (b) sharp corner, (c) shallow corner, and (d) ‘Z-shape with defect’ interfaces. In the schematics, R1, R2, and R3 represent output signal receivers and black lines enclose the interface between Type A and Type B lattices. Circuit parameters are defined as: $\beta = \pm 0.04$, $\Omega_{t-eff} = 16.0$, and $\xi = 0.79$, resulting in $\Omega_{Dirac} = 8.9$ and $\vartheta_{eff} = 2$. A harmonic out-of-plane point excitation ($\Omega_e = 8.7$) is applied where indicated by the black arrow. For steady-state response, the out-of-plane displacement amplitude is indicated by the color intensity. The steady-state displacement fields illustrate the path tunability and topological protection of the proposed metamaterial.

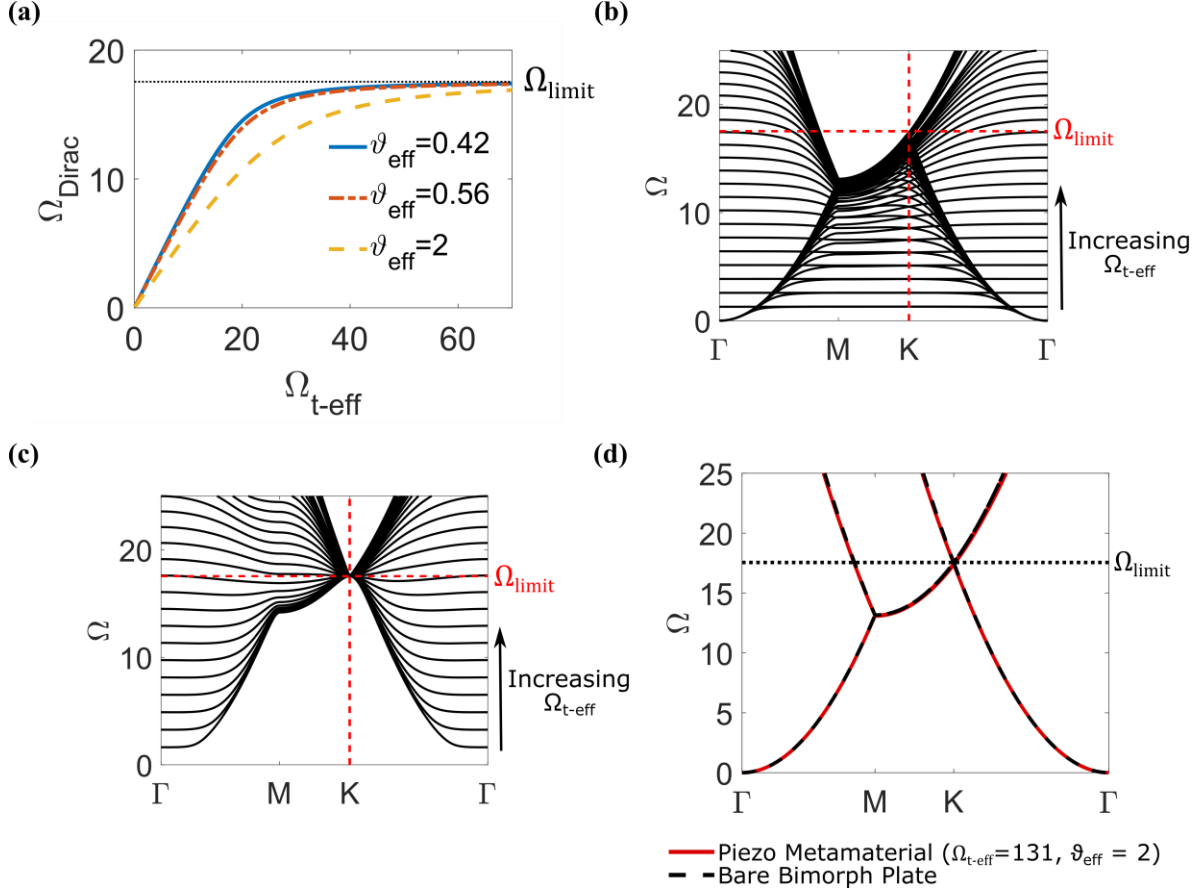


Fig 2.6. (a) Dirac frequency Ω_{Dirac} as a function of circuit tuning frequency Ω_{t-eff} for various ϑ_{eff} . The upper limiting frequency (Ω_{limit}) of 17.55 is indicated by a dotted black line. (b) Evolution of the first and second bands (all bands are shown as black lines) with increasing Ω_{t-eff} (indicated by arrow) for Ω_{t-eff} specified between 2 and 150 ($\beta = 0$ and $\vartheta_{eff} = 2$). Ω_{limit} is indicated by dashed red lines. (c) Evolution of third band for same set of parameters. (d) Band structure comparison for proposed metamaterial with high tuning frequency ($\Omega_{t-eff} = 131$, indicated by solid red lines) and bare bimorph plate (indicated by dashed black line).

metamaterial could be exploited to achieve topological phenomena that are adaptive to variable frequency requirements derived from operating conditions or external stimuli.

According to Fig 2.6a, the achievable frequency range for Ω_{Dirac} begins at $\Omega_{Dirac} \approx 0$ and asymptotically approaches $\Omega_{Dirac} = 17.55$ as Ω_{t-eff} is made very large. This frequency range is unaltered by variation of the effective electromechanical coupling (ϑ_{eff}), as can be seen in Fig 2.6a and Appendix A.4, where a parametric analysis is conducted with extreme ϑ_{eff} values. Thus, 17.55 is designated as the limiting frequency (Ω_{limit}) for the Dirac point (see dotted black line in Fig 2.6a). Insight into why this limit exists is gained by studying the evolution of the band structure with increasing Ω_{t-eff} (Fig 2.6b, Fig 2.6c, and Fig 2.6d). In Fig 2.6b, the first and second dispersion curves are plotted for Ω_{t-eff} values that are between 2 and 150, with the arrow

indicating how the bands evolve with increasing Ω_{t-eff} . As can be seen in this figure, the Dirac point (the degeneracy between the first and second bands at K) converges to $\Omega_{limit} = 17.55$ (indicated with dashed red lines) for large Ω_{t-eff} values. Fig 2.6c contains the variation of the third dispersion curve for the same Ω_{t-eff} range. The band evolution illustrated in Fig 2.6c illuminates how the frequency value of the third band at the K point remains constant at $\Omega_{limit} = 17.55$ for all Ω_{t-eff} , and thus cannot be adjusted by circuit parameters. This phenomenon causes the third band to effectively act as a “constraint” that limits the maximum frequency of the Dirac point. A physical explanation for this observation is obtainable by analysis of Fig 2.6d where the band structure for the proposed metamaterial with $\Omega_{t-eff} = 131$ (solid red lines) is compared to the band structure for the bare bimorph plate (dashed black lines). The two band structures are effectively identical because the tuning frequency has been set to such a large value that the effects of the resonant circuits are no longer present in this frequency region. Thus, for large Ω_{t-eff} , the dispersion properties of the proposed metamaterial will converge to those of the bare bimorph plate within the targeted frequency range (the range containing the first and second bands), resulting in an “upper bound” for the Dirac frequency. Although it has yet to be reported in previous investigations, this phenomenon is also observable for a thin plate with attached spring-mass resonators. The discovery of the limiting frequency Ω_{Dirac} presented in this work and the awareness of the underlying phenomena that define it could be utilized as part of a design framework in future studies that leverage local (electrical or mechanical) resonators to achieve Dirac dispersions.

2.4.2 Achievable operating region for topological interface states

A lattice perturbation must be applied to open a topological bandgap from the Dirac point and achieve topological edge states per the QVHE. While the previously presented analysis (see Section 2.3) demonstrates this working principle under a fixed set of parameters, further exploration is required to fully evaluate the tunability of the proposed metamaterial. Thus, a parametric study involving the inductance perturbation parameter β and the circuit tuning frequency Ω_{t-eff} is conducted to define an achievable operating region where adaptive topological wave propagation could exist. The classical eigenvalue problem for the unit cell (Eq. 2.13) is solved for a wide range of β and Ω_{t-eff} values, and the achievable operating region is defined by evaluating the previously specified performance criteria of (1) a nontrivial potential operating

bandwidth, as suggested by $\Omega_{bandgap-relative} > 0$, and (2) a sufficient level of topological protection, as indicated by the valley Chern number ($|C_{v-p}| \geq 0.3$ for $p = 1,2$). For this parametric study, all geometric and material parameters are selected as indicated in Table 2.1, and no negative capacitance is connected ($\xi = 0$), such that $\vartheta_{eff} = 0.42$. The magnitude of the valley Chern number ($|C_{v-p}|$) and the relative bandgap size ($\Omega_{bandgap-relative}$) are calculated and shown in Fig 2.7a and Fig 2.7b as a function of the lattice perturbation magnitude $|\beta|$ and the Dirac frequency Ω_{Dirac} (which is determined by Ω_{t-eff} , as shown in the preceding section). The magnitude of the valley Chern number is listed more generally as $|C_v|$ in Fig 2.7a, because calculations indicate that: $C_{v-1}^{Type A} = C_{v-2}^{Type B} \approx -C_{v-2}^{Type A} = -C_{v-1}^{Type B} \therefore |C_{v-p}^{Type A}| \approx |C_{v-p}^{Type B}| = |C_v|$ for $p = 1,2$. In Fig 2.7a, it is shown that the localization of the Berry curvature $|C_v|$ decreases as the inductance perturbation $|\beta|$ is increased for a fixed Ω_{Dirac} . On the other hand, results in Fig 2.7b illustrate how $\Omega_{bandgap-relative}$ increases as $|\beta|$ is made larger for a particular Ω_{Dirac} . This tradeoff between topological protection and potential operating bandwidth is a common feature of TMs mimicking the QVHE, and previous works have investigated how to overcome the limitations associated with balancing these performance criteria [159,175]. Due to the adaptivity of the proposed metamaterial, the frequency range where topological wave propagation is achievable is not restricted to the potential operating bandwidth under fixed parameters. The frequency range where topological interface states that satisfy performance criteria (1) and (2) are attainable is indicated by the dashed black lines in Fig 2.7b. This enclosed region is referred to as the “achievable operating region,” which is dependent on the predefined performance criteria. For this study, the achievable operating region spans $\Omega_{Dirac} = 4.2$ to $\Omega_{Dirac} = 11$, and examples of topological interface states derived from Dirac points at $\Omega_{Dirac} = 5.9, 8.9, \text{ and } 10.4$ are shown in Fig 2.7c (corresponding $|\beta|, \Omega_{Dirac}$ are marked with $\bullet, \blacksquare, \blacktriangle, \star, \text{ and } \blacklozenge$ in Fig 2.7b). These topological interface states are obtained by creating a Type I interface in a finite strip of 18 unit cells (see schematic in Fig 2.7c) and selecting the most localized interface mode (Λ_m , see Eq. 2.20) present in the topological bandgap of the dispersion diagram. The results illuminate how the frequency tunability of the proposed metamaterial could be utilized to achieve topological interface states over a broadband set of frequencies. In addition, the evaluation of the achievable operating region reveals that while Dirac points can be obtained with a Ω_{Dirac} between 0 and 17.55, topological interface states are attainable over a narrower frequency range (for the performance criteria

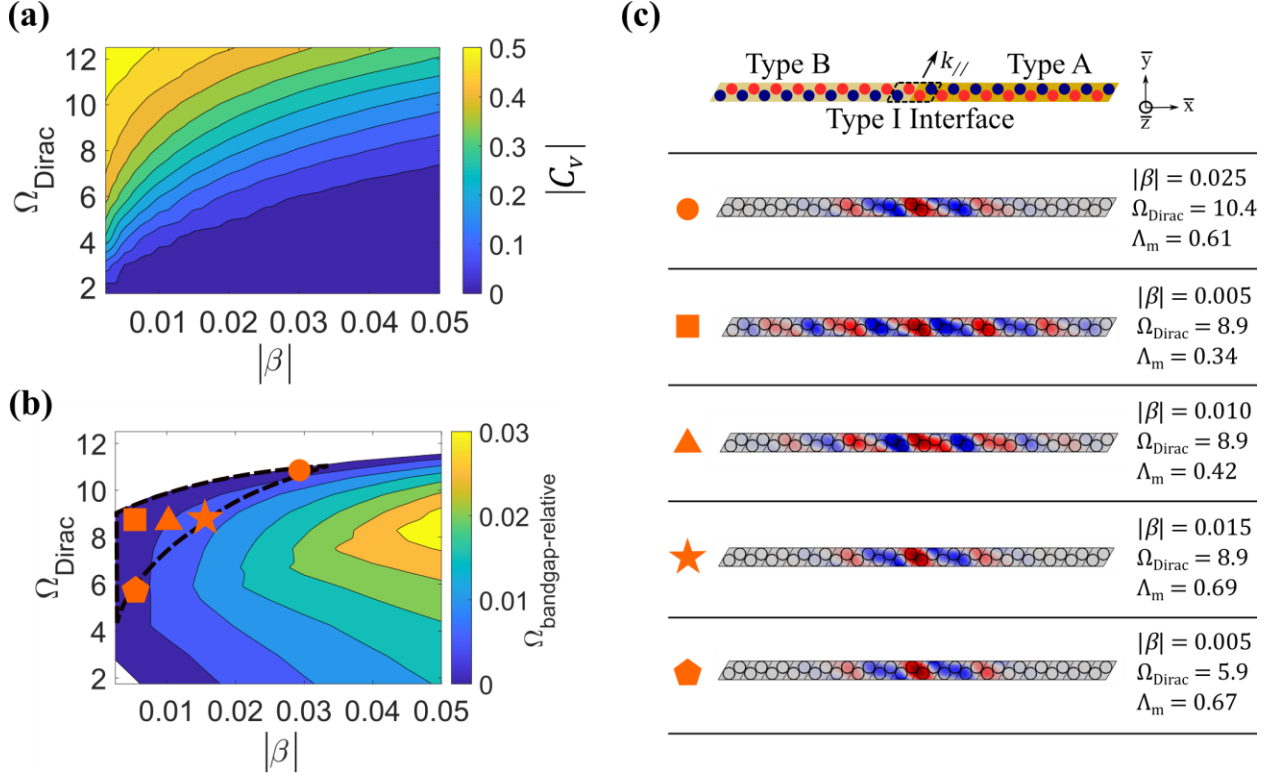


Fig 2.7. (a) Valley Chern magnitude $|C_v|$ calculated as a function of Dirac frequency Ω_{Dirac} and inductance perturbation magnitude $|\beta|$ with $\vartheta_{eff} = 0.42$. Increasing $|C_v|$ indicated by increasing brightness. (b) Relative bandgap $\Omega_{bandgap-relative}$ as a function of Dirac frequency Ω_{Dirac} and inductance perturbation magnitude $|\beta|$ with $\vartheta_{eff} = 0.42$. Increasing $\Omega_{bandgap-relative}$ indicated by increasing brightness. The achievable operating region is enclosed by the dashed black line. (c) Schematic for finite strip with Type I interface that is used to generate interface modes. Interface mode shapes for finite strip with unit cell parameters indicated by \bullet , \blacksquare , \blacktriangle , \star , and \blacklozenge markings in (b).

specified in this case: $\Omega_{Dirac} = 4.2$ to $\Omega_{Dirac} = 11$).

Aside from enabling an adjustable frequency range for topological interface states, the proposed metamaterial also facilitates the tailoring of interface mode shape and localization. The ability to adjust interface mode localization is investigated by varying the inductance perturbation parameter $|\beta|$ for a fixed Ω_{Dirac} within the achievable operating region. For each $|\beta|$, the interface mode shapes that contain maximum displacement localization (Λ_m) within the topological bandgap are selected. For $\Omega_{Dirac} = 8.9$, $|\beta|$ is set to 0.005, 0.010, and 0.015, and the corresponding interface modes are shown in Fig 2.7c (marked by \blacksquare , \blacktriangle , and \star , respectively). Analysis of the mode shapes indicates that the displacement localization at the interface increases substantially as $|\beta|$ is made larger, from $\Lambda_m = 0.34$ for $|\beta| = 0.005$ (\blacksquare in Fig 2.7c) to $\Lambda_m = 0.69$ for $|\beta| = 0.015$ (\star in Fig 2.7c). This increased mode localization is due to a progressively enhanced band inversion between the Type A and Type B unit cells that make up the interface. In addition to tailoring the

displacement localization of the interface state, the mode shape could be switched from symmetric to antisymmetric by changing to the appropriate interface type (Type I or Type II, see Fig 2.4). This capability to manipulate the interface mode could be leveraged in applications requiring adjustable displacement fields.

2.4.3 Influence of electromechanical coupling on topological wave tunability

The effect of electromechanical coupling on the vibration attenuation performance of piezoelectric metamaterials is well documented [36,220,221]. In this investigation, the influence of the effective electromechanical coupling factor ϑ_{eff} on the tunability of topological edge states in piezoelectric metamaterials is investigated for the first time. In the preceding section, a framework for the evaluation of topological edge state tunability was synthesized and applied to a baseline example case (piezoelectric layers made of PZT-5H, $\xi = 0$, $\vartheta_{eff} = 0.42$). In this section, two additional cases with identical geometric parameters are analyzed to assess the effect of enhanced electromechanical coupling: PNN-PZT piezoelectric layers with no negative capacitance circuitry ($\xi = 0$, $\vartheta_{eff} = 0.56$) and PZT-5H piezoelectric layers with a parallel-connected negative capacitor ($\xi = 0.79$, $\vartheta_{eff} = 2$). In Fig 2.8a and Fig 2.8b, the relative bandgap $\Omega_{bandgap-relative}$ is shown as a function of the inductance perturbation parameter ($|\beta|$) and the Dirac frequency (Ω_{Dirac}) for cases where $\vartheta_{eff} = 0.56$ and $\vartheta_{eff} = 2$, respectively. Dashed black lines enclose the achievable operating regions where the performance criteria ($\Omega_{bandgap-relative} > 0$ and $|C_{v-p}| \geq 0.3$) are satisfied. By comparison of Fig 2.7b with Fig 2.8a and Fig 2.8b, it is apparent that the achievable operating region is augmented by enhancing the electromechanical coupling. This expansion occurs because the band structure is “shaped” in a manner that is beneficial from the perspective of the QVHE when the electromechanical coupling is increased (see Appendix A.5 for further information).

The expansion of the achievable operating region signifies an increased level of tunability. In terms of frequency range, the achievable operating region is extended to lower frequencies (while maintaining an upper bound of approximately $\Omega_{Dirac} = 11$), as the lower boundary extends to $\Omega_{Dirac} = 3.8$ for $\vartheta_{eff} = 0.56$ and $\Omega_{Dirac} = 3.2$ for $\vartheta_{eff} = 2$, resulting in 6% and 15% increases in operating region frequency range, respectively (when compared to $\Omega_{Dirac} = 4.2$ to 11 for $\vartheta_{eff} = 0.42$). In addition, for any selected Ω_{Dirac} , a greater $|\beta|$ can be attained (i.e., the right edge of the achievable operating region is extended to larger $|\beta|$ values). As demonstrated in the previous

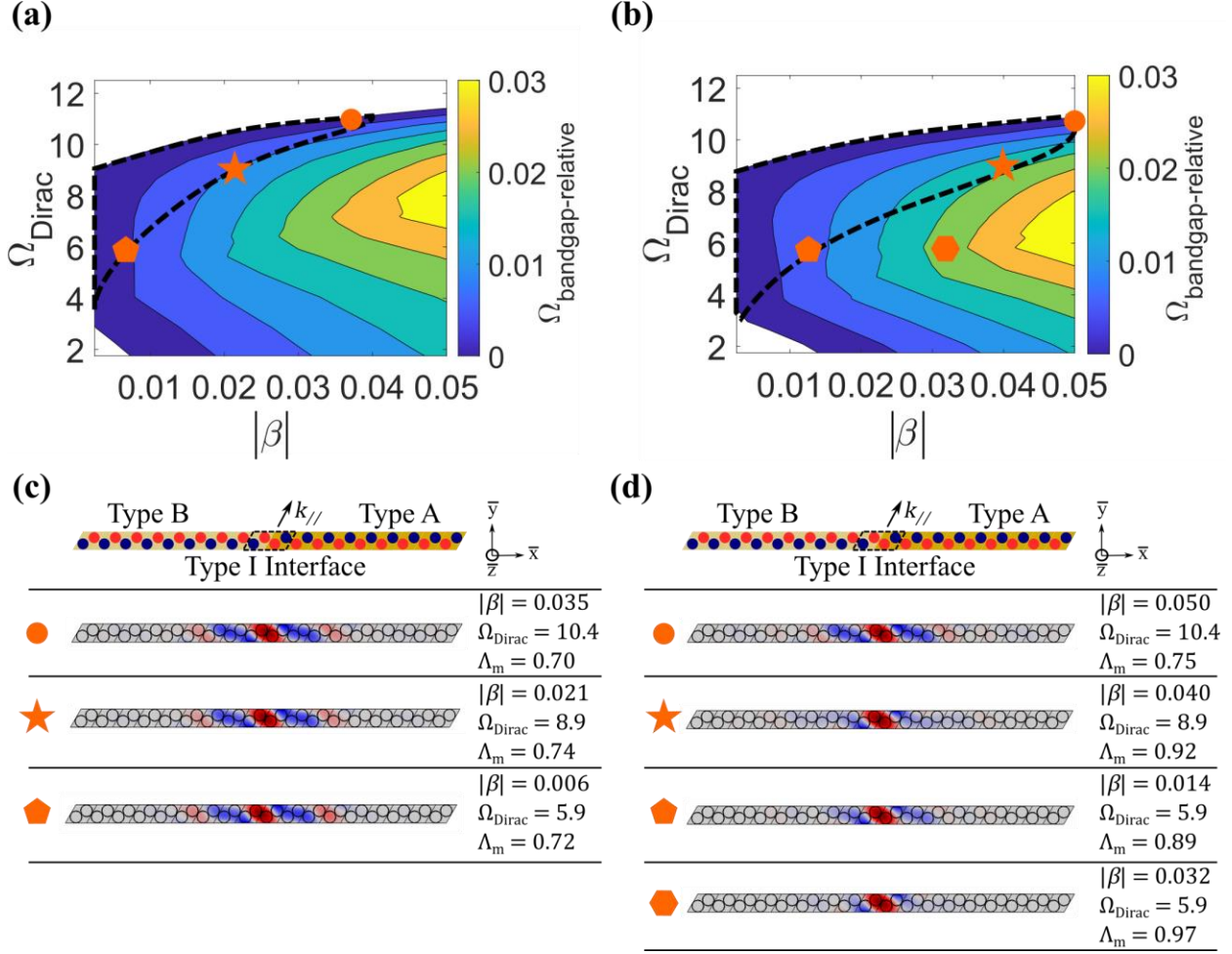


Fig 2.8. (a) Relative bandgap $\Omega_{bandgap-relative}$ as a function of Dirac frequency Ω_{Dirac} and inductance perturbation magnitude $|\beta|$ for PNN-PZT piezoelectric layers ($\vartheta_{eff} = 0.56$). Increasing $\Omega_{bandgap-relative}$ indicated by increasing brightness. The achievable operating region is enclosed by the dashed black lines. (c) Schematic for finite strip with Type I interface that is used to generate interface modes. Interface mode shapes for finite strip with unit cell parameters indicated by ●, ★, ◆, and markings in (a). (b) and (d) report the same results as (a) and (c), respectively, for PZT-5H with negative capacitance circuitry ($\vartheta_{eff} = 2$). Findings illustrate how the size of the achievable operating region, and thus tunability of the topological interface state, increases with larger ϑ_{eff} .

section, a larger $|\beta|$ corresponds to a wider potential operating bandwidth under fixed parameters ($\Omega_{bandgap-relative}$) and an amplified band inversion at the interface. Due to this increased band inversion, the topological interface mode shapes for the $\vartheta_{eff} = 0.56$ and $\vartheta_{eff} = 2$ cases (shown in Fig 2.8c and Fig 2.8d) contain greater localization at the interface than the interface modes for $\vartheta_{eff} = 0.42$ (Fig 2.7c). Regardless of the specified Ω_{Dirac} (examples shown in Fig 2.7 and Fig 2.8 are $\Omega_{Dirac} = 5.9, 8.9,$ and 10.4), the greatest achievable mode localization, which is quantified by Λ_m , increases with the effective coupling (e.g., for $\Omega_{Dirac} = 8.9, \Lambda_m = 0.69, 0.74, 0.92$ when $\vartheta_{eff} = 0.42, 0.56, 2$, respectively, see ★ in Fig 2.7c and Fig 2.8c and Fig 2.8d).

These findings indicate that electromechanical coupling plays a crucial role in determining the extent of the tunability of the topological interface state. Thus, care must be taken to maximize the effective electromechanical coupling through material selection and geometric design. In addition, negative capacitance circuitry could be utilized to artificially enhance the coupling and achieve topological interface states with a broader frequency range and increased displacement localization.

2.4.4 Finite element evaluation of frequency and mode shape tunable topological waves

FE simulations of plates constructed from the proposed metamaterial are conducted to verify that tunable topological wave propagation can be realized by activation of the topological interface states contained within the achievable operating region. Plates with straight line and Z-shaped Type I interfaces are harmonically excited at the locations indicated by the arrows in Fig 2.9a. Geometric, material, and negative capacitance ($\xi = 0.79$) parameters are selected to match the analysis presented in Section 2.3, where wave propagation for $|\beta| = 0.04$, $\Omega_{Dirac} = 8.9$ (★ in Fig 2.8b and Fig 2.8d), and $\Omega_e = 8.7$ was displayed (see Fig 2.5). To complement the results shown for $\Omega_{Dirac} = 8.9$, topological wave propagation is investigated for high frequency ($\Omega_{Dirac} = 10.4$) and low frequency ($\Omega_{Dirac} = 5.9$) Dirac points that are near the upper and lower boundaries of the achievable operating region defined in Fig 2.8b. Fig 2.9b contains the steady-state displacement fields for a plate with circuit parameters specified as $|\beta| = 0.050$ and $\Omega_{Dirac} = 10.4$ (● in Fig 2.8b and Fig 2.8d) that is harmonically excited at $\Omega_e = 10.2$. The flexural displacement is successfully guided along the interfaces. However, displacement localization at the interface is noticeably reduced from what is observed in Fig 2.5 due to a less localized interface mode ($\Lambda_m = 0.75$ for ● and $\Lambda_m = 0.92$ for ★ in Fig 2.8d). The steady-state displacements for $|\beta| = 0.032$, $\Omega_{Dirac} = 5.9$ (● in Fig 2.8b and Fig 2.8d), and $\Omega_e = 5.9$ are shown in Fig 2.9c. The flexural displacement is highly localized to the interface for both the straight line and Z-shaped cases. These high- and low-frequency results, paired with the results for $\Omega_{Dirac} = 8.9$, illustrate how guided topological wave propagation in the proposed metamaterial can be tuned across a broad frequency range. The adjustment of the displacement field (i.e., localization) at the interface is also displayed.

Notably, for the low-frequency case ($\Omega_{Dirac} = 5.9$), the inductance perturbation ($|\beta| = 0.032$) is outside of the achievable operating region (● in Fig 2.8b and Fig 2.8d). For the maximum $|\beta|$ contained within the achievable operating region ($|\beta| = 0.014$, ◆ in Fig 2.8b and Fig 2.8d), the

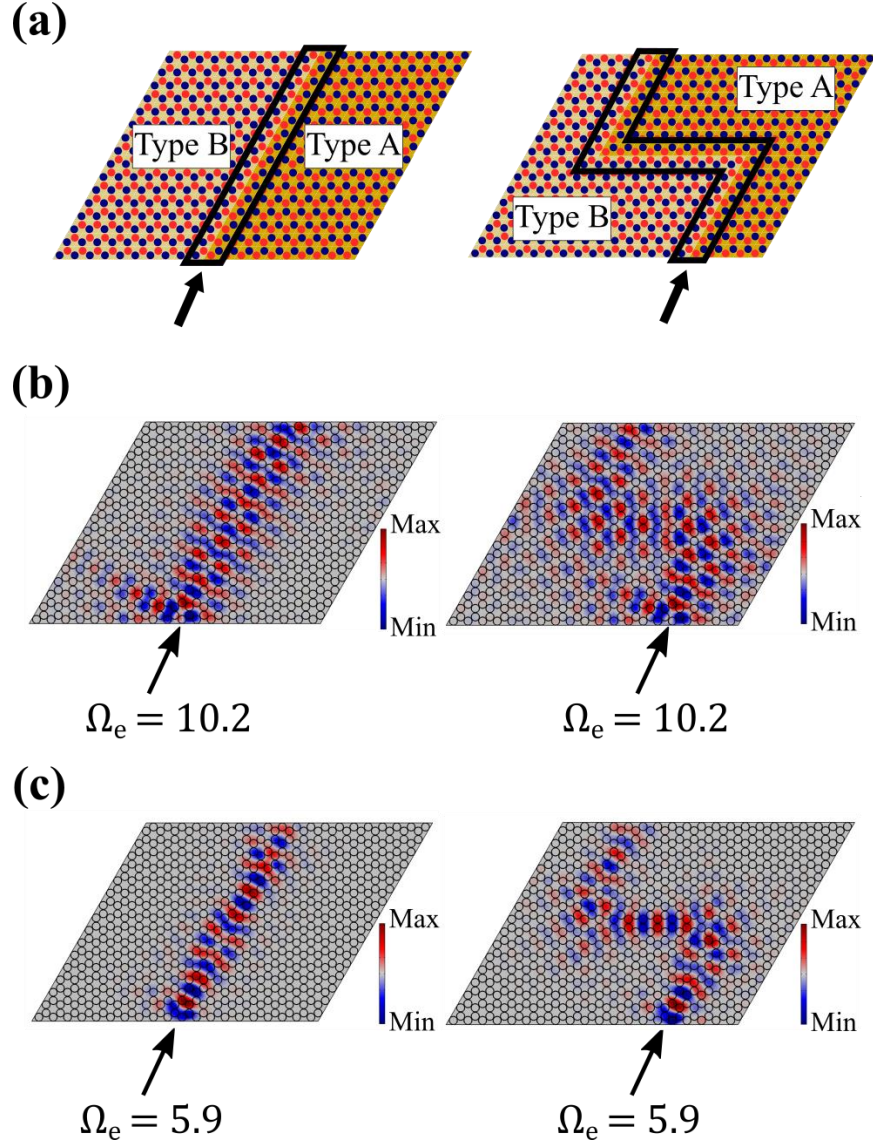


Fig 2.9. (a) Schematics for thin plate metastructures with straight and Z-shaped Type I lattice interfaces (enclosed in black lines). A harmonic out-of-plane point excitation is applied where indicated by the arrow. Negative capacitance circuitry is connected such that $\vartheta_{eff} = 2$ in all cases. (b) Steady-state displacement fields for $|\beta| = 0.050$, $\Omega_{Dirac} = 10.4$, and $\Omega_e = 10.2$. (c) Steady-state displacement fields for $|\beta| = 0.032$, $\Omega_{Dirac} = 5.9$, and $\Omega_e = 5.9$. For steady-state response, the out-of-plane displacement amplitude is indicated by the color intensity. The results illuminate how tunable topological interface states can be harnessed to achieve topological wave propagation with adjustable levels of displacement localization over a large frequency range.

flexural response does not successfully maintain localization along the sharp corners in the lattice with the Z-shaped interface (see Appendix A.6). Thus, despite the resulting reduction in valley Chern magnitude ($|C_v| = 0.015$ for $|\beta| = 0.032$), a larger $|\beta|$ (and corresponding augmented band inversion and topological bandgap) is required to successfully guide a wave along multiple sharp corners within this deep subwavelength frequency regime. This result, paired with a similar

observation reported in [175], indicates that under certain conditions (e.g., multiple sharp corners at very low frequencies), the performance criteria that define the achievable operating region may need to be modified (e.g., reducing the minimum $|C_v|$ requirement). Due to the comprehensive tunability of the proposed metamaterial, circuit adjustments could be made on-line to achieve the desired performance (as is shown in Fig 2.9c) when scenarios such as these arise (see Appendix A.6 for further discussion).

2.5 Lattice reconfiguration

The architecture of the proposed metamaterial can also be exploited to enhance adaptivity through lattice reconfiguration, which has been used in previous investigations to achieve tailorable bandgaps and waveguides in topologically trivial structures [230,231]. In this section, lattice reconfiguration is explored as a mechanism to enhance the frequency range of topological waves and obtain additional topological edge states.

2.5.1 Formation of additional Dirac point through lattice reconfiguration

Fig 2.10a contains schematics for three different lattice configurations that are attainable with the proposed metamaterial. Fig 2.10b contains the corresponding dispersion diagrams for each lattice configuration with circuit conditions specified such that $\Omega_{t-eff} = 28$ and $\vartheta_{eff} = 2$. Configuration 1 is a honeycomb lattice that contains identical resonant circuits ($\beta = 0$) and the symmetries (C_3 , SIS, TRS) required to achieve a Dirac point between the first and second bands (labeled as “Dirac 1” in Fig 2.10b). Configuration 3 is a triangular lattice that is realized by shorting one of the two circuits in the unit cell ($\beta = 1$, see Fig 2.10a). This triangular lattice also contains C_3 , SIS, and TRS symmetries, resulting in the formation of a Dirac point between the second and third bands at $\Omega_{Dirac} = 17.55$ (labeled as “Dirac 2” in Fig 2.10b). Previous works concerning triangular lattices in photonic crystals have also uncovered a Dirac point between the second and third bands [232–234], supporting this result. As shown in previous sections, Dirac 1 can be tuned from $\Omega_{Dirac} = 0$ to $\Omega_{Dirac} = 17.55$ due to the resonant characteristic of the connected circuitry. In addition, topological interface states derived from Dirac 1 are attainable for a narrower frequency range that covers $\Omega_{Dirac} = 3.2$ to $\Omega_{Dirac} = 11$. Unlike Dirac 1, the formation of Dirac 2 is the result of a Bragg scattering mechanism, and it is not frequency-tunable with resonant circuit parameters. However, it exists at a high frequency ($\Omega_{Dirac} = 17.55$) that is outside of the operating range for

topological interface states derived from Dirac 1, and thus could be exploited to further broaden the frequency range of interface states in the proposed metamaterial. Furthermore, this additional Dirac point could be employed to achieve other capabilities derived from the rich physics associated with Dirac cones, such as boundary states.

2.5.2 High-frequency interface state from Dirac 2

The same process described in previous sections for Dirac 1 is followed to construct interface states from Dirac 2. Fig 2.10a includes the schematic for a lattice (defined as Configuration 2: Perturbed Lattice) with the inductance perturbation parameter β specified to be between 0 and 1 ($|\beta| = 0.7$), which breaks SIS. Fig 2.10b contains the dispersion diagram for Configuration 2, where it is shown that bandgaps exist in place of Dirac 1 and Dirac 2. For Dirac 2, the bandgap extends from a fixed upper boundary of $\Omega = 17.55$ to lower frequencies ($\Omega_{bandgap}$ spans $\Omega = 15.13$ to $\Omega =$

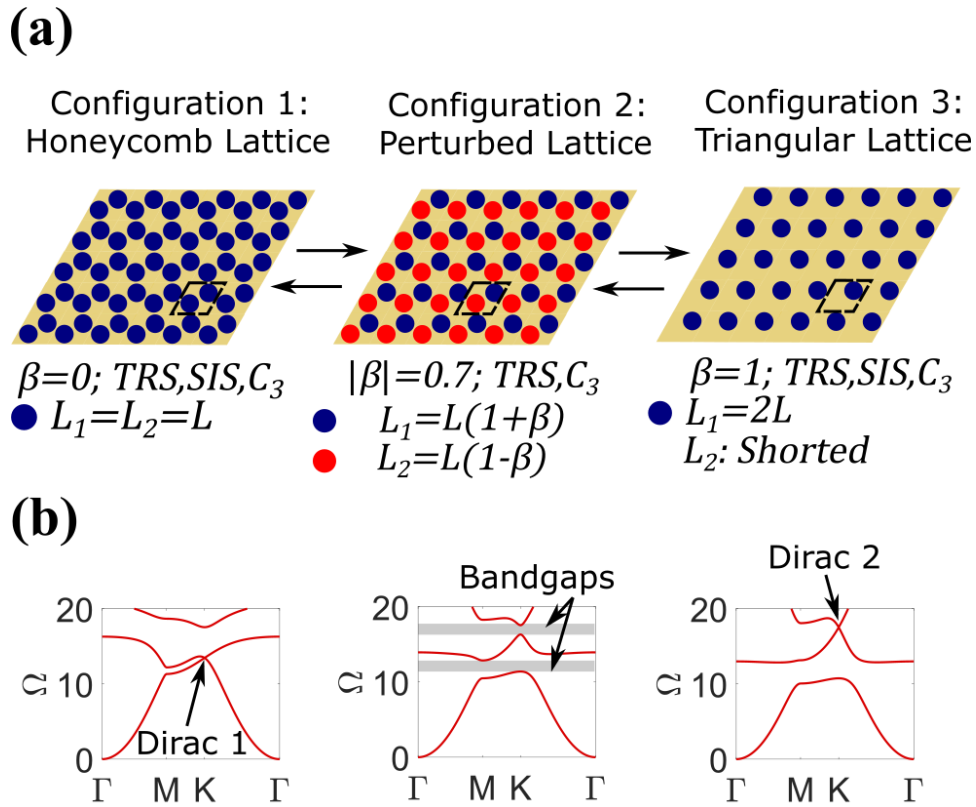


Fig 2.10. (a) Schematics for three lattice configurations attainable through circuit tailoring in the proposed metamaterial. Circuits are connected to electrodes that are represented by blue and red circles. For Configuration 3, electrodes pertaining to shorted circuits are omitted for clarity. Unit cell (enclosed in dashed black lines) circuit parameter details and lattice symmetries are listed below each schematic. (b) Dispersion diagrams corresponding to lattice Configurations 1-3 calculated using the PWE method with $\Omega_{t-eff} = 28$ and $\vartheta_{eff} = 2$. Dirac 1, topological bandgaps, and Dirac 2 are all highlighted for Configuration 1, Configuration 2, and Configuration 3, respectively.

17.55 for $|\beta| = 0.7$). To investigate whether an interface state can be obtained within this bandgap, Type A ($\beta = 0.7$) and Type B ($\beta = -0.7$) lattices are connected at a Type I interface, and a dispersion analysis is conducted for a finite strip of 18 unit cells (see schematic in Fig 2.11a). For this analysis, periodic boundary conditions are applied in the $k_{//}$ direction, and the ends are specified as free. The dispersion diagram for the finite strip is shown in Fig 2.11a, where it is apparent that a localized interface state exists within the bandgap (the interface state is the red band present in the gray shaded bandgap). A symmetric and highly localized ($\Lambda_m = 0.96$) interface mode shape evaluated at $\Omega = 16.3$ is shown in Fig 2.11b. In addition to the interface state, multiple localized edge states exist at the left and right boundaries of the finite strip, as indicated by the white circles in the band diagram (for $\Lambda \approx 0$, dispersion curves are white, Fig 2.11a). Mode shapes for two degenerate “boundary states” with flexural displacement localized at the left and right boundaries are shown for $\Omega = 17.2$ in Fig 2.11b. Similar results for a Type II interface and the corresponding antisymmetric interface state are reported within Appendix A.7.

To demonstrate guided wave propagation, plates are constructed with straight and Z-shaped Type I interfaces and excited harmonically ($\Omega_e = 16.8$) with a point source at the locations indicated by “Src” in Fig 2.11c (see schematics in top row of Fig 2.11c). The resulting steady-state displacement fields show that flexural displacement can be localized along the interfaces for these high-frequency interface states (see steady-state displacement fields in bottom row of Fig 2.11c). However, coupling between the interface states and boundary states does occur. Therefore, to selectively activate an interface state, care must be taken to specify an excitation (e.g., location at the center of the plate) that will not localize displacement at the boundaries.

2.5.3 Boundary states from Dirac 2

Results from the finite strip dispersion analysis for a Type I interface (Fig 2.11) suggest that boundary states are readily achievable from Dirac 2. To further investigate the formation of boundary states from Dirac 2, a dispersion analysis is conducted for a finite strip with 18 Type B unit cells (no interface is present, see schematic in Fig 2.12a). The left boundary is specified as fixed, the right boundary is specified as free, and periodic boundary conditions are applied in the $k_{//}$ direction. The left boundary is fixed because a fixed condition enforces dynamic behavior at the boundary that closely approximates the interface behavior for the antisymmetric interface state. As shown in Appendix A.7, the antisymmetric interface state is obtainable by creating a Type II

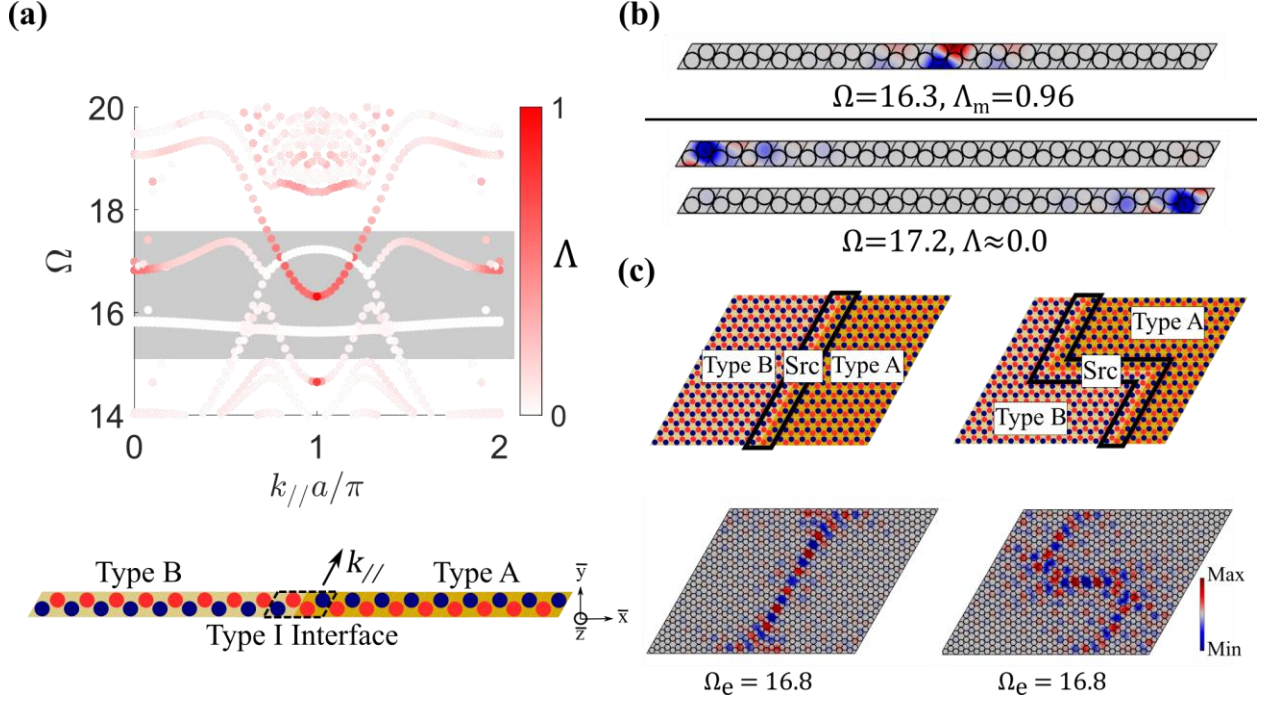


Fig 2.11. (a) Band structure for a finite strip ($|\beta| = 0.70$, $\Omega_{t-eff} = 28.0$, $\vartheta_{eff} = 2$) with a Type I interface. Dark red shading indicates localized interface states ($\Lambda \approx 1$) and white shading indicates boundary states ($\Lambda \approx 0$). The rectangular gray shaded region represents a frequency range where no bulk modes exist. (b) A symmetric mode shape that is calculated from the interface state at $\Omega = 16.3$ with a localized displacement ($\Lambda_m = 0.96$) is shown. Two boundary mode shapes that are calculated from the degenerate boundary states at $\Omega = 16.8$ ($\Lambda = 0$) are also shown. (c) (top row) Schematics for thin plate metastructures with straight and Z-shaped Type I lattice interfaces (enclosed in black lines). A harmonic ($\Omega_e = 16.8$) out-of-plane point excitation is applied where indicated by ‘Src’. (bottom row) Steady-state displacement fields illustrating guided wave propagation for the high-frequency interface states.

interface. Since the Type B unit cell at the left boundary comprises the right half of a Type II interface, the fixed condition effectively approximates the left half, and a boundary state that resembles half of the antisymmetric interface state is expected to occur [173]. Similarly, a boundary state closely approximating half of the symmetric interface state is expected to appear at the right boundary, which is designated as free. For each band in the calculated dispersion diagram, a boundary localization parameter ψ is defined to measure the amount of flexural displacement that is localized at the left and right boundaries as:

$$\psi = \frac{\iiint_{V_{boundaries}} |\bar{w}|^2 dV}{\iiint_{V_S} |\bar{w}|^2 dV} \quad (2.21)$$

where $V_{boundaries}$ is the total volume of the two unit cells at the boundaries (enclosed in the dashed black boxes in Fig 2.12a) and V_S is the volume of the entire finite strip. This boundary localization parameter is evaluated for each band and is represented in the dispersion diagram by color intensity. Boundary states are indicated in the dispersion diagram (Fig 2.12a) as dark red bands (ψ

≈ 1). One boundary state emerges from a lower frequency set of bulk modes and crosses into the bandgap (gray shaded region) towards a higher frequency set of bulk modes. The mode shape for this band with the maximum level of displacement localization at the boundary is shown in Fig 2.12a ($\psi_m = 0.92$ for $\Omega = 16.5$), indicating that this band corresponds to a left boundary state that approximates half of the antisymmetric interface state derived from Dirac 2. Another boundary state emerges from the higher frequency set of bulk modes and crosses towards the lower frequency set of bulk modes. This boundary state is localized to the right boundary, as illustrated by the mode shape calculated for $\Omega = 15.3$ ($\psi_m = 0.98$), and approximates half of the symmetric interface state.

A plate is constructed with boundary conditions (free and fixed) specified such that the outlined boundary states are supported at all four boundaries. The plate is excited harmonically ($\Omega_e = 16.5$) with a point source located as indicated by “Src” in Fig 2.12b. Results show that both boundary states are activated and compatible with each other, resulting in flexural wave propagation around

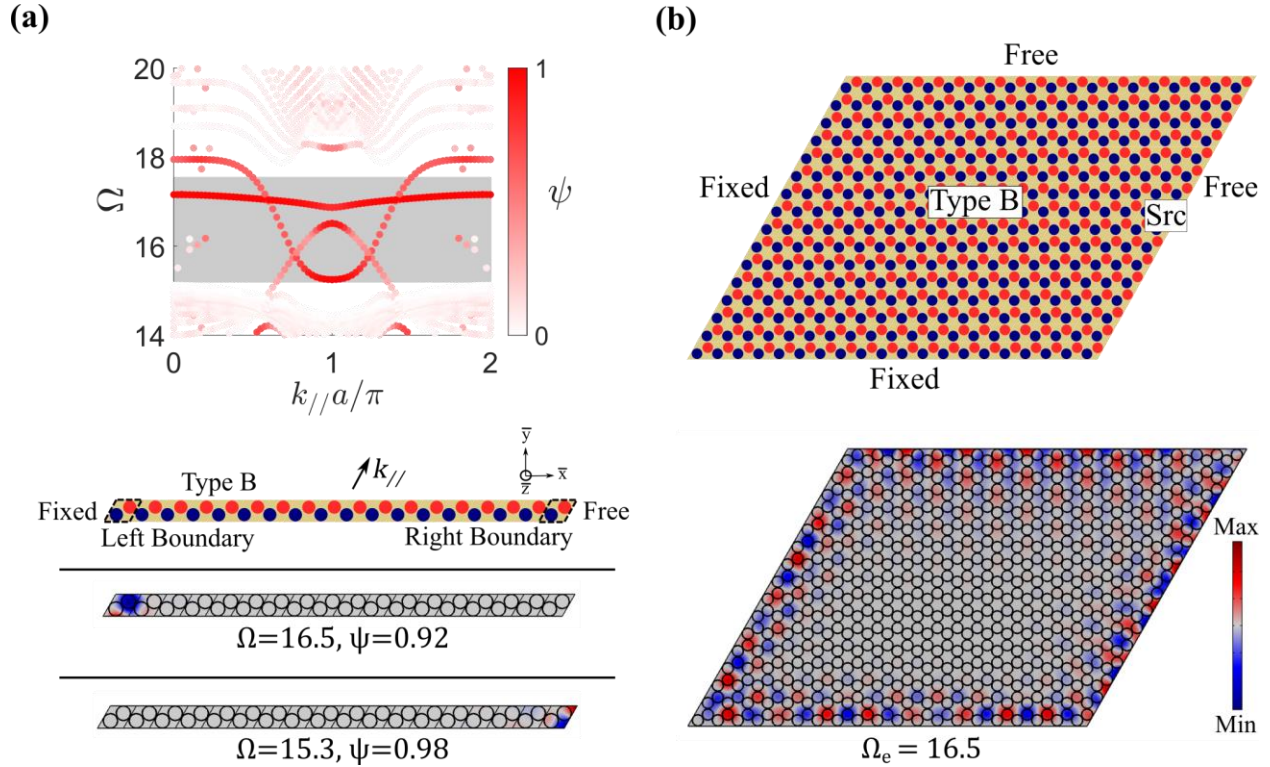


Fig 2.12. (a) Band structure for a finite strip ($|\beta| = 0.70$, $\Omega_{t-eff} = 28.0$, $\vartheta_{eff} = 2$) comprised of Type B unit cells (no interface, see schematic). Dark red shading indicates localized boundary states ($\psi \approx 1$). The rectangular gray shaded region indicates a frequency range where no bulk modes exist. Left and right boundary mode shapes are shown. (b) (top) Schematic for thin plate metastructure with fixed and free boundaries selected to attain boundary states. A harmonic ($\Omega_e = 16.5$) out-of-plane point excitation is applied where indicated by ‘Src’. (bottom) Steady-state displacement field illustrating flexural displacement confinement along plate boundaries.

multiple sharp and shallow corners that is localized to all four boundaries of the plate. This capability to achieve adaptive wave propagation along structural boundaries could be beneficial in applications requiring confinement of energy along the edges of structures, such as vibration mitigation systems.

2.6 Conclusions and discussion

The research presented in this chapter proposes and develops a TM that harnesses resonant piezoelectric circuitry to enable comprehensively tunable elastic wave control. Overall, this investigation advances the state of the art by enabling and exploring the adaptation of topological wave path, frequency, and edge mode shape in a single mechanical platform for the first time. The proposed metamaterial operates over a broad frequency bandwidth (including multiple discrete bands) and can be integrated in a compact fashion for applications that require control of large-wavelength (i.e., low-frequency) waves due to its subwavelength characteristic, which constitutes a breakthrough in the field of tunable TMs.

In this chapter, the tunability of wave path, frequency range, and edge states is explored through a systematic analysis of the dispersion properties and dynamic response characteristics of the proposed metamaterial. A subwavelength and frequency-tunable Dirac point (Dirac 1) is uncovered, and it is revealed that symmetric and antisymmetric topological interface states can be obtained from it. FE simulations illuminate how these interface states can be activated to achieve guided elastic wave transmission that is robust to disorder and defects and can be manipulated on-demand into a myriad of desired directions. A deeper understanding of the adaptive characteristics of the metamaterial is formed through parametric studies. A finite tunable frequency range and its underlying physical basis are discovered for Dirac 1. An achievable operating region is defined for topological interface states derived from Dirac 1, where it is learned that interface states that meet specified performance metrics are achievable over a wide frequency bandwidth that comprises a subset of the Dirac 1 frequencies. These findings offer new insights into frequency tunability that may be leveraged in future studies concerning Dirac dispersions and the QVHE in locally resonant EMs. Further exploration of the achievable operating region illuminates how circuit parameters can be utilized to tune the displacement field of a waveguide by tailoring the localization and shape of the interface state. The operating region is used as a framework to study the role of electromechanical coupling in topological wave propagation for the first time. Results

indicate that increased electromechanical coupling enhances the frequency range and achievable interface mode localization of the interface states. Lattice reconfiguration is also investigated as a method to tailor the topological properties of the proposed metamaterial. Analysis of a triangular lattice obtained through shorting circuits reveals that a second Dirac point (Dirac 2) can be achieved in a high-frequency range that extends beyond the operating region for Dirac 1 interface states. Boundary states and additional interface states are shown to be obtainable from Dirac 2, and numerical simulations illustrate how these states can be exploited to achieve exceptional guided elastic wave phenomena.

The outcomes from this chapter provide fundamental insights into the influence of locally resonant elements, electromechanical coupling, and lattice reconfiguration in adaptive TMs exhibiting the QVHE, presenting a basis for further exploration. The proposed TM may be employed to achieve subwavelength elastic wave control that is robust to practical considerations (e.g., sharp waveguide corners or lattice imperfections) and adaptive in real-time to shifting operating requirements and external conditions. These beneficial features could be harnessed to improve performance and expand functionalities in a range of engineering applications requiring adaptive and robust elastic wave control, such as vibration mitigation systems, wave filters/multiplexers, and energy harvesters.

Note: The reused content (text, figures, and tables) in Chapter 2 and Appendix A is reproduced from [235] under the [CC BY 4.0](https://creativecommons.org/licenses/by/4.0/) license.

Chapter 3. 3D Metastable Metamaterial

A 2D TM with exceptional tunability is presented in Chapter 2. Building from the knowledge gained from Chapter 2, the next step is to incorporate tunability into 3D TMs, which open the door to new wave control possibilities and are more challenging to design and realize when compared to 2D TMs. In Chapter 3, we address this opportunity and advance the state of the art by proposing a programmable first-order 3D TM that can be tuned adaptively via carefully designed metastability. A metastable switching methodology is developed that enables the synthesis of multiple unique topological states in a 3D mechanical metastructure. By taking advantage of the adaptivity of the proposed metamaterial, the path of 2D topological surface states is on-demand controlled for the first time, a bilayer-locked topological state is discovered, and 3D elastic wave networks with advanced filtering and splitting capabilities are realized. The findings presented in this chapter offer new insight into how topology can be used to control the flow of energy in 3D elastic structures. Furthermore, the advanced functionalities of the proposed TM could be harnessed to create intelligent and robust devices for various purposes, such as mechanologic, vibration mitigation, energy harvesting, and remote sensing.

3.1 Introduction

Most studies concerning topological phases in mechanical systems have focused on confining elastic waves through 0D point states in 1D structures [83,130,132–137] and 1D edge states in 2D structures [83,116,238–240,147,148,154,162,168,172,236,237]. Topological states in 3D structures are more difficult to obtain due to fabrication complexities, computational resource requirements, and unwanted mode conversion or coupling that result from a dense band structure. Recently, researchers have overcome these challenges to achieve 2D topological surface states in 3D mechanical structures through elastic analogues of Weyl semimetals [26,75,184–187] or the QVHE [131]. Extraordinary wave control capabilities have been achieved in 3D TMs, including robust elastic wave propagation along planar waveguides in multiple spatial directions and the introduction of the layer degree-of-freedom (DOF) to obtain layer-polarized (i.e., layer-selective) energy transmission.

While the 3D TMs studied thus far show great promise, these structures are not changeable after fabrication, limiting their potential capabilities and making them susceptible to reduced performance under variable environmental and operating conditions. The development of an adaptive 3D TM would address this research gap and enable the investigation of unexplored topological transport phenomena. The research presented in this chapter advances the state of the art by proposing a reconfigurable 3D TM that can tailor the spatial path of elastic wave propagation and select from various topological states through metastability (metastability is the coexistence of several internal stable states given a constant global topology [215]). A metastable geometry and switching methodology are crafted to achieve on-demand tunability of 2D topological surface states in a 3D mechanical structure for the first time. The reconfigurability of the proposed platform is harnessed to efficiently investigate beyond the previously established topological states and uncover a “bilayer-locked” state that is confined to two layers of a multi-layered structure. Moreover, tunable 3D topological wave networks with advanced (compared to their 2D predecessors [115,155,241]) elastic wave splitting and filtering capabilities are created by connecting multiple topological states and exploiting the additional layer DOF.

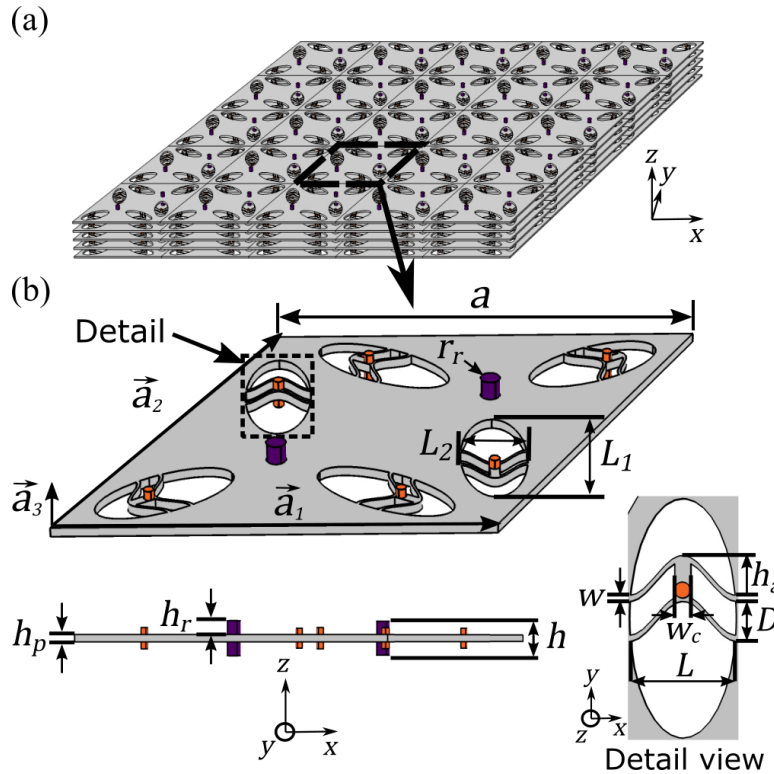


Fig 3.1. (a) Schematic of the proposed 3D EM, a dashed black box encloses the unit cell. (b) Schematic of the proposed 3D EM unit cell comprised of an aluminum thin plate (gray), two silicone rubber interconnecting rods (purple), and 12 point masses (orange). A blacked dashed box encloses a single bistable element, with a detail view provided.

3.2 Concept and theoretical model

3.2.1 Proposed EM overview

The proposed EM is a multi-layered 3D structure that consists of aluminum thin plates with thickness h_p connected by silicone rubber cylindrical rods with height h_r and radius r_r (Fig 3.1). A schematic of the EM unit cell is given in Fig 3.1b, where $\vec{a}_1 = a\hat{i}$, $\vec{a}_2 = a(\cos \pi/3 \hat{i} + \sin \pi/3 \hat{j})$, and $\vec{a}_3 = h\hat{k}$ are the lattice basis vectors, a is the in-plane (x - y plane) lattice constant, and h is the out-of-plane (z direction) lattice constant. Taking inspiration from previous work with a 2D EM [236], elliptical holes are cut into the thin plate and bistable elements are embedded within them to provide the structure with metastability (see detail view, Fig 3.1b). The elliptical holes are oriented to satisfy the D_{6h} symmetry required for the QVHE. The geometric dimensions of the internal elements are chosen such that two symmetric stable states are obtained in the force-displacement relation (see Section 3.2.3 for details on the unit cell design). Point masses (orange in Fig 3.1b) are placed on the top and bottom surfaces of each bistable element to create a locally resonant in-plane bandgap. This in-plane bandgap is paired with careful design of the interconnecting rod stiffness to adjust the band structure such that a full (i.e., covering all elastic wave polarizations) bandgap can be achieved in the target frequency range for topological states (see topological bandgap design methodology in Section 3.3). The geometry is discretized and numerical simulations are conducted using the commercial FE solver COMSOL Multiphysics (see Section 3.2.2 for information on the FE model).

3.2.2 Theoretical model

The COMSOL Multiphysics Solid Mechanics Module is used to discretize the continuous 3D solid and carry out numerical FE simulations. Small amplitude displacement, negligible damping, and perfect adhesion at all component interfaces are all assumed. Table 3.1 contains all geometric parameter values used in the presented research and Table 3.2 contains all relevant material properties.

Numerical FE simulations are used to solve the system governing equations for the band structure (i.e., perform an eigenfrequency study) and dynamic response (i.e., perform a frequency domain study). The governing equations for wave motion in a linear elastic medium are [25]:

$$\rho(\mathbf{r})\ddot{u}_i = \sum_{j=1}^3 \left\{ \frac{\partial}{\partial x_i} \left(\lambda(\mathbf{r}) \frac{\partial u_j}{\partial x_j} \right) + \frac{\partial}{\partial x_j} \left[\mu(\mathbf{r}) \left(\frac{\partial u_i}{\partial x_j} + \frac{\partial u_j}{\partial x_i} \right) \right] \right\} \text{ for } i = 1, 2, 3 \quad (3.1)$$

where $i, j = 1, 2, 3$ correspond to the coordinates x, y, z , $\mathbf{r} = (x, y, z)$ is a position vector, $\rho(\mathbf{r})$ is material density, $\mathbf{u}(\mathbf{r}) = [u, v, w]^T$ is the displacement vector, and $\lambda(\mathbf{r})$ and $\mu(\mathbf{r})$ are elastic constants.

For the band structure, a harmonic plane wave solution is used, and a single unit cell is analyzed with Floquet-Bloch periodic boundary conditions. A solution of the form $\mathbf{u}(\mathbf{r}; t) = \tilde{\mathbf{u}}(\mathbf{r})e^{i(\mathbf{k} \cdot \mathbf{r})}e^{i\omega t}$ is assumed, where t is time, ω is the temporal frequency, $\mathbf{k} = \{k_x, k_y, k_z\}$ is the Bloch wave vector, and $\tilde{\mathbf{u}}(\mathbf{r})$ is the Bloch displacement vector (which has the same periodicity as the structure). For band structure calculations, the Bloch wave vector $k = (k_x, k_y, k_z)$ is swept through reciprocal space (see a schematic of reciprocal space in Fig 3.3a), and the corresponding frequencies are calculated.

3.2.3 3D EM design methodology

The internal bistable elements grant the system with adaptivity, as lattice configurations can be altered by “switching” between metastable states (note: metastability is defined as the coexistence of several internal stable states given a constant global topology [215]). These

Table 3.1. Geometric dimensions

Symbol	Parameter	Value
a	In-plane lattice constant	86.6 mm
h	Out-of-plane lattice constant	10 mm
h_p	Thickness of thin plate	2 mm
h_r	Height of rod segment	4 mm
r_r	Radius of rod segment	2 mm
L_1	Elliptical hole major axis length	30 mm
L_2	Elliptical hole minor axis length	13.4 mm
w	Width of curved beams	0.75 mm
w_c	Width of interconnecting clamp	2 mm
h_a	Curved beam initial apex height	5 mm
D	Distance between curved beams	5 mm
L	Curved beam span	13.4 mm

Table 3.2. Material properties

Symbol	Parameter	Value
E_p	Elastic modulus: aluminum plate	70 GPa
ρ_p	Mass density: aluminum plate	2700 kg/m ³
ν_p	Poisson's ratio: aluminum plate	0.33
E_r	Elastic modulus: silicone rubber rod	50 MPa
ρ_r	Mass density: silicone rubber rod	1000 kg/m ³
ν_r	Poisson's ratio: silicone rubber rod	0.48
m_{pm}	Mass of applied point masses	0.05 kg

internal bistable elements are made up of two curved beams of span L and width w defined by the local shape function $y = h/2 (1 - \cos 2\pi x/L)$, where h_a is the initial apex height (see Fig 3.1 for full detail). The two beams are separated by a distance D and connected in parallel by a clamp of width w_c to ensure that the influence of higher-order beam modes is suppressed [242]. Geometric dimensions are selected such that two roughly symmetric stable states are created. The beam ends are assumed to be fixed, and there is no induced pre-stress in the “as-fabricated” (stable state 1) stable configuration because the curved beams are directly fabricated into this stable state. Some internal stress will exist in the other stable configuration, stable state 2.

The theoretical model proposed in [242,243] is used for all calculations. Key elements of the theoretical model are provided here; please refer to [242,243] for a full derivation. A normalized displacement is defined as $\bar{d} = \frac{d}{h_a}$ and normalized force as $\bar{F} = \frac{FL^3}{2E_p I h_a}$, where I is the initial moment of the curved beam, d is the lateral displacement (in the y direction in Fig 3.1), and F is an applied force (dimensional). Calculations for the force-displacement curve include two components of the normalized force, \bar{F}_1 and \bar{F}_3 :

$$\begin{aligned}\bar{F}_1 &= \frac{3\pi^4 Q^2}{2} \bar{d} \left(\bar{d} - \frac{3}{2} + \sqrt{\frac{1}{4} - \frac{4}{3Q^2}} \right) \left(\bar{d} - \frac{3}{2} - \sqrt{\frac{1}{4} - \frac{4}{3Q^2}} \right) \\ \bar{F}_3 &= 8\pi^4 - 6\pi^4 \bar{d}\end{aligned}\quad (3.2)$$

where $Q = \frac{h_a}{w}$ is a geometry constant that must be greater than 2.31 to ensure bistability (in this case, $Q = 6.7$). The final force-displacement curve (Fig 3.2) is a piece-wise combination of \bar{F}_1 and \bar{F}_3 (Fig 3.2 and Eq. 3.3):

$$\bar{F} = \begin{cases} \bar{F}_1 & \text{for } \bar{d}_1 < \bar{d} < \bar{d}_2 \\ \bar{F}_3 & \text{for } \bar{d} < \bar{d}_1 \text{ and } \bar{d} > \bar{d}_2 \end{cases}\quad (3.3)$$

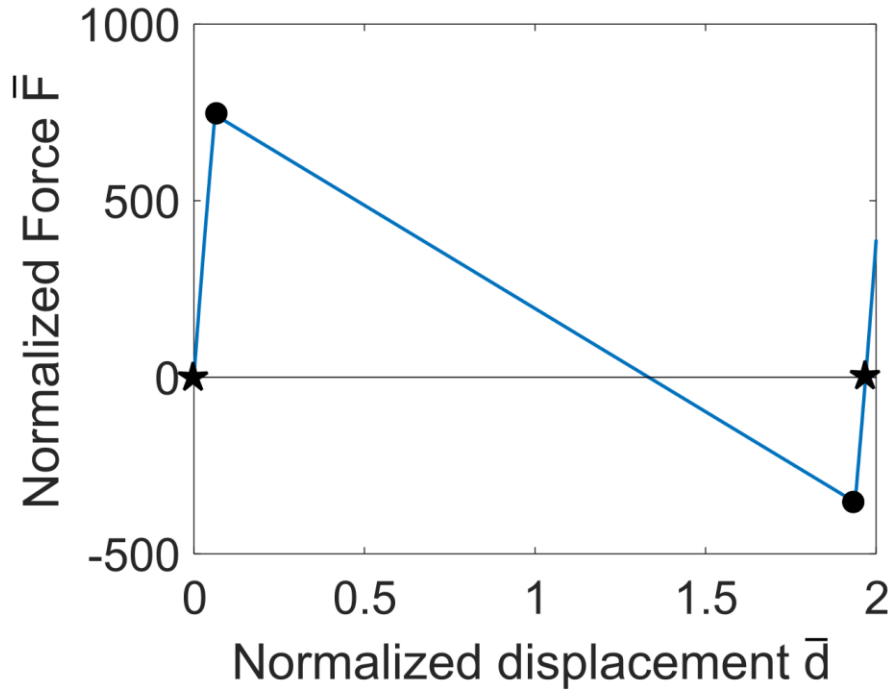


Fig 3.2. Normalized force-displacement (\bar{F} - \bar{d}) relation for the bistable internal elements. Stars mark stable states at $\bar{d} = 0$ (stable state 1) and $\bar{d} = 1.97$ (stable state 2). Circles mark intersections of \bar{F}_1 and \bar{F}_3 at $\bar{d}_1 = 0.06$ and $\bar{d}_2 = 1.94$.

where $\bar{d}_1 = 0.06$ and $\bar{d}_2 = 1.94$ are the intersection points of the \bar{F}_1 and \bar{F}_3 curves. The two stable states (i.e., this system is bistable) occur at $\bar{d} = 0$ (stable state 1) and $\bar{d} = 1.97$ (stable state 2, both stable states are marked with stars in Fig 3.2). For all COMSOL FE simulations, the displacement of the two stable states is treated as symmetric about $\bar{d} = 1$ when the bistable elements are “switched” back and forth to alter lattice configurations. For this analysis, the internal stress of the structure in stable state 2 is not considered. Physical implementation is outside the scope of this study, and artificial switching is used to change between bistable states for all theoretical modeling. A switch between stable states could be physically realized in practice using stimuli-responsive actuators. Electromagnetic [244], electrothermal [242], or electrostatic [242] actuators could be used to tune the internal bistable elements. The geometry-induced bistability of the internal beam elements is advantageous for manufacturing (e.g., 3D printing), because hinges, latches, or residual pre-stress (these are all commonly used methods for achieving bistability that are difficult to implement in 3D structures) are not required as part of the fabrication process.

Point masses:

Twelve point masses with mass $m_{pm} = 0.05$ kg are added to the unit cell at the top and bottom surfaces of the six bistable elements (two point masses per bistable element, see orange points in Fig 3.1). The influence of the point masses is measured by calculating a mass ratio metric:

$$m_{ratio} = \frac{m_{pm}}{m_{plate} + 4m_{rod}} \quad (3.4)$$

where m_{plate} is the mass of the aluminum plate in one unit cell and m_{rod} is the mass of one interconnecting rod segment. For this study, a magnitude of m_{ratio} equal to 2 is selected to help create a full (i.e., covering all mode polarizations) topological bandgap in the targeted frequency regime for topological states (see more discussion in Section 3.3 Fig 3.3 and Fig 3.4). In addition, the mass ratio must be large enough to create a sufficiently large mass redistribution when a “switch” of the bistable elements occurs, such that a Dirac nodal line degeneracy can be lifted (see further discussion in Section 3.3).

Interconnecting rods:

The interconnecting rod geometry and material are selected to ensure that a full topological bandgap can be achieved from a Dirac nodal line degeneracy. A parameter study indicated that a high interconnecting rod stiffness would be disadvantageous, and thus thin cylindrical silicone rubber (see material properties in Table 3.2) rods were chosen. See further discussion in Section 3.3 and Fig 3.5.

3.3 Unit cell analysis for 2D surface states using the elastic analog of the QVHE

The adaptivity of topological states is achieved by changing between the stable states of the bistable internal elements to adjust lattice symmetries (i.e., switching between metastable states, previously used to tune elastic wave propagation in 1D and 2D systems [80,215,236,245]). Two lattices (“Type A” and “Type B”) with D_{3h} symmetry are created by switching the bistable elements as shown in Fig 3.3b. The band structures for these lattices contain an identical full bandgap (Fig 3.3d). The topological nontriviality of this bandgap (i.e., topological bandgap) is uncovered through calculation of a topological invariant, the valley Chern number C_v (see Section 3.3.2). Equal and opposite calculated values of C_v indicate that the Type A and Type B lattices are topologically distinct. By the bulk-boundary correspondence [86,91,228] for a 3D system, a 2D

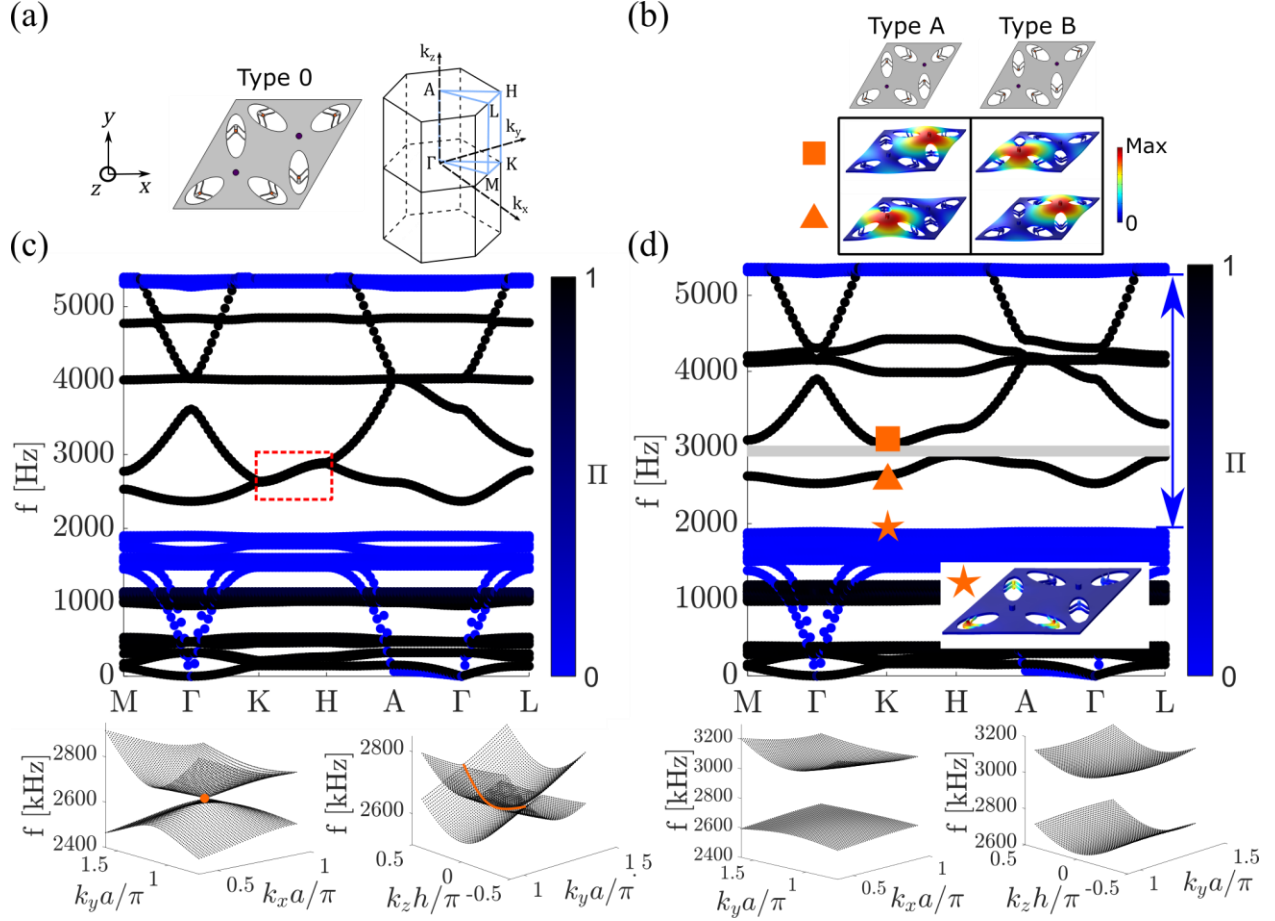


Fig 3.3. (a) Direct lattice for the Type 0 switching configuration of the proposed 3D EM. The reciprocal unit cell is shown to the right, with the IBZ outlined in light blue. (b) Type A and Type B switching configurations, and their corresponding mode shapes at the K point for the bands that border the bandgap (where marked by \blacksquare and \blacktriangle). (c) Band structure for the 3D EM in the Type 0 configuration. The two-fold Dirac nodal line is enclosed in a dotted red box. Colormap indicates the mode polarization using the metric Π . Blue modes are primarily in-plane modes; black modes are primarily out-of-plane modes. $k_x - k_y$ and $k_y - k_z$ projections are shown below, with the Dirac degeneracy marked by an orange dot and line, respectively. (d) Band structure for the 3D EM in the Type A or B configuration (identical for both). The full topological bandgap is marked by gray shading, while the blue arrows mark the partial bandgap for in-plane modes. The inset contains a mode shape evaluated at the K point at the lower boundary of the partial bandgap (see \star).

topologically protected surface state is predicted to exist at the interface between the Type A and Type B lattices.

3.3.1 Methodology for a full topological bandgap

To investigate the wave propagation characteristics of the proposed 3D EM and achieve the elastic analog of the QVHE, a unit cell analysis is undertaken, where the band structure of the unit cell in different metastable switching configurations is evaluated. Under switching configuration Type 0, where all six of the internal bistable elements are switched to the “out” position (i.e., they

are switched to the stable state furthest from the adjacent interconnecting rod) (Fig 3.3a), the EM lattice contains D_{6h} symmetry, and a two-fold Dirac nodal line degeneracy is obtained along the K - H line of high symmetry in the band structure (the IBZ used for band structure calculations is shown in blue in Fig 3.3a, and the Dirac Degeneracy is enclosed in the dotted red box in Fig 3.3c). This Dirac degeneracy is protected by the D_{6h} lattice symmetry and time-reversal symmetry [91]. A dimensionless polarization metric Π is defined and measured for each individual mode:

$$\Pi = \frac{\iiint_{V_U} |\bar{w}|^2 dV}{\iiint_{V_U} |\bar{u}|^2 + |\bar{v}|^2 + |\bar{w}|^2 dV} \quad (3.5)$$

where V_U is the volume of the unit cell, and u , v , and w are the displacement components in the x , y , and z directions, respectively. Thus, a $\Pi \sim 0$ (blue points in Fig 3.3c) indicates a predominantly in-plane modal displacement and a $\Pi \sim 1$ (black points in Fig 3.3c) indicates an out-of-plane mode polarization. The Dirac degeneracy is comprised of out-of-plane polarized modes. To better visualize this Dirac degeneracy, the band structure is projected over the $k_x - k_y$ and $k_y - k_z$ planes near the K point in reciprocal space. The $k_x - k_y$ projection reveals a Dirac cone (Fig 3.3c bottom left, Dirac point is orange dot), and the $k_y - k_z$ projection shows the Dirac degeneracy stretched into a two-fold nodal line (Fig 3.3c bottom right, orange line). To split the Dirac degeneracy and obtain a topological bandgap, three of the bistable elements are switched to the “in” position to break in-plane SIS and reduce the lattice symmetry from D_{6h} to D_{3h} . The band structure is identical regardless of whether the three bistable elements on the right side (“Type A”) or the left side (“Type B”) are switched inward (see Fig 3.3b for unit cell schematics). This band structure is shown in Fig 3.3d, where the gray shading indicates a full topological bandgap (from 2901 Hz to 3041 Hz) that is opened from the Dirac degeneracy. The mechanism that enables the opening of this topological bandgap is the redistribution of mass within the unit cell that occurs during metastable switching. As previously discussed in [236] for a 2D metamaterial, the mass ratio (m_{ratio}) must be carefully selected to ensure that there is a large enough mass redistribution to open a topological bandgap. In addition, the m_{ratio} is critical to the topological bandgap being *full* (covering all mode polarizations) in nature, a difficult characteristic to achieve in 3D EMs due to their inherently dense band structure. The $m_{ratio} = 2$ shown here leads to a partial bandgap of in-plane modes from 1895 Hz to 5297 Hz (as indicated by the blue arrows in Fig 3.3d). This in-plane partial bandgap enables the formation of the full topological bandgap from 2901 Hz to 3041

Hz because it ensures that no in-plane modes (blue modes in Fig 3.3d) cross into the frequency range near the Dirac degeneracy. Further analysis reveals that an in-plane mode with displacement localized to three of the internal bistable elements is present at the lower boundary of the in-plane partial bandgap (see inset in Fig 3.3d for the mode shape corresponding to ★), suggesting that this bandgap emerges due to a local resonance mechanism. Since this is a locally resonant bandgap, the magnitude of m_{ratio} should govern the size of this bandgap. Fig 3.4 contains band structures for different m_{ratio} values ($m_{ratio} = 2, 1.5, 1,$ and 0.75 in Fig 3.4a, Fig 3.4b, Fig 3.4c, and Fig 3.4d, respectively) confirming that the in-plane bandgap shrinks as m_{ratio} is reduced. These results demonstrate how m_{ratio} must be selected to be large enough, such that unwanted mode coupling or conversion (which may distort localized topological states) with in-plane modes does not occur (see an example of unwanted mode coupling in Fig 3.4d, where blue in-plane modes interact with the Dirac degeneracy).

Investigating beyond the m_{ratio} parameter, a band structure analysis is undertaken to evaluate how the stiffness of the interconnecting rods may also play a critical role in the obtainment of a topological bandgap. Fig 3.5a contains the Dirac nodal line (Type 0 switching configuration, left column of Fig 3.5) and topological bandgap (Type A/B switching configuration, right column of Fig 3.5) for the 3D EM with the parameters and materials described in Table 3.1 and Table 3.2 (notably, the elastic modulus of the rod material, $E_r = 50$ MPa). In a parameter study, the axial stiffness of the rods ($k_{axial-r} = A_r E_r / h_r$) is increased by selecting two values of higher E_r ($E_r = 100$ and 1000 MPa, for Fig 3.5b and Fig 3.5c, respectively). The enhancement in axial stiffness (which aligns with z) leads to a dramatic steepening (i.e., a larger slope and group velocity) of the Dirac nodal line along the K-H direction (which aligns with k_z). This dramatically increased slope can be qualitatively observed by comparing the frequency difference between the two orange circles placed at the K and H points in the Type 0 band structures (left column) shown in Fig 3.5a, Fig 3.5b, and Fig 3.5c. This characteristic of the band structure for increased E_r inhibits the opening of a topological bandgap when the metastable elements are switched from the Type 0 to the Type A/B configurations, as can be seen in Fig 3.5b and Fig 3.5c (of the Type A/B band structures in the right column, only in Fig 3.5a can a topological bandgap be opened from the Dirac degeneracy, as indicated by the gray shading). Thus, care must be taken to select the dimensions and material of the interconnecting rods to achieve a sufficiently low stiffness value that enables the opening of a topological bandgap.

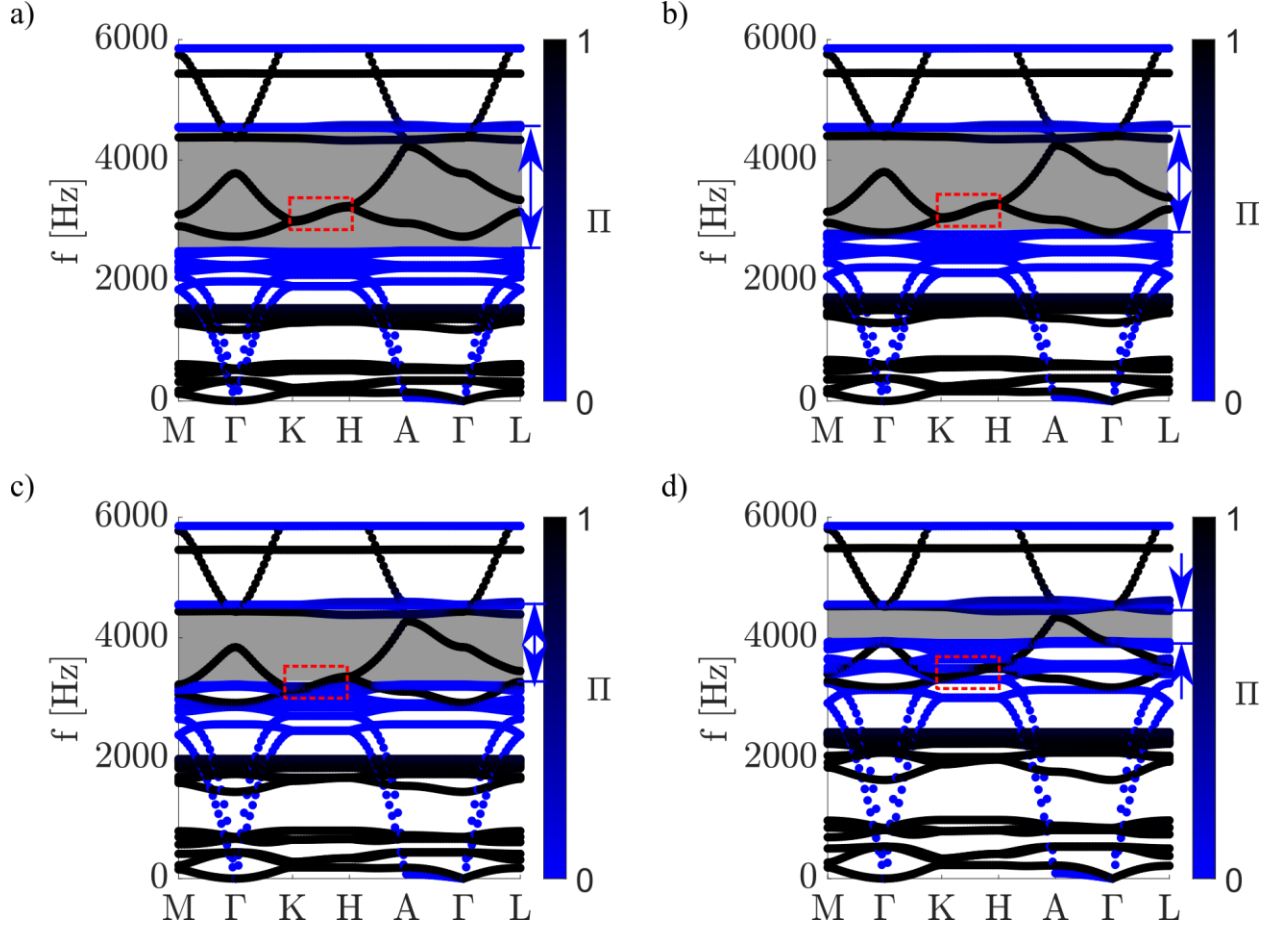


Fig 3.4. Band structure for the proposed 3D EM with various m_{ratio} values: (a) $m_{ratio} = 2$, (b) $m_{ratio} = 1.5$, (c) $m_{ratio} = 1$, and (d) $m_{ratio} = 0.75$ showing in-plane partial bandgaps of 2.5 kHz to 4.3 kHz, 2.8 kHz to 4.3 kHz, 3.2 kHz to 4.3 kHz, and 3.9 kHz to 4.4 kHz, respectively (in-plane bandgaps are indicated by blue arrows and grey shading). The two-fold Dirac nodal line is enclosed in a dotted red box. Colormap indicates the mode polarization using the metric Π . Blue modes are primarily in-plane modes; black modes are primarily out-of-plane polarized.

3.3.2 Band inversion and topological invariant calculations for the QVHE:

The topological nature of the full bandgap described in Fig 3.3d is investigated by examining the bands that border it in the context of the QVHE [86]. Switching configurations Type A and Type B (Fig 3.3b) have identical band structures containing a full topological bandgap (Fig 3.3d). The topological properties of these bands are quantified by calculation of the topological invariant for the QVHE, the valley Chern number C_{v-p} , defined as:

$$C_{v-p} = \frac{1}{2\pi} \iint_v B_p(k) d^2k \quad (3.6)$$

$$B_p(k) = \nabla_k \times A_p(k) \quad (3.7)$$

$$A_p(k) = \langle u_p(k) | i\nabla_k | u_p(k) \rangle \quad (3.8)$$

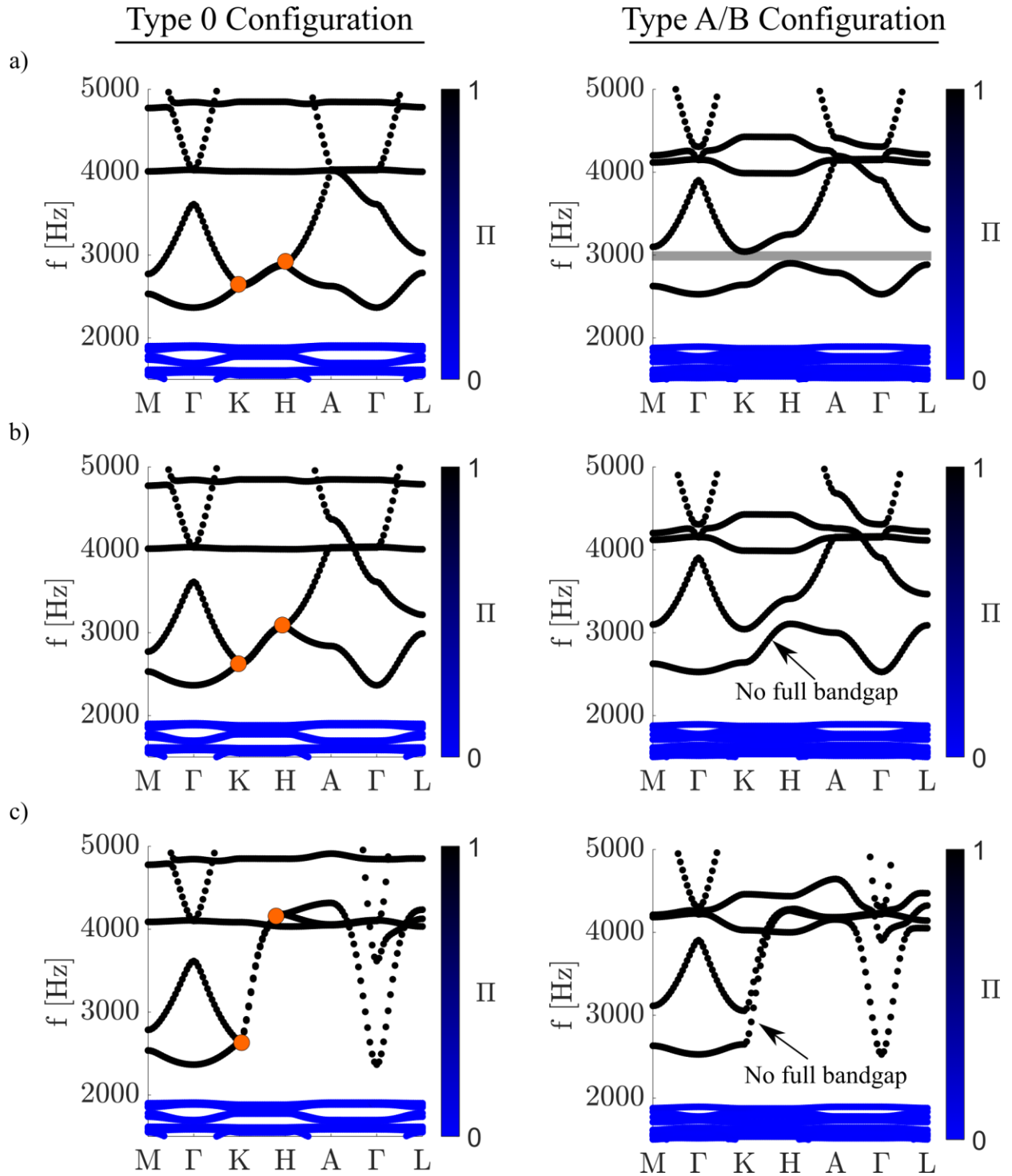


Fig 3.5. (a) Band structures for the Type 0 (left column) and Type A/B (right column) switching configurations for $E_r = 50$ MPa. The degenerate eigenmodes at the K and H points are indicated with orange circles (left). The full topological bandgap is indicated by the gray shading (right). The band structures for the Type 0 (left) and Type A/B (right) configurations are shown for (b) $E_r = 100$ MPa and (c) $E_r = 1000$ MPa. Note that in (b) and (c), the increased E_r prevents the opening of a full topological bandgap from the Dirac degeneracy.

where $A_p(k)$ is the Berry Connection, $B_p(k)$ is the Berry Curvature, $\nabla_k = \left(\frac{\partial}{\partial k_x}, \frac{\partial}{\partial k_y} \right)$ is a differential operator, $u_p(k)$ are the eigenvectors associated with the p th band (where $p = 1$ refers to the band defining the lower limit of the bandgap and $p = 2$ refers to the band defining the upper limit), and the subscript v denotes that the integral is taken at the K valley in reciprocal space [153,167,227]. To complete the calculations, the eigenvectors are normalized according to:

$$\langle u_p(k) | u_p(k) \rangle = \iiint_{V_U} u_p^*(k) u_p(k) dV \approx \sum_{N_{pts}} V_{pt} (u_{pt}^* u_{pt} + v_{pt}^* v_{pt} + w_{pt}^* w_{pt}) = 1 \quad (3.9)$$

where V_{pt} is equal to the approximate volume calculated using the COMSOL variable *meshvol*, N_{pts} is the number of extracted Gauss points, and u_{pt} , v_{pt} , and w_{pt} correspond to the x , y , and z deflection components of the eigenvector at each specific Gauss point. The Berry Connection is approximated as:

$$A_p(k) = i \iiint_{V_U} \left[\left(u^* \frac{\partial u}{\partial k_x} + v^* \frac{\partial v}{\partial k_x} + w^* \frac{\partial w}{\partial k_x} \right) \hat{i} + \left(u^* \frac{\partial u}{\partial k_y} + v^* \frac{\partial v}{\partial k_y} + w^* \frac{\partial w}{\partial k_y} \right) \hat{j} \right] dV \cong \sum_{N_{pts}} V_{pt} \left[\left(u_{pt}^* \frac{\partial u_{pt}}{\partial k_x} + v_{pt}^* \frac{\partial v_{pt}}{\partial k_x} + w_{pt}^* \frac{\partial w_{pt}}{\partial k_x} \right) \hat{i} + \left(u_{pt}^* \frac{\partial u_{pt}}{\partial k_y} + v_{pt}^* \frac{\partial v_{pt}}{\partial k_y} + w_{pt}^* \frac{\partial w_{pt}}{\partial k_y} \right) \hat{j} \right] = A_{k_x} \hat{i} + A_{k_y} \hat{j} \quad (3.10)$$

For the Type A lattice, $C_{v-1}^{Type A} = -0.06$ and $C_{v-2}^{Type A} = 0.06$; while for the Type B lattice, $C_{v-1}^{Type B} = 0.06$ and $C_{v-2}^{Type B} = -0.06$. These values are less than the idealized value of $C_v = 0.5$ (but still provide a form of topological protection [157,175]) due to the large magnitude of the symmetry breaking that is incurred when the lattice is switched from Type 0 to Type A/B. One method to increase these C_v values would be to reduce the magnitude of the displacement that occurs when the bistable elements are switched by decreasing the initial apex height of the curved beams h_a . For the C_{v-p} values reported here (where $|C_{v-p}| = 0.06$), the Berry curvature $B_p(k)$ used for calculations is shown in Fig 3.6, displaying localized $B_p(k)$ at the K valley for the considered bands and configurations. As illustrated by the C_{v-p} values, $B_p(k)$ is equal and opposite for Type A ($B_p^{Type A}$, Fig 3.6a and Fig 3.6b) and Type B ($B_p^{Type B}$, Fig 3.6c and Fig 3.6d) lattices. The nontrivial and opposite values of C_{v-p} indicate that the bands contain a topological characteristic (in terms of the QVHE) and that a band inversion exists between the Type A and Type B lattices. This band inversion is visualized by observing the equal and opposite nature of the eigenvectors (i.e., mode shapes) evaluated at the K point for bands $p = 1$ and $p = 2$ [see bottom of Fig 3.3b]. This band inversion, along with the associated C_{v-p} values, shows that the Type A and Type B

lattices are topologically distinct. By applying the bulk-boundary correspondence [86,91,228] to this 3D system, a topologically protected 2D surface state is predicted to exist at the interface between the topologically distinct Type A and Type B lattices.

3.4 On-demand reconfigurable 2D topological surface states

3.4.1 Supercell dispersion analysis

To investigate the presence of topological surface states, a supercell is constructed from four Type A unit cells connected to four Type B unit cells at an interface (see schematics in Fig 3.7a, Fig 3.7b, and Fig 3.7c). The interface is categorized as Type I (blue surface in Fig 3.7b) or Type II (red surface in Fig 3.7c) depending on the switching configuration of the connected unit cells (B-A or A-B at the interface). Periodic and low-reflecting boundary conditions are applied to the supercell where indicated in the schematic (Fig 3.7a). The band structure for the supercell is numerically calculated for each configuration by varying the wave vector along the surface BZ projected onto the $k_{y-s} - k_{z-s}$ plane (see one-half of the surface BZ in Fig 3.7a). A localization metric Λ is defined for each eigenmode to quantify the confinement of the total displacement $d = \sqrt{|u|^2 + |v|^2 + |w|^2}$ (where u, v, w are displacements in the $x, y,$ and z directions, respectively) at the interface as $\Lambda = \iiint_{V_{interface}} d^2 dV / \iiint_{V_S} d^2 dV$, where $V_{interface}$ is the total volume of the two unit cells connected at the interface and V_S is the volume of the entire supercell. The supercell band structure is plotted in Fig 3.7d, with results from Type I and Type II configurations superimposed. Two interface states (red bands) are shown within the topological bandgap (highlighted by gray shading), one for each interface type. Representative mode shapes for the Type I (at \tilde{M} , marked by the star at 3060 Hz) and Type II (at $\tilde{\Gamma}$, marked by the square at 2950 Hz) interface states with highly localized displacement ($\Lambda = 0.99$) are displayed in Fig 3.7d. These interface modes are dominated by out-of-plane displacement w (i.e., out-of-plane modes). To give a more comprehensive view of the topological states, the band structure is plotted for the entire projected surface BZ in Fig 3.7e (for a Type I interface) and Fig 3.7f (for a Type II interface).

3.4.2 Full-scale numerical simulations of on-demand tunable 2D topological surface states

Full-scale simulations are conducted to illustrate how these interface states can be activated to achieve adaptive topological wave propagation. A 3D metastructure is built from an 8x8x8 lattice

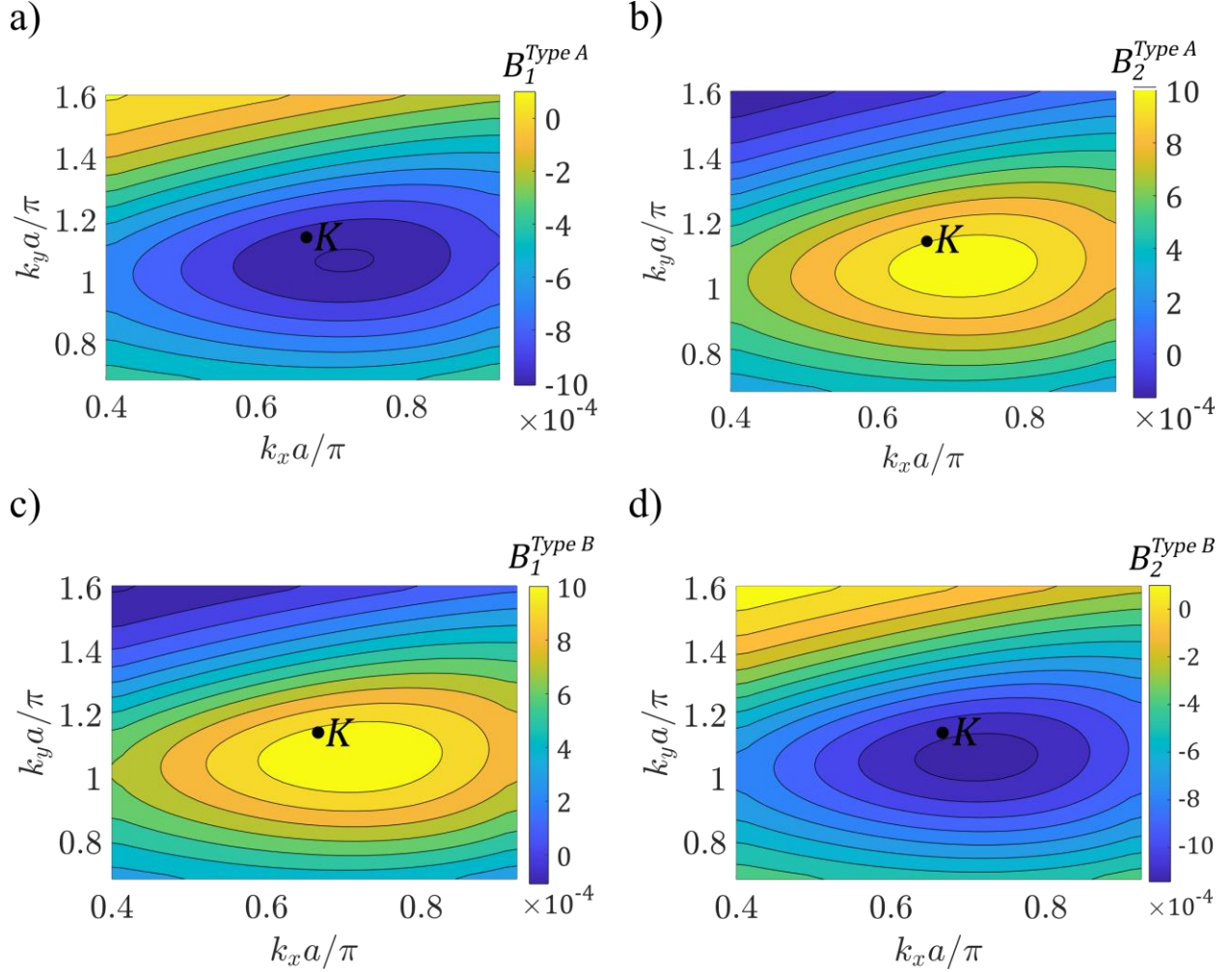


Fig 3.6. Berry Curvature $B_p(k)$ for the Type A lattice: (a) band 1 ($B_1^{Type A}$) and (b) band 2 ($B_2^{Type A}$). $B_p(k)$ for the Type B lattice: (c) band 1 ($B_1^{Type B}$) and (d) band 2 ($B_2^{Type B}$). The colormaps indicate the magnitude of $B_p(k)$.

of unit cells, and metastable switching is implemented to select three different paths for a Type I interface (straight line, 120° “sharp” corner, and zigzag, Configurations 1-3 in Fig 3.8a). A harmonic input with out-of-plane displacement is placed at the third and fourth layers of the metastructure (where marked by the black star in Fig 3.8a) and is chosen at a frequency ($f_e = 2950$ Hz) that excites the Type I interface state. To minimize backscattering at the edges of the domain, low-reflecting boundary conditions are applied to the boundaries perpendicular to the x - y plane. FE simulations are performed to obtain the steady-state displacement (d) fields. Results in Fig 3.8b illustrate how displacement is localized at the 2D interfaces (surfaces) in Configurations 1-3, with confined wave propagation travelling along all eight layers (layers 1-8 are marked as L1-L8, this naming convention holds throughout this chapter). Furthermore, the path of the 2D topological

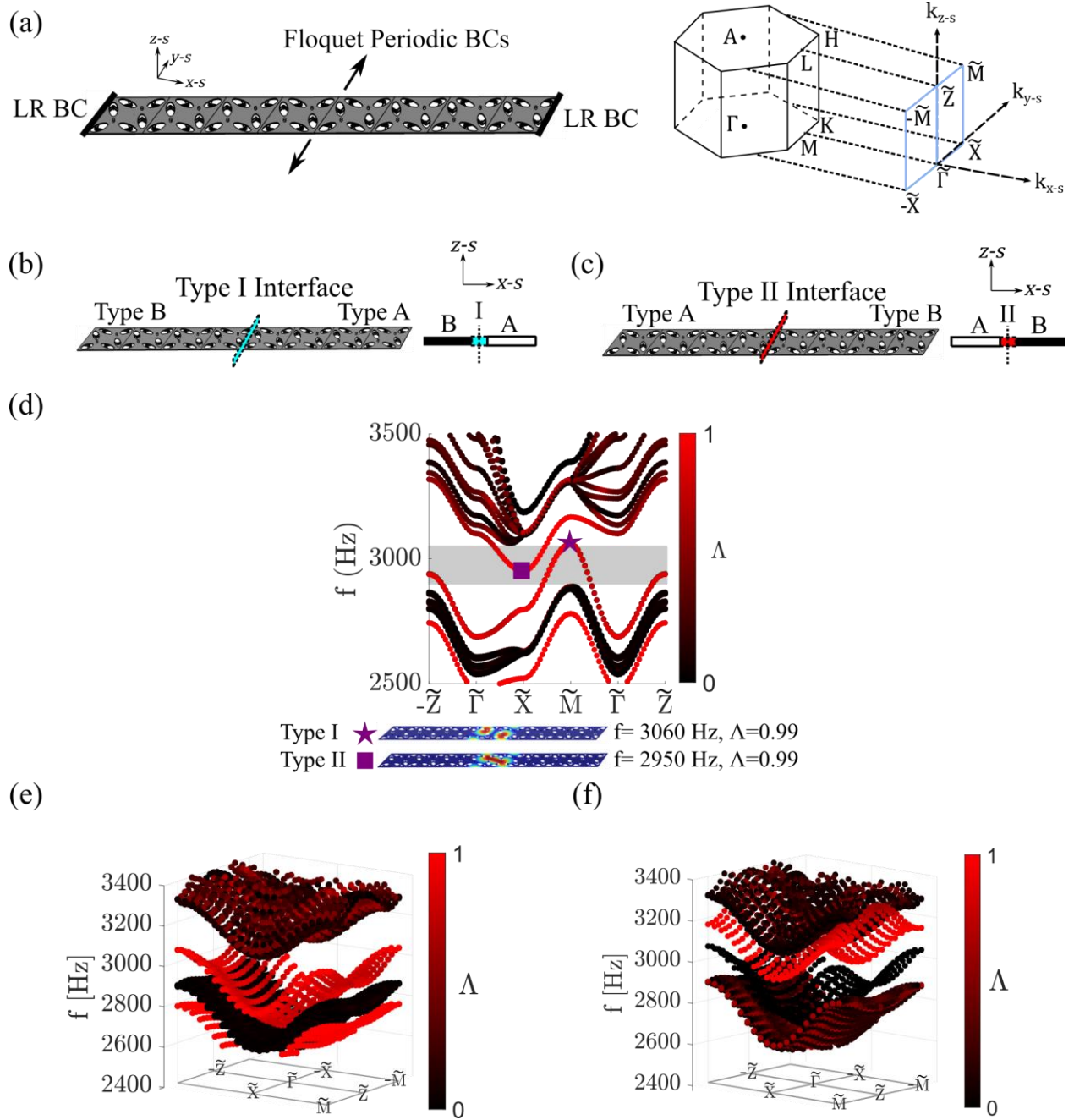


Fig 3.7. (a) Schematic of the supercell used for band structure calculations, with periodic and low-reflecting boundary conditions applied at the surfaces/directions that are indicated. Reciprocal space, where the light blue outline indicates one-half of the surface BZ projected onto the $k_{y-s} - k_{z-s}$ plane. Schematics for the proposed EM for a supercell with a (b) Type I and (c) Type II interfaces. (d) Band structure for supercells (both Type I and Type II interface configurations are superimposed). Topological bandgap is marked by gray shading. Colormap indicates confinement of mode displacement at the interface, with red indicating interface modes ($\Lambda \approx 1$) and black indicating bulk modes (if outside topological bandgap and $\Lambda < 1$) or boundary modes (if inside topological bandgap and $\Lambda \approx 0$). Mode shapes for Type I (purple star) and Type II (purple square) interfaces are at the bottom. (e) Band structure for the entire projected surface BZ for the supercell with a Type I interface. (f) Band structure for the entire projected surface BZ for the supercell with a Type II interface.

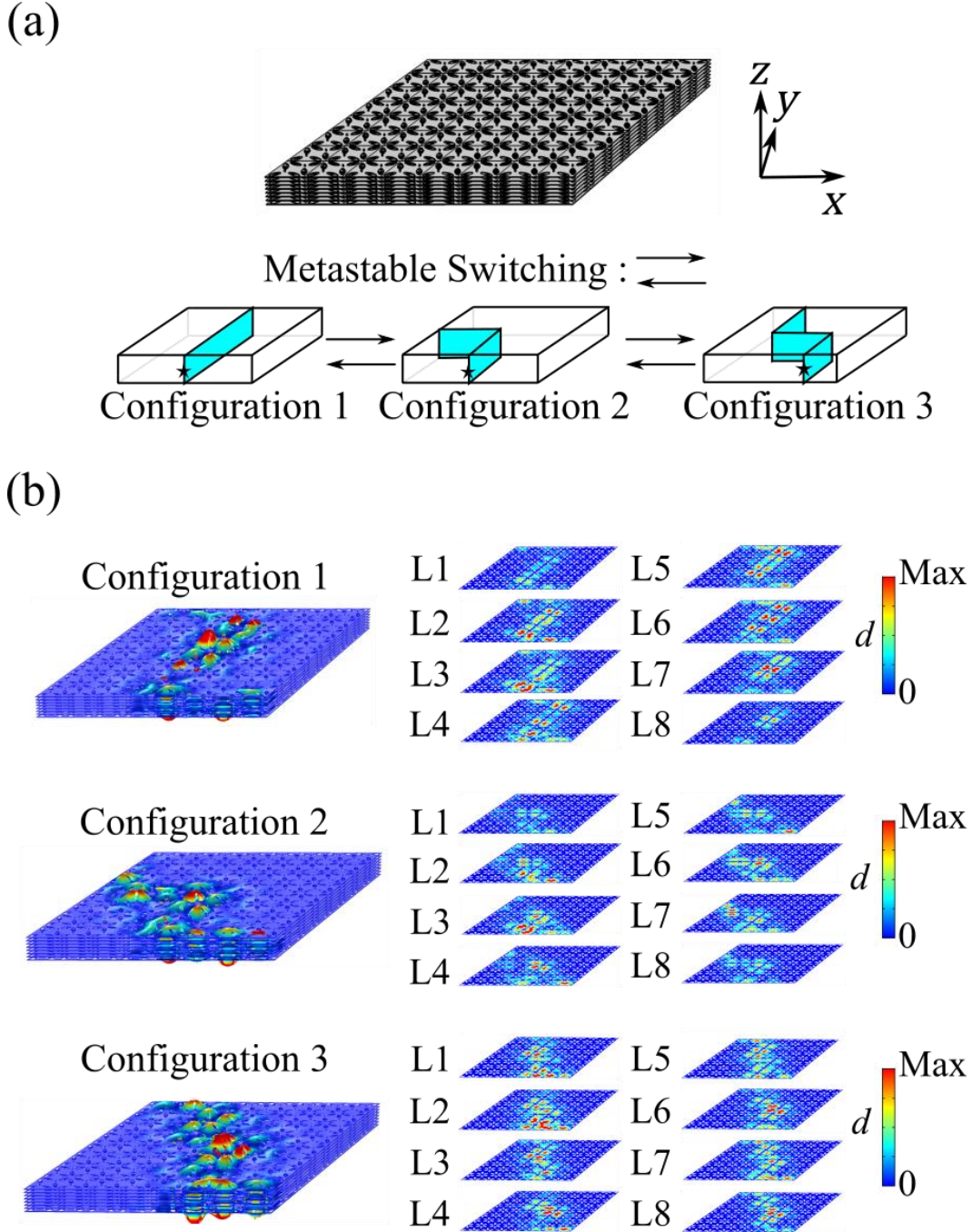


Fig 3.8. (a) 3D metastructure built from $8 \times 8 \times 8$ unit cells and a schematic of three waveguide configurations used for full-scale modeling, where the input is marked by a black star. (b) Reconfigurable topological wave propagation illustrated by steady-state displacements for Configurations 1-3. Independent layer responses are marked by L1-L8, with L1 being the bottom layer.

surface state is reconfigured by the strategic switching of metastable states (Fig 3.8a and Fig 3.8b), demonstrating on-line tunability of elastic waveguides in the 3D topological EM. Layer-polarized topological states

3.5 Layer-polarized topological states

The flexibility of the proposed EM is used to investigate additional topological states that exploit the layer DOF available in 3D periodic systems. A topological state with layer-polarized behavior is constructed by using a band folding methodology (to create layer pseudospin [121,131,246,247]) that involves stacking two unit cells in the z direction to form a bilayer unit cell (Fig 3.9). The same techniques employed to analyze the 2D topological surface states in Sections 3.3 (unit cell dispersion analysis) and 3.4.1 (supercell dispersion analysis) are employed to investigate the layer-polarized topological states (see Sections 3.5.1 and 3.5.2, respectively). Layer-polarized topological wave propagation is then shown using numerical simulations of a full-scale 3D metastructure (Section 3.5.3).

3.5.1 Unit cell dispersion analysis for layer-polarized topological states

Two unit cells with a Type 0 switching configuration (see the definition of Type 0 configuration in Section 3.3, Fig 3.3a) are stacked in the z direction to form a “bilayer” unit cell (Fig 3.9a). This creates a band folding effect, where the two bands that form the Dirac degeneracy for the monolayer unit cell in Section 3.3 (see Dirac degeneracy in Fig 3.3c) are folded into four bands [247] that create a nodal ring along the K - H line of symmetry (enclosed in orange box in Fig 3.9a). This nodal ring narrows as the wave vector is varied away from K to form a four-fold Dirac degeneracy at H . For a full picture of the degeneracy, the band structure is projected over the $k_x - k_y$ and $k_y - k_z$ planes near H . The $k_x - k_y$ projection reveals a double Dirac cone (Fig 3.9c left, Dirac point is orange dot), and the $k_y - k_z$ projection shows the four-fold Dirac degeneracy at the H point (Fig 3.9c right, orange dot). This four-fold Dirac degeneracy is protected by D_{6h} symmetry, where both in-plane (referring to the x - y plane) SIS and out-of-plane (referring to the z direction) mirror symmetry are intact. To break this degeneracy and obtain a topological bandgap, two bilayer switching configurations (denoted as Type C and Type D) made up of one Type A monolayer and one Type B monolayer are devised (see schematics in Fig 3.9b and Fig 3.9e). Both Type C and Type D configurations contain glide symmetry. In these switching configurations, the D_{6h} symmetry has been reduced to D_3 symmetry, where both in-plane SIS and out-of-plane mirror symmetry are broken. As seen in the Type C/Type D band structure (the band structure is identical for both configurations, see Fig 3.9b and Fig 3.9d), two two-fold degenerate states are formed that border a full topological bandgap (marked with gray shading). These two-

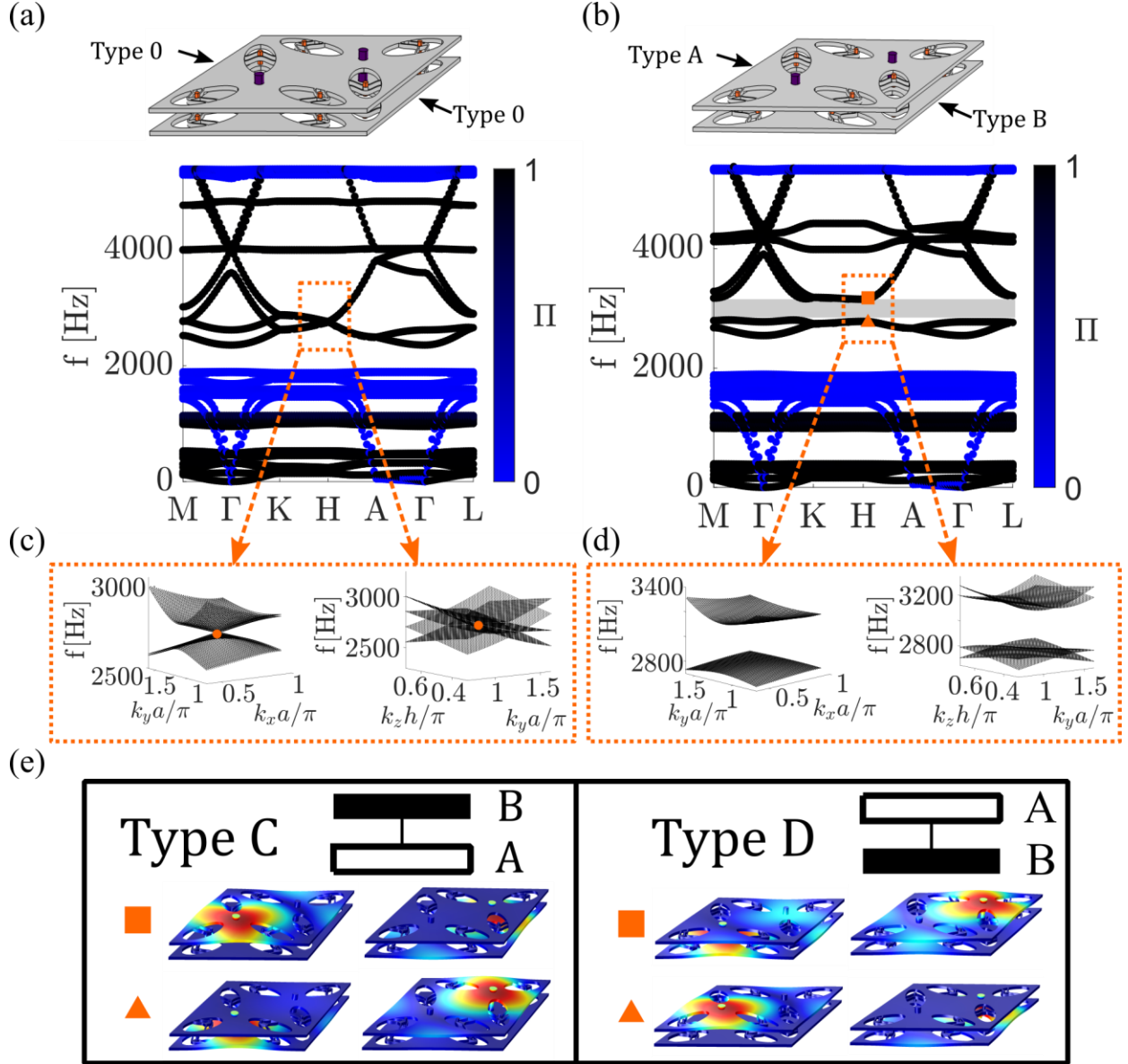


Fig 3.9. (a) Schematic of the bilayer unit cell comprised of two Type 0 monolayer unit cells stacked in the z direction. Band structure for this configuration is shown below, with a four-fold Dirac degeneracy at H enclosed in an orange box. The projection of the band structure over the $k_x - k_y$ and $k_y - k_z$ planes near H is shown in (c). (b) Schematic for the bilayer unit cell in the Type D switching configuration (Type A over Type B). Band structure for the 3D EM in Type C or D configuration (identical for both) is shown below. The full topological bandgap is marked by gray shading. The projection of the band structure over the $k_x - k_y$ and $k_y - k_z$ planes near H is shown in (d). (e) Diagram of the Type C (left) and Type D (right) bilayer unit cell switching configurations. Below are mode shapes at the H point for the bands that border the bandgap (as marked in (b) by \blacksquare and \blacktriangle), indicating a band inversion between the Type C and Type D lattices.

fold degenerate states are used to create layer pseudospins that can be harnessed to obtain layer-polarized behavior [100,246,247].

The topological nature of the full bandgap described in Fig 3.9b is investigated by examining the topology of the doubly degenerate bands that border it. The valley Chern numbers C_{v-p} (where p indicates the band number) for the two bands that border the bandgap from below (as marked by the \blacktriangle in Fig 3.9b) are calculated as described in Section 3.3.2 (see Eqs. 3.6-3.10). To properly obtain the pseudospin-valley Chern number C_{sv}^L [247,248], the valley Chern numbers are calculated at H (C_{H-1} and C_{H-2}) and H' ($C_{H'-1}$ and $C_{H'-2}$). The layer-polarized topological invariant C_{sv}^L is calculated as [247,248]:

$$C_{sv}^L = (C_{H-2} - C_{H'-2} - C_{H-1} + C_{H'-1})/2 \quad (3.11)$$

For a Type D lattice, $C_{sv}^L = -0.14$ (see the $B_{H/H'-p}^{Type D}$ used for these calculations in Fig 3.10), whereas for a Type C lattice, $C_{sv}^L = 0.14$. These nontrivial C_{sv}^L values indicate a pseudospin-derived and layer-polarized topological characteristic. In addition, the equal and opposite nature of C_{sv}^L for the Type C and Type D lattices indicates that these lattice configurations are topologically distinct and that a band inversion exists between them (this band inversion can be visualized by observing the inverted Type C and Type D eigenvectors in Fig 3.9e). Two layer-polarized topological states with opposite group velocities are predicted to exist at an interface between the Type C and Type D lattice types [100,247].

3.5.2 Supercell dispersion analysis for layer-polarized topological states

Type C and Type D lattices are connected at an interface in a supercell constructed from eight bilayer unit cells (see a detailed schematic in Fig 3.11a). The interface, identified here as a ‘‘Type III-1’’ interface, is comprised of a Type II interface on the lower layer (‘‘L1’’) and a Type I interface on the upper layer (‘‘L2’’). Calculation of the band structure (Fig 3.11b) reveals two layer-polarized topological interface states that emerge in the topological bandgap (the two localized interface states are the red bands that cross into the topological bandgap, which is represented by gray shading). To illustrate the layer-polarized (i.e., layer-dependent) behavior, eigenvectors (mode shapes) extracted from each of the two topological states are shown in Fig 3.11c. Each of the two modes has displacement that is confined at the interface on one of the two supercell layers (L2 for the mode calculated at 2937 Hz, L1 for the mode calculated at 3064 Hz). Aligning with the interface geometry, these mode shapes can be described as having a Type I interface state on the top layer (for the 2937 Hz mode) or a Type II interface state on the bottom layer (for the 3064 Hz

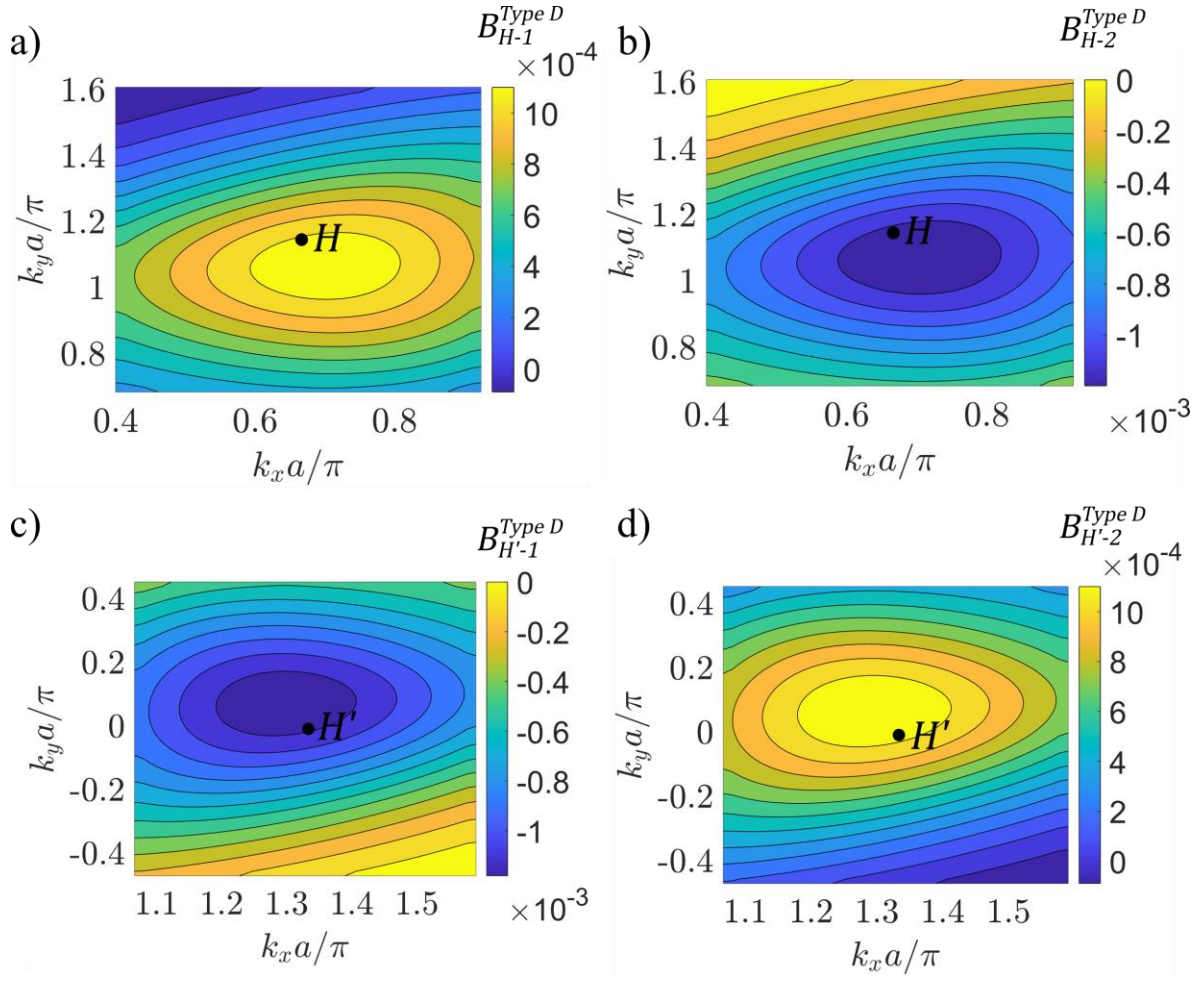


Fig 3.10. (a) Berry Curvature $B_p(k)$ for the Type D lattice: (a) band 1 near H ($B_{H-1}^{Type D}$), (b) band 2 near H ($B_{H-2}^{Type D}$), (c) band 1 near H' ($B_{H'-1}^{Type D}$), (d) band 2 near H' ($B_{H'-2}^{Type D}$). The colormaps indicate the magnitude of $B_p(k)$.

mode).

In addition to the Type III-1 interface, metastable switching can be used to adjust the supercell such that a “Type III-2” interface is created. A supercell with a Type III-2 interface is the reflection of a supercell with a Type III-1 interface in the z direction (see schematic in Fig 3.11a). Thus, the Type III-2 interface consists of a Type I interface on the lower layer (L1) and a Type II interface on the upper layer (L2). The band structure is identical to that of a Type III-1 interface (Fig 3.11b), but the layer polarizations (the layer polarizations for Type III-1 supercell are shown in Fig 3.11c) are interchanged.

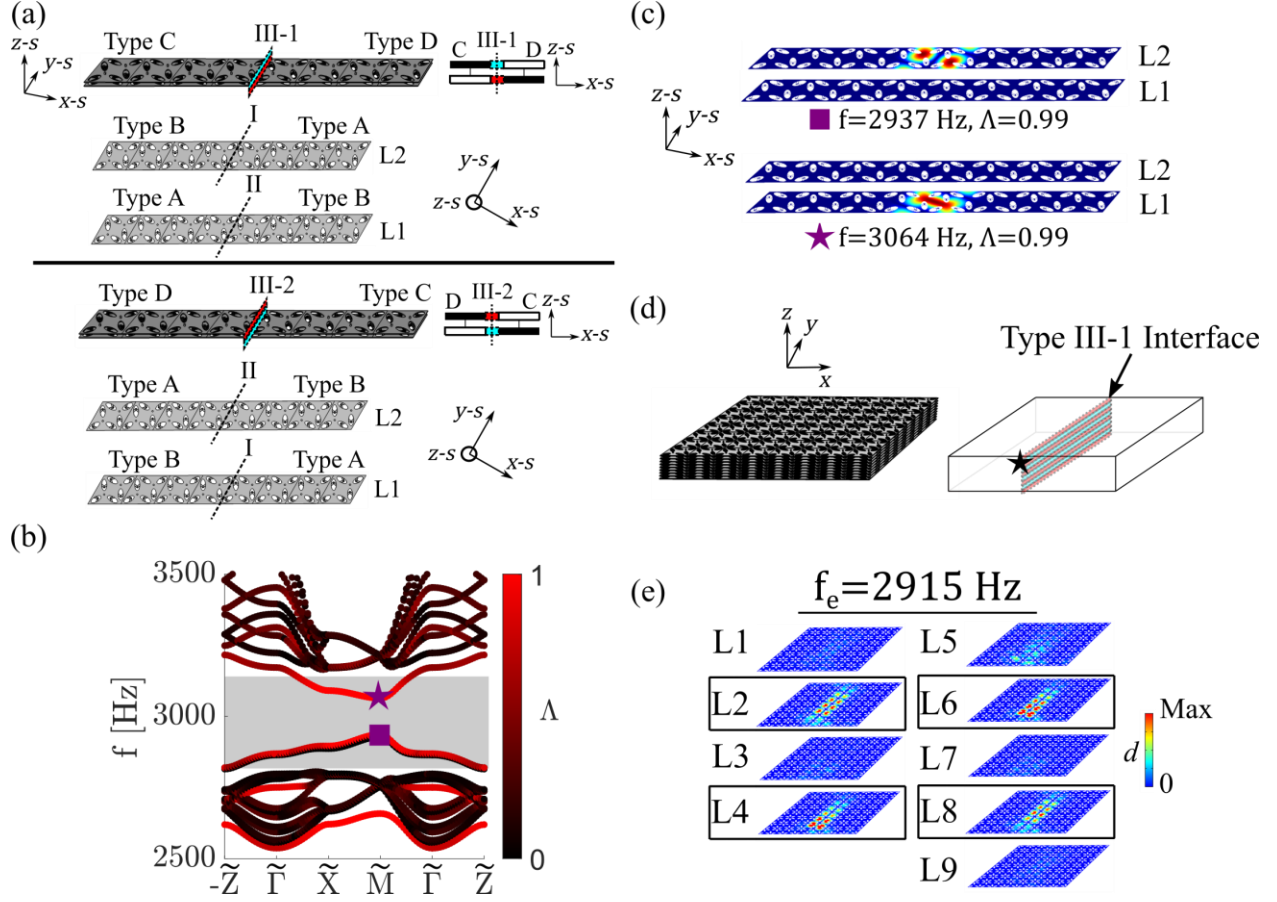


Fig 3.11. (a) Schematic of the bilayer supercell in metastable switching configurations with a Type III-1 (top) or Type III-2 (bottom) interface. (b) Band structure for the proposed EM for a supercell with a Type III-1 interface (note: Type III-2 band structure is identical). The colormap indicates the mode localization with metric Λ . Red modes are localized to the interface ($\Lambda \approx 1$), while black modes are bulk modes (if outside topological bandgap and $\Lambda < 1$) or boundary modes (if inside topological bandgap and $\Lambda \approx 0$). Representative mode shapes for the topological interface states (at \tilde{M}) are shown in (c). (d) 3D metastructure built from $8 \times 8 \times 9$ unit cells and a schematic of the waveguide configuration used for full-scale modeling, where the input is marked by a black star. (e) Layer-polarized topological wave propagation illustrated by steady-state displacement that is confined to four specific layers (outlined with dashed black lines). Independent layer responses are marked by L1-L9, with L1 being the bottom layer.

3.5.3 Full-scale numerical simulations for layer-polarized topological wave propagation in a 3D metastructure

Full-scale simulations are conducted to illustrate how the layer-polarized interface states can be activated to achieve layer-dependent topological wave propagation. A 3D metastructure is built from an $8 \times 8 \times 9$ pattern of unit cells, and metastable switching is implemented to create a Type III-1 interface (Fig 3.11d). For this interface configuration, a harmonic input is placed at the eighth layer (L8) of the metastructure (where marked by the black star in Fig 3.11d) and is chosen at a frequency ($f_e = 2915$ Hz) that excites the lower frequency interface state from Fig 3.11c. To

minimize backscattering at the edges of the domain, low-reflecting boundary conditions are applied to the boundaries perpendicular to the x - y plane. FE simulations are performed to obtain the steady-state displacement (d) field. Results in Fig. 11e illustrate how displacement is localized along the L2, L4, L6, and L8 layers, with minimal wave transmission on L1, L3, L5, L7, and L9. Thus, metastable switching can be used in the proposed 3D EM to achieve layer-dependent topological wave transmission.

3.6 Bilayer-locked topological states

The layer-polarized states are used as building blocks to create a novel bilayer-locked topological state. A supercell composed of an eight-layer stack ($8 \times 1 \times 8$ unit cells) is constructed by placing four layers with a Type III-2 interface on top of four layers with a Type III-1 interface, creating a Type IV interface parallel to the \bar{x} - s - \bar{y} - s plane (Fig 3.12a). Periodic boundary conditions are applied in the \bar{y} - s direction and the band structure of the supercell is evaluated, revealing eight interface states in the topological bandgap (bandgap is shaded in gray, interface bands are red in Fig 3.12a), an identical number to the number of layers (eight) in the stack (see Appendix B.1 for a full description of the eight topological states). Six of these interface states are defined as “monolayer” states, where modal displacement is confined to one specific layer (see two examples of monolayer interface states on L2 and L7 in Fig 3.12a). The remaining two interface states contain localized displacement at the two layers (L4 and L5) bordering the Type IV interface, forming “bilayer-locked” states (see an example of a bilayer-locked state in Fig 3.12a). These bilayer-locked states arise due to the coupling of two layer-polarized topological interface states on adjacent layers of the mechanical structure (the example in Fig 3.12a is formed from adjacent Type I interface states that are embedded into layer-polarized lattices). The 3D metastructure in Fig 3.8 is reconfigured to support bilayer-locked states, with dynamic response for a 2950 Hz excitation that is positioned on L4 and L5 shown in Fig 3.12b. Note that topological wave propagation is confined to reconfigurable waveguides in two specifically targeted layers (L4 and L5) of the eight-layer structure, illuminating a new capability for 3D mechanical systems. Comprehensive diagrams of the 3D metastructure with a tunable bilayer-locked state are found in Appendix B.1.

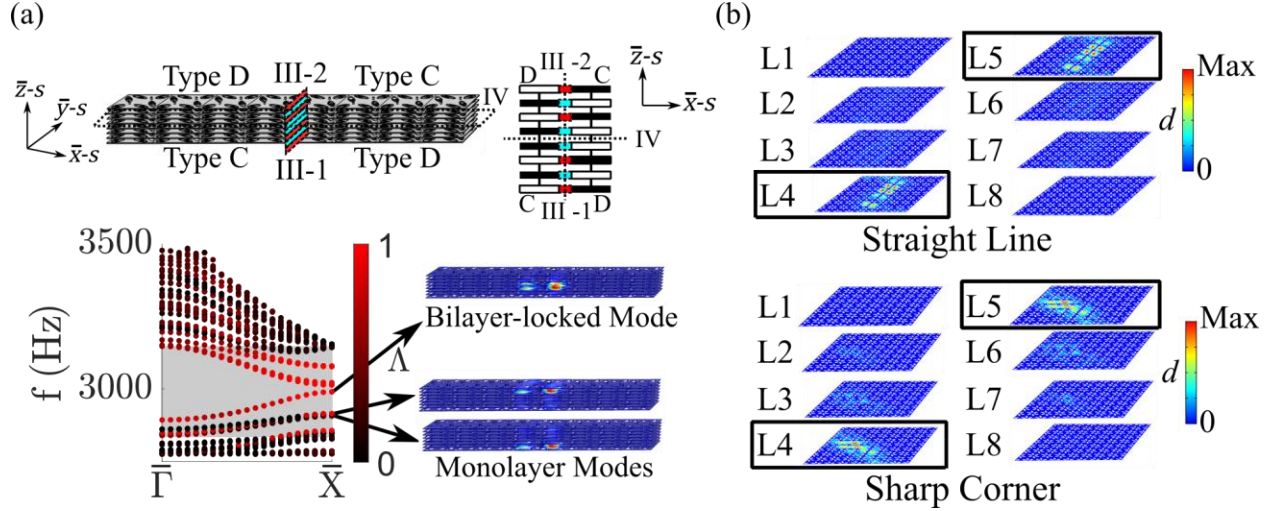


Fig 3.12. (a) Schematic (isometric and front views) of an eight-layer stack supercell, consisting of a four-layer Type III-2 interface stacked onto a four-layer Type III-1 interface, creating a Type IV interface. Band structure for the supercell with bilayer-locked and monolayer modes. Topological bandgap is marked by gray shading. Colormap indicates confinement of mode displacement at the interface, with red indicating interface modes ($\Lambda \approx 1$) and black indicating bulk modes (if outside topological bandgap and $\Lambda < 1$) or boundary modes (if inside topological bandgap and $\Lambda \approx 0$). Two bilayer-locked modes and six monolayer modes exist within the topological bandgap. One example of a bilayer-locked mode and two examples of monolayer modes are displayed to the right of the band structure. (b) Adaptive topological wave propagation of bilayer-locked state in 3D metastructure (straight line and sharp corner), calculated from full-scale numerical simulations.

3.7 Advanced 3D elastic wave networks

The exceptional features of the topological states obtained with the proposed EM are integrated together to create advanced 3D topological wave networks. An elastic wave layer converter is constructed in a 3D metastructure comprised of $8 \times 12 \times 8$ unit cells with sections defined as S1, S2, and S3 to delineate different metastable switching configurations (Fig 3.13a). S1 contains a harmonic excitation at L2 and L3 and a Type I interface on L1-L4, S2 contains a Type I interface on L1-L8, and S3 contains a Type I interface on L5-L8 (see Fig 3.13a for a schematic, where Type I interfaces are marked with blue surfaces). Type II interfaces exist at the boundaries of S1-S2 and S2-S3 in L5-L8 and L1-L4, respectively (red surfaces, Fig 3.13a). By selecting an excitation frequency ($f_e = 2920$ Hz) that solely activates the Type I topological surface state (Fig 3.7b), wave energy is converted from the bottom four layers to the top four layers as it passes in a straight line from S1 to S3 (see “Layer Conversion” steady-state displacement in Fig 3.13a). If the excitation frequency is chosen such that both Type I and Type II interface states are activated ($f_e = 3020$ Hz), a wave splitting behavior is generated in addition to the layer conversion, and a portion of the wave energy is diverted (along the Type II interfaces) from the original straight-line interface (see “Wave

Splitting” in Fig 3.13a). These findings, along with other network functionalities shown in Appendix B.2, reveal how frequency-dependent wave splitting behavior can be obtained from 2D topological states in 3D structures.

The 3D metastructure in Fig 3.13a is reconfigured to support topological surface states and bilayer-locked states arranged into a “wave-focusing gate.” In this setup, S1 and S3 contain a Type I interface on L1-L8, S2 contains the switching configuration required for a bilayer-locked state (Fig 3.12a), and various monolayer Type I and Type II interfaces exist at the borders of S1-S2 and S2-S3 (see schematic in Fig 3.13b). If an input frequency is selected such that both the Type I interface and bilayer-locked states are excited ($f_e = 2950$ Hz), wave energy passes from L1-L8 in S1 through a “funnel” that focuses energy on L4-L5 of S2 to L1-L8 on S3 (“ON” in Fig 3.13b). For an input frequency that is outside of the range for the bilayer-locked state (but still activates the Type I interface state, $f_e = 3000$ Hz), the wave can no longer propagate through S2, turning “OFF” the flow of wave energy and trapping it in S1 (“OFF” in Fig 3.13b). More complicated layer-dependent transport can be achieved by selecting a frequency that excites various interface states (see Appendix B.2). The results indicate that the bilayer-locked state can be interfaced with other topological states to control elastic waves in exotic ways.

3.8 Conclusions and discussion

The research presented in this chapter advances the state of the art through the development of a metastable EM that enables tunable topological wave control in a 3D mechanical structure. A comprehensive design methodology is established by investigating the critical features of bistable curved beam dimensions, interlayer coupling (i.e., the stiffness of the interconnecting rods, E_r), and locally resonant mass ratio m_{ratio} . Several metastable switching methodologies are generated to manipulate the spatial path of wave propagation on-demand and select between three topological states (2D surface, layer-polarized, and bilayer-locked). By harnessing the reconfigurability of the EM, the bilayer-locked topological state is uncovered, where elastic wave energy is trapped in two targeted layers of a multilayered structure. Programmable 3D topological wave networks that partition, divert, and focus energy in a layer- and frequency-dependent fashion are created, exploiting the added dimensionality and the multitude of topological states present in the 3D structure to extend beyond the capabilities of 2D elastic wave networks [115,155,241]. Overall, the research outcomes presented in this chapter will pave the way for the future development of

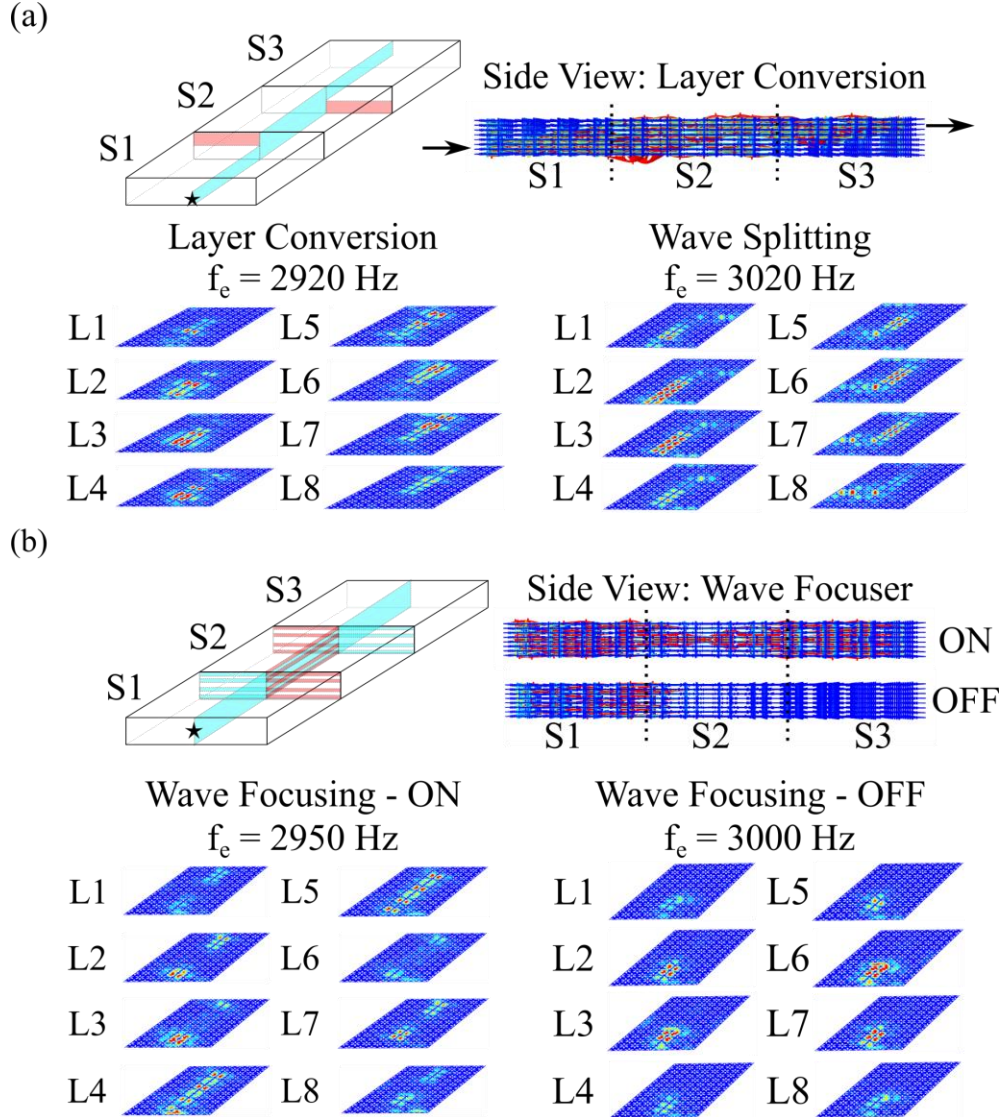


Fig 3.13. (a) Layer converter schematic and steady-state displacement (side view and layer views) for excitation located at the star. Type I interfaces are marked in blue and Type II interfaces are marked in red. Steady-state displacement results illustrate layer conversion ($f_e = 2920$ Hz) and wave splitting ($f_e = 3020$ Hz) behavior (b) Wave-focusing gate schematic and steady-state displacement (side view and layer views) for excitation located at the star. Steady-state displacement results show a wave-focusing behavior that can act as a frequency-dependent ON/OFF gate.

adaptive topological states in 3D mechanical [90–93] systems and inspire further studies in the adjacent fields of topological photonics [99,100] and acoustics [91,97,98]. The exceptional ability of the proposed EM to control the flow of energy in 3D structures may find application in the future development of logic elements, splitters, and filters for artificial mechanical structures that contain intrinsic “intelligence” [12,249,250] and enable enhanced performance in contemporary engineering applications such as vibration mitigation [104], energy harvesting [105,106,251], and on-chip transduction [27,109,110,252].

Note: The reused content (text, figures, and tables) in Chapter 3 and Appendix B is reproduced from [253] with written permission from the publisher.

Chapter 4. 3D Multimodal Locally Resonant Metamaterial

The outcomes from the theoretical investigation reported in Chapter 3 include the discovery of innovative wave control capabilities that are unlocked by the added dimensionality available in 3D TMs. These outcomes point toward a promising potential for manipulating elastic waves using 3D TMs. Chapter 4 delves deeper into this potential and expands upon the insights gleaned from Chapter 3 through the investigation of a novel 3D TM that achieves additional 3D elastic wave control behaviors and is experimentally realized and tested. In Chapter 4, we advance the state of the art through the synthesis and experimental realization of a first-order 3D TM that exploits multimodal local resonance to enable low-frequency (i.e., few Hz to 20 kHz) elastic wave control over multiple distinct frequency bands. The proposed 3D TM is geometrically configured to create multimodal local resonators whose frequency characteristics govern the emergence of four unique low-frequency topological states. Numerical simulations uncover how these topological states can be employed to achieve polarization-, frequency-, and layer-dependent wave manipulation in 3D mechanical structures. An experimental study results in the attainment of complete wave fields that illustrate 2D topological waveguides and multi-polarized wave control in a physical testbed. The outcomes from this chapter provide insight that will aid future research on 3D TMs and reveal the applicability of the proposed metamaterial for wave control applications.

4.1 Introduction

While 3D TMs have exhibited the potential to surpass what is possible in 1D and 2D TMs, research gaps exist that inhibit their successful implementation in practice. Despite numerous theoretical studies [26,75,184,187,188,253], there is very little experimental evidence of elastic wave control in 3D TMs [131], due to the challenges associated with the fabrication and testing of intricate 3D mechanical architectures. Furthermore, despite previous studies demonstrating multiband operation in 2D TMs [254–259], the 3D TMs established thus far are constrained to function in a single frequency band. This single-band characteristic limits the working bandwidth and information-carrying capacity of 3D TMs, reducing their suitability for multiband wave-based applications such as lasers [209], filters [210], resonators [211], on-chip circuits [212], isolators

[213,214], and wireless networks [260]. Finally, the previously developed 3D TMs largely function in a high-frequency regime (i.e., the ultrasonic range: 20 kHz to ~1 GHz), resulting in a lack of 3D mechanical platforms that accomplish low-frequency topological wave manipulation.

This research addresses the aforementioned gaps and advances the state of the art through the synthesis and experimental realization of a novel 3D TM that harnesses multimodal local resonance for low-frequency and multiband elastic wave control. The geometry of the proposed TM is configured to obtain four distinct low-frequency (<6 kHz) topological states derived from multimodal local resonances that can be tailored without changing the lattice constant. Rich polarization-dependent behavior is encoded into the metamaterial by taking advantage of the multiple unique polarizations of the resonant topological modes. Dispersion analyses and full-scale response simulations illustrate how these topological states emerge through the QVHE and can be exploited to obtain frequency- and layer-dependent elastic waveguides in 3D structures. Moreover, a comprehensive experimental investigation validates the theoretical predictions and produces the first measurements of complete elastic wave fields and multi-polarized elastic waveguides in a 3D TM. The findings presented within this chapter establish a foundation for further experimental research on 3D TMs and illuminate the multifaceted features of the proposed metamaterial that would be valuable for vibration engineering applications.

4.2 Concept and theoretical model

The proposed TM is a 3D periodic structure with aluminum interconnecting rods (for interconnection in the z direction, with radius $r_r = 0.93$ mm, $E_r = 69$ GPa, $\rho_r = 2700$ kg·m⁻³, $\nu_r = 0.33$) and two resonators in the unit cell (Fig 4.1a,b). The schematic for the unit cell is given in Fig 4.1b, where $a = 50$ mm is the in-plane (x - y) lattice constant, $h_o = 25$ mm is the out-of-plane (z) lattice constant, and $\vec{a}_1 = a\hat{x}$, $\vec{a}_2 = a(1/2\hat{x} + \sqrt{3}/2\hat{y})$, and $\vec{a}_3 = h_o\hat{z}$ are the lattice basis vectors. The resonators are created using cylindrical steel masses ($E_m = 200$ GPa, $\rho_m = 8000$ kg·m⁻³, $\nu_m = 0.30$) of radius $r_m = 7.0$ mm and baseline height $h_m = 14.3$ mm that are attached to aluminum spring ligaments ($E_l = 69$ GPa, $\rho_l = 2700$ kg·m⁻³, $\nu_l = 0.33$) of height $h_l = 1.5$ mm and width $w_{l1,l2} = 1.5$ mm through a circular ($r_{platform} = r_m = 7.0$ mm) aluminum platform. Each resonator mass is comprised of two sub-masses that have heights defined as $h_{m1} = \frac{h_m}{2}(1 - \alpha)$ and $h_{m2} = \frac{h_m}{2}(1 + \alpha)$, where α is the mass height perturbation parameter.

The local resonance phenomenon, which enables wave control near the natural frequencies of the resonators [60], is exploited to obtain multiband and low-frequency wave dispersion characteristics through the design of the resonant elements. A reticular (i.e., mesh-like) lattice geometry is created from the spring ligaments and steel is selected as the material for the resonant masses to obtain a large mass ratio $\gamma = \frac{m_m}{m_l + m_r}$ within a reasonable volumetric envelope, where m_m is the cumulative mass of the steel masses, m_l is the cumulative mass of the aluminum ligaments, and m_r is the cumulative mass of the aluminum interconnecting rods. A mass ratio value that is greater than unity ($\gamma = 13.9$ with the baseline design parameters) is deliberately attained to ensure that the resonant masses provide a significant impact on the dynamic response of the proposed metamaterial. Previous works have shown that the magnitude of the mass ratio, which governs the relative influence of the resonant elements on the system response, plays a crucial role for achieving broad low-frequency bandgaps [60,61] and effective topological wave propagation [83,261] in locally resonant mechanical metamaterials. Furthermore, previous research has revealed that multimodal resonances can be harnessed to create multiple low-frequency bandgaps in mechanical metamaterials [214,262,263]. In the proposed 3D TM, the large mass ratio and relative compliance of the mesh-like aluminum lattice structure facilitate the achievement of multiple low-frequency out-of-plane and in-plane translational and torsional resonances. This rich set of resonances opens opportunities for multi-polarized and multiband response in a low-frequency regime.

The interconnecting rods create a structural coupling between the 2D layers that contain the mass-spring resonators (Fig 4.1a,b), providing a mechanism for elastic waves to propagate along the z-direction in the 3D structure. The geometry and material properties of the interconnecting rods may be used to modify the wave propagation characteristics of the metamaterial. The metamaterial lattice is arranged into a honeycomb pattern in the x - y plane such that it contains D_{6h} lattice symmetry (see the top view in the lower panel of Fig 4.1a), which is used to acquire nontrivial topological features through the QVHE [151–153,163]. A detailed numerical analysis of the design considerations outlined in this section is provided in Section 4.3.

4.3 Unit cell dispersion and multimodal resonance effect

The wave dispersion characteristics of the unit cell are analyzed first to investigate the topological characteristics and unique wave propagation features of the proposed metamaterial.

As shown in Fig 4.1c, a unit cell with equivalent mass heights ($\alpha = 0$) is designated as a Type 0 lattice. The band structure is calculated using the commercial FE solver COMSOL Multiphysics (see Appendix C.1 for further details on the simulation methods). The D_{6h} symmetry present in the Type 0 lattice leads to four distinct Dirac nodal line degeneracies appearing along the K-H line in the band structure across a wide frequency range (Fig 4.1c) [86,91,151]. These Dirac degeneracies are labeled as D1, D2, D3, and D4 in order of lowest to highest frequency, $f_{d-D1} = 0.37$ kHz, $f_{d-D2} = 1.41$ kHz, $f_{d-D3} = 3.66$ kHz, and $f_{d-D4} = 4.76$ kHz, which is computed at the midpoint of the K-H line. A polarization parameter $\Pi = \frac{\iiint_{V_U} |w|^2 dV}{\iiint_{V_U} (|u|^2 + |v|^2 + |w|^2) dV}$ is defined and measured for each mode in the band structure, where V_U is the volume of the unit cell, and u , v , and w are the displacement components in the x , y , and z directions, respectively. The Dirac degeneracies in Fig 4.1c each contain different polarizations, with D1 being predominantly out-of-plane polarized ($\Pi \approx 1$, yellow in Fig 4.1c), D2 having a hybrid polarization ($\Pi = 0.5$, green in Fig 4.1c), and D3/D4 containing in-plane polarized displacements ($\Pi \approx 0$, blue in Fig 4.1c). To follow the requirements of the QVHE [151–153,163], the D_{6h} symmetry is reduced to D_{3h} symmetry by perturbing the mass heights from the baseline configuration ($\alpha \neq 0$). The lattice is designated as Type A for $\alpha < 0$ or Type B for $\alpha > 0$ (Fig 4.1d). Calculation of the band structure for the cases of $\alpha = \pm 0.11$ reveals that this reduction in symmetry splits the Dirac degeneracies and leads to bandgaps opening along the K-H line (Fig 4.1d, note that the Type A and Type B band structures are superimposed, as they are identical for $|\alpha| = 0.11$). For the case of $|\alpha| = 0.11$, partial bandgaps are obtained from the Dirac degeneracies D2, D3, and D4 that cover the frequency ranges of $f = 1.3$ to 1.5 kHz, $f = 3.5$ to 3.8 kHz, and $f = 4.5$ to 5.1 kHz, respectively. The split D2, D3, and D4 degeneracies and the frequency ranges of the partial bandgaps that are opened from them are represented with gray shading in Fig 4.1d. A partial bandgap may also be opened from D1 if the mass perturbation $|\alpha|$ is increased further (see the evolution of all four bandgaps with respect to $|\alpha|$ and a D1 topological state for $|\alpha| = 0.40$ in Appendix C.2). While the bandgaps are incomplete (i.e., they do not cover the entire B of reciprocal space), previous works have demonstrated that complete bandgaps are not strictly required for effective topological wave control using the QVHE [156,173,235], so long as there is no coupling between the non-topological bands that cross through the partial bandgaps and the topological bands of interest. Further discussion clarifying

why the partial nature of the bandgaps does not inhibit the construction of topological waveguides in the proposed metamaterial is included in later sections.

The topological nature of the D2, D3, and D4 bandgaps is evaluated by computing the valley Chern number $C_{v-p} = \frac{1}{2\pi} \iint_{\mathcal{B}_p} B_p(k) d^2k$ for the bands bordering each bandgap, where $B_p(k)$ is the Berry curvature, $p = 1$ refers to the band delineating the low-frequency bandgap boundary, and $p = 2$ refers to the band delineating the high-frequency bandgap boundary (see Appendix C.3 for more details on the C_{v-p} calculations). The resulting C_{v-p} are $C_{v-1}^{Type A} = 0.11$, $C_{v-2}^{Type A} = -0.09$, $C_{v-1}^{Type B} = -0.11$, $C_{v-2}^{Type B} = 0.09$ for the D2 bandgap; $C_{v-1}^{Type A} = -0.14$, $C_{v-2}^{Type A} = 0.17$, $C_{v-1}^{Type B} = 0.15$, $C_{v-2}^{Type B} = -0.18$ for the D3 bandgap; and $C_{v-1}^{Type A} = 0.25$, $C_{v-2}^{Type A} = -0.30$, $C_{v-1}^{Type B} = -0.26$, $C_{v-2}^{Type B} = 0.30$ for the D4 bandgap. The nonzero C_{v-p} values reveal the topological characteristic for each bandgap, while the equal and inverted C_{v-p} calculated for the Type A and Type B configurations indicate that they are topologically distinct. These nontrivial C_{v-p} magnitudes confirm that topological protection is present in the metamaterial. However, they are less than the idealized $|C_{v-p}| = 0.5$ due to the large amplitude of the perturbation to the mass height [157,175,229,235]. Previous research has shown that a $0 < |C_{v-p}| < 0.5$ does endow a sufficient level of topological protection for wave propagation and indicates that the amplitude of the mass perturbation $|\alpha|$ could be reduced to increase $|C_{v-p}|$ if necessary [157,175,229,235]. While calculations shown in Appendix C.2 demonstrate that the bandgaps could be further broadened by increasing $|\alpha|$, $|\alpha| = 0.11$ is selected for the presented results to conserve the calculated $|C_{v-p}|$ values. In practice, the tradeoff between bandgap width and $|C_{v-p}|$ must be considered when specifying $|\alpha|$.

Further analysis of the unit cell dispersion uncovers the multimodal resonant characteristic of the proposed 3D metamaterial and elucidates how this feature enables low-frequency topological bandgaps over multiple frequency bands. The mode shapes for the bands bordering each of the four topological bandgaps in the $|\alpha|=0.11$ case are shown in Fig 4.1e. All of these mode shapes contain displacement that is largely confined to the resonator masses, a distinguishing characteristic of the local resonance mechanism for bandgap formation [60,177]. Furthermore, each set of modes displays a distinct resonant behavior: out-of-plane translational for D1 ($\Pi \approx 1$), hybrid torsional for D2 ($\Pi = 0.6$), in-plane torsional for D3 ($\Pi \approx 0$), and in-plane translational for D4

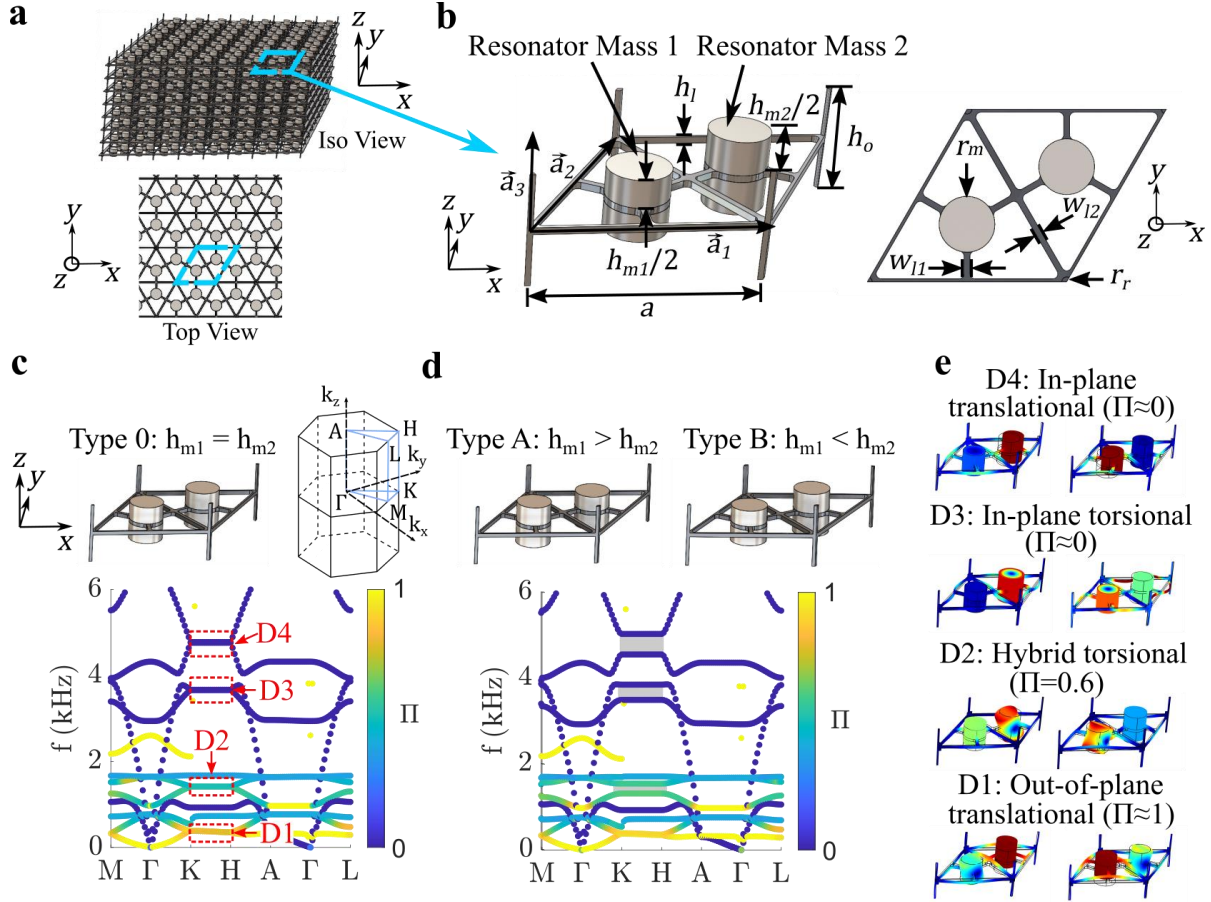


Fig 4.1. (a) A schematic of the 3D TM. (b) Isometric and top views of the metamaterial unit cell. (c) The band structure for the Type 0 lattice ($\alpha = 0$). The four Dirac nodal line degeneracies are indicated by the dotted red boxes. The colorbar indicates the mode polarization quantified by the parameter Π . (d) The band structure for the Type A/B ($\alpha = -0.11/0.11$) lattices. The band structures for Type A and Type B lattices are identical and superimposed. The three split Dirac degeneracies are marked by gray shading. (e) The mode shapes (taken along K - H) for the bands that border the four (D1, D2, D3, and D4) topological bandgaps in the $|\alpha|=0.11$ case, illustrating multimodal resonance.

($\Pi \approx 0$), illustrating how the engineered multimodal resonance of the proposed metamaterial is the source of the four distinct topological bandgaps (see Appendix C.4 for further details on these modes).

A parameter study is conducted to study the influence of the multimodal resonator design on the Dirac degeneracies D1-D4 presented in Fig 4.1c for the $\alpha=0$ case. Results from this parameter study (shown in Fig 4.2) illustrate how the respective frequencies f_{d-D1} , f_{d-D2} , f_{d-D3} , and f_{d-D4} of the four Dirac degeneracies can be tailored by adjusting the frequency characteristics of the resonators. Fig 4.2a reveals that the Dirac frequencies have an inverse relationship with the resonator mass, which is adjusted using the mass height parameter h_m . By increasing the resonator mass height, the Dirac frequencies for D1-D4 can be dramatically reduced, and the four degeneracies can be spectrally separated from extraneous high-frequency modes that would make

it difficult to construct topological bandgaps (and furthermore, effective topological waveguides within those bandgaps). The lowest frequency of the extraneous modes is 6.5 kHz for all h_m (i.e., it is not effected by h_m) and is marked by the horizontal dashed red line in Fig 4.2a. These modes are dominated by displacements of the outer aluminum ligaments (with width w_{l2} in Fig 4.1b) and interconnecting rods that contain a hybrid polarization ($\Pi \approx 0.65$, see an example mode in the inset of Fig 4.2a), and are thus referred to as ligament/rod modes. For the given system parameters, a minimum mass height of $h_m = 8.0$ mm, (corresponding to a mass ratio of $\gamma = 7.8$) is required to ensure that all four f_d are below the 6.5 kHz threshold. The mass height of $h_m = 14.3$ mm (marked by the vertical dashed black line in Fig 4.2a, corresponding to $\gamma = 13.9$) is selected in this study to ensure that the Dirac degeneracies, and thus the topological bandgaps that are opened from them, are well isolated from the ligament/rod modes. Further details on how interaction with the ligament/rod modes can inhibit the formation of topological bandgaps/waveguides and how these undesirable modes can be separated from the Dirac degeneracies are given in Appendix C.5. By employing the local resonance mechanism to isolate the Dirac dispersions in this way, the proposed metamaterial unclutters the intrinsically dense band structure of 3D EMs, which has often impeded low-frequency and multiband topological wave control in previous investigations.

In contrast to the inverse relationship with the resonant mass, the Dirac frequencies exhibit a direct relationship to the stiffness of the resonator spring, which is modified through the ligament width w_{l1} (Fig 4.2b). Notably, the f_d for D3 (f_{d-D3}) is the most affected by increasing w_{l1} from 1 mm to 3 mm (168% increase in f_{d-D3} , compared to 37% for f_{d-D1} , 66% for f_{d-D2} , and 77% for f_{d-D4}). This large shift in f_{d-D3} is due to the heightened sensitivity of the in-plane torsional mode to w_{l1} , compared to the other three sets of modes presented in Fig 4.1e. The cause of this greater sensitivity can be clarified by treating the spring ligaments as idealized cantilevered beams of length L_l . Under this assumption, the bending stiffness for the D1 mode is $S_{D1} = \frac{3w_{l1}h_l^3}{4L_l^3}$ [264], while for D3 $S_{D3} = \frac{3h_lw_{l1}^3}{4L_l^3}$ [264], explaining the dramatically enhanced influence of w_{l1} on the frequency f_{d-D3} of the D3 degeneracy when compared with f_{d-D1} . These findings show how the unique stiffness mechanisms for each of the four resonant modes in the multimodal design can be exploited to tune the Dirac frequencies (and thus topological bandgap frequencies) for D1, D2, D3, and D4 relative to each other. In selecting a proper w_{l1} , care must be taken to ensure that all four Dirac degeneracies remain below the dashed red line in Fig 4.2b, which indicates the lower

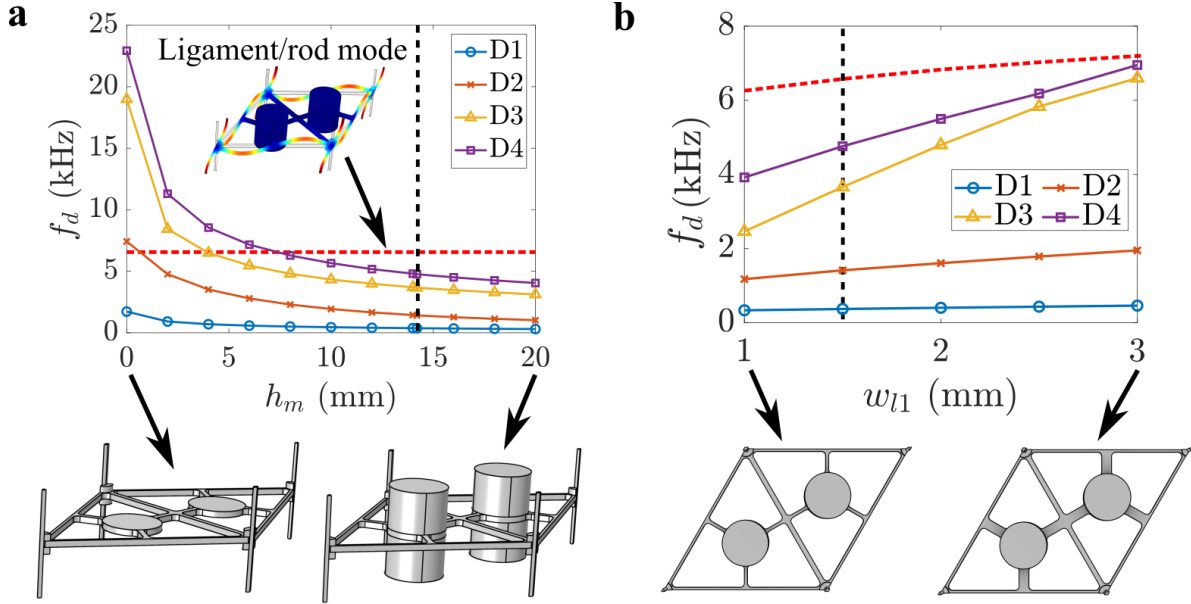


Fig 4.2. Parameter study illustrating the effect of the (a) mass height h_m and (b) spring ligament width w_{l1} on the Dirac nodal line frequency f_d , which is taken at the midpoint between K and H for each D1-D4 (f_{d-D1} , f_{d-D2} , f_{d-D3} , and f_{d-D4}). All presented values are for the Type 0 lattice configuration ($\alpha = 0$). The insets show the unit cell geometries for the minimum and maximum specified values of h_m and w_{l1} . The vertical dashed black lines indicate the specified h_m and w_{l1} for all presented results in this chapter. The dashed red lines indicate the minimum frequency of the ligament/rod modes.

frequency boundary of the ligament/rod modes. For the $w_{l1} = 1.5$ mm chosen in this study (indicated by the vertical dashed black line in Fig 4.2b), the Dirac degeneracies f_{d-D1} , f_{d-D2} , f_{d-D3} , and f_{d-D4} are well removed from the ligament/rod modes. Apart from establishing the design considerations of the proposed metamaterial, the results of the presented unit cell parameter studies illuminate how the multimodal resonance of the 3D metamaterial enables topological bandgaps at low frequencies that can be controlled without needing to alter the lattice constants a or h_o , a significant advantage for volume-constrained applications.

4.4 Supercell analysis for 2D topological states

To obtain 2D topological states, an eight-unit supercell is constructed that consists of four Type A unit cells connected to four Type B unit cells at a Type I interface (Fig 4.3a). Floquet periodic boundary conditions are applied along the $y-s$ and $z-s$ directions, while the left and right boundaries are left free. According to the bulk-boundary correspondence [86,91], 2D topological states with displacement localized at the interface (i.e., interface states) are expected to emerge within the topological bandgaps, since the Type A and Type B lattices are topologically distinct. The band structure for the supercell is calculated along the surface BZ projected onto the $k_{y-s} -$

k_{z-s} plane (Fig 4.3b,c). A localization parameter $\Lambda_i = \iiint_{V_{interface}} d^2 dV / \iiint_{V_S} d^2 dV$ (where $V_{interface}$ is the volume of the two unit cells at the interface and V_S is the total volume of the supercell) is defined to measure the confinement of the total displacement $d = \sqrt{|u|^2 + |v|^2 + |w|^2}$ at the interface for each eigenmode. Thus, interface modes have $\Lambda_i \approx 1$ (represented by the red bands in the band structure) and bulk modes have $\Lambda_i \approx 0$ (represented by the black bands in the band structure). As shown in Fig 4.3c, topological interface states emerge within the D2, D3, and D4 partial bandgaps, satisfying the bulk-boundary correspondence. Representative mode shapes for each topological interface state are shown at the bottom of Fig 4.3c, illustrating hybrid torsional (found over a frequency range of 1.3 to 1.5 kHz), in-plane torsional (3.6 to 3.8 kHz), and in-plane translational (4.4 to 5.4 kHz) modes with displacement fields that match the unit cell resonant modes for D2, D3, and D4 displayed in Fig 4.1e. Similarly, a supercell is constructed from eight Type B unit cells, and the resulting band structure is shown in Fig 4.3d. The band structure for the Type B supercell is nearly identical to that of the supercell with the Type I interface. A localization parameter $\Lambda_b = \iiint_{V_{boundary}} d^2 dV / \iiint_{V_S} d^2 dV$ (where $V_{boundary}$ is the volume of the unit cells at the two supercell boundaries) is defined to measure the modal displacement contained at the boundaries of the Type B supercell. Hybrid torsional, in-plane torsional, and in-plane translational topological states are uncovered with displacements that are trapped at the left boundary of the supercell ($\Lambda_b \approx 1$, Fig 4.3d). Similar observations of topological boundary states that emerge due to a topological transition at the boundary of a lattice are reported in several previous works and predicted by the bulk-boundary correspondence [86,91,133,167,173,235,236]. These topological boundary states emerge within the D2, D3, and D4 topological bandgaps and align with the frequency ranges for the interface states reported in Fig 4.3c. The findings gleaned from this supercell analysis reveal that the multimodal resonance of the proposed metamaterial facilitates the achievement of multiband topological interface and surface states.

Further inspection of the band structures in Fig 4.3c,d reveals that there are bulk modes that cross through the gray D2, D3, and D4 partial bandgaps. While care must be taken to excite the D3 topological interface state without activating the coexisting bulk modes (e.g., by specifically exciting the structure at the location of maximum displacement amplitude for the D3 topological state, see Section 4.5), the bulk modes that cross through the D2 and D4 partial bandgaps near $\tilde{\Gamma}$

contain polarizations that preclude unwanted interactions with the topological states (see more details in Appendix C.6). Another important feature of the supercell band structure is the sharp notch (with a steep slope) that is observed in the hybrid torsional (1.3 to 1.5 kHz) topological states for the $-\tilde{Z} - \tilde{\Gamma}$ and $\tilde{\Gamma} - \tilde{Z}$ directions. Since this steep slope (i.e., large group velocity) occurs near $\tilde{\Gamma}$ and the band is flat for the rest of the $-\tilde{Z} - \tilde{\Gamma} - \tilde{Z}$ wavenumber region, this indicates that the interconnecting rods undergo quasi-rigid body (or very long wavelength) motion that transmits wave energy along the z direction (see Appendix Figure C.18). In contrast, the two in-plane topological states are flat (i.e., zero group velocity) and/or gapped for the entire $-\tilde{Z} - \tilde{\Gamma} - \tilde{Z}$

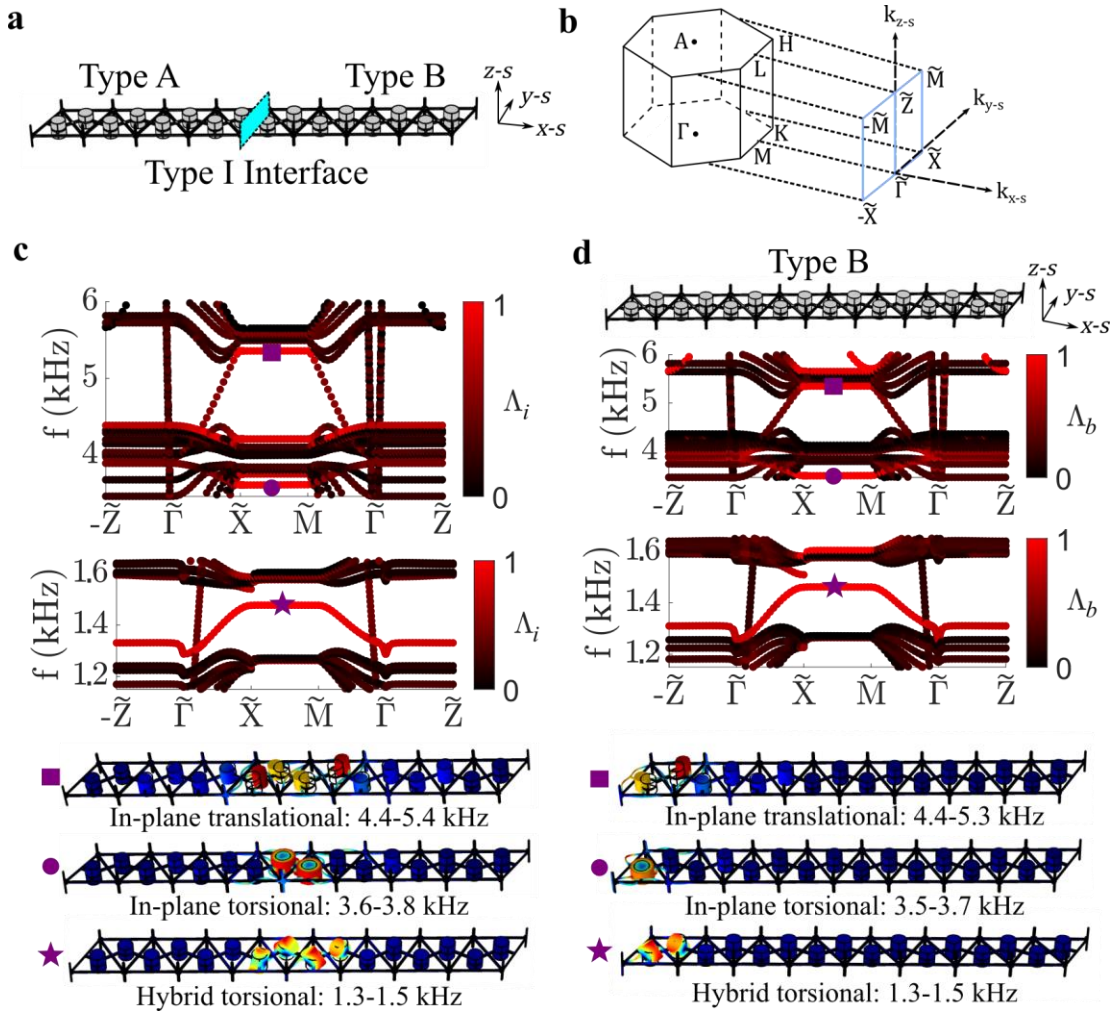


Fig 4.3. (a) Schematic of an eight-unit supercell with a Type I interface indicated by the blue planar surface. (b) The reciprocal space, with one-half of the surface BZ projected onto the $k_{y-s} - k_{z-s}$ plane outlined in light blue. (c) The band diagram for the supercell presented in (a). The red bands ($\Lambda_i \approx 1$) are interface modes and the black bands ($\Lambda_i \approx 0$) are bulk modes. Representative mode shapes for the hybrid torsional (purple star), in-plane torsional (purple circle), and in-plane translational (purple square) topological interface states are shown at the bottom. (d) The schematic and band diagram for a supercell comprised of eight Type B unit cells. The red bands ($\Lambda_b \approx 1$) are boundary modes and the black bands ($\Lambda_b \approx 0$) are bulk modes. Representative mode shapes for the topological boundary states are shown at the bottom.

wavenumber region, and thus do not transmit wave energy along z . As is shown and discussed in Appendix C.6, this dichotomy in z direction transport behavior occurs because the hybrid torsional modes couple with the motion of the interconnecting rods, while the in-plane torsional and in-plane translational resonant modes do not. This distinction in z direction response for the three different topological states opens the door to polarization- and layer-dependent wave control functionality in full-scale 3D structures.

4.5 Topological waveguides in full-scale 3D metastructures

Full-scale FE simulations are conducted to investigate the elastic wave control capabilities of the metamaterial in finite 3D metastructures (a metastructure is defined in this chapter as a mechanical structure with finite boundary conditions that is created from the metamaterial). A 3D metastructure is constructed from an $8 \times 8 \times 6$ tessellation of the metamaterial unit cell (Fig 4.4a). The four corners at the base of the metastructure are fixed and all other boundaries are left free. Two different elastic waveguides are created in the metastructure by specifying the distribution of Type A and Type B unit cells. The V-shaped waveguide (blue shading in the middle schematic in Fig 4.4a) is created from the topological boundary states, while the Z-shaped waveguide (blue shading in the right schematic in Fig 4.4a) is generated by connecting the topological boundary and interface states in series. A harmonic excitation is placed on all six metastructure layers (L1-L6) at one end of the waveguide. The excitation polarization and frequency are selected to activate each of the three unique topological states: out-of-plane at 1.3 kHz for the hybrid torsional state, in-plane at 3.6 kHz for the in-plane torsional state, and in-plane at 4.9 kHz for the in-plane translational state. The resulting steady-state displacement fields (Fig 4.4b) reveal a dynamic vibration response that follows the designated 2D waveguides and is polarized according to the corresponding topological state ($\Pi=0.6$ for the hybrid torsional waveguides and $\Pi \approx 0$ for the in-plane waveguides). The degree of waveguide localization, as quantified by $\Lambda = \frac{\iiint_{V_{waveguide}} d dV}{\iiint_{V_{all}} d dV}$ (where $V_{waveguide}$ is the volume of the waveguide region, as defined by the unit cells adjacent to the specified waveguide route, and V_{all} is the volume of the entire 3D metastructure) varies for the three different topological states. At the given frequencies, the hybrid torsional waveguides both have $\Lambda = 0.7$, the in-plane torsional waveguides both have $\Lambda = 0.6$, and the in-plane translational waveguides have $\Lambda = 0.4$ and $\Lambda = 0.5$. These topological waveguides exhibit unconventional polarization- and frequency-dependent behaviors. For

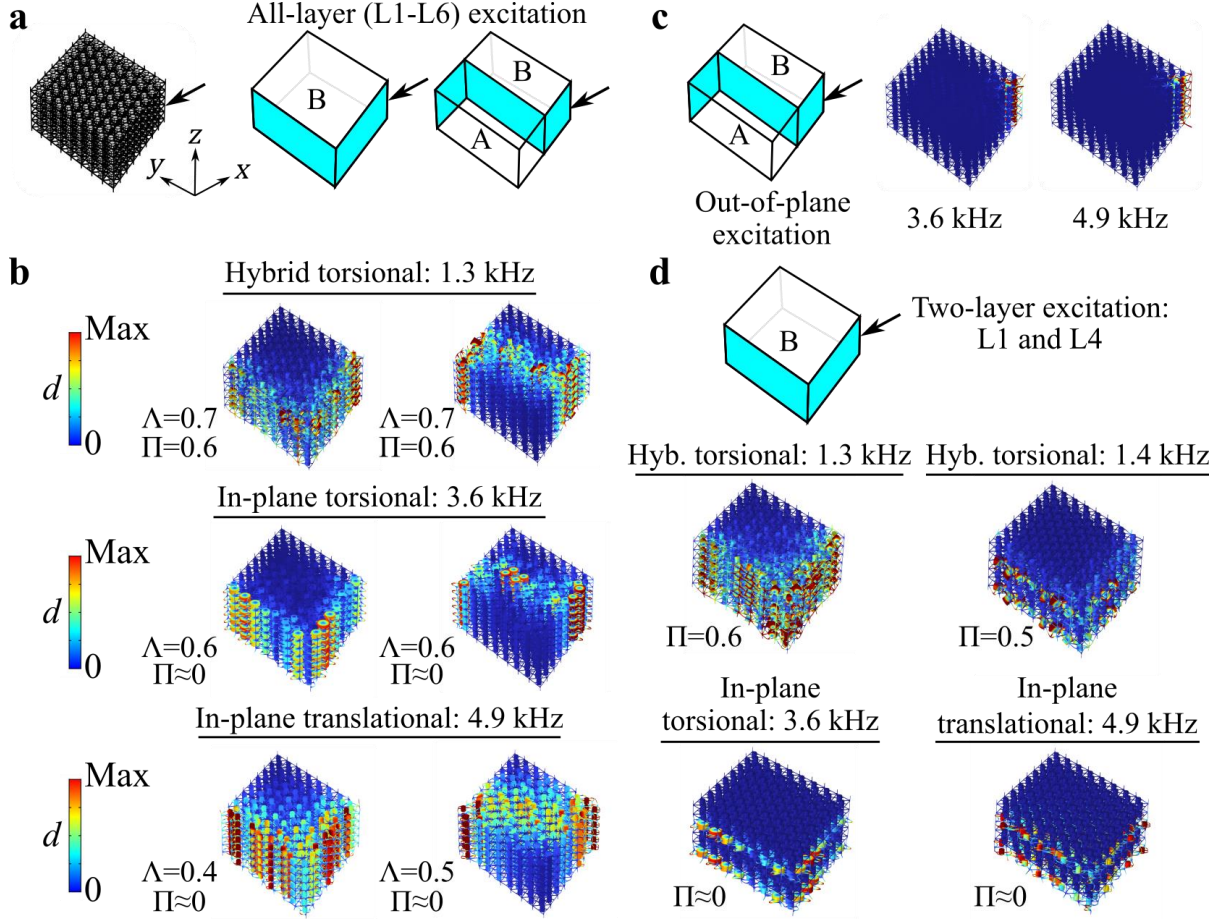


Fig 4.4. (a) Schematic of a full-scale 3D metastructure constructed from an 8x8x6 pattern of the metamaterial unit cell (left) and illustrations of V-shaped (middle) and Z-shaped (right) waveguides. The distribution of Type A and Type B unit cells is denoted by the letters “A” and “B.” (b) Steady-state displacement fields illustrating waveguides for all-layer (L1-L6) input excitations of 1.3 kHz (hybrid torsional), 3.6 kHz (in-plane torsional), and 4.9 kHz (in-plane translational). (c) Wave attenuation when an out-of-plane excitation is used in the frequency ranges of the in-plane topological states. (d) Steady-state displacement fields illustrating layer-locked waveguiding for two-layer (L1 and L4) input excitations of 1.4 kHz (hybrid torsional), 3.6 kHz (in-plane torsional), and 4.9 kHz (in-plane translational). For a two-layer input of 1.3 kHz, the hybrid torsional state exhibits wave transmission across all six layers.

example, if an out-of-plane excitation is applied in the frequency range for an in-plane topological state, the wave is attenuated by the topological bandgap and will not propagate beyond the input location (Fig 4.4c). Moreover, if the input excitation is provided on layers 1 and 4 (L1 and L4) of the metastructure, the in-plane topological states display layer-locked wave propagation (Fig 4.4d). The dynamic response is locked to L1 and L4 and there is no transfer of wave energy along the z direction, which aligns with the supercell band structure for these two topological states. In the case of the hybrid torsional state, the waves propagate along all six layers for a two-layer input with a frequency of 1.3 kHz and undergo layer-locked transport if the two-layer input frequency is increased to 1.4 kHz (Fig 4.4d). This frequency-selective behavior is explained by examining

the supercell band structure, which predicts that the waves will propagate in the z direction for 1.28 to 1.33 kHz and exhibit more layer-locked behavior from 1.33 to 1.46 kHz due to the shape of the band over $-\tilde{Z} - \tilde{\Gamma} - \tilde{Z}$ (Fig 4.3c,d, see more detail in Appendix C.6). These results illuminate how the multimodal topological states of the 3D metamaterial can be harnessed for polarization-, frequency-, and layer-dependent wave control in finite 3D metastructures. As shown in Appendix C.7, this multimodal mechanism can also be exploited in a 2D TM, underscoring the generalizability of the proposed concept.

4.6 Experimental realization

An experimental investigation is undertaken to validate the theoretical predictions and implement the proposed 3D metamaterial in a practical setting. The experimental testbed is a 3D metastructure made up of a 4x4x4 tessellation of the Type B metamaterial unit cell (Fig 4.5a, see Appendix C.8 for a detailed description of the fabrication and experimental testing). A supercell analysis (for a four-unit supercell) reveals a topological boundary state with a hybrid torsional polarization that emerges in the frequency range of 1.3 to 1.5 kHz (Fig 4.5b). This boundary state is employed to design a V-shaped waveguide in the 3D metastructure, as indicated by the blue shading in the schematic located in the top right corner of Fig 4.5c. A periodic chirp vibration input with a bandwidth of 0 to 5 kHz is provided at the middle two layers (L2 and L3) of the metastructure where indicated in Fig 4.5c. The excitation is provided by a piezoelectric (lead zirconate titanate, or PZT) actuator pair that provides a harmonic bending displacement in the z direction. A scanning laser Doppler vibrometer (SLDV, Polytec PSV-500) is used to acquire non-contact measurements for the out-of-plane velocity magnitude $v_{op} = |\dot{w}|$, which only requires the use of a single laser. The measurements are obtained for all four layers L1-L4 of the metastructure by guiding the laser in between the gaps in the layers closest to the vibrometer head. An out-of-plane velocity v_{op} field taken at $f_{m1} = 1.3$ kHz illustrates the successful confinement of the dynamic response within the designated 2D waveguide and closely aligns with FE simulations (Fig 4.5c). The frequency response is gathered for a point inside the waveguide (Point A in Fig 4.5c) and a point outside the waveguide (Point B in Fig 4.5c) on each of the four layers. The frequency response displayed in Fig 4.5d reveals that there is a wide frequency range (indicated by gray shading, from 1.26 kHz to 1.47 kHz) where the out-of-plane velocity v_{op} taken at the point inside the waveguide (Point A, results represented by solid lines) is significantly higher than the

velocity at the point outside the waveguide (Point B, results represented by dashed lines) for all four layers (see Appendix C.9 for additional frequency response data). Observation of multiple velocity fields for L4, which are shown in Fig 4.5e, confirm that the desired waveguiding behavior is occurring across the frequency range identified in Fig 4.5d. These results represent a clear advancement, in that this is the first time that full-field dynamic response information illustrating

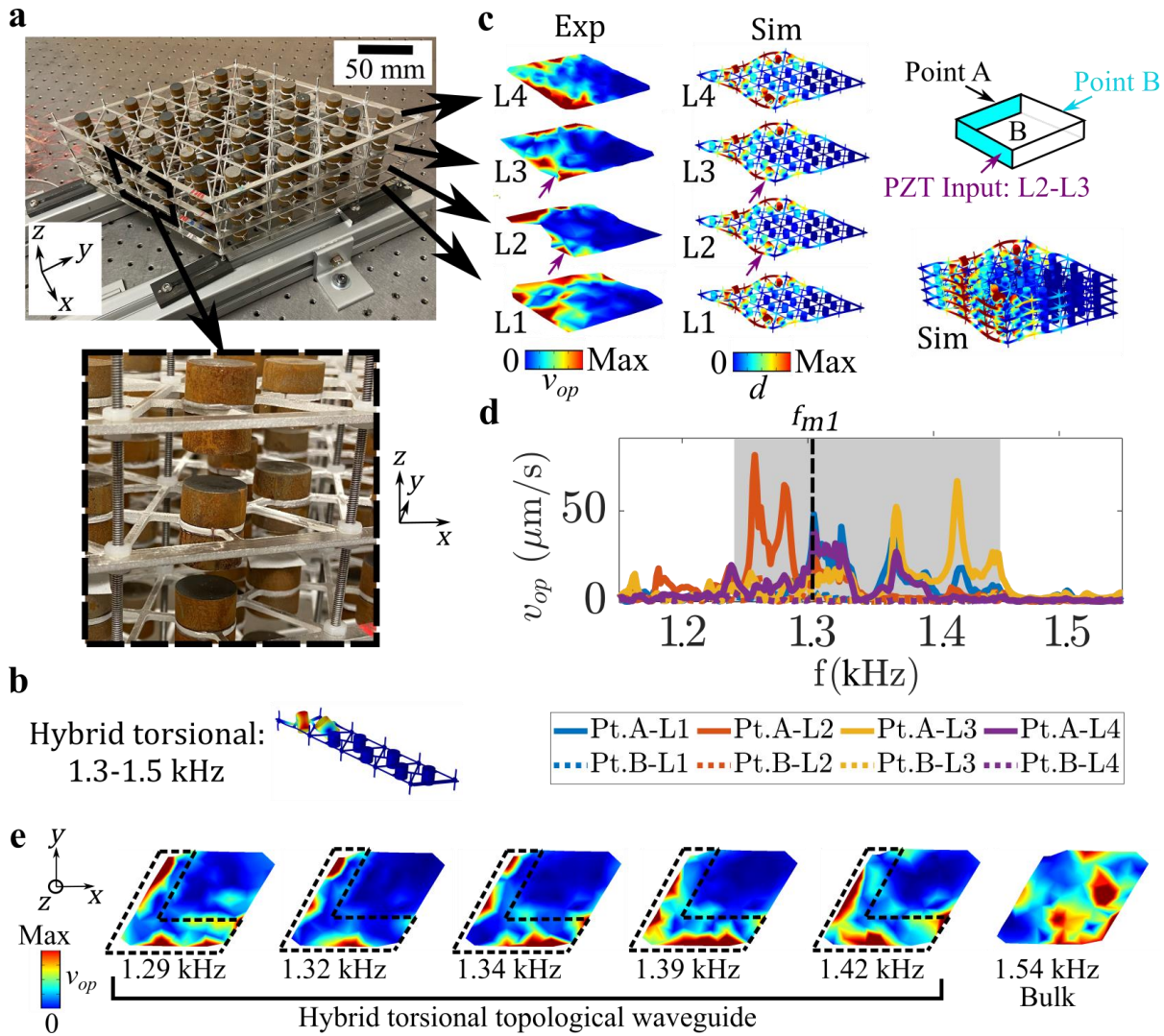


Fig 4.5. (a) The experimental testbed with an inset showing detail for a unit cell. (b) A topological boundary state with hybrid torsional polarization that is found in the band structure of a four-unit supercell. (c) Experimentally measured out-of-plane velocity field (left) and FE simulated displacement field (right) for the 3D metastructure obtained at $f_{m1} = 1.3$ kHz. For clarity, both the full-scale and layer views of the simulated displacement field are shown. The schematic of the 3D metastructure testbed is given in the top right, where the blue shading represents the V-shaped waveguide. (d) The experimentally measured out-of-plane velocity (v_{op}) for Point A (solid lines) and Point B (dashed lines) on each of the four layers. The frequency range for effective waveguiding is marked by the gray shading. (e) Experimentally measured out-of-plane velocity fields for L4 that illustrate the topological waveguide across a wide frequency range. A bulk response is demonstrated at 1.54 kHz.

a 2D topological waveguide has been experimentally acquired for vibrations in a 3D mechanical structure.

The in-plane torsional and in-plane translational topological states are also experimentally characterized in the 3D metastructure. An in-plane torsional state (shown at the bottom of Fig 4.6a) is used to construct a waveguide that follows the two planar boundaries identified by the red shading in Fig 4.6a. A piezo-stack actuator is utilized to apply an in-plane periodic chirp (with a bandwidth of 0 to 10 kHz) excitation to L4 of the structure. The in-plane velocity components \dot{u} and \dot{v} are measured using a 3D SLDV (Polytec PSV QTec 3D) and the total in-plane velocity magnitude is calculated as $v_{ip} = \sqrt{|\dot{u}|^2 + |\dot{v}|^2}$. The in-plane measurements require the use of three lasers, and thus the only surface accessible for measurement is L4, the layer closest to the 3D SLDV head. The velocity field measured at $f_{m2} = 3.7$ kHz shows that the dynamic response follows the waveguide created by the in-plane torsional state and matches FE simulations (Fig 4.6b). The frequency response measured for a point inside the waveguide and a point outside the waveguide (see the schematic in Fig 4.6a) reveals that waveguiding behavior occurs over the frequency range of 3.5 to 3.8 kHz (Fig 4.6c), which is enclosed within the bandwidth (3.5 to 3.7 kHz) of the in-plane torsional state. The same experimental approach is followed for the in-plane translational topological state. A waveguide is constructed to follow the blue surfaces in Fig 4.6d and experimental measurements illustrate waveguiding at $f_{m3} = 4.4$ kHz (Fig 4.6e). Results displayed in Fig 4.6f indicate that the wave field follows the prescribed path over a frequency range of 4.3 to 4.9 kHz, which overlaps with the bandwidth (4.4 to 5.3 kHz) of the in-plane translational state reported in Fig 4.6d. To complement the frequency response calculations, the in-plane velocity fields for multiple different frequencies are displayed in Fig 4.6g, illustrating in-plane waveguiding behavior across the bandwidths identified in Fig 4.6c,f. The experimental velocity fields for the in-plane waveguides shown in Fig 4.6b,e,g reveal less localized dynamic response (the majority of the response in these cases is confined within two unit cells of the boundary, as indicated by the dashed lines in Fig 4.6g) than the hybrid torsional waveguide reported in Fig 4.5c,e (the majority of the response in the hybrid torsional case is confined within one unit cell of the boundary, as indicated by the dashed lines in Fig 4.5e). This relatively reduced confinement is a consequence of the in-plane topological states being less localized than the hybrid torsional state, as can be seen by comparing the mode shapes of the three topological states in Fig 4.5b, Fig 4.6a, and Fig 4.6d. Furthermore, these differences are in agreement with the FE

simulations presented in Fig 4.4b, where the hybrid torsional state enables better waveguiding performance ($\Lambda=0.7$) than the two in-plane topological states ($\Lambda = 0.4-0.6$). Despite this comparatively lower localization, the results displayed in Fig 4.6 do illustrate the experimental realization of in-plane polarized elastic wave control that follows waveguides constructed in the 3D metastructure. Altogether, the outcomes from this experimental study advance beyond the previous research on 3D TMs, which has overwhelmingly concentrated on the theoretical

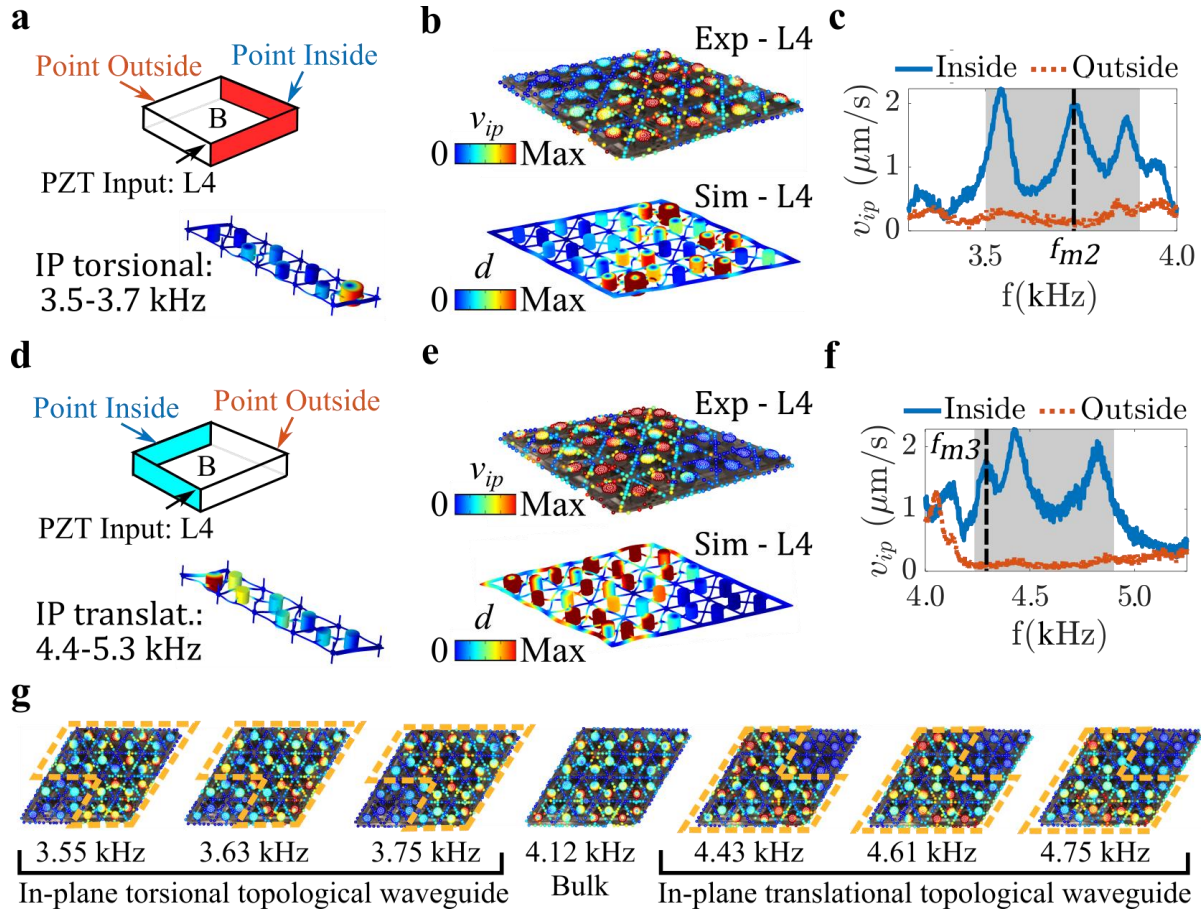


Fig 4.6. (a) (top) A schematic of the 3D metastructure testbed where the red shading represents the path of a V-shaped waveguide. (bottom) A topological boundary state with an in-plane torsional polarization that is found in the band structure of a four-unit supercell. (b) Experimentally measured in-plane velocity field and FE simulated displacement field for L4 of the 3D metastructure obtained at $f_{m2} = 3.7$ kHz. (c) The experimentally measured in-plane velocity (v_{ip}) for a Point Inside and a Point Outside the waveguide on L4. The frequency range for effective waveguiding is marked by the gray shading. (d) (top) A schematic of the 3D metastructure testbed where the blue shading represents the path of a V-shaped waveguide. (bottom) A topological boundary state with an in-plane translational polarization that is found in the band structure of a four-unit supercell. (e) Experimentally measured in-plane velocity field and FE simulated displacement field for L4 of the 3D metastructure obtained at $f_{m3} = 4.4$ kHz. (f) The experimentally measured in-plane velocity (v_{ip}) for a Point Inside and a Point Outside the waveguide on L4. The frequency range for effective waveguiding is marked by the gray shading. See Appendix C.9 for the transmission ratio plots that accompany (c) and (f). (g) Experimentally measured in-plane velocity fields for L4 that illustrate the in-plane topological waveguides across a wide frequency range. A bulk response is demonstrated at 4.12 kHz.

investigation of a single topological state [26,75,131,184,187,188,253], to attain experimental wave fields of topological waveguides with multiple (i.e., three: hybrid torsional, in-plane torsional, and in-plane translational) distinct polarizations and frequency bandwidths.

4.7 Conclusions and discussion

The research presented in this chapter advances the state of the art through the creation of a 3D TM that exploits multimodal local resonance to enable low-frequency and multiband elastic wave manipulation. A band structure analysis reveals four topological states that emerge in distinct frequency regions that are associated with out-of-plane translational, hybrid torsional, in-plane torsional, and in-plane translational resonances. A parameter study is used to develop a deeper understanding of the connection between the frequency range for each topological state and the fundamental characteristics of the respective resonant modes (i.e., the mass and stiffness for each mode). This parametric analysis illuminates how the topological states can be attained over a broad bandwidth and at low frequencies (e.g., all below 6 kHz) by adjusting the mass and stiffness properties of the local resonators, without needing to increase the metamaterial volume. Finite element simulations of full-scale 3D metastructures uncover how the topological states can be employed to achieve 2D planar and layer-locked waveguides with complex frequency- and polarization-dependent behaviors. To complement the theoretical findings, experiments are conducted to validate the numerical predictions and establish a benchmark for the experimental investigation of topological phenomena in 3D mechanical structures. The experimental advancements reported in this chapter include the attainment of complete wave fields that unequivocally illustrate 2D topological waveguides and the measurement of multi-polarized wave control in a 3D structure. These outcomes may inspire future experimental research on wave control and topological physics in 3D mechanical systems. In contrast to 3D topological photonic metamaterials [100], which generally operate in the microwave frequency regime, the 3D TM described in this chapter is constructed from traditional load-bearing materials and can operate at frequencies (<10 kHz) that are relevant to structural applications. The multifaceted capabilities of the proposed 3D metamaterial could help to improve performance in engineering applications that involve low-frequency and multiband elastic wave control, such as vibration energy harvesters and mitigation systems [104–108,213,214]. Moreover, the rich 3D, multiband, frequency-dependent, and polarization-dependent features of the metamaterial could be utilized to construct information-

dense phononic circuitry (i.e., elastic wave-based, with information-density derived from the three distinct elastic wave polarizations: two quasi-shear and one quasi-longitudinal) for mechanical computers, wave filters, and on-chip devices [50,109–112,114]. For example, the proposed metamaterial may be used as the building block of 3D phononic circuits with multiple working channels that route waves in a layer-dependent fashion based on the polarization and frequency of external inputs. In order to harness the full potential of the proposed metamaterial in practical applications, future endeavors may entail two primary aspects: a design optimization aimed at achieving complete topological bandgaps and enhancing wave localization in the waveguides, and an exploration of advanced manufacturing methods (e.g., multi-material 3D printing [265]) to facilitate efficient production and testing of geometries featuring complex 3D waveguide paths.

Note: The reused content (text, figures, and tables) in Chapter 4 and Appendix C is reproduced from [266] under the [CC BY 4.0](https://creativecommons.org/licenses/by/4.0/) license.

Chapter 5. 2D Higher-Order Locally Resonant Metamaterial

A novel methodology is synthesized in Chapter 4 that utilizes multimodal resonance to attain multifunctional elastic wave control capabilities spanning multiple frequency bands. As the insights gleaned in Chapter 4 are obtained through the study of the first-order TM, a compelling next step entails the harnessing of multimodal resonance in a HOTM. In Chapter 5, we explore this opportunity and advance the state of the art by creating a novel 2D HOTM that exploits higher-order topological phases and multimodal resonance to obtain multiband 0D corner states. The 2D HOTM is a thin plate with embedded resonators that are geometrically configured to enable bending and torsional resonances in low-frequency regimes. The distance between the resonant masses is modulated to obtain higher-order topological physics by emulating the 2D SSH model. Dispersion analyses for the 2D HOTM expose four distinct topological bandgaps that materialize due to the multi-resonant nature of the metamaterial and facilitate the formation of four gapped 1D edge states. An eigenfrequency study illuminates in-gap 0D corner states that emerge concurrently with the gapped edge states in each of the topological bandgaps, and dynamic response simulations uncover efficient wave confinement across several frequency bands. Further analysis reveals that the multiband corner states contain a diverse set of localization, coupling, and symmetry traits. The intriguing characteristics of these multiband states are harnessed to create frequency-dependent wave-based logic elements and explore elastic wave control in fractal TMs for the first time. The research findings presented in this chapter illuminate the potential of higher-order mechanical structures for information processing and fractal topological physics. Furthermore, the outcomes illustrate how the novel 2D HOTM is a promising platform for elastic wave trapping, harvesting, and sensing in practical applications.

5.1 Introduction

The 2D HOTMs studied thus far (see Section 1.2.2) enable the manipulation of elastic waves through coexisting gapped 1D edge states and in-gap 0D corner states, surpassing the capabilities of their first-order TM predecessors. Nevertheless, the previously studied 2D HOTMs are predominantly limited to operating in a single frequency band (i.e., one specific mode of

operation), a drawback that curtails their working bandwidth, information-carrying capacity, and suitability for many practical applications. To address this research gap and advance the state of the art, this research proposes a novel 2D HOTM that harnesses multimodal local resonance and higher-order topological phases to achieve 0D corner states across multiple frequency bands. The proposed 2D HOTM is a thin plate with periodically embedded spring-mass resonators that are designed to facilitate bending and torsional resonances in separate frequency ranges. To obtain 0D corner states, the resonators are arranged into a C_4 -symmetric lattice, and the coupling between them is modulated to emulate the 2D SSH model. Band structure and eigenfrequency studies uncover coexisting in-gap 0D corner states and gapped 1D edge states that emerge in four different topological bandgaps. A further examination reveals unique localization, coupling, and symmetry characteristics for each topological state and illuminates how they can be tailored through lattice reconfiguration. Frequency response simulations illustrate how elastic waves can be highly confined by the topological states when the 2D HOTM is subjected to dynamic excitations. The diverse attributes of the higher-order corner states in this HOTM platform are then exploited to achieve enhanced wave-based information processing and explore nontrivial topology in fractal mechanical lattices for the first time. The findings discussed in this chapter illuminate several elastic wave manipulation capabilities of the proposed 2D HOTM that would be beneficial in wave control applications. Moreover, these outcomes illustrate the promise of HOTMs for elastic wave-based information processing and open the door to future research on higher-order topological phases in fractal EMs.

5.2 2D higher-order topological metamaterial description

The 2D HOTM is comprised of an aluminum ($E_p = 70$ GPa, $\rho_p = 2700$ kg·m⁻³, $\nu_p = 0.33$) thin plate of thickness $h_p = 2.0$ mm that has surface-mounted steel ($E_m = 200$ GPa, $\rho_m = 7850$ kg·m⁻³, $\nu_m = 0.30$) masses. A schematic of the 2D HOTM is shown in Fig 5.1a, where the aluminum plate is light gray and the steel masses are dark gray. Incomplete right triangles are cut into the aluminum substrate to create right triangular platforms of side length $s_m = 17.1$ mm, spring ligaments of width $w_l = 2.5$ mm, and connector ligaments of with $w_c = 5.0$ mm. A resonator site is defined as being contained within a square inclusion of side length $s_h = 23.0$ mm, where the triangular platforms act as the resonator mass and the ligaments act as the resonator stiffness (see the detail view of one resonator site in Fig 5.1a). There are two platforms in one resonator site, linked by the

connector ligaments and separated by a relief distance $w_r = 5.0$ mm. The steel masses, which are right triangular prisms of side length $s_m = 17.1$ mm and height $h_m = 10$ mm, are affixed on both sides of the substrate's triangular platforms to add extra mass. The 2D HOTM lattice is defined by the basis vectors $\vec{a}_1 = a\hat{x}$ and $\vec{a}_2 = a\hat{y}$, where $a = 100$ mm is the lattice constant for the unit cell

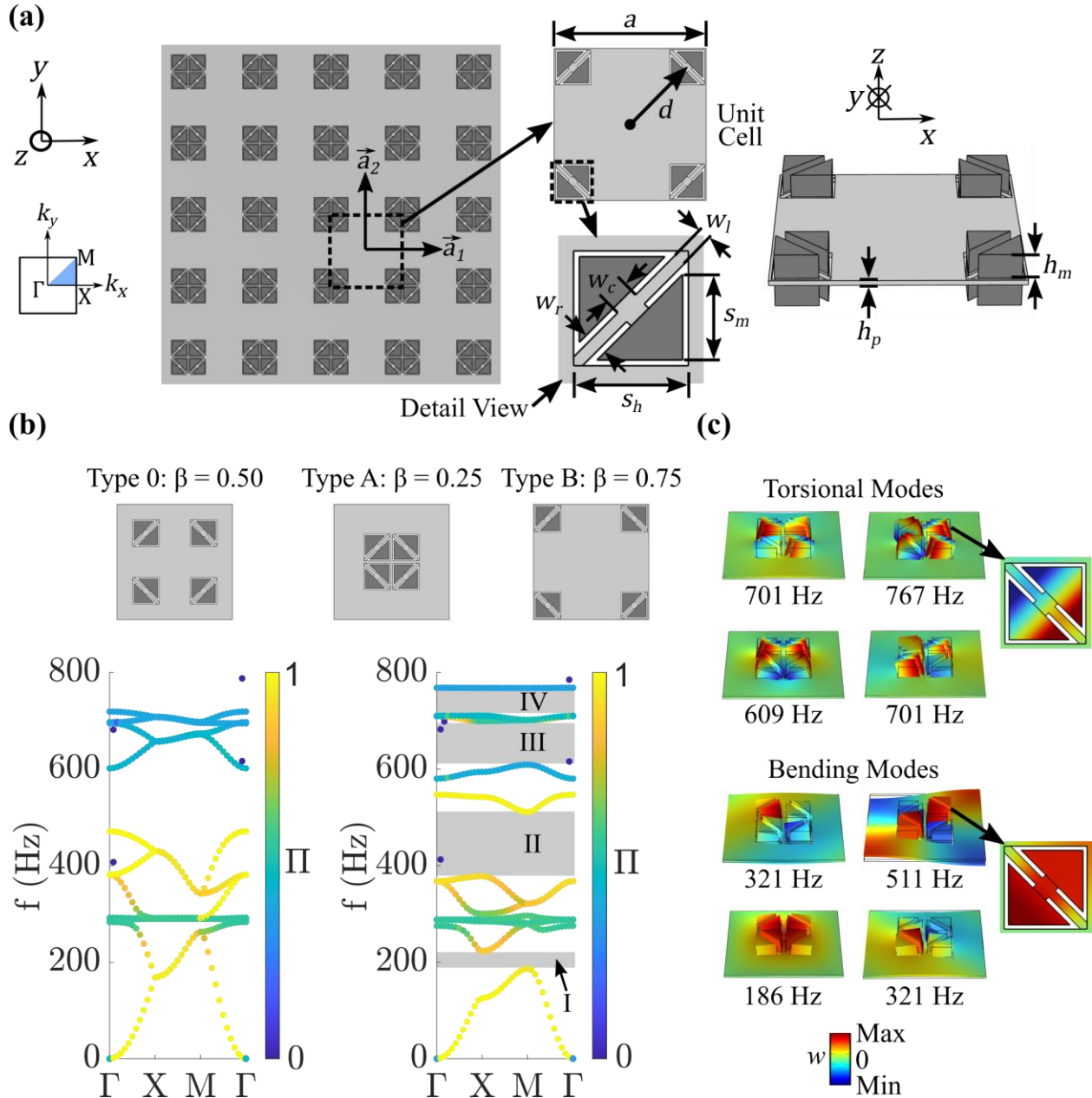


Fig 5.1. Description of the 2D HOTM and unit cell analysis. (a) Schematic of the 2D HOTM in a Type B lattice configuration, including a detail view of one resonator site. The aluminum substrate is light gray and the steel masses are dark gray. (b) Schematics and band structures for Type 0 and Type A/B lattices. The colormap indicates the mode polarization per the parameter Π . The four topological bandgaps are marked with gray shading and labeled I, II, III, and IV. (c) The mode shapes taken at M for the bands bordering the four topological bandgaps, illustrating the bending and torsional resonances. The out-of-plane displacement (w) fields are presented.

(top and isometric views of the unit cell are given on the right side of Fig 5.1a). There are four resonator sites in the unit cell, each defined to be a distance $d = \beta \frac{a}{\sqrt{2}}$ along a 45° angle from the unit cell center, where β is a spatial parameter used to define the location of the resonators. The resonator sites are geometrically designed, oriented, and patterned into a lattice arrangement that enforces C_4 symmetry to achieve C_n -protected corner modes by emulating the 2D SSH model [267–269]. Moreover, the resonator design enables bending (about the long spring ligaments of width w_l) and torsional (about the short connector ligaments of width w_c) resonances that couple with the flexural vibrations of the host plate. This multimodal resonance is prescribed to unlock multiband functionality in the 2D HOTM.

5.3 Unit cell band structure and multimodal resonance effect

A unit cell analysis is conducted to investigate the wave dispersion characteristics of the 2D HOTM. The 2D HOTM is defined as having a Type 0 lattice configuration for $\beta = 0.5$ and $d = \frac{a}{2\sqrt{2}}$, where the resonators are located at the center of the four quadrants of the unit cell, as displayed on the left side in Fig 5.1b. The band structure for the Type 0 lattice is evaluated using the commercial FE solver COMSOL Multiphysics (see Appendix D.1 for a complete overview of the theoretical methods) and plotted in Fig 5.1b. A polarization parameter $\Pi = \frac{\iiint_{V_U} |w|^2 dV}{\iiint_{V_U} (|u|^2 + |v|^2 + |w|^2) dV}$ is measured for each band and represented by a colormap in the band structure, where V_U is the volume of the unit cell, and u , v , and w are the displacement components in the x , y , and z directions, respectively. For the Type 0 lattice, there are four separate two-fold line degeneracies along $X - M$ as a result of the C_4 symmetry, band folding, and equivalent inter- and intra-cell couplings between resonators (the couplings are determined by the inter- and intra-cell distances between neighboring resonators) [270]. These four degeneracies are split into two sets: a lower-frequency set of modes that are more out-of-plane (z direction) polarized (yellow, $f \approx 200$ and 400 Hz, and $\Pi = 0.85$ - 0.99 in Fig 5.1b) and a higher-frequency set with a hybrid polarization (light blue, $f \approx 665$ and 703 Hz, and $\Pi = 0.38$ - 0.46 in Fig 5.1b). All four degeneracies are located in a low-frequency (<1 kHz) regime.

To break the degeneracies in accordance with the 2D SSH model [206,270–272], the inter- and intra-cell couplings are mistuned by adjusting the resonator distance d so that the resonators are no longer equidistant from the center and outer corners of the unit cell. A Type A lattice is defined

as having $\beta < 0.5$ ($d < \frac{a}{2\sqrt{2}}$) and the intra-cell coupling is greater than the inter-cell coupling. In contrast, a Type B lattice has $\beta > 0.5$ ($d > \frac{a}{2\sqrt{2}}$) and a larger inter-cell coupling than intra-cell coupling (see schematics for Type A and Type B unit cells in Fig 5.1b). The band structure for a Type A lattice with $\beta = 0.25$ ($d = \frac{a}{4\sqrt{2}}$) is superimposed with the band structure for a Type B lattice with $\beta = 0.75$ ($d = \frac{3a}{4\sqrt{2}}$) and shown on the right side of Fig 5.1b (note that the two band structures are identical). The degeneracies are broken, and four bandgaps emerge from them that encompass the frequency ranges of $f_{\text{Gap I}} = 186 \text{ Hz to } 223 \text{ Hz}$, $f_{\text{Gap II}} = 377 \text{ Hz to } 511 \text{ Hz}$, $f_{\text{Gap III}} = 608 \text{ Hz to } 710 \text{ Hz}$, and $f_{\text{Gap IV}} = 710 \text{ Hz to } 768 \text{ Hz}$ (all bandgaps are shaded in gray in Fig 5.1b). It is worth noting that there are purely in-plane modes (blue dots for $\Pi \approx 0$ near Γ) that cross the bandgaps, but these modes do not couple with the out-of-plane and hybrid modes that are the focus of this investigation, and as will be shown in the proceeding sections, do not impede the attainment of higher-order topological states. The mode shapes are evaluated at the M point for each of the bands bordering the bandgaps, whose out-of-plane displacement (w) profiles give insight into the origin of the bandgaps [43,60,177] (Fig 5.1c). These mode shapes reveal multimodal behaviors for the resonators of the 2D HOTM, indicating that bandgaps I and II are opened due to bending resonances of the spring ligaments (w_l), while bandgaps III and IV are derived from torsional resonances, where the resonators exhibit a torsional motion centered on the connector ligaments (w_c). The band structure findings illuminate how the multimodal resonance of the proposed 2D HOTM unlocks multiple distinct bandgaps. As was done in Chapter 4, the frequencies of these bandgaps could be adjusted lower (i.e., into a deep subwavelength/low-frequency regime) by tuning the stiffness and mass characteristics of the multimodal resonators without increasing the lattice constant a (e.g., using the h_m , w_c , w_l parameters). Two additional line degeneracies appear at 289 and 291 Hz (see the green bands for Type 0, $\Pi = 0.55$ in Fig 5.1b) that are related to torsional modes centered on the spring ligaments (w_l). However, a bandgap is not opened from these degeneracies with the selected system parameters for Type A/Type B lattices, and they do not impact the formation of bandgaps I-IV. These extra bands are ignored for the forthcoming analysis, but do indicate the potential to exploit additional resonant modes in the 2D HOTM.

Despite having identical band structures, the Type A and Type B lattices of the 2D HOTM are topologically distinct. The higher-order topology of the 2D HOTM is C_n -symmetry ($n = 4$ in this case) protected and can be characterized by calculating the topological indices, bulk polarizations,

and corner charges (i.e., the relevant topological invariants) of the Type A and Type B lattices [88,196,269,272,273]. The topological index $\chi^{(4)}$ for a C_4 -symmetric HOTI is:

$$\chi^{(4)} = \left([X_1^{(2)}], [M_1^{(4)}], [M_2^{(4)}] \right) = \left(\#X_1^{(2)} - \#\Gamma_1^{(2)}, \#M_1^{(4)} - \#\Gamma_1^{(4)}, \#M_2^{(4)} - \#\Gamma_2^{(4)} \right) \quad (5.1)$$

where $\#\Pi_p^{(n)}$ ($\Pi = \Gamma, X, M$ denote the high-symmetry points in reciprocal space) is the number of

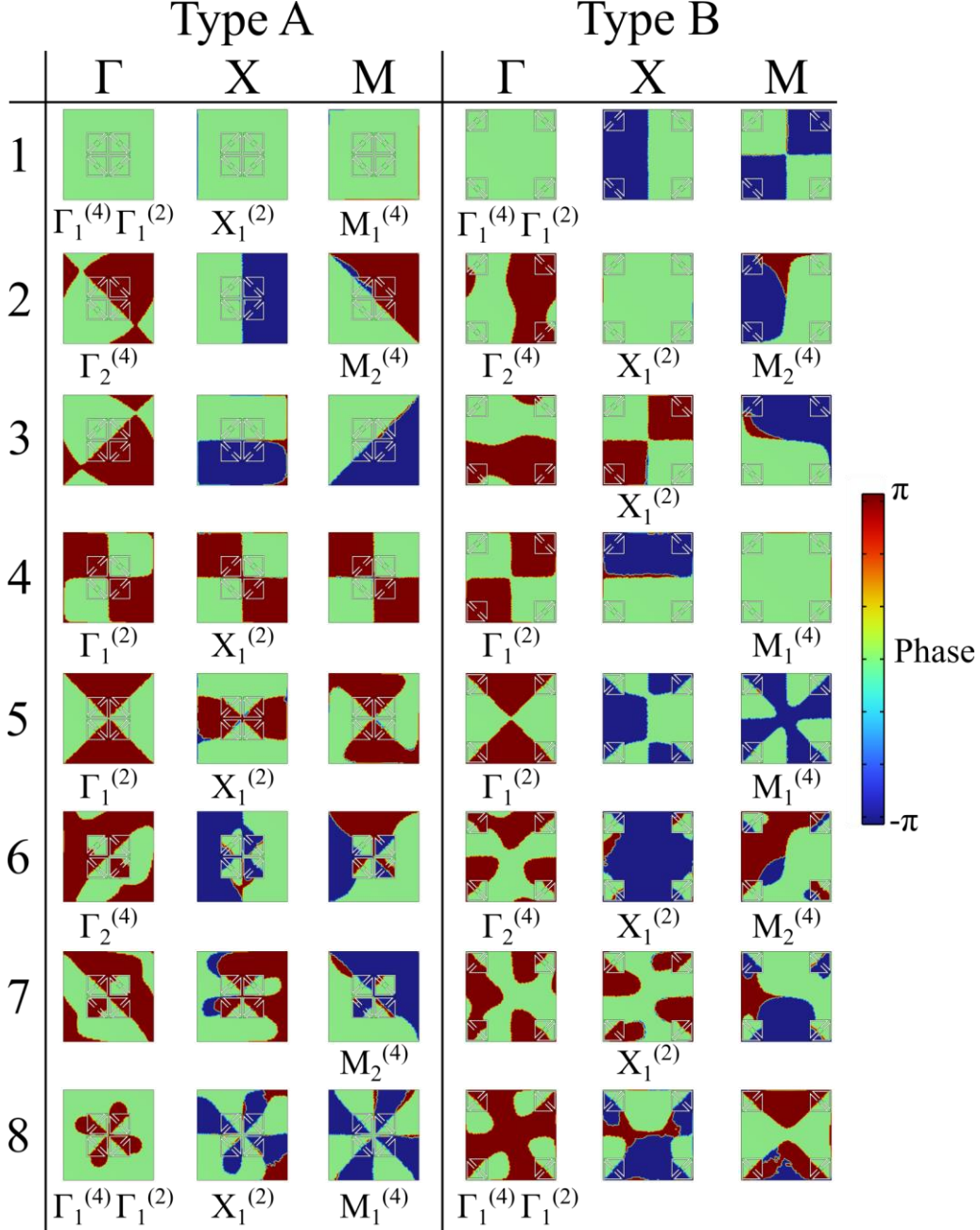


Fig 5.2. Phase profiles of the eigenmodes for bands 1-8, in order of lowest to highest frequency. Bands 1-4 are the lower-frequency bending modes and bands 5-8 are the higher-frequency torsional (about the connector ligaments) modes. The phase profiles are calculated at each of the high-symmetry points (Γ, X, M) for the Type A (left column) and Type B (right column) lattice configurations. The C_n rotation eigenvalues are labeled below each phase profile.

bands with C_n rotation eigenvalue $\Pi_p^{(n)} = e^{2\pi i(p-1)/n}$ ($p = 1, \dots, n$) below the bandgap under consideration [196,269,272,273]. If $\chi^{(4)}$ is zero (nonzero), the metamaterial domain is trivial (nontrivial). The bulk polarization can be defined as [196]:

$$P_x = P_y = \frac{1}{2} \left([X_1^{(2)}] \right) \text{ mod } 1 \quad (5.2)$$

Moreover, the fractional corner charge Q that characterizes the higher-order band topology in a $2\pi/n$ sector is quantified as [196]:

$$Q = \frac{1}{4} \left([X_1^{(2)}] + 2[M_1^{(4)}] + 3[M_2^{(4)}] \right) \text{ mod } 1 \quad (5.3)$$

Eqs. 5.1-5.3 are calculated for bandgaps I, II, III, and IV for both the Type A ($\beta = 0.25$) and Type B ($\beta = 0.75$) lattice configurations presented in Fig 5.1b (see Appendix D.2 for complete details on all topological invariant calculations). The phase profiles for the eigenmodes below the bandgaps in question are displayed in Fig 5.2, where bands 1-4 are the profiles for the lower-frequency bending eigenmodes and bands 5-8 are the profiles for the higher-frequency torsional (about the connector ligaments) eigenmodes. To solve Eqs. 5.1-5.3, the relevant C_n rotation eigenvalues are evaluated and labeled for each eigenmode in Fig 5.2. For the Type A lattice, the calculations for bandgaps I, II, III, and IV all yield the same result: $\chi^{(4)} = (0,0,0)$, $P_x = P_y = 0$, $Q = 0$, indicating that the bandgaps are topologically trivial. For the Type B lattice, the calculations for bandgap 1 are $\chi^{(4)} = (-1, -1, 0)$, $P_x = P_y = 1/2$, and $Q = 1/4$, with the nonzero values indicating that bandgap I for the Type B lattice is topologically nontrivial. Similarly, the results for bandgaps II, III, and IV in the Type B lattice are: $\chi^{(4)} = (1, -1, 0)$, $P_x = P_y = 1/2$, and $Q = 3/4$, $\chi^{(4)} = (-1, 1, 0)$, $P_x = P_y = 1/2$, and $Q = 1/4$, and $\chi^{(4)} = (1, 1, 0)$, $P_x = P_y = 1/2$, and $Q = 3/4$, respectively, illuminating how these bandgaps are also topologically nontrivial. These results suggest that the 2D HOTM successfully emulates the 2D SSH model, where lattices with greater inter-cell coupling are topologically nontrivial while those with greater intra-cell coupling are topologically trivial [88,268,274,275]. The topologically distinct nature of the Type A and Type B lattices indicates that a band inversion exists between them (see Appendix Figure D.24 and Appendix D.2 for further details on the band inversion). According to the higher-order band topology, coexisting gapped edge and in-gap corner states are expected to materialize at the interface of the topologically distinct Type A and Type B lattices [88,100].

5.4 Supercell analysis for multiband 1D topological states

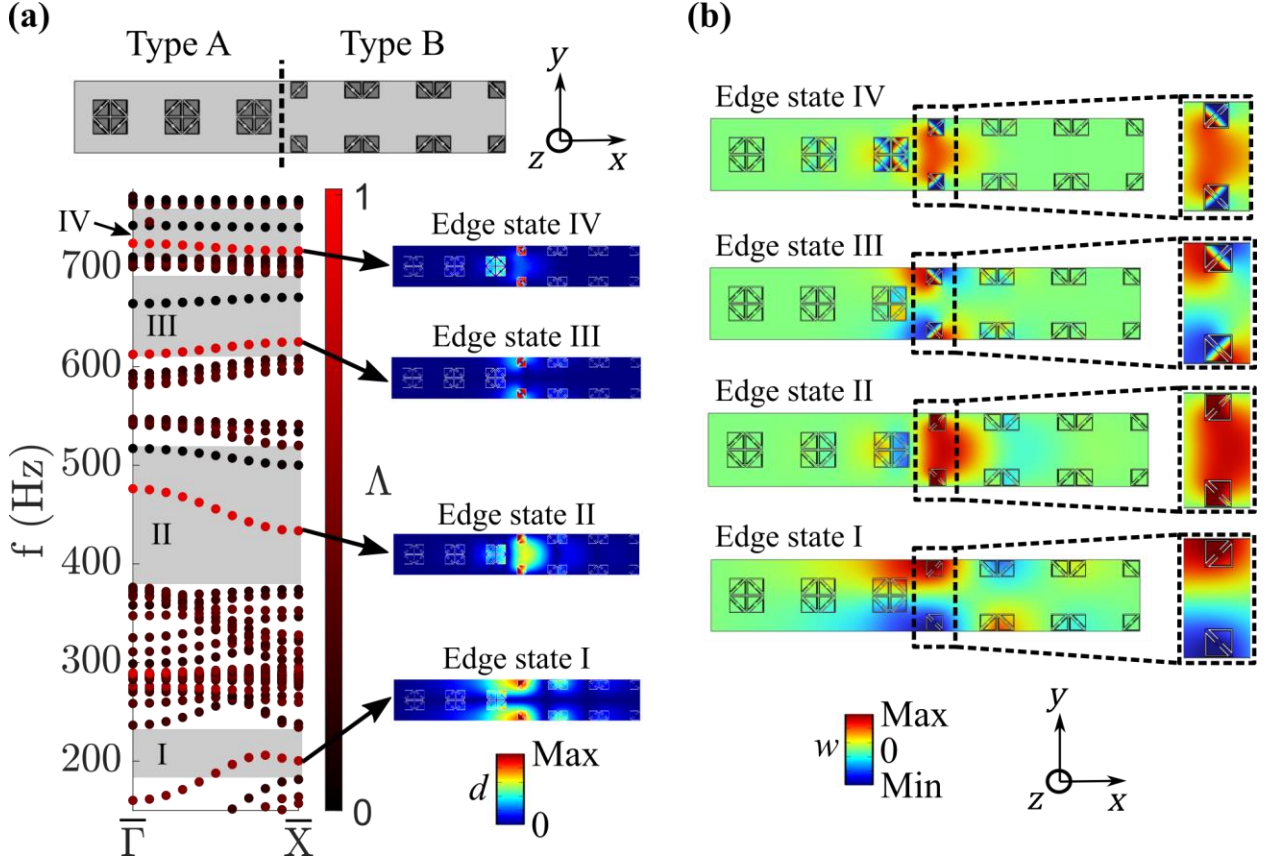


Fig 5.3. Supercell analysis for multiband edge states in the 2D HOTM. (a) A schematic of the supercell, where the interface between Type A and Type B sublattices is marked by the dashed black line. Below is the band structure, with the four topological bandgaps (I, II, III, and IV) uncovered in the unit cell analysis shaded in gray. Within the bandgaps, the red bands are topological edge states ($\Lambda \approx 1$) and the black bands are boundary states ($\Lambda \approx 0$). All other bands in the band structure are bulk bands ($0 < \Lambda < 1$). The total displacement (d) fields of the Edge state I, II, III, and IV eigenmodes are also included. (b) The out-of-plane displacement (w) fields for each of the four edge states, illustrating the bending (Edge states I and II) and torsional (Edge states III and IV) eigenmodes.

A six-unit supercell is constructed to explore the emergence of topological 1D edge states in the 2D HOTM. To create the supercell, three Type A unit cells are adjoined with three Type B unit cells at an interface (see the schematic at the top of Fig 5.3a, where the dashed line represents the interface). Low-reflecting boundary conditions are applied to the left and right edges (in the x direction), and Floquet periodic boundary conditions are applied along the y direction. To detect topological edge states, a localization parameter is defined as $\Lambda = \frac{\iiint_{V_{interface}} d^2 dV}{\iiint_{V_S} d^2 dV}$, where $V_{interface}$ is the volume of the two adjacent unit cells at the interface, V_S is the total supercell volume, and $d = \sqrt{|u|^2 + |v|^2 + |w|^2}$ is the total displacement. Evaluation of the supercell band structure (Fig 5.3a) reveals that 1D edge states appear in each of the four topological bandgaps (I,

II, III, and IV) identified in the unit cell analysis (the bandgaps are marked with gray shading in Fig 5.3a). The mode shapes for these edge states, which are labeled as Edge states I, II, III, and IV in Fig 5.3a, illustrate wave fields that are confined at the topological interface. This interface confinement is quantified as $\Lambda \approx 1$ and is indicated by the red bands in the band structure. The black bands that cross into or reside within bandgaps II, III, and IV contain wave fields that are highly localized to the left and right (in the x) boundaries of the supercell, resulting in $\Lambda \approx 0$. In practice, these so-called boundary states can be adjusted or suppressed by selecting the proper boundary conditions and are unlikely to couple with topological edge and corner states (e.g., Section 2.5.3 and [173]), as will be shown in the following sections. Further examination of the edge state eigenmodes is conducted by evaluating the out-of-plane displacement w for each. The out-of-plane wave fields shown in Fig 5.3b illuminate how the multiband edge states originate from the multimodal resonances of the 2D HOTM (see Fig 5.1c and Section 5.3); Edge states I and II contain bending resonances, and Edge states III and IV contain torsional resonances. Critically, all four topological edge states are gapped (i.e., they do not completely cross the topological bandgap they reside within; see Fig 5.3a), leaving the opportunity for easily identifiable topological corner states to emerge in the remaining bandgap frequency range.

5.5 Emergence of multiband topological corner states

An eigenfrequency study is conducted to investigate the emergence of multiband topological 0D corner states in the 2D HOTM. A full-scale structure with an interface between Type A and Type B domains is constructed from a 12 x 12 tessellation of unit cells (Fig 5.4a). In this configuration, a 6 x 6 lattice of Type B unit cells is enclosed within a Type A lattice to create a topological interface that has monomer corners, i.e., where there is a single resonator site at each of the four corners of the interface between the two sublattices (see a monomer corner in the inset of Fig 5.4a). Low-reflecting boundary conditions are applied to all four external boundaries of the Type A domain. The eigenfrequency spectra calculated for this structure are shown for frequency ranges that include bandgaps I, II, and III/IV in Fig 5.4b, Fig 5.4c, and Fig 5.4d, respectively. In these figures, the bandgaps are indicated by the light gray shading, while the 0D corner states are marked with red points, 1D edge states with blue points, and bulk states with black points. The localization of the edge and corner states is quantified by the parameters γ_{edge} and γ_{corner} , which measure the average localization from all eigenmodes associated with each edge or corner state

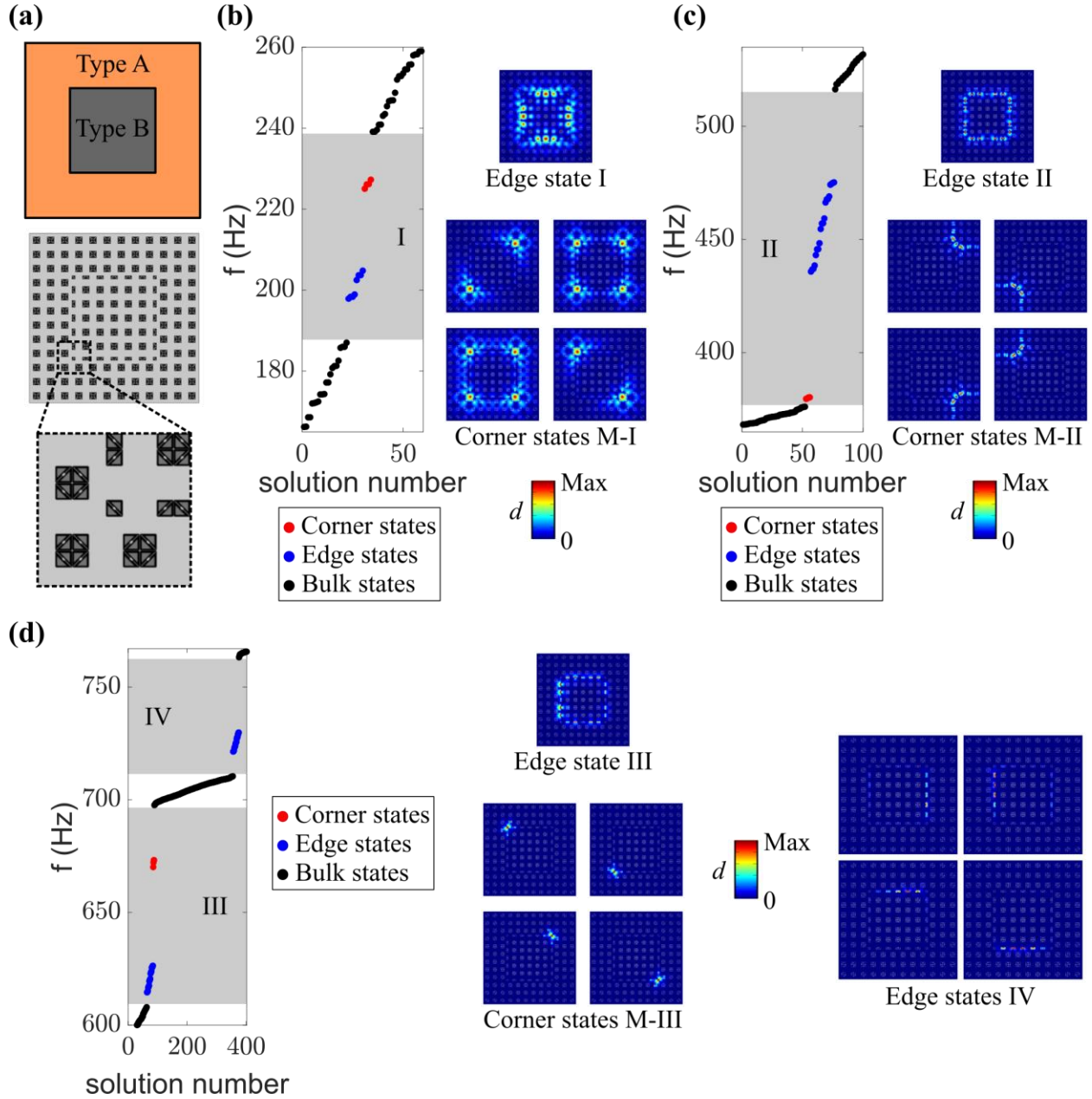


Fig 5.4. Eigenfrequency study for the full-scale structure with monomer corners. (a) Schematic of the full-scale structure with the Type B domain enclosed within the Type A domain, with the inset showing a monomer corner. Eigenfrequency spectra for topological (b) bandgap I, (c) bandgap II, and (d) bandgaps III and IV. The corner states are marked in red, edge states in blue, and bulk states in black. The bandgaps are indicated by the light gray shading. Eigenmodes illustrating the total displacement (d) fields for each of the edge states and corner states are also provided.

according to:

$$\gamma_{edge} = \frac{1}{N_{edge}} \sum_{i=1}^{N_{edge}} \iiint_{V_{edge}} d_i^2 dV / \iiint_{V_t} d_i^2 dV \quad (5.4)$$

$$\gamma_{corner} = \frac{1}{N_{corner}} \sum_{i=1}^{N_{corner}} \iiint_{V_{corner}} d_i^2 dV / \iiint_{V_t} d_i^2 dV \quad (5.5)$$

where N_{edge} is the number of edge eigenstates, N_{corner} is the number of corner eigenstates, V_{edge} is the volume of the 40 edge resonator masses, V_{corner} is the volume of the four corner resonator masses, and V_t is the total volume of all 576 resonator masses in the structure. As shown in Fig 5.4b, eight edge eigenstates and four corner eigenstates emerge within bandgap I, referred to as Corner states M-I (225-227 Hz, $\gamma_{corner} = 0.05$) and Edge state I (194-204 Hz, $\gamma_{edge} = 0.24$). Eigenmodes that demonstrate the wave confinement at the interface for the edge and corner states are shown on the right side of Fig 5.4b. The eigenmodes for Corner states M-I include a monopole mode, two dipole modes, and a quadrupole mode (see more details in Appendix D.3), an indication of evanescent coupling (an overlap between decaying fields of neighboring corner states) between the corner modes that has been observed in previous investigations [271,272,276]. For bandgap II, there are four corner modes (Corner states M-II, 379-380 Hz, $\gamma_{corner} = 0.06$) and 20 edge modes (Edge state 2, 436-475 Hz, $\gamma_{edge} = 0.57$) that appear (Fig 5.4c). Unlike Corner states M-I, Corner states M-II are decoupled from each other (i.e., each corner state is localized at one specific corner), as there are no interactions between their evanescent wave fields [271]. Likewise, four highly localized and decoupled corner eigenstates (Corner state M-III, 670-673 Hz, $\gamma_{corner} = 0.39$) and 20 edge eigenstates (Edge state III, 615-626 Hz, $\gamma_{edge} = 0.57$) emerge in bandgap III, and 20 edge eigenstates emerge in bandgap IV (Edge state IV, 721-730 Hz, $\gamma_{edge} = 0.68$), as displayed in Fig 5.4d. Apart from differing levels of localization and coupling, Corner states M-I, M-II, and M-III contain distinct symmetry characteristics. As is explained in Appendix D.3, Corner states M-I and M-II are symmetric about the corner's angular bisector. On the other hand, Corner state M-III is asymmetric in relation to the bisector, because the orientation of the resonator defines the direction of the torsional resonance to be perpendicular to the angular bisector.

The eigenfrequency spectrum is also calculated for an inverted scheme, where the Type A domain is embedded within the Type B domain to create a lattice with trimer corners (Fig 5.5a). Edge state I (191-209 Hz, $\gamma_{edge} = 0.28$) once again emerges in bandgap I; however, there are no longer corner states in this bandgap (Fig 5.5b). Edge state II is found in bandgap II (20 eigenmodes, 436-475 Hz, $\gamma_{edge} = 0.52$), and two sets of four corner modes are also uncovered: Corner states T-IIA from 379-380 Hz with $\gamma_{corner} = 0.18$ and T-IIB from 459-465 Hz with $\gamma_{corner} = 0.21$

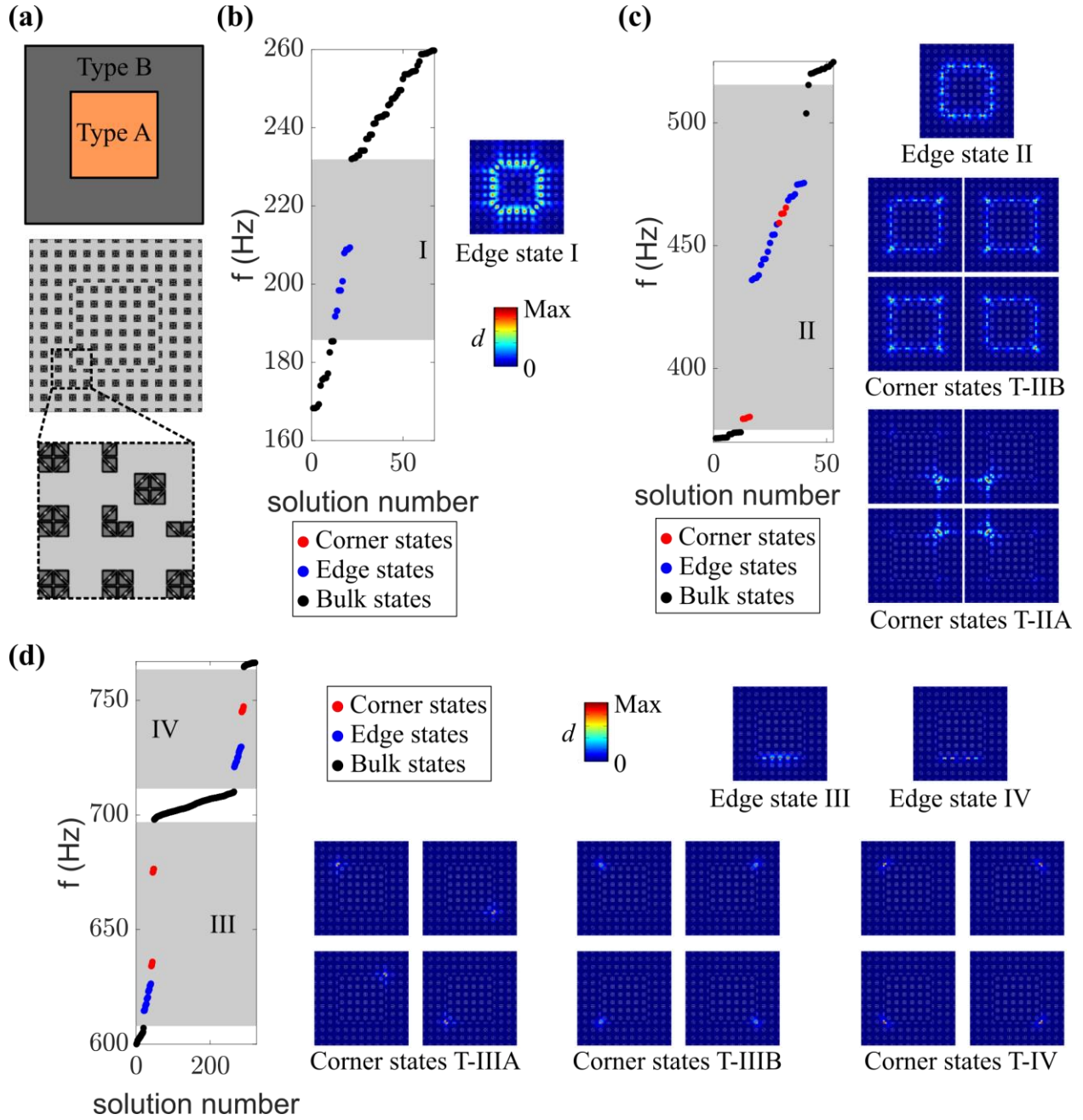


Fig 5.5. Eigenfrequency study for the full-scale structure with trimer corners. (a) Schematic of the full-scale structure with the Type A domain enclosed within the Type B domain, with the inset showing a trimer corner. Eigenfrequency spectra for topological (b) bandgap I, (c) bandgap II, and (d) bandgaps III and IV. The corner states are marked in red, edge states in blue, and bulk states in black. The bandgaps are indicated by the light gray shading. Eigenmodes illustrating the total displacement (d) fields for each of the edge states and corner states are also provided.

(Fig 5.5c). Intriguingly, Corner states T-IIB are embedded with the Edge state II modes, leading to a multipolar coupling between the corners and interactions between corner and edge wave phenomena (see the eigenmodes in Fig 5.5c and Appendix D.3). Edge state III (20 eigenmodes, 615-626 Hz, $\gamma_{edge} = 0.54$) and two sets of four corner modes (Corner states T-IIIA and T-III-B, at

634-636 Hz and 675-676 Hz, with $\gamma_{corner} = 0.46$ and $\gamma_{corner} = 0.61$, respectively) with decoupled and highly localized energy confinement are found in bandgap III (Fig 5.5d). Furthermore, Edge state IV (20 eigenmodes, 721-730 Hz, $\gamma_{edge} = 0.66$) and a set of four well-confined corner states (Corner states T-IV, 745-747 Hz, $\gamma_{corner} = 0.68$) are found in bandgap IV (Fig 5.5d). The trimer corners present in this lattice configuration unlock a diverse set of different corner state wave fields (Fig 5.5b,c,d and Appendix D.3) with symmetric (T-IIB, T-IIIB) or asymmetric (T-IIA, T-IIIA, T-IV) displacements and cases where two (T-IIA, T-IIIB) or three (T-IIB, T-IIIA, and T-IV) resonator sites are activated. The edge states reported in the trimer lattice case are identical in displacement profile and frequency to those reported in the monomer lattice case, since the dimerized resonators that form the 1D interfaces between sublattices are the same in both configurations. For this reason, the edge states are labeled Edge states I, II, III, and IV for both lattice cases. The eigenfrequency results for both lattice configurations illuminate how the multimodal resonance of the 2D HOTM enables the achievement of multiband topological corner states with a rich variety of wave symmetry, localization, and coupling characteristics (see more details on the corner states in Appendix D.3). In total, there are eight unique corner states and four unique edge states that are identified, each with their own distinctive features. The intriguing characteristics of the topological states identified in this eigenfrequency study could open the door for switchable and frequency-selective wave control functionalities that can be engineered through resonator and lattice design, as will be discussed in the following sections.

FE simulations are conducted to investigate how the corner and edge states can be utilized for elastic wave and vibration control in dynamic systems. A harmonic excitation is applied to the monomer and trimer lattices, and the frequency response is measured within the bulk, at an edge, and at a corner, where indicated in Fig 5.6a for the monomer case and Fig 5.7a for the trimer case. For the monomer lattice configuration, the frequency response displayed in Fig 5.6b,c,d,e illustrates the successful confinement of wave energy within Edge states I, II, III, and IV and Corner states M-I, M-II, and M-III, with frequencies and displacement distributions that align with the eigenstates reported in Fig 5.4b,c,d. For the multipolar Corner state M-I, there are three peaks in the frequency response that correspond to the monopolar, quadrupolar, and one dipolar mode; the other dipolar mode is not activated by this excitation (Fig 5.6b). In contrast, the M-II and M-III corner states each have a singular peak because there is no coupling between the displacement fields at neighboring corners, and only the corner state (bottom left corner in Fig 5.6a) nearest to

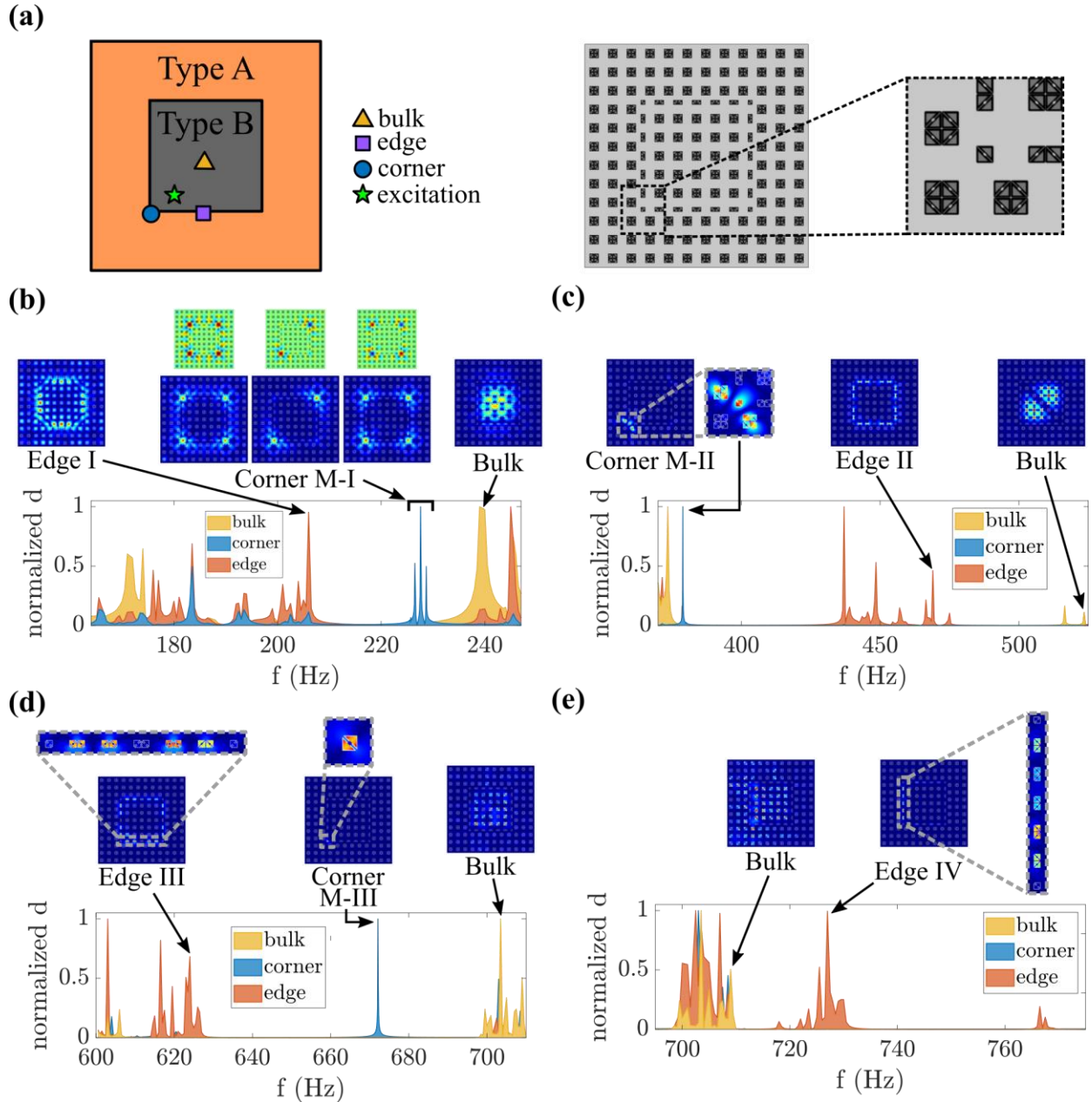


Fig 5.6. Schematic of the full-scale plate in the monomer lattice configuration, with locations marked for the excitation (green star) and measurements of the bulk (yellow triangle), edge (purple square), and corner (blue circle) dynamic response. Normalized frequency response for Bandgaps I (b), II (c), III (d), and IV (e), with the insets showing displacement fields of edge, corner, and bulk states at specific frequency values. The displacement is normalized according to the maximum value calculated at the bulk, corner, and edge positions in the respective frequency ranges.

the chosen excitation is activated (Fig 5.6c,d). For the trimer lattice case, Edge states I, II, III, and IV and Corner states T-IIA, T-IIB, T-IIIA, T-IIIB, and T-IV all effectively confine the dynamic wave response (see the frequency response in Fig 5.7b,c,d,e) per the frequency and spatial characteristics of the eigenstates reported in Fig 5.5b,c,d. For both lattice cases, these results reveal how the edge and corner states of the 2D HOTM can be harnessed to achieve 0D and 1D

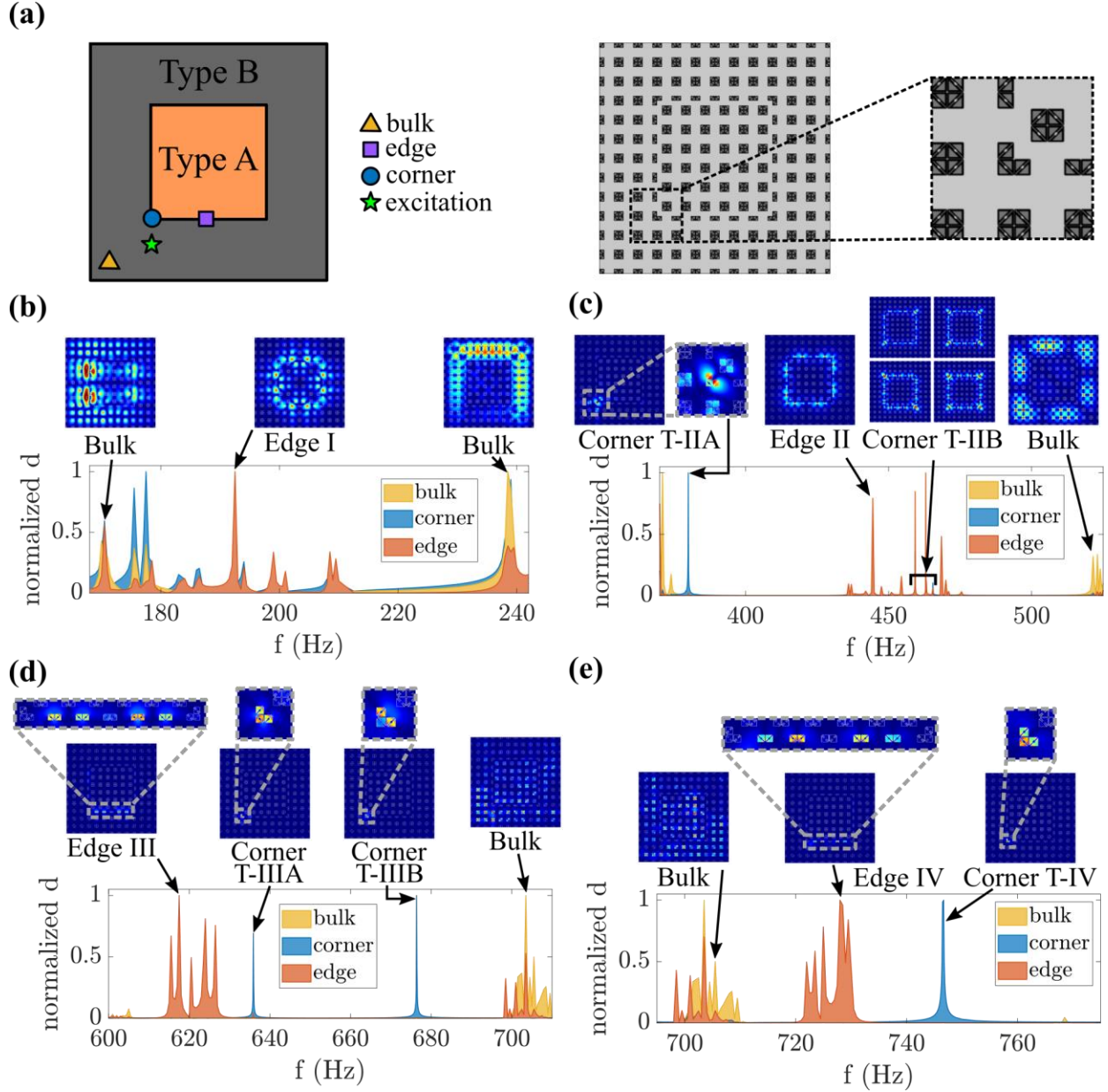


Fig 5.7. Schematic of the full-scale plate in the trimer lattice configuration, with locations marked for the excitation (green star) and measurements of the bulk (yellow triangle), edge (purple square), and corner (blue circle) dynamic response. Normalized frequency response for Bandgaps I (b), II (c), III (d), and IV (e), with the insets showing displacement fields of edge, corner, and bulk states at specific frequency values. The displacement is normalized according to the maximum value calculated at the bulk, corner, and edge positions in the respective frequency ranges.

waveguides with localized dynamic response in multiple frequency bands. Additional analysis suggests that these highly confined corner states will not be destroyed by the introduction of damping into the system, which is unavoidable in practical settings (Appendix D.3).

5.6 Multiband corner states for multifunctional wave-based computing

The diverse features of the topological corner states in the 2D HOTM can be exploited to achieve multifunctional wave-based computing. In Fig 5.8a, two harmonic excitations are placed symmetrically about the angular bisector of the bottom left corner (labeled Q_T and marked with a blue circle in the schematic) in a trimer lattice. The phases of excitation A (yellow star) and excitation B (purple star) are θ_0 and $\theta_0 + \theta$, respectively, where θ_0 is the baseline phase and θ is a phase offset between the two inputs. To measure the variation in dynamic response over a range of θ , the absolute magnitude of the out-of-plane displacement $|w|$ is normalized by its maximum value over all θ for a given excitation frequency f : normalized $|w| = |w(\theta)|/\text{Max}\{|w(\theta)|\}_f$. This normalized $|w|$ is calculated at Q_T for excitation frequencies that excite each of the trimer corner states: $f = 380.0$ Hz for T-IIA, $f = 635.9$ Hz for T-IIIA, $f = 676.4$ Hz for T-IIIB, and $f = 746.6$ Hz for T-IV (T-IIB is omitted from this study due to its interactions with Edge state II) and the phase offset θ varied from 0 to 2π (Fig 5.8a). The normalized $|w|$ reaches a maximum at $\theta = \pi$ for the corner states with asymmetric wave fields (T-IIA, T-IIIA, and T-IV) due to constructive interactions between the out-of-phase inputs and the asymmetric eigenmode shapes. On the other hand, the normalized $|w|$ for the corner state with a symmetric wave field (T-IIIB) reaches a maximum at $\theta = 0, 2\pi$, as constructive interactions occur between the in-phase inputs and symmetric eigenmode shapes. For an in-phase excitation pair, the asymmetric T-IIA, T-IIIA, and T-IV corner states are all suppressed, and for an out-of-phase excitation pair, the symmetric T-IIIB corner state is suppressed. The suppressed corner states have a normalized $|w| \leq 0.036$, indicating a significant attenuation of dynamic response, which can be visualized by the wave field shown in the inset at the bottom of Fig 5.8a. An analysis of the monomer lattice case, with a corner labeled Q_M , yields similar outcomes (Fig 5.8b). For an in-phase ($\theta = 0, 2\pi$) excitation A and B pair, the symmetric corner states M-I and M-II are activated, while for an out-of-phase excitation pair ($\theta = \pi$), the asymmetric corner state M-III is triggered. A dynamic response suppression of normalized $|w| \leq 0.017$ is achieved for the in-phase (out-of-phase) excitation of asymmetric (symmetric) corner states (bottom of Fig 5.8b). These results reveal how the diverse symmetry properties of the topological corner states in the 2D HOTM can be exploited to amplify or suppress response based on the frequency and displacement profiles of external excitations. This is a useful functionality that can be harnessed for computing operations by treating the wave response as a binary bit. Previous works have shown the potential of mechanical (i.e., analog) computing that

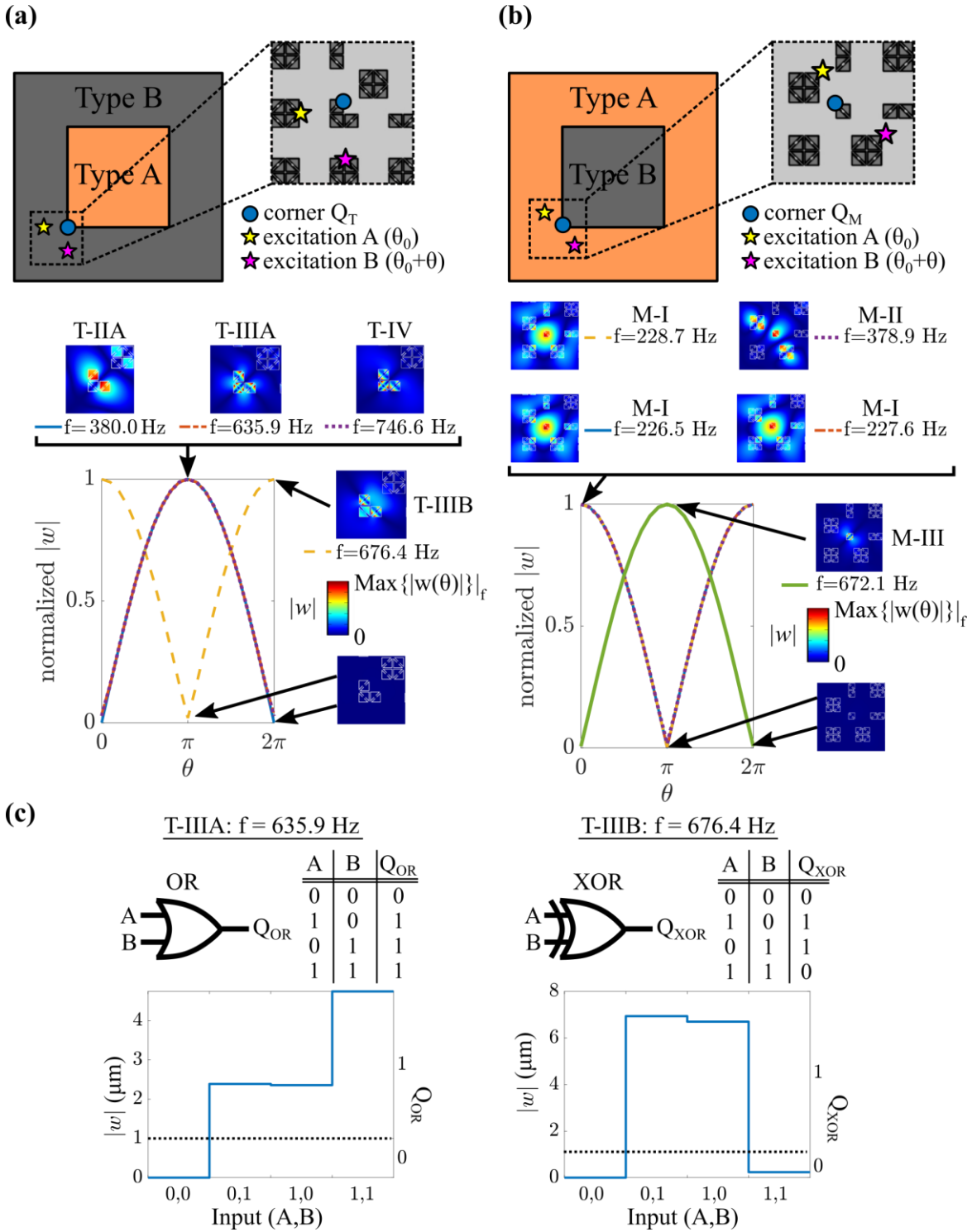


Fig 5.8. Wave-based computing with the 2D HOTM. Schematics and normalized $|w|$ as a function of the phase offset θ for the (a) trimer and (b) monomer lattices. The excitations A and B have a baseline phase of θ_0 and are located where indicated by the yellow and purple stars. The displacement response is measured at corner Q_T or Q_M , where marked by the blue circles. The insets show the out-of-plane displacement $|w|$ fields calculated for each excitation frequency f , scaled to $\text{Max}\{|w(\theta)|\}_f$. (c) A frequency-dependent logic gate constructed from the trimer lattice configuration by exciting the T-IIIA and T-IIIB corner states. The output threshold delineating 0 and 1 bits is marked by the horizontal dashed line. Truth tables are given for the OR and XOR logic operations.

uses elastic waves as bits [277–279]; however, utilizing the unique features of topological corner states for wave-based computing operations has only been explored in a single-band photonic metamaterial [280].

A simple example of how the multiband corner states of the 2D HOTM can be valuable for wave-based computing is presented here, with the construction of a frequency-dependent logic gate using the trimer lattice from Fig 5.8a. A threshold of $|w| = 1 \mu\text{m}$ is set to be the delineation between a 0 bit and a 1 bit for the output, an active(inactive) excitation is a 1(0) bit for the inputs (A and B), and the phase offset for the inputs is chosen to be $\theta = \pi$ (i.e., this is an out-of-phase excitation pair). For an excitation with $f = 635.9$ Hz, the asymmetric T-III A corner mode creates an OR gate, meaning the output Q_{OR} is 1 if either A or B or both A and B are 1 (the truth table and measured $|w|$ are shown on the left side of Fig 5.8c). Alternatively, if the excitation frequency is changed to $f = 676.4$ Hz, the symmetric T-III B mode creates an XOR gate, where the output Q_{XOR} is 1 if either excitation A or B, but not both, are active (the truth table and measured $|w|$ are shown on the right side of Fig 5.8c). This case study illustrates how the diverse multiband corner states of the novel 2D HOTM can be exploited to construct and switch between two unique (in this case, OR and XOR) logic operations in a frequency-dependent fashion. The investigation presented in Fig 5.8 suggests that the capabilities of the 2D HOTM could be valuable for multichannel and multifunctional information processing. Further investigations may involve constructing all seven of the fundamental logic elements (XOR and OR gates are two of the seven fundamental logic elements [281]) and cascading them together to accomplish more sophisticated computing tasks.

5.7 Higher-order topological states in a fractal TM

The unit cell geometry of the 2D HOTM (Fig 5.1a) is used to synthesize and explore higher-order topological phases in fractal mechanical lattices for the first time. Recently, topological phases have been derived and theoretically investigated in fractal quantum systems [282–291]. In a fractal crystal, the crystal lattice exhibits a non-integer dimension and contains self-similarity across multiple scales [292,293]. This non-integer dimension can be quantified as the Hausdorff dimension d_h [294]:

$$d_h = \frac{\log(S)}{\log(L)} \quad (5.6)$$

where L is a linear scaling and S is the resulting characteristic size of an object. Unlike conventional integer-dimensional systems (i.e., 1D, 2D, and 3D), fractals do not have a well-defined internal “bulk”. Due to this lack of a clear bulk, fractals have a rich set of internal and external boundaries that suggest the possibility of unconventional topological wave control capabilities. While fractal topological phases have been predicted in condensed matter physics [282–291], practical macroscale platforms and a fundamental understanding of fractal topological phases in classical wave systems are still lacking. Initial investigations on photonic [295,296] and acoustic [297–299] systems have illuminated intriguing features (e.g., faster wave speed, higher-order topological phases, and wave control along myriad internal/external boundaries) in fractal topological lattices. Despite the established potential of fractal topological phases, they have yet to be explored in TMs that control vibrations and elastic waves. The research presented in this section seeks to address this unexplored opportunity.

To create a fractal HOTM, The 2D HOTM unit cell presented in Section 5.2 (Fig 5.1a) is tessellated into two configurations that have a fractal patterning of the metamaterial resonators. The fractal lattice depicted in Fig 5.9a,b is known as a Sierpiński Carpet, which has a Hausdorff dimension of $d_h = 1.89$ ($S = 8$ for $L = 3$ in Eq. 5.6). For the 2D HOTM, topological interfaces that host topological states exist at the four corners and four edges that make up the large square border between the Type A and Type B subdomains (Fig 5.4a and Fig 5.5a). Beyond these eight external interfaces, the 1.89D fractal HOTM adds numerous internal interfaces (36 edges and 36 corners) along one medium and eight small square subdomain borders, each of which may host additional topological states. All small, medium, and large square Type A/Type B subdomain borders are marked with dashed lines in the schematics of Fig 5.9a,b. To investigate the emergence of topological states in the fractal HOTM, the eigenfrequency spectra are calculated for Configuration 1 (Fig 5.9a) and Configuration 2 (Fig 5.9b) and plotted in Fig 5.9c and Fig 5.9d, respectively. The four exterior boundaries of the Configuration 1 and Configuration 2 structures are fixed for this analysis. The frequency range under investigation is selected to encompass bandgaps III and IV from the 2D HOTM, due to the high degree of localization exhibited by the torsional topological corner states (see Section 5.5 and Appendix D.3). As revealed in Fig 5.9c and Fig 5.9d, a significant number of topological edge (marked with blue points) and corner states (marked with points of various colors) appear in the frequency ranges of bandgaps III and IV for both Configuration 1 and Configuration 2. All bulk (i.e., eigenmodes that are not localized at a

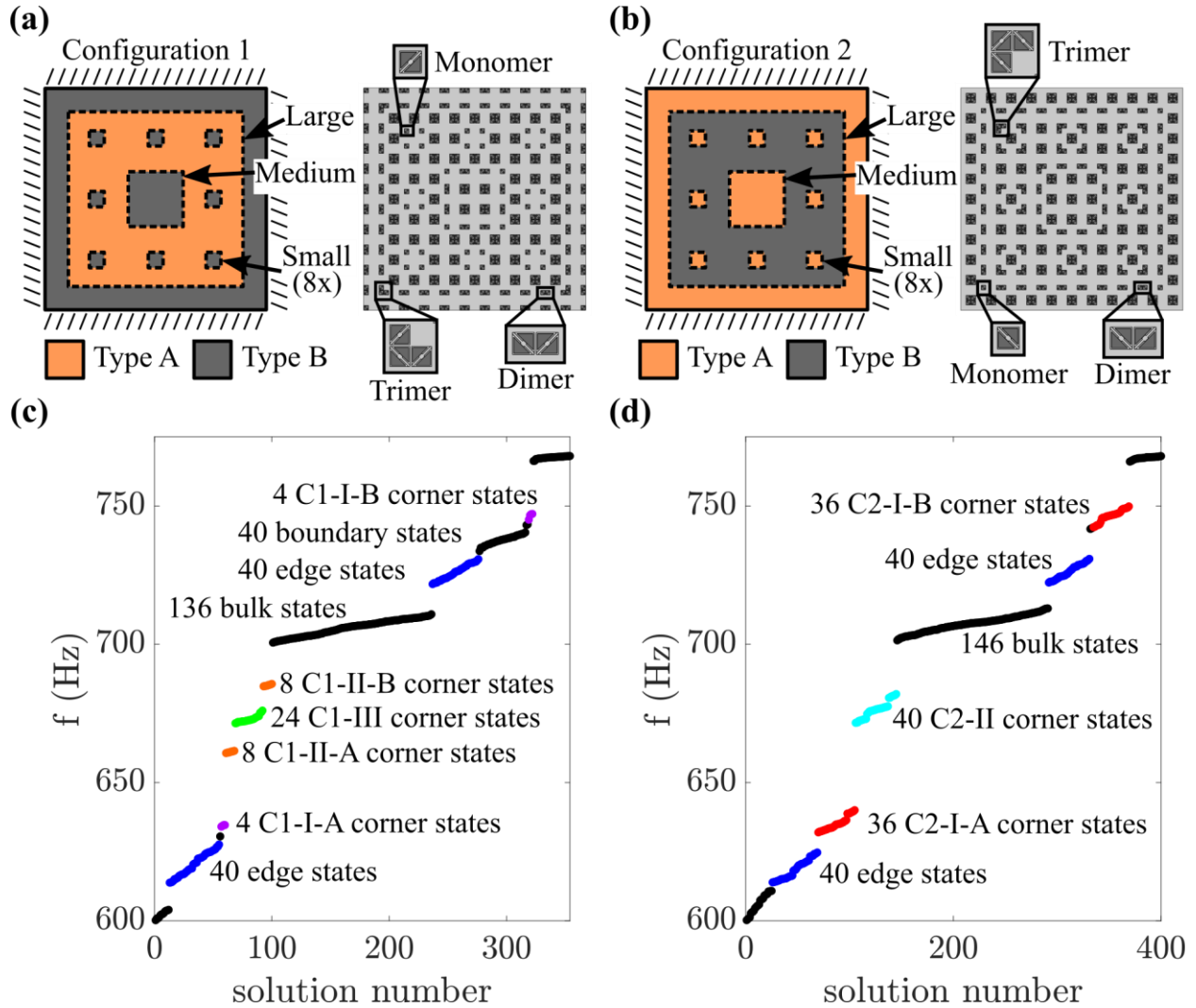


Fig 5.9. An investigation of higher-order topological states in fractal lattices. Schematics and top views of (a) Configuration 1 and (b) Configuration 2 of the fractal HOTM. The two unique configurations of fractal lattices are created by patterning the Type A (orange) and Type B (gray) subdomains to create 1.89D Sierpiński Carpets. The borders (i.e., topological interfaces) between Type A and Type B subdomains are marked by dashed lines. There are eight small square subdomain borders, one medium square subdomain border, and one large square subdomain border. The four edges of the plate that make up the exterior boundary are fixed, as indicated by the slanted lines. The insets show a monomer corner, a dimer resonator pair, and a trimer corner for each lattice configuration. The eigenfrequency spectra for (c) Configuration 1 and (d) Configuration 2. The bulk and boundary states are indicated with black points, the topological edge states with blue points, and the topological corner states with points of various colors.

topological interface or fixed boundary) and boundary (i.e., eigenmodes that are localized at a fixed boundary) modes are indicated by the black points. A more detailed discussion on the bulk and boundary states for this fractal HOTM, all of which do not adversely affect the appearance of topological states, is provided in Appendix D.4. The topological edge and corner states are categorized into distinct classes and labeled according to the spectral clusters in which they appear. The quantity and spatial location of topological states in the fractal HOTM lattices can be predicted

by the arrangement of the metamaterial resonators [297]. For configuration 1 (Fig 5.9a): $N_{external\ corners} = 3N_3 = 12$, $N_{edge} = 2N_2 = 80$, $N_{internal\ corners} = N_1 = 36$, where N_1 , N_2 , N_3 are the number of monomer corners (i.e., a corner with one resonator), dimer resonator pairs, and trimer corners (i.e., a corner with three resonators) located at the Type A/Type B subdomain interfaces, $N_{external\ corners}$ is the number of topological corner states with wave energy confined to the corners of the external (i.e., large) square subdomain borders, N_{edge} is the number of topological edge states, and $N_{internal\ corners}$ is the number of topological corner states with wave energy confined to the corners of the internal (i.e., eight small and one medium) square subdomain borders. When the Type A and Type B subdomains are exchanged to create Configuration 2 (Fig 5.9b): $N_{external\ corners} = N_1 = 4$, $N_{edge} = 2N_2 = 80$, $N_{internal\ corners} = 3N_3 = 108$. Between Configurations 1 and 2, the quantity and frequencies of the edge states are unchanged, since the number and arrangement of the dimer resonator pairs remain constant. However, the total number of corner states is increased from 48 in Configuration 1 to 112 in Configuration 2 due to the interchange of trimer and monomer corners between the two configurations ($N_1 = 36$ and $N_3 = 4$ for Configuration 1; $N_1 = 4$ and $N_3 = 36$ for Configuration 2). These results illuminate how the introduction of fractal geometry significantly increases the quantity of topological corner states (160 total topological corner states) when compared to the 16 total corner states uncovered in bandgaps III and IV for the traditional 2D HOTM (Section 5.5). Moreover, this analysis shows how the placement of the monomer and trimer corners can be engineered to alter the quantity of topological corner states, change topological corner state frequencies, and tailor the location of confined wave energy within the fractal mechanical structure. These outcomes suggest generalizability, in that the arrangement of monomer and trimer corners could be prescribed to achieve desired topological corner state properties (e.g., number, frequency, and location) in other fractal metamaterial geometries.

Representative mode shapes for each class of topological states are provided in Fig 5.10a for Configuration 1 and Fig 5.10b for Configuration 2. For Configuration 1, an exemplar bulk mode at 603 Hz exhibits a delocalized displacement field (Fig 5.10a). The exemplar topological edge modes evaluated at 624, 625, 728, and 730 Hz illuminate wave fields that are highly localized along inner and outer edge interfaces (Fig 5.10a). Furthermore, a diverse collection of corner states appears in the eigenspectrum of Configuration 1. The four C1-I-A (634 Hz in Fig 5.10a) and four C1-I-B (747 Hz in Fig 5.10a) corner states have displacement that is well confined to the four

corners of the large square subdomain interfaces. The eight C1-II-A (661 Hz in Fig 5.10a) and eight C1-II-B (685 Hz in Fig 5.10a) corner states have wave fields that are localized to the corners of the eight small square subdomain interfaces. The 24 C1-III (671, 672, and 675 Hz in Fig 5.10a) corner states exhibit energy confinement at the corners of all three sets (eight small, one medium, and one large) of square subdomain interfaces. In the case of Configuration 2, the topological edge states (620, 621, 729, 730 Hz in Fig 5.10b) are virtually unchanged in frequency and displacement field profile, and the bulk modes (605 Hz in Fig 5.10b) cover the same frequency ranges (Fig 5.9d). On the other hand, the eigenfrequencies for Configuration 2 contain a different array of topological corner states when compared to Configuration 1 due to the interchange of the trimer and monomer corners. For Configuration 2, 36 C2-I-A (632, 636, and 639 Hz in Fig 5.10b) and 36 C2-I-B (742, 744, 746, and 749 Hz in Fig 5.10b) corner states emerge that trap wave energy at the corners of the nine (eight small and one medium) internal square subdomain interfaces. Moreover, 40 C2-II (672, 672, 676, and 682 Hz in Fig 5.10b) corner states emerge with displacement localized at the corners of all small, medium, and large subdomain interfaces. The rich hierarchy of topological edge and corner states displayed in Fig 5.10 underscores how the distinctive geometry of the fractal HOTM enables the manipulation of elastic waves across numerous dimensions, locations, and frequencies.

Further analysis of the corner states uncovers intriguing coupling and symmetry characteristics. Select eigenmodes for the corner states of Configurations 1 and 2 are presented in Fig 5.11a and Fig 5.11b, where the insets (which depict out-of-plane displacement w) provide insight into the symmetries of the mode shapes. The displacement fields for C1-II-A, C1-III, and C1-II-B (661, 671, and 685 Hz in Fig 5.11a) reveal that the corner states confined at the eight small square subdomain interfaces exhibit multipolar behavior, because the close proximity of the four monomer corners leads to the evanescent coupling of their respective deformations (see a discussion on multipolar corner states in Section 5.5). The eight C1-II-A (661 Hz in Fig 5.11a) states are monopolar, the 16 C1-III (671 Hz in Fig 5.11a) states localized to the small square subdomain interfaces are dipolar, and the eight C1-II-B (685 Hz in Fig 5.11a) states are quadrupolar. Identical observations are made for the trimer corner states located at the eight small square subdomain interfaces for Configuration 2. In that case, The 32 C2-I-A, 32 C2-II, and 32 C2-I-B corner states that are localized at the small square interfaces each contain sets of eight monopolar (636, 672, and 742 Hz in Fig 5.11b), eight quadrupolar (639, 682, and 749 Hz in

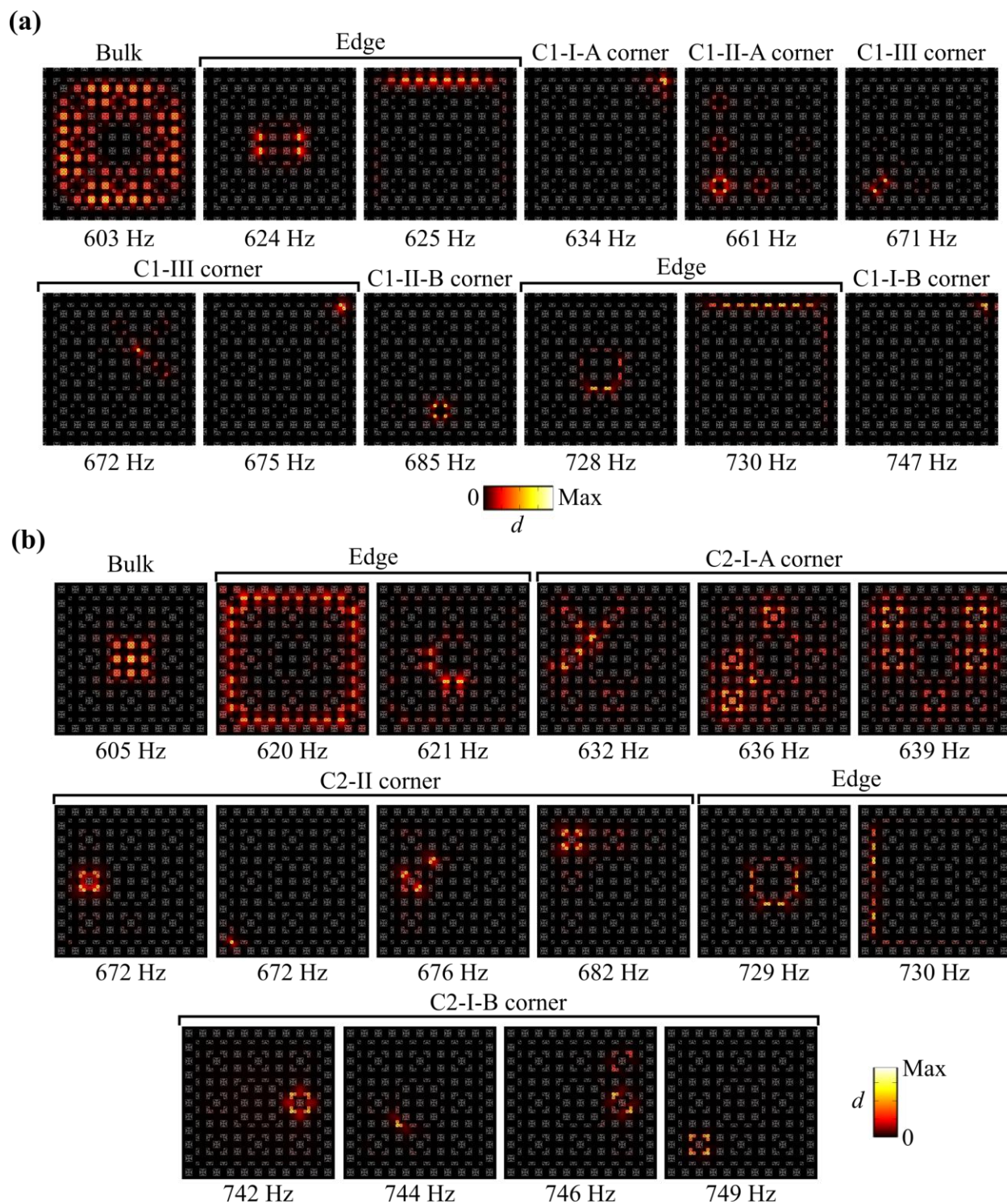


Fig 5.10. Exemplar bulk, edge, and corner eigenmodes for the fractal HOTM in (a) Configuration 1 and (b) Configuration 2 that illustrate the wave confinement of the topological states. A larger total displacement d is indicated by increasing brightness.

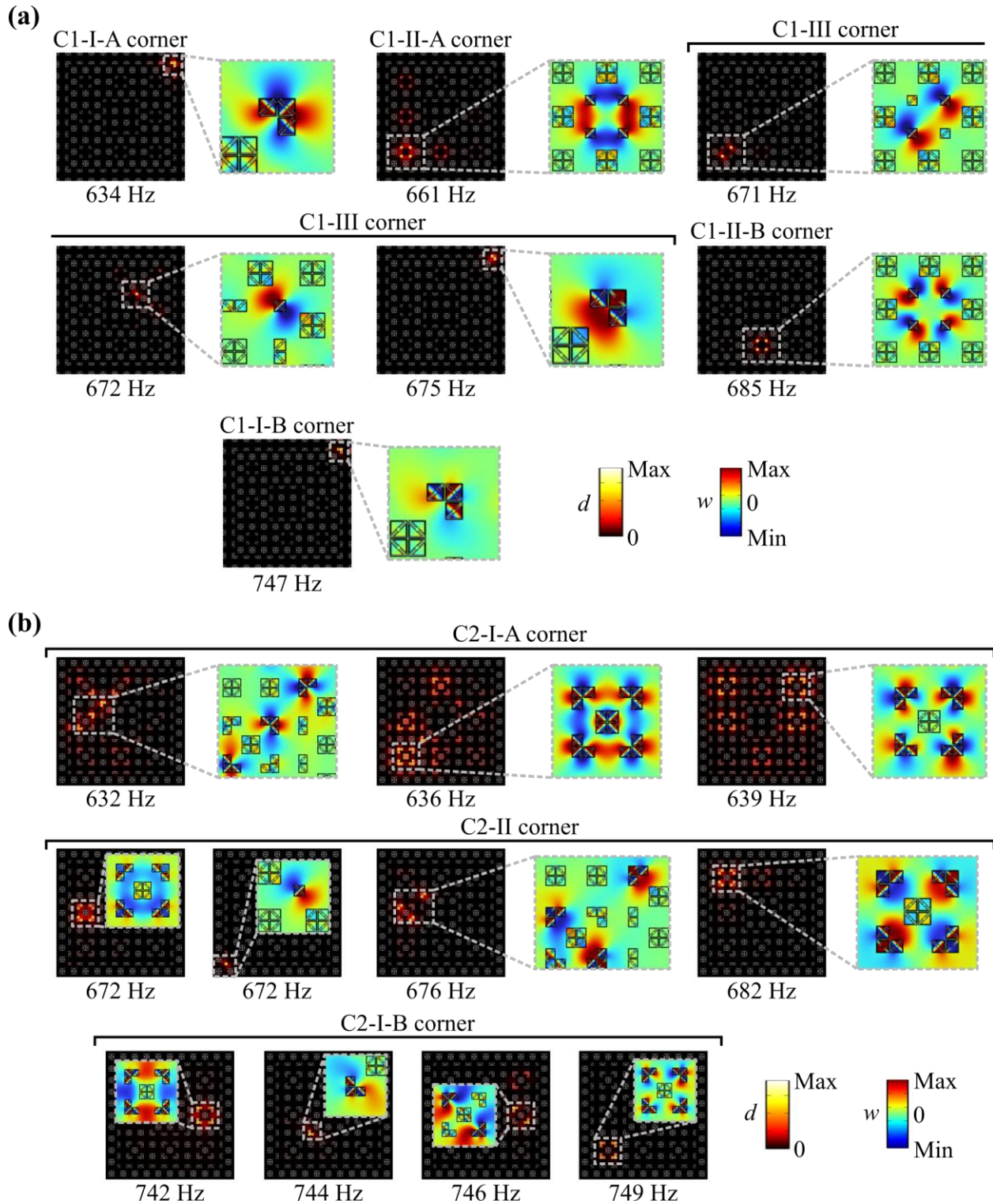


Fig 5.11. Eigenmodes for the corner states of the fractal HOTM in (a) Configuration 1 and (b) Configuration 2. For the full-scale results, a larger total displacement d is indicated by increasing brightness. Insets of the out-of-plane displacements w are included to elucidate the symmetry characteristics of each mode.

Fig 5.11b), and 16 dipolar (632, 676, and 746 Hz in Fig 5.11b) eigenmodes. On the other hand, the corner states (C1-I-A, C1-III, C1-I-B, C2-I-A, C2-II, and C2-I-B) located at the medium and large square subdomain interfaces do not exhibit multipolar behavior due to the larger distance between the corners (634, 672, 675, 747 Hz in Configuration 1, Fig 5.11a; 632, 672, 676, and 744 Hz in Configuration 2, Fig 5.11b).

Apart from multipolar coupling, a pattern is detected in the coupling between the monomer and trimer corner states of the fractal HOTM. The C1-III and C2-II classes of corner states each contain eigenmodes with wave localization at both monomer and trimer corners (Fig 5.11a,b). The trimer corner states in both the C1-III and C2-II classes have symmetric eigenmodes about the angular bisector (675 Hz in Fig 5.11a and 672, 676, 682 Hz in Fig 5.11b). In contrast, the C1-I-A, C1-I-B, C2-I-A, and C2-I-B trimer corner states have asymmetric eigenmodes (634 and 747 Hz in Fig 5.11a and 632, 636, 639, 742, 744, 746, and 749 Hz in Fig 5.11b) and do not couple with any monomer corner states (i.e., there are no monomer corner states in the C1-I-A, C1-I-B, C2-I-A, and C2-I-B classes). These outcomes reveal that the symmetric trimer corner states of the fractal HOTM couple with monomer corner states that emerge in the same frequency range, while the asymmetric trimer corner states do not couple to monomer corner states and are thus spectrally isolated. The understanding of the monomer-trimer and multipolar couplings of the corner states in the fractal HOTM could be leveraged to create elastic waveguides with prescribed displacement symmetries that are confined at multiple (or singular) spatial locations.

5.8 Conclusions and discussion

The research presented in this chapter advances the state of the art through the synthesis and exploration of a novel 2D HOTM that harnesses multimodal local resonance to enable higher-order topological corner states in multiple frequency bands. A band structure investigation uncovers four low-frequency (<1 kHz) topological bandgaps that are derived from bending and torsional resonances and the adjustment of intra- and inter-cell resonator couplings according to the 2D SSH model. A supercell study reveals four gapped 1D edge states that appear within the topological bandgaps, two of which have bending local resonances and two of which have torsional local resonances. Calculation of the eigenspectra for full-scale structures illuminates the emergence of a rich collection of eight 0D corner states across the four topological bandgaps. The multiband corner states have a diverse set of displacement field characteristics (localization,

symmetry, and number of activated masses), exhibit multipolar or decoupled behavior, and have frequency-selective capabilities that are controllable through lattice design (e.g., prescribing monomer or trimer corners). Dynamic response simulations illustrate how vibrations and elastic waves can be effectively confined by the topological edge and corner states of the 2D HOTM. The outcomes from this research reveal how multimodal resonance can be exploited to attain topological 0D corner states across multiple frequency regimes. The distinctive characteristics of the hierarchy of topological states achieved in the 2D HOTM may unlock multifunctional and multichannel wave focusing for energy harvesting, sensing, and signal processing applications. As an example, a frequency-dependent logic gate is constructed from the 2D HOTM. The frequency-dependent gate switches between OR and XOR logic operations based on the wave excitation frequency by selecting between two unique corner states, illustrating the potential usefulness of the 2D HOTM for wave-based computing. The capabilities of the 2D HOTM platform are also leveraged to construct the first fractal HOTM that controls vibrations and elastic waves. An eigenfrequency analysis uncovers corner and edge states that trap wave energy at the myriad corner and edge boundaries of a 1.89D Sierpiński carpet. The fractal HOTM unlocks 160 corner states in two topological bandgaps, surpassing the 16 that materialize in the same bandgaps of the 2D HOTM. This study provides insight into the attainment of higher-order topological states in fractal TMs that localize elastic waves across various dimensions, locations, and frequencies, opening the door for future research of topological phases in mechanical metamaterials with fractal architectures.

Chapter 6. Scholarly Contributions, Broader Impacts, and Future Opportunities

6.1 Summary of scholarly contributions

This dissertation advances the state of the art through the synthesis of a new class of advanced TMs that achieve exceptional control over elastic wave propagation in mechanical structures. As part of the development of these advanced TMs, innovative methodologies that harness comprehensive adaptivity, local resonance, higher-order topological phases, and 3D mechanical architectures are created and explored. The TMs established within this dissertation exhibit wave control that is on-demand tunable (i.e., responsive), broadband, multiband, subwavelength (i.e., easily integrated into volume-constrained and low-frequency applications), and multidimensional (i.e., wave control is attained across a hierarchy of 0D, 1D, 2D, and layer-dependent topological states). In addition to yielding sophisticated elastic wave control capabilities, new insight is uncovered on the interactions between topological and elastic wave physics. The TMs generated in this dissertation are shown in Fig 6.1a and a visual overview of the scholarly contributions is given in Fig 6.1b,c,d (note that the four symbols in Fig 6.1 indicate the connection between each of the TMs and the scholarly contributions). The primary contributions of this dissertation are summarized below:

- ***New electromechanical and metastable design methodologies are uncovered that enable the realization of 2D and 3D TMs with multiple on-demand tunable characteristics (Fig 6.1b):*** Investigations uncover system parameters that govern the on-demand tunability of the TMs and reveal the true attainable range of adaptive functionality. In Chapter 2, concurrent adaptivity of the frequency, path, and shape of 1D topological edge states is realized through the creation of a 2D TM with resonant piezoelectric circuitry. Using a semi-analytical tool (dispersion relation derived from the PWE method), an achievable operating region for locally resonant topological states is derived, and its physical

explanation is obtained. A systematic analysis reveals how resonant circuitry, electromechanical coupling, and lattice reconfiguration can be exploited to increase the tunable frequency range, enhance achievable mode localization, and switch between multiple unique topological states. In Chapter 3, a 3D metastable TM is developed that enables wave path tunability and on-demand selection between several multidimensional (2D surface, layer-polarized, and mono/bilayer-locked) topological states, establishing the first on-line programmable 3D TM. Wave control functionality that exceeds what is achievable in 2D TMs is demonstrated by switching between and connecting these multidimensional topological states within adaptive 3D metastructures. These contributions are published in [235,253].

- ***Novel 2D tunable TM, 3D TM, and 2D HOTM are created that harness local resonance to operate in subwavelength, multiband, and broadband frequency regimes (Fig 6.1c):*** In Chapter 2, locally resonant LC circuits are used in the tunable 2D piezoelectric TM to attain subwavelength topological states and adjust the frequency of topological wave propagation over a broad frequency range. Lattice reconfiguration (through the strategic shorting of circuits) is used to uncover a set of topological states in an additional discrete frequency region, facilitating multiband wave control. In Chapter 4, a 3D TM is created that achieves low-frequency and multiband wave control by utilizing multimodal local resonance. Four low-frequency (<6 kHz) topological states are attained through four locally resonant modes (out-of-plane translational, hybrid torsional, in-plane torsional, and in-plane translational) that can be adjusted without changing the lattice constant. Parametric studies are used to uncover critical system parameters and predict the frequency ranges of the four distinct low-frequency topological states that emerge from the careful design of embedded spring-mass resonators. These insights inspire the synthesis of a novel 2D HOTM in Chapter 5, where multimodal resonance and higher-order topological phases are exploited to achieve a hierarchy of multiband topological states in a low-frequency (<1 kHz) regime. Bending and torsional resonances are engineered in the 2D HOTM to achieve a set of eight 0D corner states and four 1D edge states that exhibit a wide variety of displacement field characteristics (wave localization, displacement symmetries, corner mode couplings, and number of activated resonators). The unconventional wave control

capabilities of the 2D HOTM are harnessed to construct multifunctional wave-based logic gates and attain higher-order topological states in fractal TMs for the first time. These contributions are published in [235,266]. The contributions from Chapter 5 will be published in a journal publication that is in preparation.

- ***The rich dimensionality of 3D mechanical architectures is exploited to create 3D TMs that unlock unprecedented wave control functionality through 2D surface, polarization-dependent, and layer-dependent topological states (Fig 6.1d):*** The programmable 3D TM presented in Chapter 3 enables the discovery of a novel bilayer-locked topological state where elastic wave energy is trapped in two layers of a multilayered (eight total layers) 3D metastructure. A supercell analysis reveals that the bilayer-locked state, which contains a strong coupling between the displacement on adjacent layers (layers 4 and 5), is accompanied by monolayer-locked states on all other layers (layers 1,2,3,6,7, and 8). A design methodology is created that would generalize these results such that bilayer- and monolayer-locked states could be achieved on any targeted layers of multilayered 3D metastructures. The 3D TM in Chapter 3 is also used for the construction of sophisticated 3D elastic wave networks (wave layer converter, wave focuser, wave splitter) with frequency- and layer-dependent wave conversion that is achieved through the interaction of several unique multidimensional (2D surface, layer-polarized, and mono/bilayer-locked) topological states. These 3D elastic wave networks harness additional dimensionality to exceed the capabilities of their 2D predecessors [115,155,241]. The 3D TM synthesized in Chapter 4 achieves rich polarization-dependent and frequency-dependent wave control in 2D planar and layer-locked topological waveguides. Depending on the frequency and polarization characteristics of a vibration input, elastic waves can be routed along different layers and directions in a full-scale 3D structure. The experimental investigation of this novel metamaterial results in the first measurements of complete wave fields for 2D topological waveguides and multi-polarized topological waveguides in a 3D mechanical structure. These contributions are published in [253,266].

6.2 Broader impacts and opportunities for future research

As described in Section 6.1, the contributions of this thesis research include enhanced elastic wave control functionality in mechanical systems and new fundamental knowledge in topological and elastic wave physics. The exceptional capabilities of the TMs developed in this dissertation will have a profound impact on many contemporary engineering applications, such as vibration mitigation devices, energy harvesters, sensors, and information processors (see some examples in Fig 6.2a), that serve critical functions in numerous industries (e.g., energy generation [15], manufacturing [16,17], transportation [18], civil infrastructure [19,20], and aerospace/defense [21–23]). The new fundamental knowledge gained within this research will advance the field of EMs and, more broadly, provide inspiration in the fields of condensed matter physics [86–89], acoustics [97,98], and electromagnetics/photonics [99–102] (Fig 6.2b). The TMs and novel physical insights defined herein may also help to form the building blocks of the next generation of mechanical structures, including artificial structures with embodied “intelligence” [12,249,250,300]. This section includes an overview of the broader impacts of this dissertation research and suggests promising opportunities for future research directions.

6.2.1 Advanced elastic wave control in contemporary engineering applications

The advanced TMs developed in this thesis research enable robust (i.e., with minimal losses when exposed to manufacturing- or wear-related imperfections) and tunable control of elastic waves across a hierarchy of dimensions, nearly arbitrary directions, and broad/multiple frequency regimes (that are at low frequencies, <20 kHz, relevant to many structural applications). These properties could be very useful in many classical engineering applications that require the ability to control the flow of vibrations and elastic waves but suffer performance degradation due to a lack of robustness, functionality, and/or range of operation. For example, vibration mitigation devices may benefit from the ability to reroute vibrational energy (e.g., away from critical electronics and towards sacrificial dissipative elements, see the top left panel in Fig 6.2a) and operate over a wide and adjustable frequency bandwidth in a subwavelength manner [2,301]. These characteristics of the piezoelectric 2D TM developed in Chapter 2 may be used to enhance performance and create more compact vibration mitigation materials for structural systems such as aircraft, vehicles, and industrial machinery. Vibration mitigation systems may also find new functionality by using 3D TMs. By using 3D TMs such as those devised in Chapter 3 and Chapter

4, vibration mitigation systems can be designed to selectively absorb wave energy in specific regions of a system, while converting or transmitting energy in others (e.g., the wave layer converter in Fig 3.13 and Appendix Figure B.9 or the frequency-dependent layer-locked behavior in Fig 4.4). The TMs developed within this thesis may also be employed in vibration energy harvesting systems [29,30,217,302] where tunable, broadband, and multiband functionality would be beneficial. The piezoelectric 2D TM (which is already composed of commonly used energy harvesting components: piezoelectric plates) from Chapter 2 could be used to guide vibrational energy to harvesting elements in a lossless and adaptive manner. The ability to adjust on-demand to external input frequency or location changes would greatly enhance the performance as it would facilitate efficient operation in practical environments. The TMs in this thesis also could have potential applications in structural health monitoring (SHM) systems for non-destructive evaluation (NDE) of civil infrastructure, energy pipelines, and sea/air/spacecraft [303–306]. The TMs developed in Chapter 5 harness higher-order topological physics in a way that can obtain signals across multiple bands that are highly localized and have a high signal-to-noise ratio, which are signal properties that may be of great benefit in many SHM/NDE techniques (see a basic schematic of how the 2D HOTM described in Chapter 5 can be used for SHM/NDE and vibration energy harvesting in the top right panel of Fig 6.2a).

The elastic wave capabilities of the advanced TMs described in this thesis research may also be of benefit in many of the modern engineering applications that are presently being developed and realized. With the dramatic expansion of interconnected networks of devices that can sense and compute (those found in smart homes, connected vehicles, wearables, manufacturing equipment, healthcare, farming, civil infrastructure, environmental monitoring, transportation and logistics, 5G networks, and more), known colloquially as the “Internet of Things” [307–309], the progress of on-chip communications and other critical information processing components (i.e., integrated circuitry) has become a top research priority. Owing to their many advantageous attributes (e.g., having high information density, low losses, and low susceptibility to noise, see Section 1.1.1), EMs are a promising platform to create the wave splitters, filters, and processing/logic elements that make up integrated circuitry. In other words, integrated phononic circuitry can be built from EMs by using elastic phonons as the information carrier, replacing the electrons used in conventional electrical circuits (see [27,109–112] for some examples of phononic circuitry). TMs such as those developed in this thesis research may provide high efficiency and

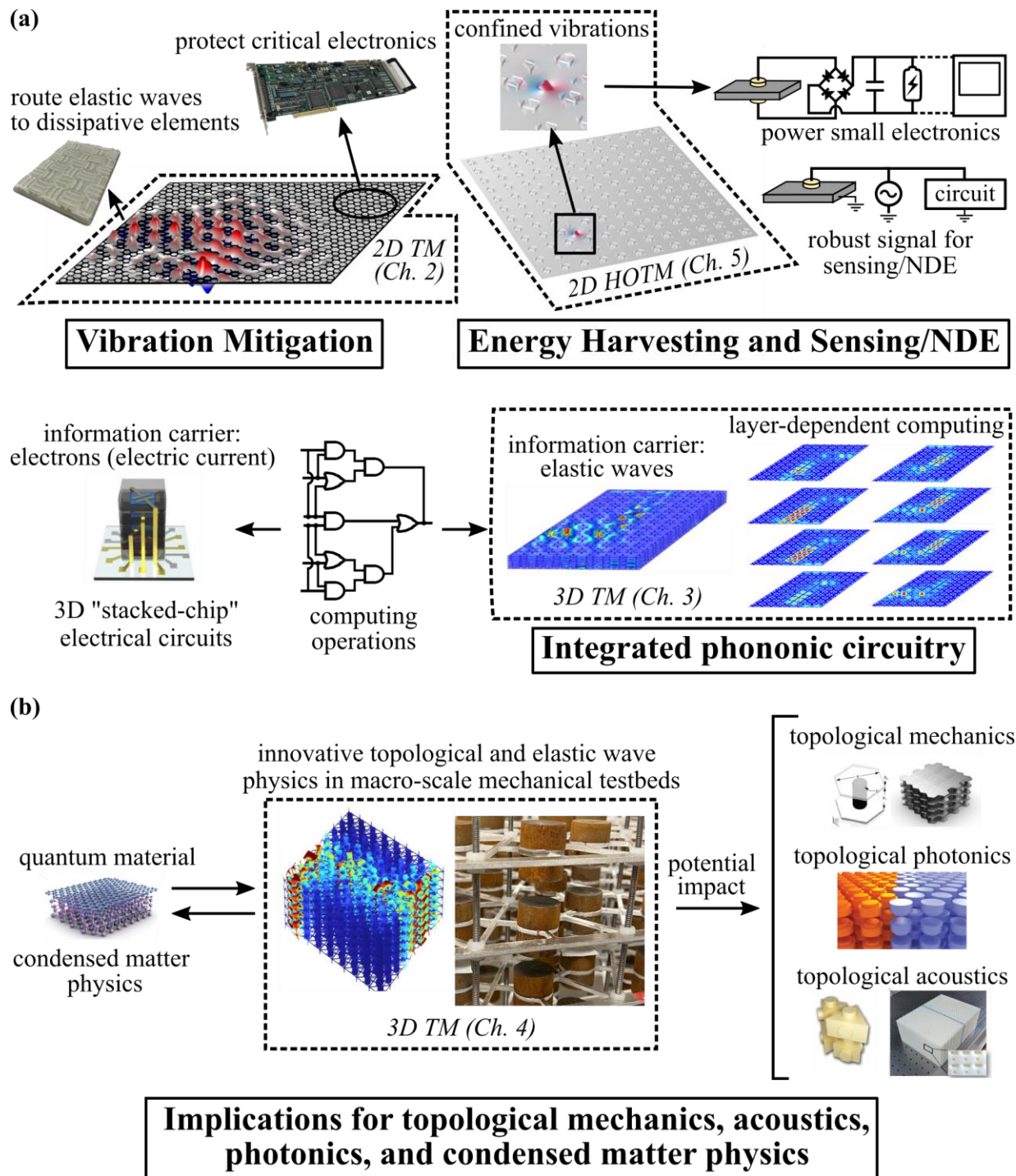


Fig 6.2. Broader impacts of the novel class of TMs synthesized in this dissertation. The images of the TMs from this dissertation are enclosed in dashed black lines. (a) Examples of ways the novel TMs can enhance performance in engineering applications, including vibration mitigation, energy harvesting, sensing/NDE, and integrated phononic circuitry. The image of the 3D “stacked-chip” electrical circuit is reused from [310] under license [CC BY 4.0](#). (b) The TMs and fundamental insight gained from this dissertation may inspire future research in the fields of topological mechanics, acoustics, photonics, and condensed matter physics. The quantum material image is reused from [311] with written permission from the publisher. The topological mechanics image is reused from [75] under license [CC BY 4.0](#). The topological photonics image is reused from [312] with written permission from the publisher. The topological acoustics image is reused from [247] under license [CC BY 4.0](#).

unique functionality for integrated phononic circuit devices due to their remarkable wave control characteristics. Since the TMs synthesized in this thesis rely on symmetry to obtain their intriguing properties, the insight gained from this research is applicable at multiple scales (from on-chip phononic circuits to macro-scale phononic circuits) and frequencies (from low to high, Hz to MHz). An example of a macro-scale phonic circuit element is provided in Section 5.6, where the multiband topological states of the 2D HOTM are employed to create wave-based logic gates that can adapt to certain spatial and frequency properties of an external input. Furthermore, recent developments in the field of semiconductors indicate a new wave of 3D circuit devices. In an effort to increase computing power and alleviate manufacturing limitations, semiconductor manufacturers have created and continue to develop 3D “stacked-chip” systems, which enable more efficient on-chip communications by reducing the interconnect distance when compared to traditional 2D integrated circuit chips [310,313–315]. The 3D TMs synthesized in this dissertation are capable of harnessing this 3D interconnect concept in 3D phononic circuits. The multidimensional and multi-polarized topological states observed in the 3D TMs developed in Chapter 3 and Chapter 4 of this thesis could be used to build complex elastic wave networks, such as those described in Section 3.7, that provide innovative and efficient ways to route energy and information in communications systems (e.g., see the bottom panel of Fig 6.2a). 3D TMs, such as the TM fabricated and experimentally analyzed in Chapter 4, may also prove to be easy-to-test (i.e., relatively inexpensive and easy to measure and adjust when compared to semiconductor manufacturing and testing) macroscale platforms for 3D interconnect methodologies, an advantage that could support the creation of novel 3D electrical interconnect architectures in traditional semiconductor devices.

6.2.2 Innovative topological physics for mechanics (elastic wave), acoustics, photonics/ electromagnetics, and condensed matter physics

This thesis research uncovers new fundamental knowledge on the interactions between topological physics and elastic wave physics. This new understanding could be exploited in future fundamental research and the development of application-oriented devices in the fields of topological mechanics [90–96], acoustics [97,98], photonics/electromagnetics [99–102], and condensed matter physics [86–89] (Fig 6.2b). Chapter 3 and Chapter 4 illuminate the ability to project 2D topological valley physics (i.e., QVHE) into 3D layered structures and manipulate the

layer configurations and interlayer coupling to achieve bilayer- and monolayer-locked topological states. In those chapters, new insight is gained concerning the interactions of 2D surface, layer-polarized, and layer-locked states, and novel elastic wave networks are constructed from their interconnection. The outcomes from these research studies could be leveraged to create and study innovative 3D topological materials in the adjacent fields of acoustics, photonics, and condensed matter physics. In Chapter 2, an “achievable operating region” for topologically protected elastic wave propagation is explored, and its bounds are defined based on minimally acceptable topological invariant and bandgap magnitudes. The limitations (specifically, on the frequency range and achievable wave localization) of adaptive topological states are studied in the context of a locally resonant system, and the critical system properties of short circuit band dispersion, circuit resonator frequency, and electromechanical coupling are identified. Takeaways from this chapter could be leveraged in the synthesis of other tunable classical wave (i.e., elastic, acoustic, and photonic/electromagnetic) systems that are constructed via analogies to topological phases in condensed matter physics. For on-demand tunable systems in each of these fields, a map of the true adjustable range (e.g., frequency range or mode localization range) would facilitate more efficient design and better integration in practical applications. More fundamentally, derivation of these achievable operating regions in future works would provide a deeper understanding of the interactions and constraints imposed by the mechanics (or acoustics or photonics/electromagnetics) of a system when creating analogies to topological phases. The investigations outlined in Chapter 2, Chapter 4, and Chapter 5 also uncover new information on the role of local resonance in TMs, illuminating how multimodal local resonance can be leveraged to obtain first-order and higher-order topological phases with distinct frequencies and polarizations in 2D and 3D systems. Apart from the clear relevance to topological mechanics, many of these outcomes could be employed in the design of resonant topological acoustic and photonic crystals. Finally, the first evidence of nontrivial topology in fractal mechanical lattices is uncovered in Chapter 5, where practical macroscale platforms are created that may inspire future investigations on topological phases in fractal architectures, which are yet to be explored in mechanical systems (outside of this work, to the best of our knowledge). Future research would focus on uncovering generalizable rules and establishing a deeper understanding of the physics that governs the emergence of topological states in fractal mechanical lattices.

The physical platforms and theoretical investigations described within this dissertation have created a deeper understanding of multidimensional (0D, 1D, 2D, and layer-dependent) topological states and how they interact with each other. These outcomes provide a foundation for future research exploring unique topological phases and how they interface with each other in classical wave (e.g., elastic, acoustic, and photonic/electromagnetic) physics. Recently, researchers have created an automated algorithm that identifies topological electronic materials, finding 8,056 topologically nontrivial materials with numerous unique topological invariants and bulk/boundary transport phenomena [316]. In addition, topological electronic materials have previously been classified according to their topological phase signatures [317,318], and recent works have endeavored to map each topological electronic material to classical wave analogs in passive metamaterials [319,320]. In future research, machine learning (which has already been shown to be an effective tool for designing and analyzing metamaterials [321–323]) could be used to investigate how the previously mapped topological electronic materials can be manipulated in classical wave systems to uncover new hierarchies of multidimensional topological states and achieve advanced functional goals (i.e., how to take a topological electronic material and adjust its intrinsic properties in a classical wave system to achieve bulk/boundary waveguides along a hierarchy of desired dimensions and within a targeted frequency range). Furthermore, multidimensional topological phases from multiple unique candidate electronic materials could be strategically interfaced in mechanical testbeds (i.e., by creating TMs that interface multiple unique topological phases, as was done with the 3D TM in Chapter 3 of this dissertation) to achieve and understand rich new wave transport behaviors using machine learning and/or advanced evolutionary algorithms (e.g., the evolutionary pipeline defined in [324]). Such a methodology could feasibly be generalized for the investigation of unconventional topological electronic materials in classical wave systems, such as materials with aperiodicity (e.g., fractals, see Section 5.7 of this dissertation) or unconventional BZs that exhibit projective symmetries (e.g., a symmetry about a glide plane or screw axis that cannot be described by a combination of translations and rotations), including the recently developed Möbius insulators [325–327].

6.2.3 Next-generation mechanical structures and systems with physical intelligence

Significant research attention is currently being directed at the development of physical systems with embodied “intelligence” that emulates the intelligence possessed by humans

[50,249,250,328]. Systems with intelligence have the capability to perceive (e.g., sense), process (e.g., compute and decision-make), and store information (e.g., learn or retain memory), such that they can adapt their configuration/behaviors (e.g., actuate) based on a changing external environment. Many modern engineering systems achieve intelligent behaviors using integrated electronics and digital computers, which can be computationally expensive/inefficient, cumbersome to embed, and vulnerable to extreme environments and cyberattacks. To address these shortcomings, systems with physical intelligence (PI) have the features of intelligence directly embodied within their physical components [50,249,250,328]. Recent studies have unveiled mechanical structures and robotic systems that exhibit some form of embodied PI [52,329–334], creating a new paradigm that advances beyond mechanical systems with more traditional electronically embedded intelligent features. EMs have emerged as a promising building block in the quest for mechanical systems with embodied PI due to the many features of EMs that are advantageous for actuation (e.g., intriguing mechanical properties), sensing (e.g., single-sensor vibration identification and frequency-sensitive response), computation (e.g., wave-based phononic computing), and memory (e.g., non-volatile long-term memory) [12,27,338,44,49,51,54,110,335–337]. TMs, in particular, have recently been shown to make analog computation more robust to structural imperfections [114], and future research could further capitalize on the advantages and capabilities of advanced TMs (such as those developed in this thesis) in PI systems. Building upon the results in [114], where a 1D TM was used, more advanced 2D and 3D structural systems could be synthesized with robust and adaptive wave-based computing functionalities using innovative 2D/3D TMs such as those described in this dissertation. This robust functionality could extend all the way to quantum computing, where higher-order topological states have emerged as a potential route to enable and stabilize quantum computations [88,128]. As shown and discussed in Sections 3.7, 4.5, 5.6, and 6.2.1, advanced TMs can be used to create wave networks that have the potential to function as phononic processing circuits, essentially embodying computations and decision-making directly within mechanical structures (and thus minimizing the need for electronics). In the next step toward achieving PI, future research could involve the investigation of more sophisticated (beyond the logic gates and networks described in Sections 3.7, 4.5, 5.6; e.g., by building and interconnecting multiple logic elements to achieve more complex logic) wave-based computing capabilities in TMs. Another prospective line of study could investigate how to utilize TM-enabled wave-based computing as a foundation

that unlocks and integrates sensing, actuation, and memory in mechanical structures. For example, one could envision a mechanical structure that can direct its own shape change and property tailoring in response to an external vibration input based on logic computations that are processed using robust TM-enabled phononic circuitry that is integrated within its design (an intriguing recent work demonstrated a non-topological 1D EM example of this idea [339]). The combination of the novel methodologies and advanced TMs developed in this dissertation with the emerging exploration of PI offers an exciting future research opportunity involving the pursuit of next-generation mechanical structures that can autonomously and intelligently operate in various sophisticated technological applications.

Appendices

Appendix A: Supplemental Information for Chapter 2

Appendix A.1: Matrices for eigenvalue problem calculations

The classical eigenvalue problem is defined as: $([\mathbf{K}] - \lambda[\mathbf{M}])[\mathbf{u}] = 0$ (Eq. 2.13) within Section 2.2.3. Below is the explicit definition of the matrices defined in Eq. 2.13 of Section 2.2.3 and used for computation of the dispersion relation:

$$[\mathbf{K}] = \begin{bmatrix} K_{11} & K_{12} \\ K_{21} & K_{22} \end{bmatrix} \quad [\mathbf{M}] = \begin{bmatrix} M_{11} & M_{12} \\ M_{21} & M_{22} \end{bmatrix} \quad [\mathbf{u}] = \begin{bmatrix} \{W_{m,n}\} \\ v_1 \\ v_2 \end{bmatrix}$$

$$K_{11} = \begin{bmatrix} a^4 |k + G|_1^4 & 0 & 0 \\ 0 & \ddots & 0 \\ 0 & 0 & a^4 |k + G|_{N^2}^4 \end{bmatrix}$$

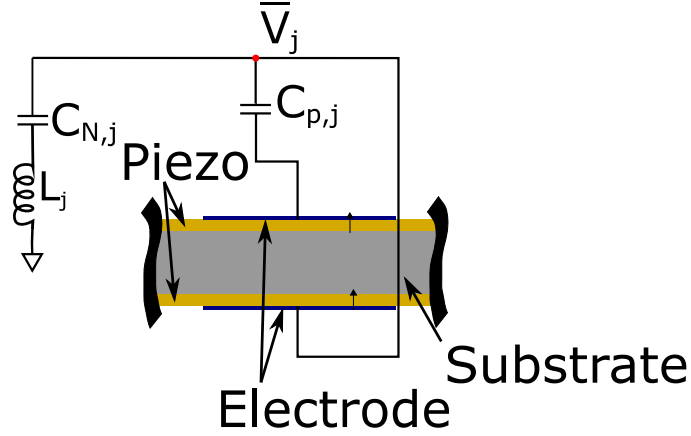
$$K_{12} = \frac{\vartheta}{1 - \xi} \frac{a^2}{A_c} \frac{a^2}{A_e} a^2 \begin{bmatrix} |k + G|_1^2 \iint_{D_1} e^{ia(k+G)_1 \cdot r} d^2r & |k + G|_1^2 \iint_{D_2} e^{ia(k+G)_1 \cdot r} d^2r \\ \vdots & \vdots \\ |k + G|_{N^2}^2 \iint_{D_1} e^{ia(k+G)_{N^2} \cdot r} d^2r & |k + G|_{N^2}^2 \iint_{D_2} e^{ia(k+G)_{N^2} \cdot r} d^2r \end{bmatrix}$$

$$K_{21} = [0]_{2 \times N^2} \quad K_{22} = \frac{\Omega_t^2}{1 - \xi} \begin{bmatrix} \frac{1}{1 + \beta} & 0 \\ 0 & \frac{1}{1 - \beta} \end{bmatrix}$$

$$M_{11} = [I]_{N^2 \times N^2}; M_{12} = [0]_{N^2 \times 2}; M_{21} = [0]_{2 \times N^2}; M_{22} = [I]_{2 \times 2}$$

$$M_{21} = -a^2 \begin{bmatrix} |k + G|_1^2 \iint_{D_1} e^{-ia(k+G)_1 \cdot r} d^2r & \dots & |k + G|_{N^2}^2 \iint_{D_1} e^{-ia(k+G)_{N^2} \cdot r} d^2r \\ |k + G|_1^2 \iint_{D_2} e^{-ia(k+G)_1 \cdot r} d^2r & \dots & |k + G|_{N^2}^2 \iint_{D_2} e^{-ia(k+G)_{N^2} \cdot r} d^2r \end{bmatrix}$$

Appendix A.2: Negative capacitance series connection



Appendix Figure A.1. Schematic of a single resonant circuit with negative capacitor connected in series.

In Section 2.2.4, the parallel connection for negative capacitance is chosen as a method to enhance electromechanical coupling. In the derivation contained in this section, it is shown that enhanced electromechanical coupling can also be achieved for a negative capacitance connected in series.

Dimensional governing equations for the metamaterial with resonant circuits connected to a negative capacitance in series (these are derived using the same methods used to derive Eqs 2.2 and 2.3 in Chapter 2):

$$D_T \bar{\nabla}^4 \bar{w}(\bar{r}, t) + \sum_{j=1}^{N_e} \frac{\theta^2}{C_{p,j}} \bar{\nabla}^2 \bar{\chi}_j(\bar{r}) \iint_{\bar{D}_j} \bar{\nabla}^2 \bar{w}(\bar{r}, t) d^2 \bar{r} - \sum_{j=1}^{N_e} \frac{\theta^2}{C_{p,j}(1-\gamma_j)} \bar{\nabla}^2 \bar{\chi}_j(\bar{r}) \iint_{\bar{D}_j} \bar{\nabla}^2 \bar{w}(\bar{r}, t) d^2 \bar{r} + m \frac{\partial^2 \bar{w}(\bar{r}, t)}{\partial t^2} - \theta \sum_{j=1}^{N_e} \frac{C_{T,j}}{C_{p,j}} \bar{\nabla}^2 \bar{v}_j(t) \bar{\chi}_j(\bar{r}) = 0 \quad (\text{A.1})$$

$$L_j C_{T,j} \frac{\partial^2 \bar{v}_j(t)}{\partial t^2} + \bar{v}_j(t) + \frac{\theta}{1-\gamma_j} \iint_{\bar{D}_j} L_j \frac{\partial^2}{\partial t^2} \bar{\nabla}^2 \bar{w}(\bar{r}, t) d^2 \bar{r} = 0, \quad j = 1 \dots N_e \text{ electrode pairs} \quad (\text{A.2})$$

$C_{T,j}$ is the total capacitance and γ_j is the series negative capacitance factor for the j th circuit, and all other parameters are explicitly defined in Chapter 2. $C_{T,j}$ and γ_j are further defined below:

$$C_{T,j} = \left(\frac{1}{C_{p,j}} - \frac{1}{C_{N,j}} \right)^{-1} \quad (\text{A.3})$$

$$\gamma_j = \frac{C_{p,j}}{C_{N,j}}$$

To maintain stability, $\gamma_j < 1$. The governing equations are nondimensionalized to generalize results, with the following nondimensional variables:

$$w = \frac{\bar{W}}{a} \quad v_j = \frac{1}{a} \frac{C_{p,j}}{\theta} \bar{V}_j \quad \tau = \sqrt{\frac{1}{L_j C_{p,j}}} t \quad (\text{A.4})$$

A harmonic response is assumed at frequency ω , and nondimensional variables are substituted as such:

$$\begin{aligned} \bar{w}(\bar{r}, t) &= \bar{W}(\bar{r}) e^{i\omega t} = w a e^{i\omega \sqrt{L_j C_{p,j}} \tau} \\ \bar{v}_j(t) &= \bar{V}_j e^{i\omega t} = \frac{\theta a}{C_{p,j}} v_j e^{i\omega \sqrt{L_j C_{p,j}} \tau} \end{aligned} \quad (\text{A.5})$$

Finally, the PWE method is applied to obtain the dispersion relation:

$$\begin{aligned} &\left(a^4 |k + G|^4 - \Omega^2 + a^4 |k + G|^4 \vartheta \sum_{j=1}^{N_e} \frac{A_{e,j}}{A_c} \left(1 - \frac{1}{1 - \gamma_j} \right) \right) W(G) + \\ &\sum_{j=1}^{N_e} \frac{\vartheta}{1 - \gamma_j} \frac{a^2}{A_c} \frac{a^2}{A_{e,j}} a^2 |k + G|^2 \iint_{D_j} v_j e^{ia(k+G) \cdot r} d^2 r = 0 \end{aligned} \quad (\text{A.6})$$

$$\begin{aligned} &\left(\frac{\Omega_{t,j}^2 (1 - \gamma_j)}{(1 - (-1)^j \beta)} - \Omega^2 \right) v_j + \Omega^2 a^2 \sum_G W(G) |k + G|^2 \iint_{D_j} e^{-ia(k+G) \cdot r} d^2 r = 0 \\ &j = 1 \dots N_e \text{ electrode pairs} \end{aligned} \quad (\text{A.7})$$

As seen in Eq. A.6, for the series configuration, the effective electromechanical coupling can be enhanced according to:

$$\vartheta_{eff} = \frac{\vartheta}{1 - \gamma} \quad (\text{A.8})$$

Therefore, the effective coupling can be significantly enhanced by careful selection of γ . Per Eq. A.7, the effective tuning frequency of resonant circuits with a series-connected negative capacitor is:

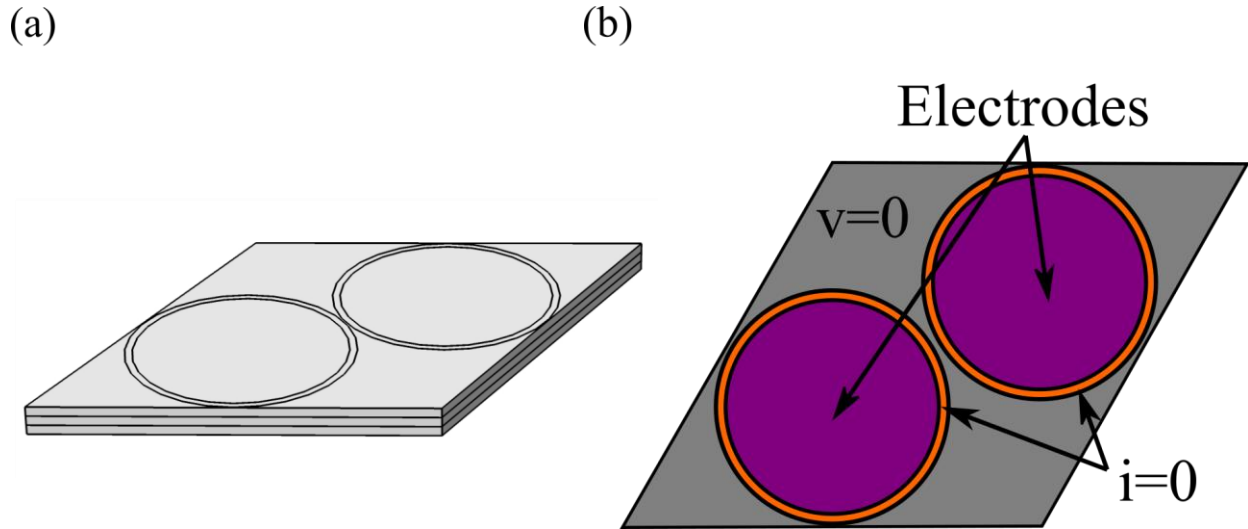
$$\Omega_{t-eff}^2 = \Omega_t^2 (1 - \gamma) \quad (\text{A.9})$$

Thus, as γ approaches unity, the electromechanical coupling present in the system is enhanced, while the effective tuning frequency is shifted to a *lower* value (as opposed to *higher* for parallel connection), which may be advantageous for applications that must function at exceptionally low frequencies.

As shown in the derivation, connection of the negative capacitance in series effectively augments the inherent capacitance contained in a resonant circuit ($C_T = (1/C_p - 1/C_N)^{-1}$) and thus reduces the magnitude of inductance required to attain a specific tuning frequency. A drawback of connecting the negative capacitor in series is that the magnitude of the negative capacitance must be larger (when compared to parallel operation) to maintain stability ($\gamma < 1$ versus $\xi < 1$). While the practical advantages and disadvantages of parallel and series connection of negative capacitance circuitry must be considered for each specific application, the same outcome of an enhanced electromechanical coupling is obtainable in either configuration.

Appendix A.3: COMSOL Multiphysics model for FE simulations

A.3.1: COMSOL FE model schematic and description



Appendix Figure A.2. Isometric (a) and top (b) views of COMSOL geometry for unit cell dispersion analysis. All dimensions and materials are specified to match those utilized in the PWE model (see Table 2.1 in Chapter 2). The top view (b) contains distinctions for the different circuit conditions that are specified at the surface of the metamaterial. The gray area is at short circuit ($v = 0$), the orange area is at open circuit ($i=0$), and the purple area is the electrode surfaces that are connected to external circuitry. The open circuit (orange) area is not explicitly included in the PWE derivation, but is included in the COMSOL FE model to prevent the occurrence of a voltage discontinuity.

The low-reflecting boundary is a feature that is built into the COMSOL Structural Mechanics module, and is used in multiple sections of this dissertation in full-scale finite element simulations that model the dynamic response to an input excitation. The intention of the low-reflection boundary is to create a boundary where waves can pass through without reflection. This is accomplished within COMSOL by creating an impedance match (for both longitudinal and shear waves) using the material data of the domain adjacent to the boundary [340]. Put simply, this boundary condition imposes a force proportional to velocity on the boundary, as described by the following equation:

$$\boldsymbol{\sigma} \cdot \mathbf{n} = -\rho c_l \left(\frac{\partial \mathbf{u}}{\partial t} \cdot \mathbf{n} \right) \mathbf{n} - \rho c_s \left(\frac{\partial \mathbf{u}}{\partial t} \cdot \mathbf{t} \right) \mathbf{t} \quad (\text{A.10})$$

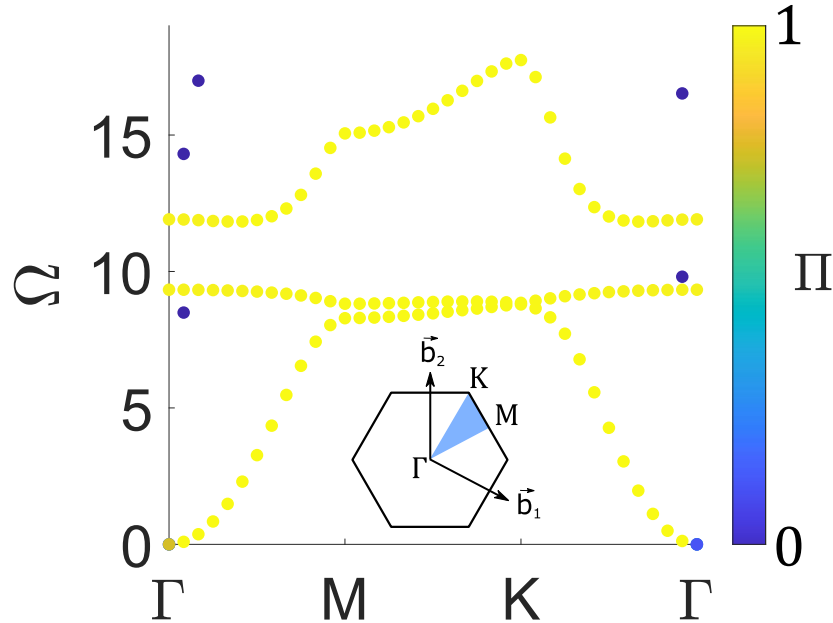
where $\boldsymbol{\sigma}$ is Cauchy stress, t is time, \mathbf{u} is the displacement field vector, ρ is the material density, c_l and c_s are the wave speeds for the longitudinal and shear waves in the material, and \mathbf{n} and \mathbf{t} are the unit normal and tangent vectors at the boundary [340].

A.3.2: FE Result- Unit Cell Dispersion Diagram with Mode Polarization

The band structure obtained from the FE model includes modes dominated by in-plane (i.e., \bar{x} - \bar{y} plane, perpendicular to the thickness of the plate) or out-of-plane (i.e., flexural, \bar{z} direction) displacement, which are referred to in this study as in-plane and out-of-plane polarized modes. A polarization parameter Π is defined to quantify the polarization for each individual mode as:

$$\Pi = \frac{\iiint_{V_U} |\bar{w}|^2 dV}{\iiint_{V_U} |\bar{u}|^2 + |\bar{v}|^2 + |\bar{w}|^2 dV} \quad (\text{A.11})$$

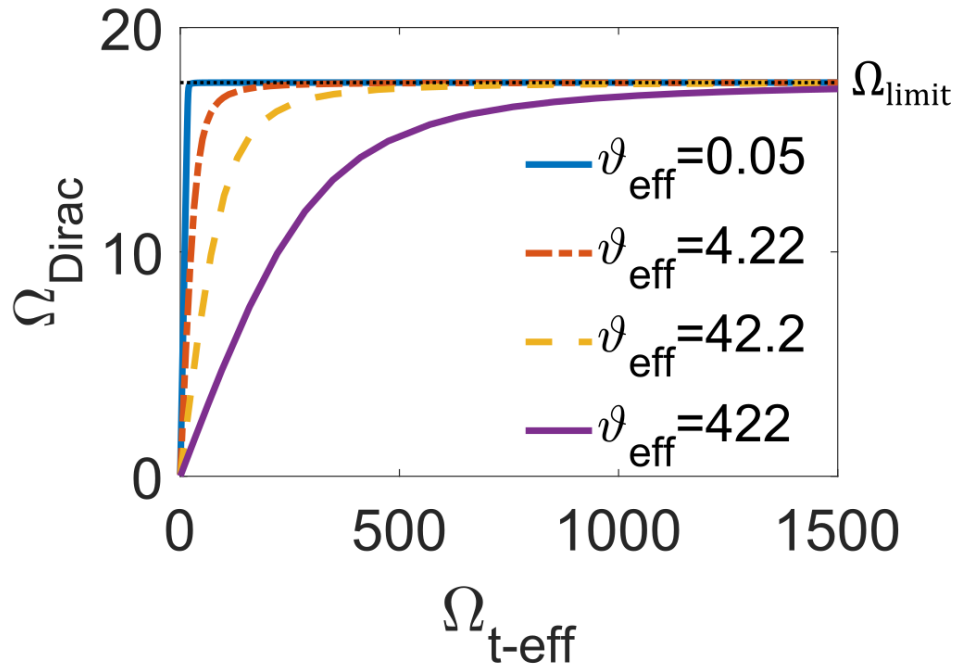
where V_U is the volume of the unit cell, and \bar{u} , \bar{v} , and \bar{w} are the displacement components in the \bar{x} , \bar{y} , and \bar{z} directions, respectively. For an in-plane polarized mode, Π is close to 0. On the other hand, Π is close to 1 for an out-of-plane mode. The unit cell band structure generated from COMSOL as shown in Fig 2.2 of Section 2.3 (with $\beta = 0$ and $\Omega_{t\text{-}eff} = 16.0$) is displayed in Appendix Figure A.3 with the polarization of each mode indicated by a colormap for Π . Flexural (out-of-plane) modes are indicated by light yellow circles, while in-plane modes are indicated by dark blue circles. It is observed that the in-plane modes obtained near Γ do not hybridize or couple



Appendix Figure A.3. Dispersion diagram for unit cell with $\beta = 0$ and $\Omega_{t\text{-}eff} = 16.0$ computed from the COMSOL FE model. The colormap indicates the polarization of the modal displacement through the polarization parameter Π . Light yellow shading indicates modes dominated by out-of-plane (flexural) displacement ($\Pi \approx 1$). Dark blue shading indicates modes dominated by in-plane ($\Pi \approx 0$) displacement.

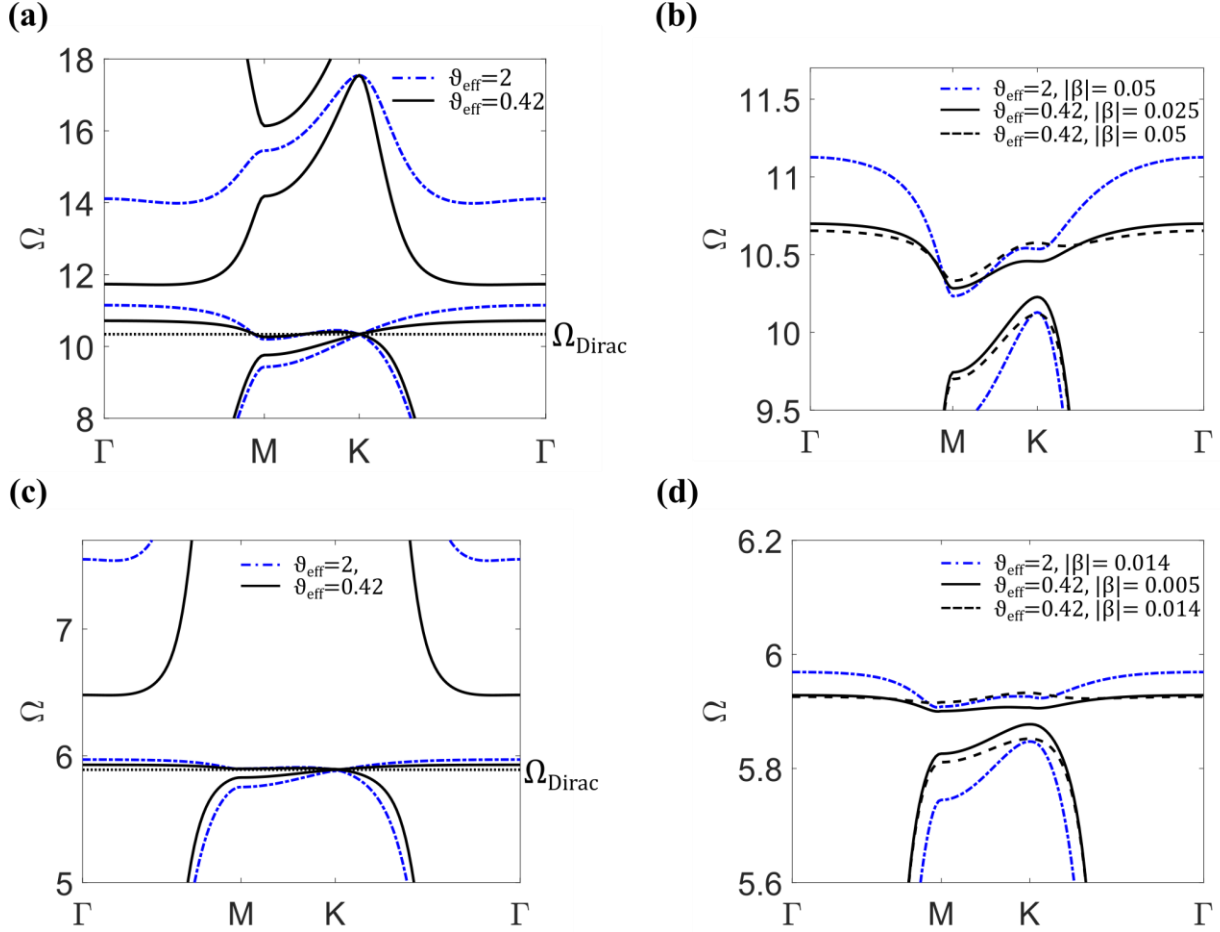
directly to the out-of-plane modes of interest in this investigation (the three light yellow bands), as there are no observable interactions between the in-plane and out-of-plane bands in the presented frequency range. As shown in previous studies [66,156] and in Section 2.3 of this dissertation, the presence of in-plane modes that are decoupled from the relevant out-of-plane modes does not inhibit the obtainment of topologically-protected flexural waves.

Appendix A.4: Frequency tunability of the Dirac point for cases of extreme electromechanical coupling



Appendix Figure A.4. Dirac frequency Ω_{Dirac} as a function of circuit tuning frequency Ω_{t-eff} for extreme ϑ_{eff} . The upper limiting frequency (Ω_{limit}) of 17.55 is indicated by a dotted black line. Ω_{limit} is unchanged, even for extremely small ($\vartheta_{eff} = 0.05$) or large ($\vartheta_{eff} = 422$) effective coupling values.

Appendix A.5: Electromechanical coupling study- band structure analysis



Appendix Figure A.5. (a) Band structure for $\vartheta_{eff} = 0.42$ (solid black lines) and $\vartheta_{eff} = 2$ (dash-dot blue lines) with $\beta = 0$ and Ω_{t-eff} selected such that $\Omega_{Dirac} = 10.4$. (b) Band structure for $\vartheta_{eff} = 0.42$ (solid and dashed black lines) and $\vartheta_{eff} = 2$ (dash-dot blue lines) with various inductance perturbations $|\beta|$ to open the Dirac point located at $\Omega_{Dirac} = 10.4$. (c) Band structure for $\vartheta_{eff} = 0.42$ (solid black lines) and $\vartheta_{eff} = 2$ (dash-dot blue lines) with $\beta = 0$ and Ω_{t-eff} selected such that $\Omega_{Dirac} = 5.9$. (d) Band structure for $\vartheta_{eff} = 0.42$ (solid and dashed black lines) and $\vartheta_{eff} = 2$ (dash-dot blue lines) with various $|\beta|$ to open the Dirac point located at $\Omega_{Dirac} = 5.9$.

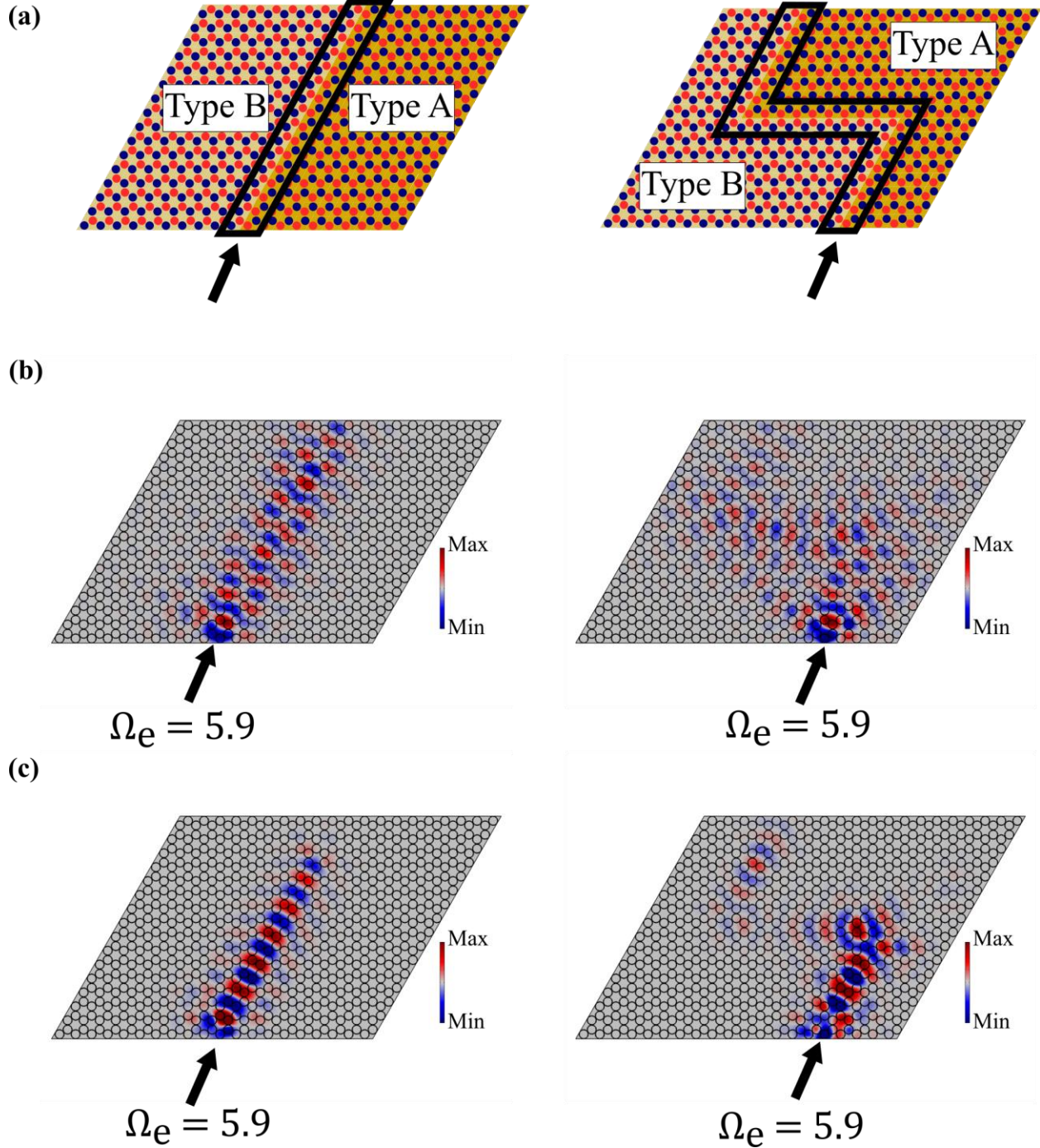
Appendix Figure A.5 contains band diagrams that illustrate how increased electromechanical coupling “shapes” the dispersion curves in a way that is beneficial to the topological properties of the metamaterial. In Appendix Figure A.5a, a Dirac point is formed at $\Omega_{Dirac} = 10.4$ for cases where $\vartheta_{eff} = 0.42$ (solid black lines) and $\vartheta_{eff} = 2$ (dash-dot blue lines). Analysis of the band structure reveals that the locally resonant bandgap that opens between the second and third bands due to the connected resonant circuitry is significantly larger for the $\vartheta_{eff} = 2$ case (bandgap spans $\Omega = 11.1$ to $\Omega = 14.0$) than it is for the $\vartheta_{eff} = 0.42$ case (bandgap spans $\Omega = 10.7$ to $\Omega = 11.7$). Due to the larger separation between bands in the case with larger coupling, the influence of the third

band and other higher order bands on the $|C_v|$ calculations is reduced, and a greater localization of the Berry curvature is possible at the K point. Thus, the valley Chern number $|C_v|$ is anticipated to be larger after applying a lattice perturbation (β) and breaking the Dirac point. This hypothesis is supported by previous investigations that discussed how separation of the two dispersion curves that create the Dirac point from other bands may lead to a larger C_v [83,159].


Apart from creating a greater separation between bands, higher electromechanical coupling also alters the shape of the second band in a manner that is conducive to a larger $|C_v|$. From further examination of Appendix Figure A.5a, the difference between Ω_{Dirac} and Ω calculated at the Γ point ($\Omega(\Gamma)$) for the second band is larger for the $\vartheta_{eff} = 2$ case ($\Omega(\Gamma) - \Omega_{Dirac} = 0.8$) than it is for the $\vartheta_{eff} = 0.42$ case ($\Omega(\Gamma) - \Omega_{Dirac} = 0.3$). Therefore, when an inductance perturbation ($|\beta|$) is applied, the second band of the $\vartheta_{eff} = 0.42$ case tends to “flatten out” (i.e., Ω is the same value for all points in IBZ of reciprocal space: $\Gamma - M - K - \Gamma$) for a smaller value of $|\beta|$, when compared to the higher coupling case. The “flattening” of the second band leads to a more rapid delocalization of the Berry curvature, as the dispersion surfaces are no longer Dirac cone-like. This phenomenon is illustrated in Appendix Figure A.5b. If an identical $|\beta|$ of 0.05 is applied to both coupling cases, the resulting $|C_v|$ is 0.3 for the high coupling case (band structure in dash-dot blue lines) and $|C_v| = 0.2$ for the lower coupling case (dashed black lines). It is observed that the second band has become “flat” for the lower coupling case, and a delocalization of the Berry curvature has followed (as indicated by the lower $|C_v|$ value). To obtain a $|C_v| = 0.3$ for the lower coupling case, $|\beta|$ must be reduced by half, from 0.05 to 0.025 (solid black lines).

To support the generality of these results across the entire Dirac frequency range, the analysis conducted for $\vartheta_{eff} = 0.42$ (solid black lines) and $\vartheta_{eff} = 2$ (dash-dot blue lines) with $\Omega_{Dirac} = 10.4$ is repeated at a lower Dirac frequency. For $\Omega_{Dirac} = 5.9$, the band structures for both coupling cases with $\beta = 0$ and $|\beta| \neq 0$ are given in Appendix Figure A.5c, and Appendix Figure A.5d. Once again, a larger band separation is observed in Appendix Figure A.5c for the higher coupling case. In Appendix Figure A.5d it can be seen that the “flattening” of the second band leads to a $|C_v| = 0.12$ for the lower coupling case with $|\beta| = 0.014$, compared to a $|C_v| = 0.30$ for the higher coupling case subjected to the same $|\beta|$. To obtain a $|C_v| = 0.3$ for the lower coupling case, $|\beta|$ must be reduced dramatically, from 0.014 to 0.005 (solid black lines).

Appendix A.6: Deep subwavelength (low-frequency) topological wave propagation

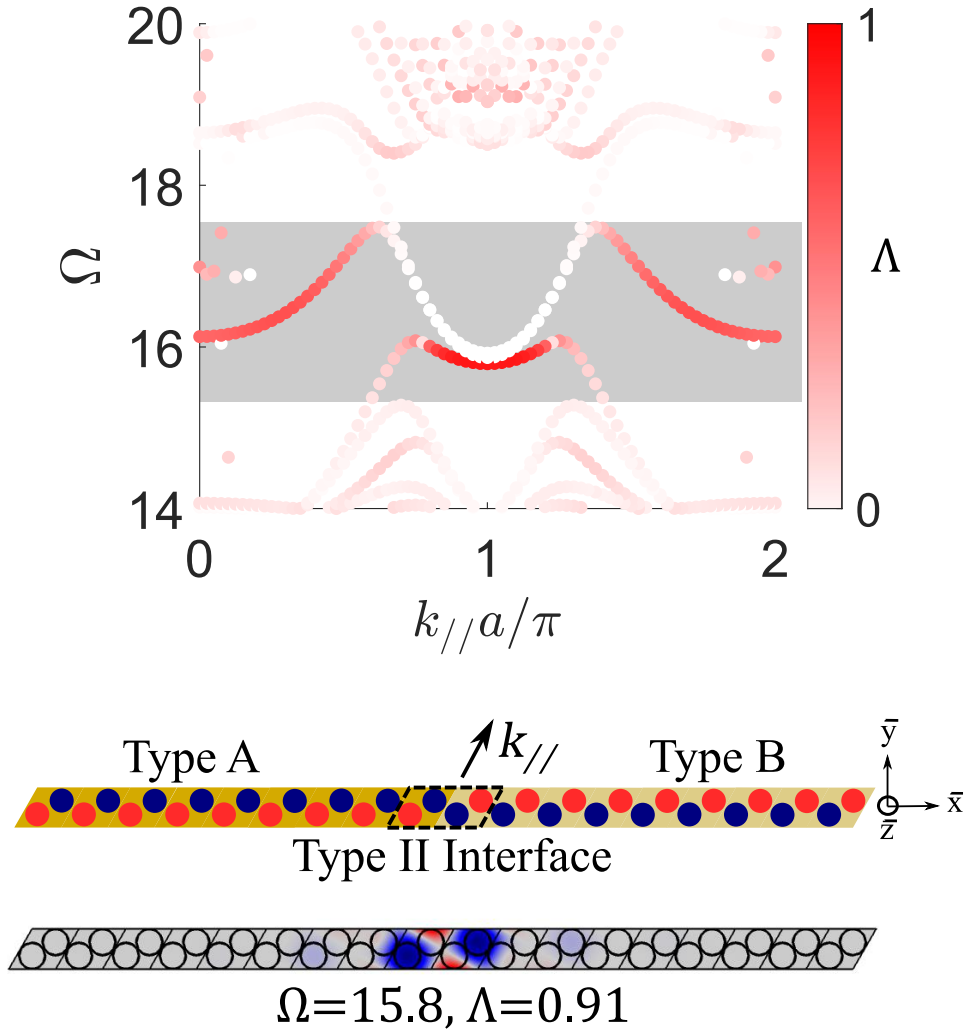


Appendix Figure A.6. (a) Schematics for thin plate metastructures with straight and Z-shaped Type I lattice interfaces (enclosed in black lines). A harmonic out-of-plane point excitation is applied where indicated by the black arrow. Negative capacitance circuitry is connected such that $\vartheta_{eff} = 2$ in all cases. (b) Steady-state displacement fields for $|\beta| = 0.014$, $\Omega_{Dirac} = 5.9$, and $\Omega_e = 5.9$. (c) Steady-state displacement fields for $|\beta| = 0.060$, $\Omega_{Dirac} = 5.9$, and $\Omega_e = 5.9$. For steady-state response, the out-of-plane displacement amplitude is indicated by the color intensity. The results illuminate how wave propagation can become delocalized at sharp corners for a $|\beta|$ that is specified as too small or too large.

FE simulations are conducted to evaluate the excitation of topological interface states at low (deep subwavelength) frequencies. Geometric, material, and negative capacitance ($\xi = 0.79$) parameters are selected to match the case presented in Fig 2.9c of Chapter 2, where $\vartheta_{eff} = 2$, $\Omega_{Dirac} = 5.9$, and $\Omega_e = 5.9$. Appendix Figure A.6 shows steady-state displacement fields for large ($|\beta| = 0.060$) and small inductance perturbation ($|\beta| = 0.014$) parameters. For $|\beta| = 0.014$, which is within the achievable operating region (see  in Fig 2.8b of Chapter 2), the flexural response is guided without a significant reduction in amplitude along the straight interface path (Appendix Figure A.6b). The flexural response is also steered along the waveguide for the Z-shaped interface route. However, significant amplitude reduction is observed at each of the sharp corners, due to energy leakage into the bulk. Thus, the specified $|\beta|$ (and corresponding band inversion and topological bandgap) is not large enough to achieve sufficient displacement localization in this case, as observed in [175]. For $|\beta| = 0.060$, the flexural response is guided along the interfaces (Appendix Figure A.6c). However, there is a significant reduction in amplitude along the Z-shaped interface at the sharp corners (Appendix Figure A.6c). This occurs because the magnitude of the lattice perturbation is too large, causing a rapid delocalization of the Berry curvature ($|C_v| = 0.005$). Due to the nearly trivial topological properties of the interface state (as indicated by the low $|C_v|$ value), unwanted delocalization and scattering occurs due to the disorder introduced at the sharp corners.

These two cases, paired with the results shown in Chapter 2 for $|\beta| = 0.032$ (successful waveguiding along multiple sharp corners, see Fig 2.9c), illustrate that within this low frequency region, a $|\beta|$ must be selected that achieves sufficient interface state localization (cannot specify $|\beta|$ too low) but does not completely sacrifice the nontrivial topological characteristics of the lattice (cannot specify $|\beta|$ too large). In a practical implementation, the adaptivity of the proposed metamaterial could provide an avenue to evaluate which $|\beta|$ provides the best performance through on-line tuning.

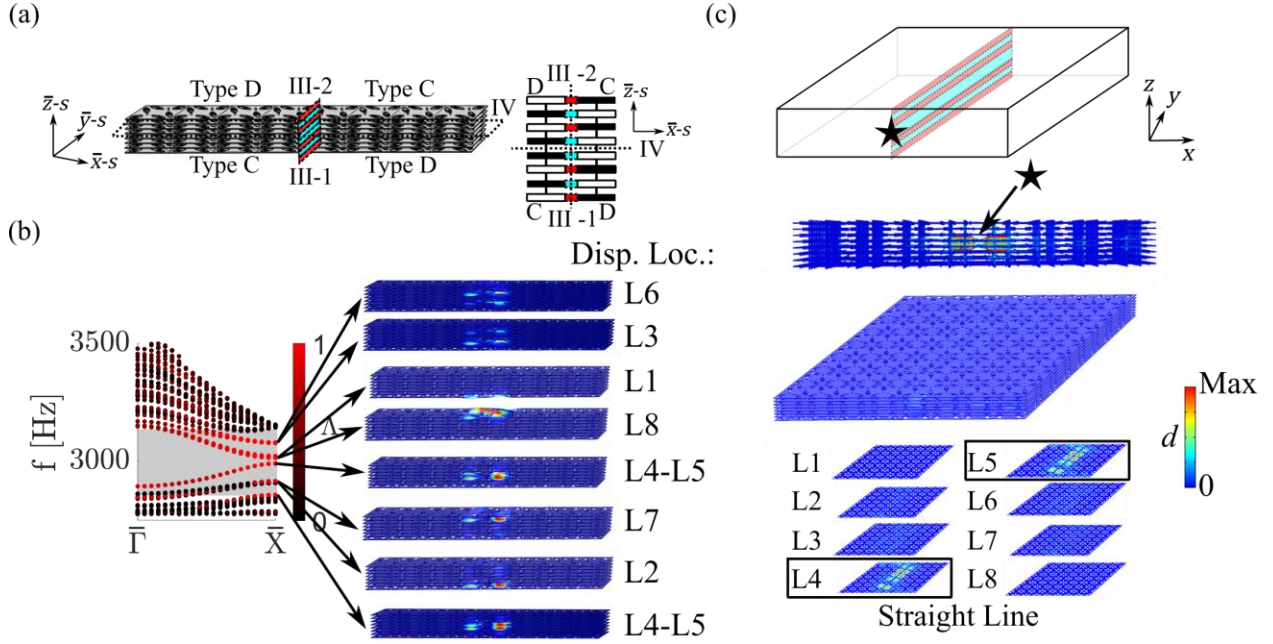
Appendix A.7: Finite strip dispersion analysis for Type II interface: antisymmetric Dirac 2 (high-frequency) interface state



Appendix Figure A.7. Band structure for a finite strip ($|\beta| = 0.70$, $\Omega_{t-eff} = 28.0$, $\vartheta_{eff} = 2$) with a Type II interface. Dark red shading indicates localized interface states ($\Lambda \approx 1$) and white shading indicates boundary states ($\Lambda \approx 0$). The rectangular gray shaded region indicates a frequency range where no bulk modes exist. Below the band structure, an antisymmetric mode shape that is calculated from the interface state at $\Omega = 15.8$ with a localized displacement ($\Lambda = 0.91$) is shown.

Appendix B: Supplemental Information for Chapter 3

Appendix B.1: Bilayer-locked topological states



Appendix Figure B.8. (a) Schematic (isometric and front views) of an eight-layer stack supercell, consisting of a four-layer Type III-2 interface stacked onto a four-layer Type III-1 interface, creating a Type IV interface. (b) Band structure for the eight-layer supercell. Topological bandgap is marked by gray shading. Colormap indicates confinement of mode displacement at the interface, with red indicating interface modes ($\Lambda \approx 1$) and black indicating bulk modes (if outside topological bandgap and $\Lambda < 1$) or boundary modes (if inside topological bandgap and $\Lambda \approx 0$). Two bilayer-locked modes and six monolayer modes exist within the topological bandgap. Displacement is localized at an interface on the layers indicated under the “Disp. Loc.” heading (e.g., for the mode with displacement localized to layer 1, “L1” is indicated to the right of the mode shape). The two L4-L5 modes are the bilayer-locked states, while the other six (L1, L2, L3, L6, L7, and L8) are monolayer states. (c) Schematic, side view, isometric view, and layer view of topological wave propagation of a bilayer-locked state in a 3D metastructure. The excitation location is marked by a black star.

The schematic of the eight-layer supercell used to investigate the bilayer-locked states is given in Appendix Figure B.8. Four layers with a Type III-2 interface are stacked onto four layers with a Type III-1 interface (see the schematic for Type III-1 and Type III-2 interfaces in Fig 3.11 a). The band structure for this supercell is numerically calculated using FE simulations, revealing eight layer-polarized topological interface states (Appendix Figure B.8b). There are eight of these topological states because this eight-layer stack is comprised of four bilayer supercells (see Fig 3.11a), which are shown in Section 3.5.2 to have two topological states each (i.e., for each layer

with a unique interface in the supercell, there is one topological state, which is predicted by the bulk-boundary correspondence [86,91]). Six of the topological states contain a displacement amplitude that is mostly localized at the interface on one specific layer. Mode shapes for these six “monolayer” states are given in Appendix Figure B.8b, where they are labeled with the layer number where their displacement is localized (L1, L2, L3, L6, L7, and L8). The monolayer states occur in pairs (L3 and L6, L2 and L7, L1 and L8, see Fig. S11(b)) on layers that are symmetric about the x - y plane. The two other topological states contain displacement that is confined at the interface on two adjacent layers, L4 and L5. Mode shapes for these “bilayer-locked” states are marked with “L4-L5” in Appendix Figure B.8b. These bilayer-locked states arise due to the coupling of two layer-polarized topological interface states on adjacent layers of the mechanical structure (the bilayer-locked states in Appendix Figure B.8b are formed from adjacent Type I interface states that are embedded into layer-polarized lattices, as can be seen from the schematic in Appendix Figure B.8a). The monolayer state pairings also contain a small amount of displacement coupling, but modal displacement is still confined primarily to one of the two layers, and this coupling is dramatically reduced for layers further from the x - y plane (i.e., the displacement of the L1 and L8 modes is nearly completely decoupled, see Appendix Figure B.8b).

The knowledge of these eight topological states, and their layer-dependent behavior, could be harnessed to achieve various advanced waveguiding capabilities. Several of these capabilities are discussed in Appendix B.2 and Section 3.7. In this Appendix B.1, comprehensive diagrams describing the 3D metastructure and switching methodology used to achieve bilayer-locked topological wave propagation in Section 3.6 are provided in Appendix Figure B.8c. In Appendix Figure B.8c, the top schematic is a diagram of the switching methodology implemented for the 3D metastructure (which is an $8 \times 8 \times 8$ lattice of unit cells). An excitation is applied where marked by the black star, at a frequency ($f_e = 2950$ Hz) and location (on L4 and L5) that selectively excites one of the bilayer-locked states. To successfully activate the bilayer-locked state, care must be taken in specifying the input excitation to be at or near the interface on L4 and L5. To minimize backscattering at the edges of the domain, low-reflecting boundary conditions are applied to the boundaries perpendicular to the x - y plane. Below the switching schematic in Appendix Figure B.8c are three separate views (isometric, side, and layer view, respectively) of the displacement field that are obtained under the specified excitation. Wave propagation is confined to the interface on L4 and L5, with negligible displacement on all other layers.

Appendix B.2: Advanced 3D elastic wave networks

Extraordinary control over the flow of elastic waves can be achieved by constructing elastic wave networks from the topological surface, layer-polarized, and bilayer-locked states of the proposed 3D EM. Networks with layer conversion and wave splitting capabilities are presented in the Section 3.7 (Fig 3.13). Further details on these wave networks and illustrations of the wave control capabilities of the proposed 3D EM are provided here with three additional cases: surface state wave splitter, reconfigurable layer converter, and multi-state wave splitter.

Surface State Wave Splitter:

The 3D metastructure comprised of an 8x8x8 lattice of unit cells from Fig 3.8 in Section 3.4 is reconfigured, such that a Type I interface (marked by blue shading in the schematic) exists for a straight line configuration (Configuration 1 in Fig 3.8) on L1-L4 and a 120° sharp corner configuration (Configuration 2 in Fig 3.8) on L5-L8 (see schematic in Appendix Figure B.9a). A harmonic excitation is chosen at 2950 Hz (to excite the Type I interface state) and placed on L3 and L4 (where marked by the black star in Appendix Figure B.9a). Results in Appendix Figure B.9b showing the steady-state displacement (d) of the metastructure indicate that topological wave propagation is split into two pathways. The wave propagates along the straight line path for L1-L4, while “turning” along the sharp corner for L5-L8. Therefore, a single topological 2D surface state can be split into two surface states with unique paths by using the reconfigurability of the 3D EM. This basic phenomenon could be used as a building block for more complicated wave filters or energy splitter networks.

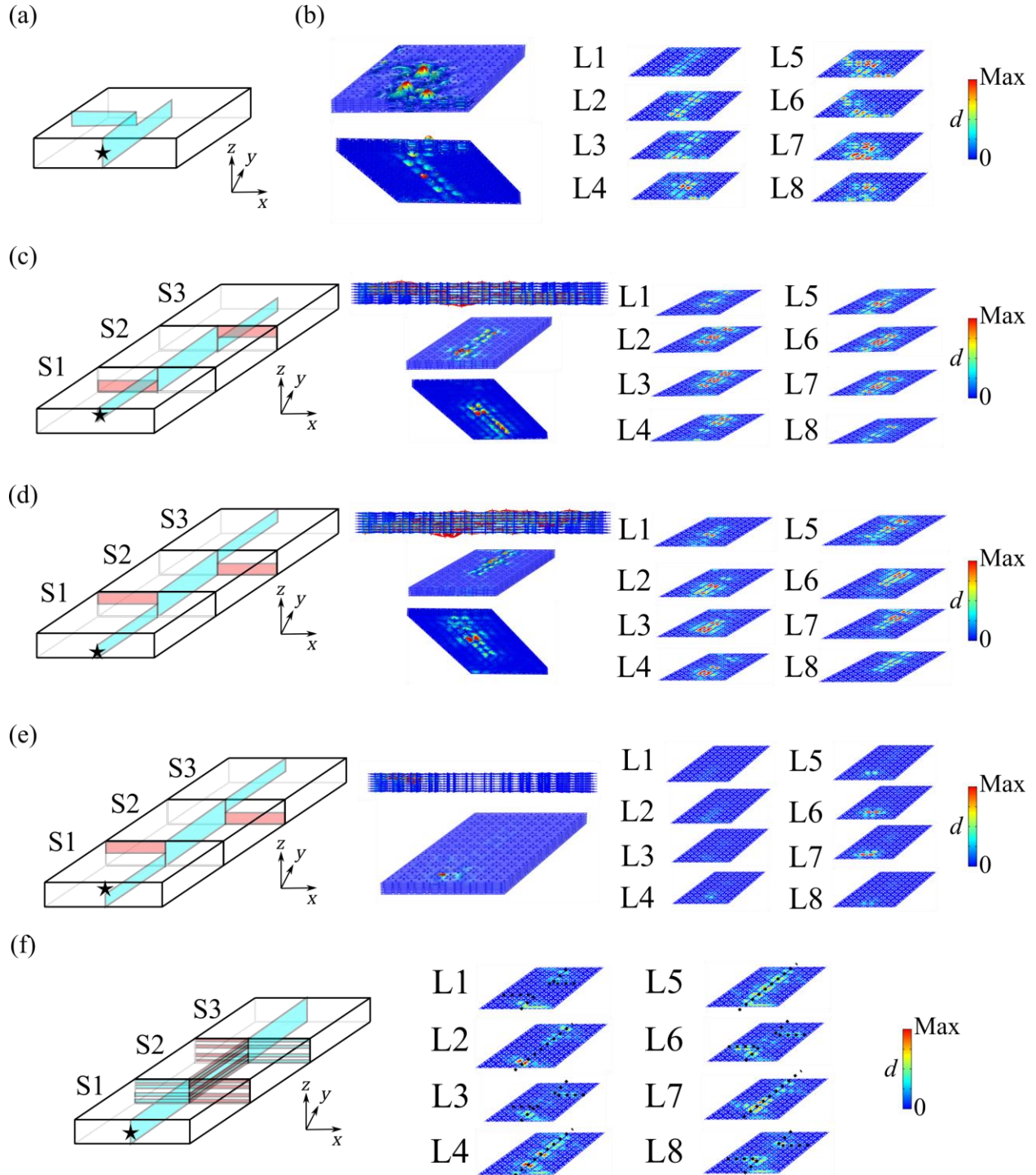
Reconfigurable Layer Converter:

An elastic wave layer converter is created in a 3D metastructure made from an 8x12x8 lattice of unit cells. The layer converter has sections defined as S1, S2, and S3 to delineate different metastable switching configurations (left side of Appendix Figure B.9c, Appendix Figure B.9d, and Appendix Figure B.9e). In the example presented in the Section 3.7, the switching configurations of S1, S2, and S3 are selected such that topological wave propagation flows from L1-L4 in S1 to L5-L8 in S3 (see schematic on the left side of Appendix Figure B.9d), given an excitation on L1-L4 in S1 that excites the Type I interface states present in the structure ($f_e = 2920$ Hz; see side view, iso views, and layer view of the steady-state displacement field d on the right side of Appendix Figure B.9d). If the 2920 Hz input excitation is placed on metastructure layers that do not contain a Type I interface (e.g., L5-L8 in S1), the displacement rapidly attenuates due

to the topological bandgap, and there is no wave propagation from S1 to S2/S3 (Appendix Figure B.9e). Thus, the layer conversion only occurs if the input is located on the correct input layer(s). If the metastable switching configuration of the layer converter is inverted (see schematic on the left side of Appendix Figure B.9c), a 3D metastructure is created that converts an input on L5-L8 in S1 to wave propagation on L1-L4 in S3 (see the steady-state displacement field for $f_e = 2920$ Hz on the right side of Appendix Figure B.9c). This result demonstrates how the direction of the layer converter may be programmed on-demand by harnessing the metastable switching capabilities of the 3D EM.

Multi-State Wave Splitter:

The combination of 2D topological surface states and layer-dependent behavior in the “wave-focusing gate” from Section 3.7 (see a schematic on the left side of Appendix Figure B.9f) can be used to create a complex multi-directional wave splitter. Given an input excitation with a frequency of $f_e = 2910$ Hz in S1, the Type I surface state is excited in S1 and S3, along with the bilayer-locked state (on L4-L5) and L2 and L7 monolayer states (see Section 3.6 and Appendix B.1 for further information on bilayer-locked and monolayer states) in S2 (Appendix Figure B.9f). In addition, at the connections between S1-S2 and S2-S3, there exists layer-dependent Type I and Type II interfaces (on L1, L3, L6, and L8), which have been previously shown to enable layer-polarized wave propagation [121]. These layer-dependent Type I interface states are also activated by $f_e = 2910$ Hz (but not the Type II layer-dependent states, see Section 3.5.2 for detail), resulting in complex and multi-directional wave splitting behavior (Appendix Figure B.9f). This intricate wave-splitting behavior could be harnessed to create elastic wave networks with numerous exotic functionalities by exploiting the combination of 2D surface, layer-polarized, bilayer-locked, and monolayer topological states that are achievable in the proposed 3D EM.



Appendix Figure B.9: (a) Schematic of the surface state wave splitter. The excitation location is marked by a black star. (b) Side view, isometric views (From above and below), and layer view of topological wave propagation in the surface state wave splitter. Schematic and steady-state displacement fields for (c-e) reconfigurable layer converter and (f) multi-state wave splitter. In all schematics (left side, a-f), Type I interfaces are indicated by blue shading and Type II interfaces by red shading. S1, S2, and S3 are sections of the 3D metastructure with specified metastable switching configurations. L1-L8 are the eight layers of the metastructure, with L1 being the bottommost layer. For all configurations in this figure (a-f), low-reflecting boundary conditions are applied to the boundaries perpendicular to the x - y plane.

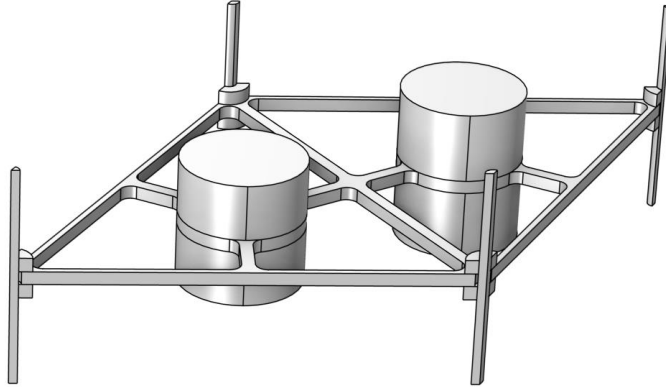
Appendix C: Supplemental Information for Chapter 4

Appendix C.1: Description of finite element simulation methods

The COMSOL Multiphysics Solid Mechanics Module is used for all band structure and dynamic response calculations. Appendix Figure C.10 contains a schematic of the unit cell used in the FE numerical simulations. The interconnecting rods are attached to the aluminum spring ligaments via hollow cylinders that approximate the nylon coupling nuts used in the experiments ($h_{nut} = 1.6$ mm, $r_{nut-outer} = 2.4$ mm, $\rho_{nut} = 1140$ kg·m⁻³, $\nu_{nut} = 0.42$, and $E_{nut} = 2.41$ GPa). The FE simulations are used to solve the governing equations for wave motion in a linear medium, represented as [25]:

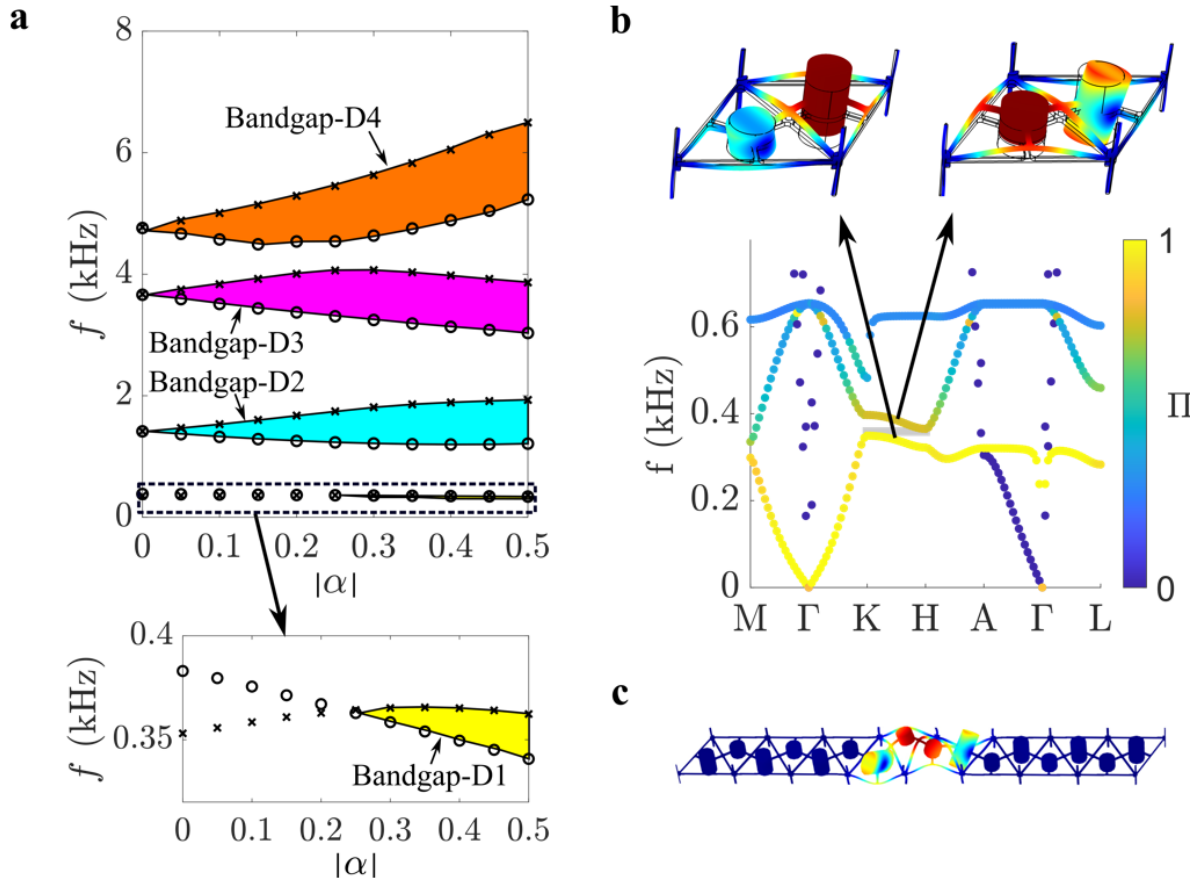
$$\rho(\mathbf{r})\ddot{u}_i = \sum_{j=1}^3 \left\{ \frac{\partial}{\partial x_i} \left(\lambda(\mathbf{r}) \frac{\partial u_j}{\partial x_j} \right) + \frac{\partial}{\partial x_j} \left[\mu(\mathbf{r}) \left(\frac{\partial u_i}{\partial x_j} + \frac{\partial u_j}{\partial x_i} \right) \right] \right\} \text{ for } i = 1,2,3 \quad (C.1)$$

where $\mathbf{r} = (x, y, z)$ is a position vector, $\rho(\mathbf{r})$ is material density, $\mathbf{u}(\mathbf{r}) = [u, v, w]^T$ is the displacement vector, $\mu(\mathbf{r})$ and $\lambda(\mathbf{r})$ are elastic constants, and $i, j = 1, 2, 3$ correspond to the coordinates x, y, z . Floquet-Bloch periodic boundary conditions are applied and a harmonic plane wave solution is used to calculate the band structure for the unit cell. A solution of the form $\mathbf{u}(\mathbf{r}; t) = \tilde{\mathbf{u}}(\mathbf{r}) e^{i(\mathbf{k} \cdot \mathbf{r})} e^{i\omega t}$ is assumed, where $\mathbf{k} = \{k_x, k_y, k_z\}$ is the Bloch wave vector, $\tilde{\mathbf{u}}(\mathbf{r})$ is the Bloch displacement vector, t is time, and ω is the temporal frequency. To construct the band structure, the eigenfrequencies are calculated for \mathbf{k} that is swept along the boundaries of the IBZ.



Appendix Figure C.10: COMSOL model for the metamaterial unit cell used in FE simulations.

Appendix C.2: Unit cell analysis of topological bandgaps



Appendix Figure C.11: (a) Evolution of the D1, D2, D3, and D4 partial bandgaps as a function of the mass perturbation magnitude $|\alpha|$. Open circles and crosses denote the lower and upper boundaries of the bandgaps opened from the four Dirac degeneracies. The D1, D2, D3, and D4 bandgaps are represented by the yellow, cyan, purple, and orange shaded regions, respectively. (b) Band structure for the large mass perturbation ($|\alpha| = 0.40$) case. The topological partial bandgap opened from the Dirac degeneracy D1 is marked with gray shading. The mode shapes for the bands bordering the bandgap illustrate the out-of-plane translational displacements of the resonators ($\Pi \approx 1$). (c) An interface mode that emerges within the D1 topological bandgap with displacement confined at the interface between the Type A and Type B segments in an eight-unit supercell.

Appendix C.3: Berry curvature and valley Chern number

The topological invariant, or the valley Chern number C_{v-p} , is calculated for each of the bands bordering the topological bandgaps that emerge from D2, D3, and D4 (Fig 4.1d). C_{v-p} is calculated as [153,227]:

$$A_p(k) = \langle u_p(k) | i \nabla_k | u_p(k) \rangle \quad (C.2)$$

$$B_p(k) = \nabla_k \times A_p(k) \quad (C.3)$$

$$C_{v-p} = \frac{1}{2\pi} \iint_v B_p(k) d^2k \quad (C.4)$$

where $A_p(k)$ is the Berry Connection, $B_p(k)$ is the Berry Curvature, $\nabla_k = \left(\frac{\partial}{\partial k_x}, \frac{\partial}{\partial k_y} \right)$ is a differential operator, $u_p(k)$ are the eigenvectors associated with the p th band (where $p = 1$ refers to the band delineating the low-frequency bandgap boundary and $p = 2$ refers to the band delineating the high-frequency bandgap boundary), and the subscript v denotes that the integral is taken around the K or H valley in reciprocal space. The eigenvectors are extracted using COMSOL with MATLAB. To ensure smoothness in the phase ambiguity over k_x - k_y , the eigenvectors are processed by a gauge transformation $|u_p(k)\rangle \rightarrow e^{i\theta^{(p)}(k)} |u(k)\rangle$, where $\theta^{(p)}(k) = \angle w^{(p)}(r_{ref}, k)$ is a reference phase calculated at an r_{ref} with non-vanishing $w^{(p)}(r_{ref}, k)$ [341,342]. The eigenvectors are then normalized according to:

$$\langle u_p(k) | u_p(k) \rangle = \iiint_{V_U} u_p^*(k) u_p(k) dV \approx \sum_{N_{pts}} V_{pt} (u_{pt}^* u_{pt} + v_{pt}^* v_{pt} + w_{pt}^* w_{pt}) = 1 \quad (C.5)$$

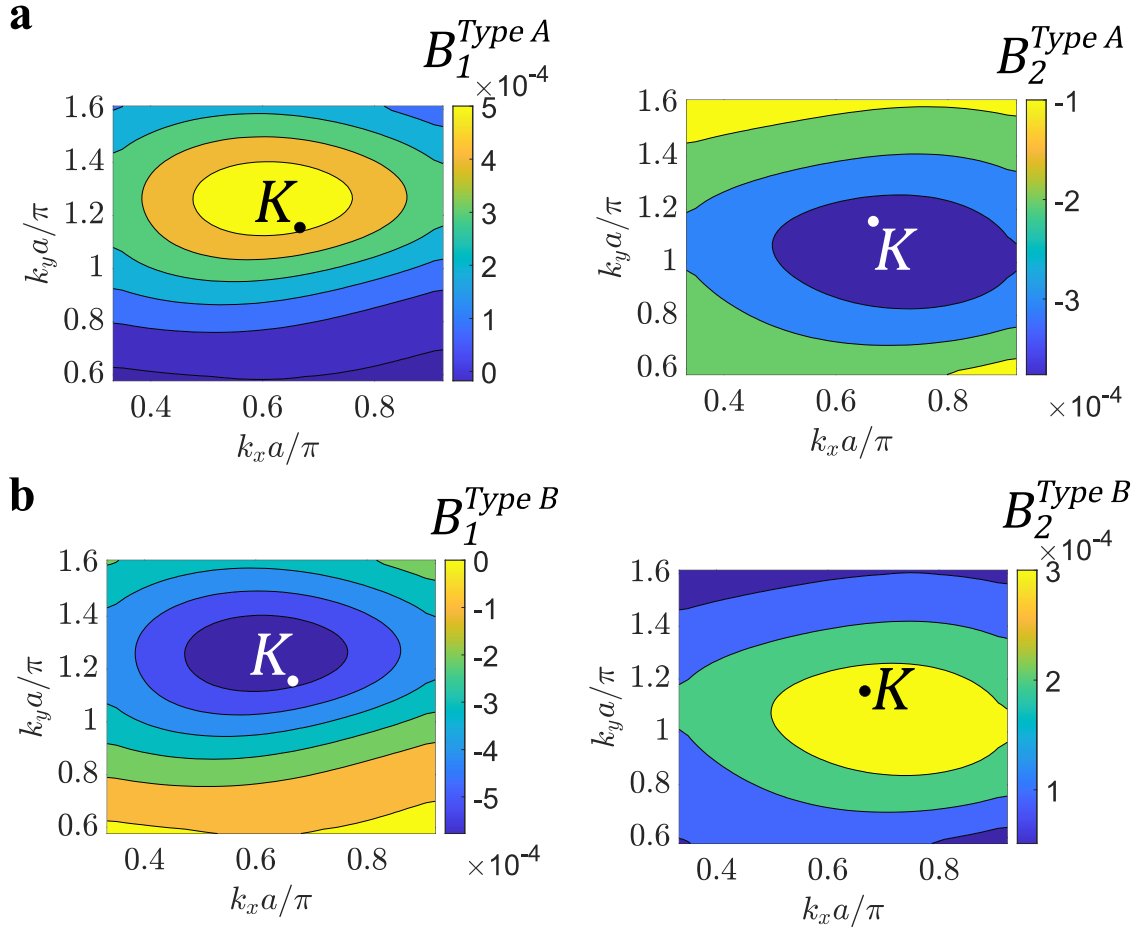
where N_{pts} is the number of considered Gauss points, V_{pt} is equal to the approximate volume around each Gauss point calculated in COMSOL, and u_{pt} , v_{pt} , and w_{pt} are the x , y , and z components of the eigenvector at each Gauss point. Eq. C.2 is evaluated as:

$$\begin{aligned} A_p(k) &= i \iiint_{V_U} \left[\left(u^* \frac{\partial u}{\partial k_x} + v^* \frac{\partial v}{\partial k_x} + w^* \frac{\partial w}{\partial k_x} \right) \hat{i} + \left(u^* \frac{\partial u}{\partial k_y} + v^* \frac{\partial v}{\partial k_y} + w^* \frac{\partial w}{\partial k_y} \right) \hat{j} \right] dV \cong \\ &\sum_{N_{pts}} V_{pt} \left[\left(u_{pt}^* \frac{\partial u_{pt}}{\partial k_x} + v_{pt}^* \frac{\partial v_{pt}}{\partial k_x} + w_{pt}^* \frac{\partial w_{pt}}{\partial k_x} \right) \hat{i} + \left(u_{pt}^* \frac{\partial u_{pt}}{\partial k_y} + v_{pt}^* \frac{\partial v_{pt}}{\partial k_y} + w_{pt}^* \frac{\partial w_{pt}}{\partial k_y} \right) \hat{j} \right] = A_{k_x} \hat{i} + \\ &A_{k_y} \hat{j} \end{aligned} \quad (C.6)$$

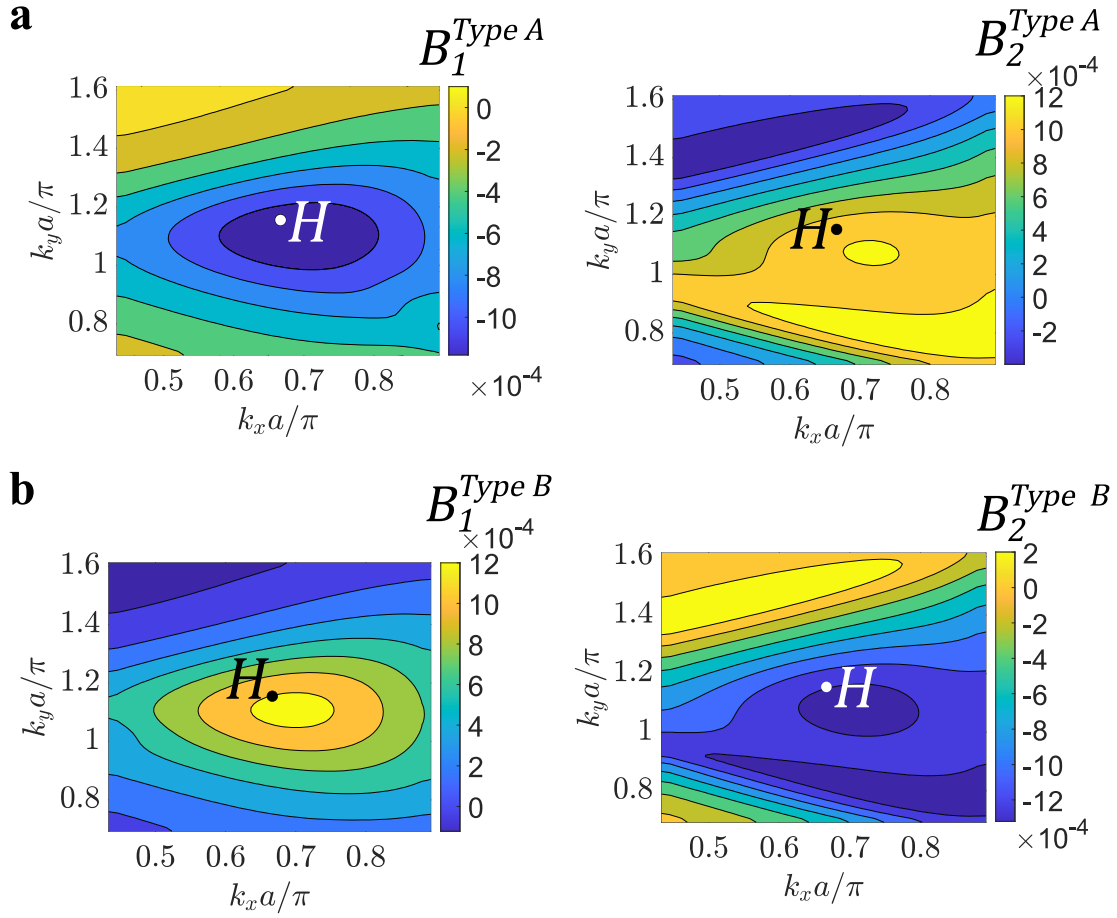
MATLAB is then used to evaluate Eqs. C.2-C.6, with the calculated C_{v-p} values listed in Appendix Table C.1 and the calculated $B_p(k)$ shown in Appendix Figure C.12, Appendix Figure C.13, and Appendix Figure C.14.

Appendix Table C.1: Valley Chern numbers calculated for D2, D3, and D4

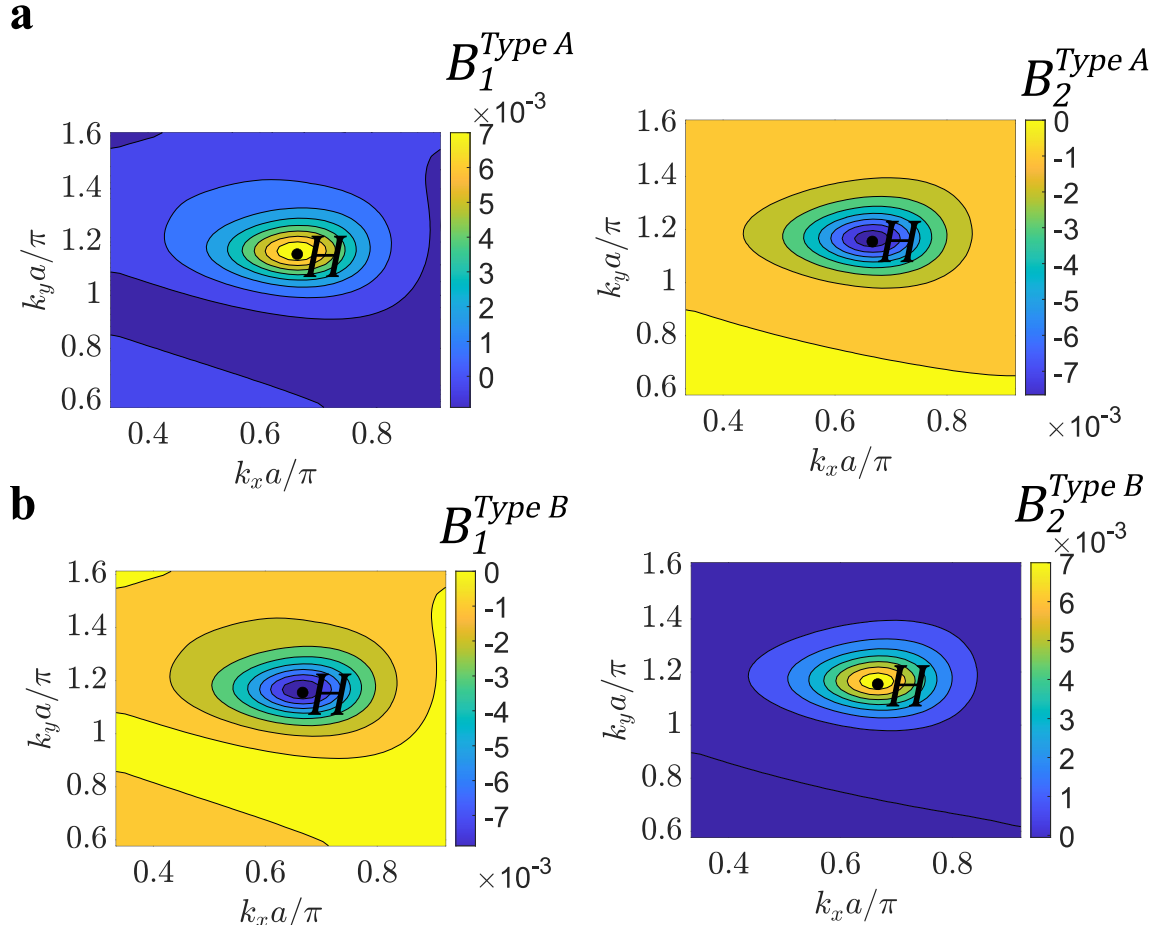
Valley Chern	D2	D3	D4
$C_{v-1}^{Type A}$	0.11	-0.14	0.25
$C_{v-2}^{Type A}$	-0.09	0.17	-0.30
$C_{v-1}^{Type B}$	-0.11	0.15	-0.26
$C_{v-2}^{Type B}$	0.09	-0.18	0.30



Appendix Figure C.12. Berry Curvature $B_p(k)$ evaluated for the bands bordering the topological bandgap that emerges from D2. (a) $B_p(k)$ for band 1 ($B_1^{Type A}$) and band 2 ($B_2^{Type A}$) of the Type A lattice. (b) $B_p(k)$ for band 1 ($B_1^{Type B}$) and band 2 ($B_2^{Type B}$) of the Type B lattice. The colorbars indicate the magnitude of $B_p(k)$. The opposite $B_p(k)$ values illustrate the band inversion between Type A and Type B lattices.

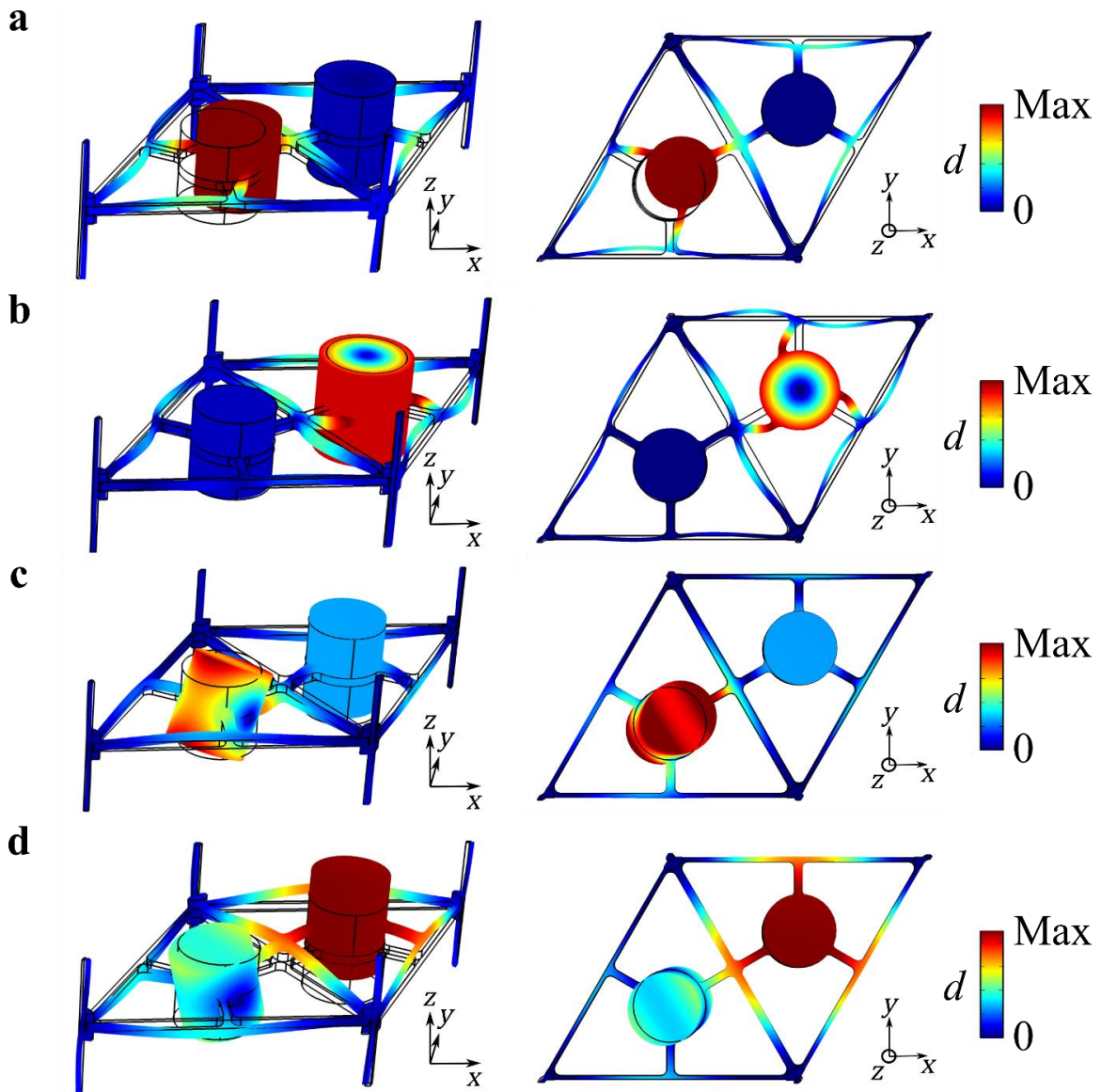


Appendix Figure C.13. Berry Curvature $B_p(k)$ evaluated for the bands bordering the topological bandgap that emerges from D3. (a) $B_p(k)$ for band 1 ($B_1^{Type A}$) and band 2 ($B_2^{Type A}$) of the Type A lattice. (b) $B_p(k)$ for band 1 ($B_1^{Type B}$) and band 2 ($B_2^{Type B}$) of the Type B lattice. The colorbars indicate the magnitude of $B_p(k)$. The opposite $B_p(k)$ values illustrate the band inversion between Type A and Type B lattices.



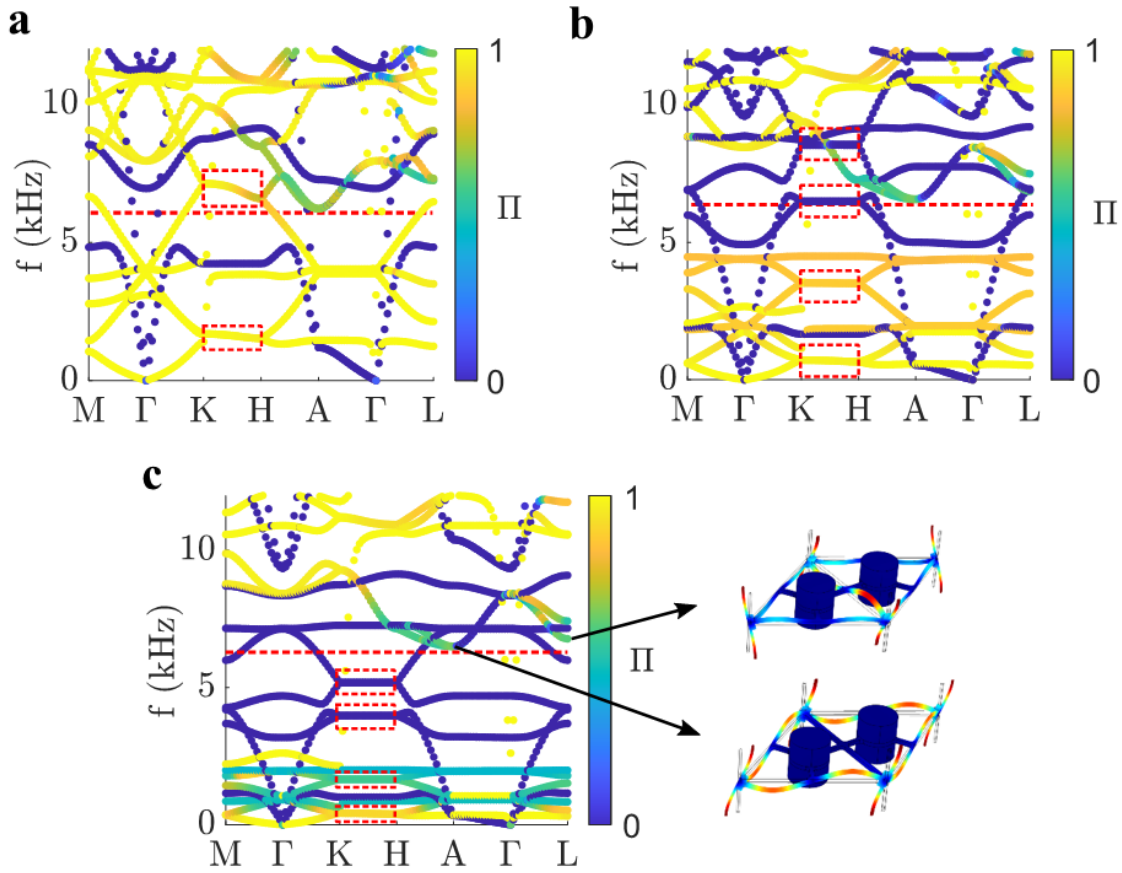
Appendix Figure C.14. Berry Curvature $B_p(k)$ evaluated for the bands bordering the topological bandgap that emerges from D4. (a) $B_p(k)$ for band 1 ($B_1^{Type A}$) and band 2 ($B_2^{Type A}$) of the Type A lattice. (b) $B_p(k)$ for band 1 ($B_1^{Type B}$) and band 2 ($B_2^{Type B}$) of the Type B lattice. The colorbars indicate the magnitude of $B_p(k)$. The opposite $B_p(k)$ values illustrate the band inversion between Type A and Type B lattices.

Appendix C.4: Mode shapes illustrating multimodal resonance

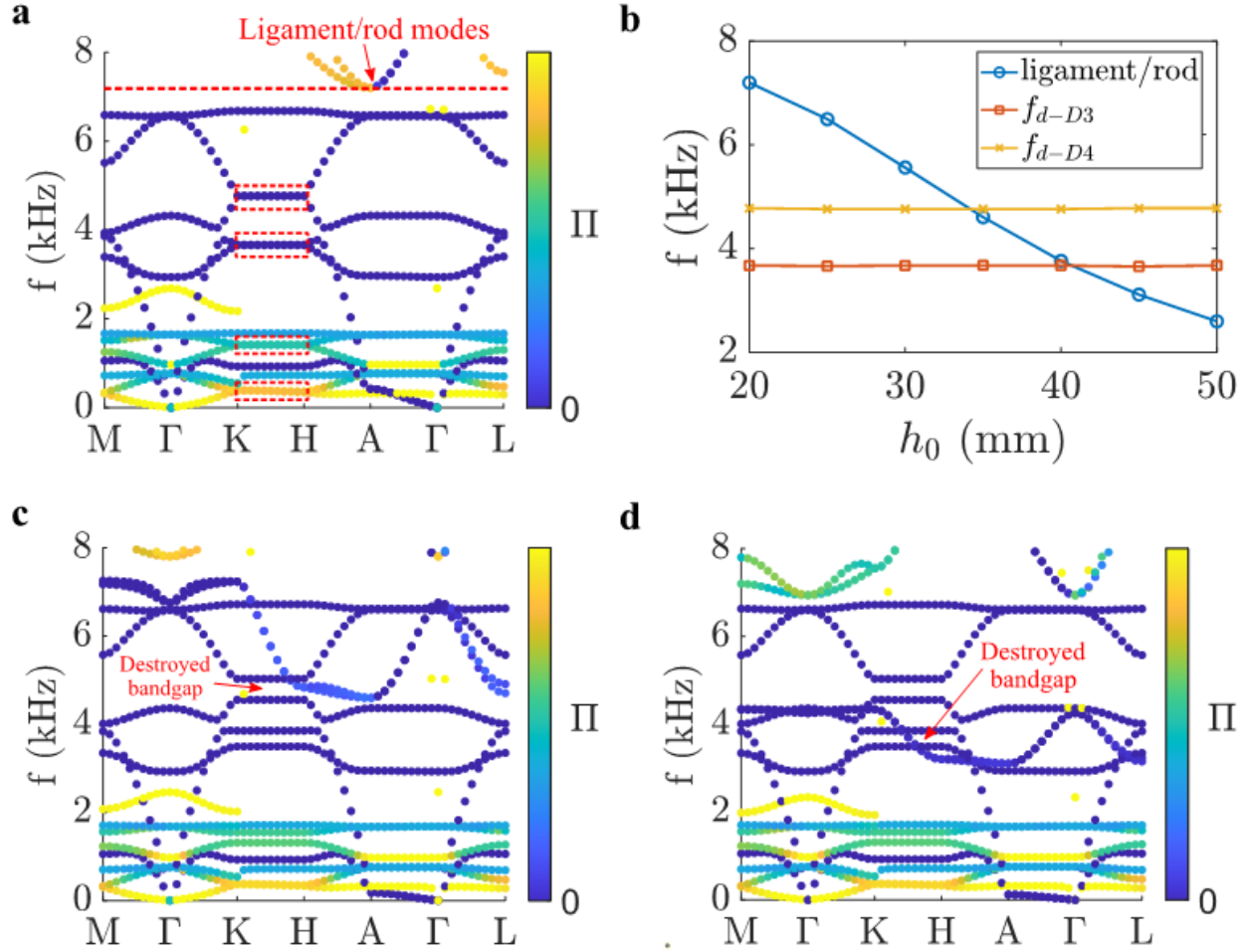


Appendix Figure C.15. Selected mode shapes for the bands bordering the four topological bandgaps that emerge when $|\alpha| = 0.11$, illustrating the four primary resonant modes of the metamaterial: (a) D4: in-plane (x - y) translational at 5.0 kHz ($\Pi \approx 0$), (b) D3: in-plane (x - y) twisting at 3.5 kHz ($\Pi \approx 0$), (c) D2: rocking at 1.5 kHz ($\Pi = 0.6$), and (d) D1: out-of-plane translational at 0.36 kHz ($\Pi \approx 1$). Both isometric and top views are provided. These mode shapes are taken for a wave vector k specified at the midpoint of the K - H line in the reciprocal unit cell.

Appendix C.5: Design considerations for Dirac frequency separation from ligament/rod modes

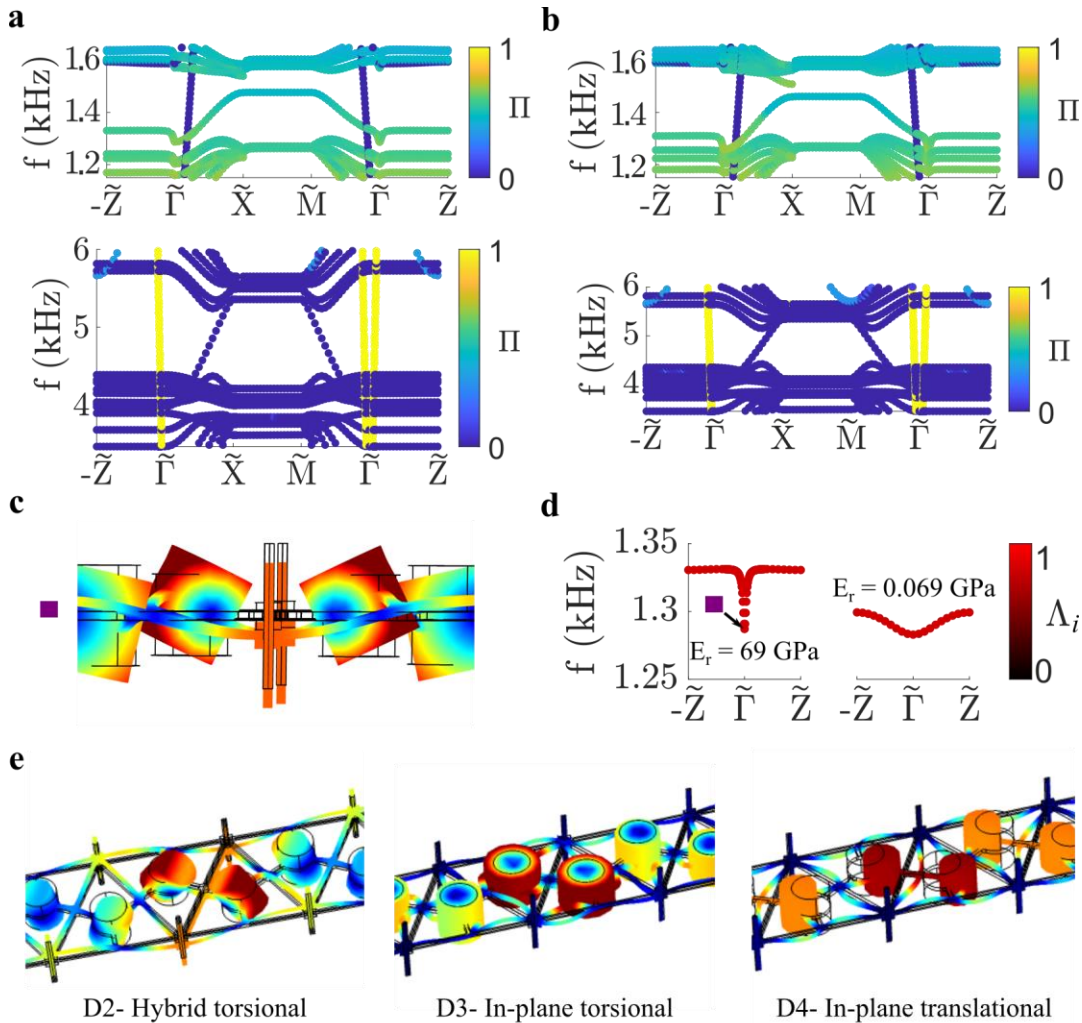


Appendix Figure C.16. Band structure for the $\alpha = 0$ case with (a) $h_m = 0$ mm (no mass), (b) $h_m = 4$ mm, and (c) $h_m = 12$ mm. The Dirac degeneracies are enclosed in dotted red boxes. These plots illustrate how increasing the resonator mass lowers the frequency f_d of the D1, D2, D3, and D4 (f_{d-D1} , f_{d-D2} , f_{d-D3} , and f_{d-D4}) degeneracies and separates them from the ligament/rod modes that exist above 6.5 kHz. The horizontal red dashed line indicates the frequency (6.5 kHz) where the undesirable ligament/rod modes emerge that may interact with the topological bands and inhibit the successful formation of topological bandgaps and waveguides. The insets illustrate how these modes are dominated by the displacements of the aluminum ligaments and interconnecting rods. For the $h_m = 0$ mm (no mass) scenario in a), only D1 and D2 are visible at frequencies less than 12 kHz, and the band structure is heavily contaminated with modes that would make it difficult to open topological bandgaps. This dense band structure is a common feature of 3D EMs, and makes the realization of low-frequency and multiband topological states in 3D structures challenging. Conversely, for a higher value of $h_m = 12$ mm, all four degeneracies D1-D4 are well separated from the ligament/rod modes in the frequency domain (i.e., f_{d-D1} , f_{d-D2} , f_{d-D3} , and f_{d-D4} are all well below the red dashed line) and are thus not susceptible to interactions with them.



Appendix Figure C.17. Analysis establishing the design criteria for the out-of-plane lattice constant h_0 , which defines the height of the interconnecting rods. (a) Band structure for $\alpha = 0$ and $h_0 = 20$ mm. The Dirac degeneracies are enclosed in dotted red boxes and the horizontal red dashed line indicates the lowest frequency of the ligament/rod modes. For this case, the ligament/rod modes emerge at 7.20 kHz, well distanced from the D3 and D4 Dirac degeneracies that are located at $f_{d-D3} = 3.66$ kHz, and $f_{d-D4} = 4.76$ kHz. (b) The ligament/rod mode frequencies are evaluated as a function of h_0 . As h_0 is increased, the mass of the interconnecting rods increases and the lateral stiffness decreases, leading to a reduction in the ligament/rod mode frequency boundary. For $h_0 \geq 35$ mm, the ligament/rod modes overlap with f_{d-D3} and f_{d-D4} . The band structures for $|\alpha| = 0.11$ are calculated with (c) $h_0 = 35$ mm and (d) $h_0 = 45$ mm. These band structures provide examples of why overlap of the topological bands with the ligament/rod modes is detrimental to the formation of topological bandgaps. The negative effects of this scenario are twofold: (i) the topological bandgaps are destroyed by the ligament/rod mode band crossing and (ii) the topological properties, as quantified by valley Chern number calculations (see Appendix C.3), are contaminated. An out-of-plane lattice constant of $h_0 = 25$ mm is chosen in Chapter 4 to ensure that no undesired band crossing occurs and provide sufficient mechanical clearance for $|\alpha|$ up to a value of $|\alpha| = 0.50$.

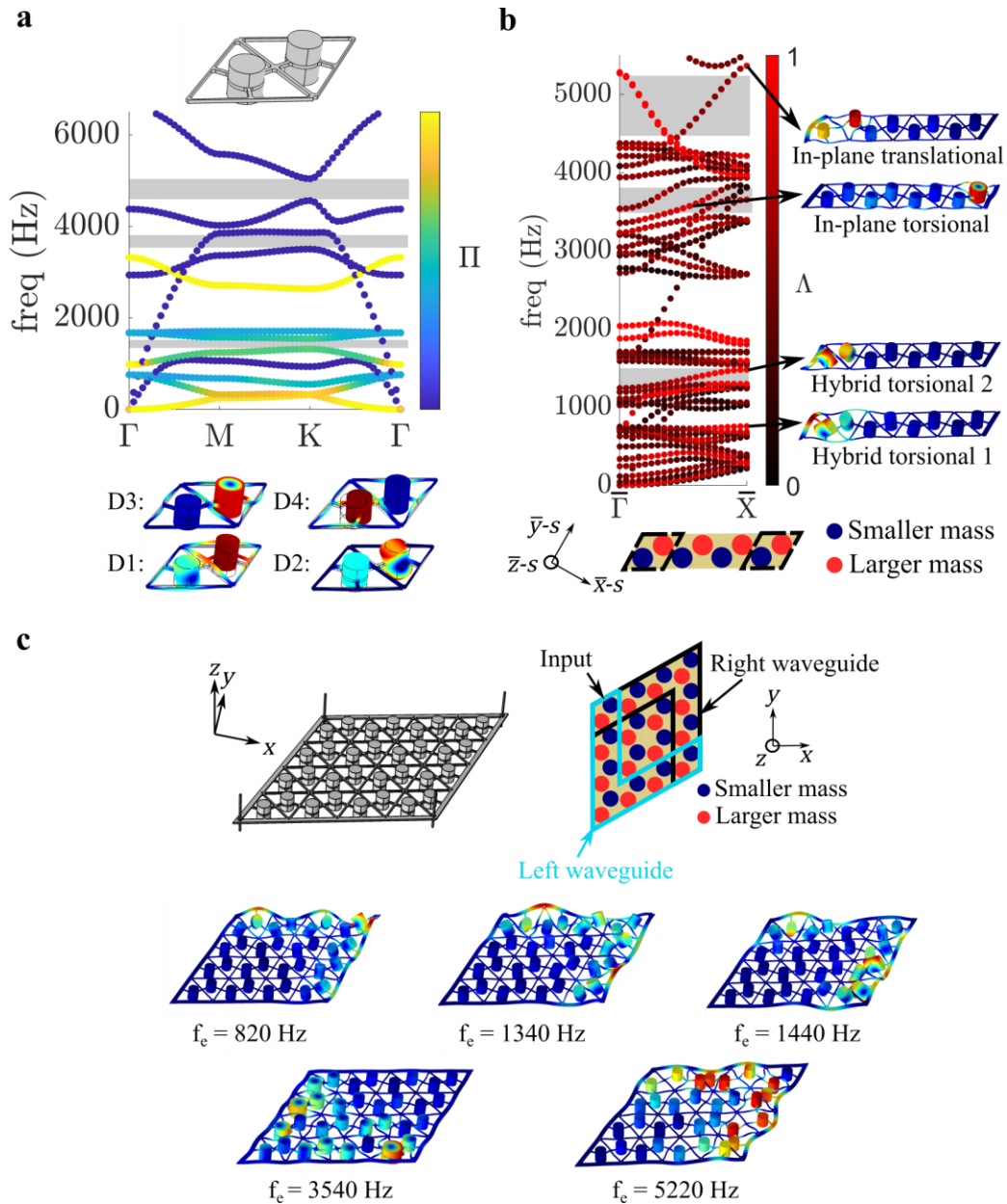
Appendix C.6: Supercell band structure analysis



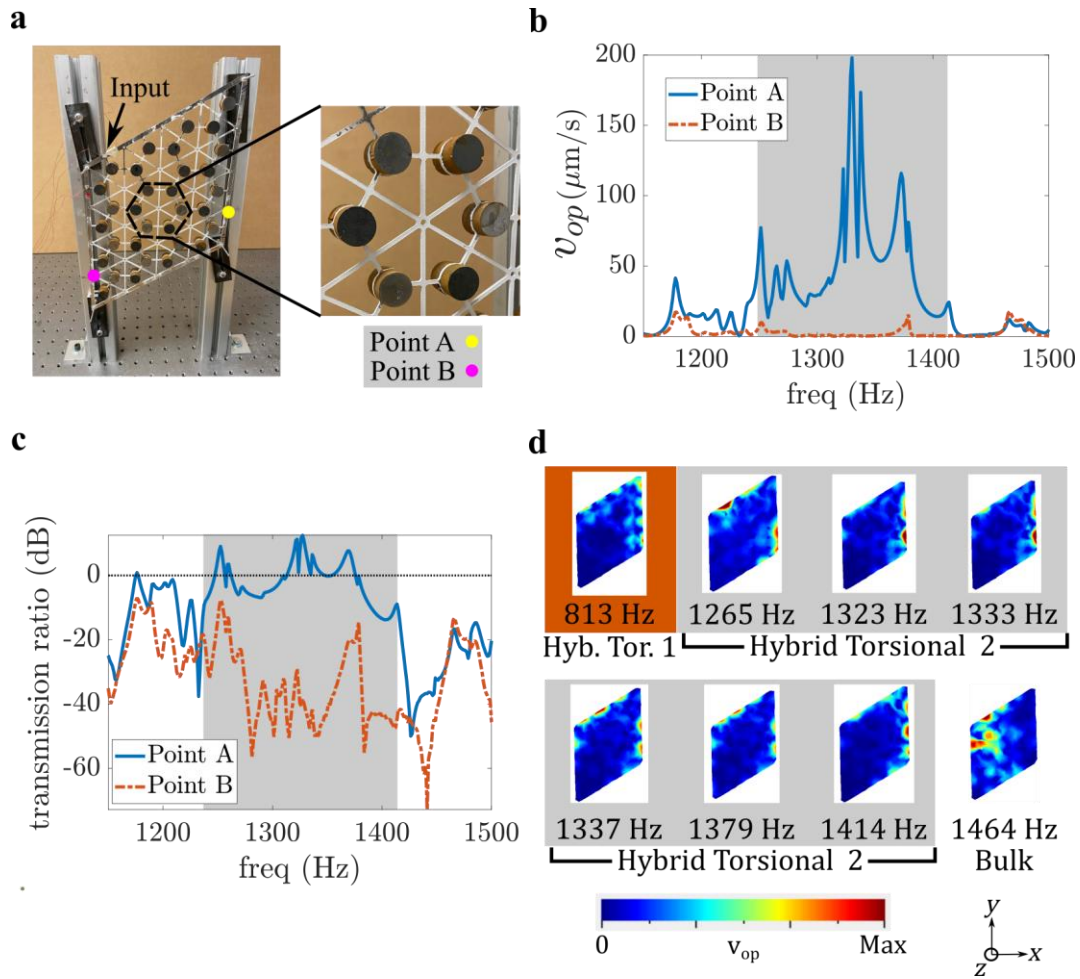
Appendix Figure C.18. (a) The band structure for the supercell with a Type I interface presented in Fig 4.3a of Chapter 4. (b) The band structure for the supercell constructed from all Type B unit cells presented in Fig 4.3d of Chapter 4. In (a) and (b), the blue bands ($\Pi \approx 0$) are in-plane modes, the yellow bands ($\Pi \approx 1$) are out-of-plane modes, and the green bands ($\Pi \approx 0.5$) are modes with mixed polarization. The bulk modes that pass through the D2 (1.3 to 1.5 kHz) and D4 (4.5 to 5.1 kHz) bandgaps contain different polarizations than the respective topological states that exist in each of the bandgaps and do not visibly interact (e.g., veering or modal energy exchange) with them. These characteristics limit the possibility of unwanted mode hybridization or coupling of bulk modes with the topological states. (c) A mode shape taken at $\tilde{\Gamma}$ (see the purple square in d) that illustrates the quasi-rigid body motion of the interconnecting rods. (d) Demonstration of how the supercell (eight-unit supercell with Type I interface) band structure can be tailored by adjusting the elastic modulus of the interconnecting rods E_r . For aluminum rods ($E_r = 69$ GPa), wave energy transmission in the z direction is limited to the long wavelength regime for a frequency range of 1.28 to 1.33 kHz. Above 1.33 kHz, the $\tilde{\Gamma}$ - \tilde{Z} directional bandgap leads to layer-locked wave propagation (e.g., given a 1.4 kHz excitation in Fig 4.4). On the other hand, for rods made from a rubber-like material ($E_r = 0.069$ GPa), the frequency range of z direction transmission shrinks to 1.28 to 1.30 kHz and the portion of the band with nonzero group velocity extends beyond the long wavelength regime. (e) A comparison of the supercell modes for the D2 hybrid torsional, D3 in-plane torsional, and D4 in-plane translational topological states. All mode shapes are evaluated at $\tilde{\Gamma}$. The mode shapes illustrate how the D2 hybrid torsional state transmits energy in the z direction by coupling the hybrid torsional resonant mode with the motion of the interconnecting rods. The D3 and D4 in-plane resonances do not couple well with the interconnecting rods (which show negligible displacement in those cases) and as a result do not propagate elastic waves in the z direction, creating layer-dependent behavior.

Appendix C.7: 2D multimodal topological metamaterial theory and experiments

The concept discussed in Chapter 4 is generalizable to 2D systems as well. A theoretical study (Appendix Figure C.19) and experiments (Appendix Figure C.20) are undertaken to show multimodal and multiband topological wave control in a 2D topological metamaterial. The 2D topological metamaterial is synthesized using the same parameters as the 3D topological metamaterial from Chapter 4, minus the hex nuts and interconnecting rods.



Appendix Figure C.19. Theoretical investigation of the 2D topological metamaterial. (a) Unit cell analysis. (b) Supercell study. (c) Full-scale simulations of topological wave control.

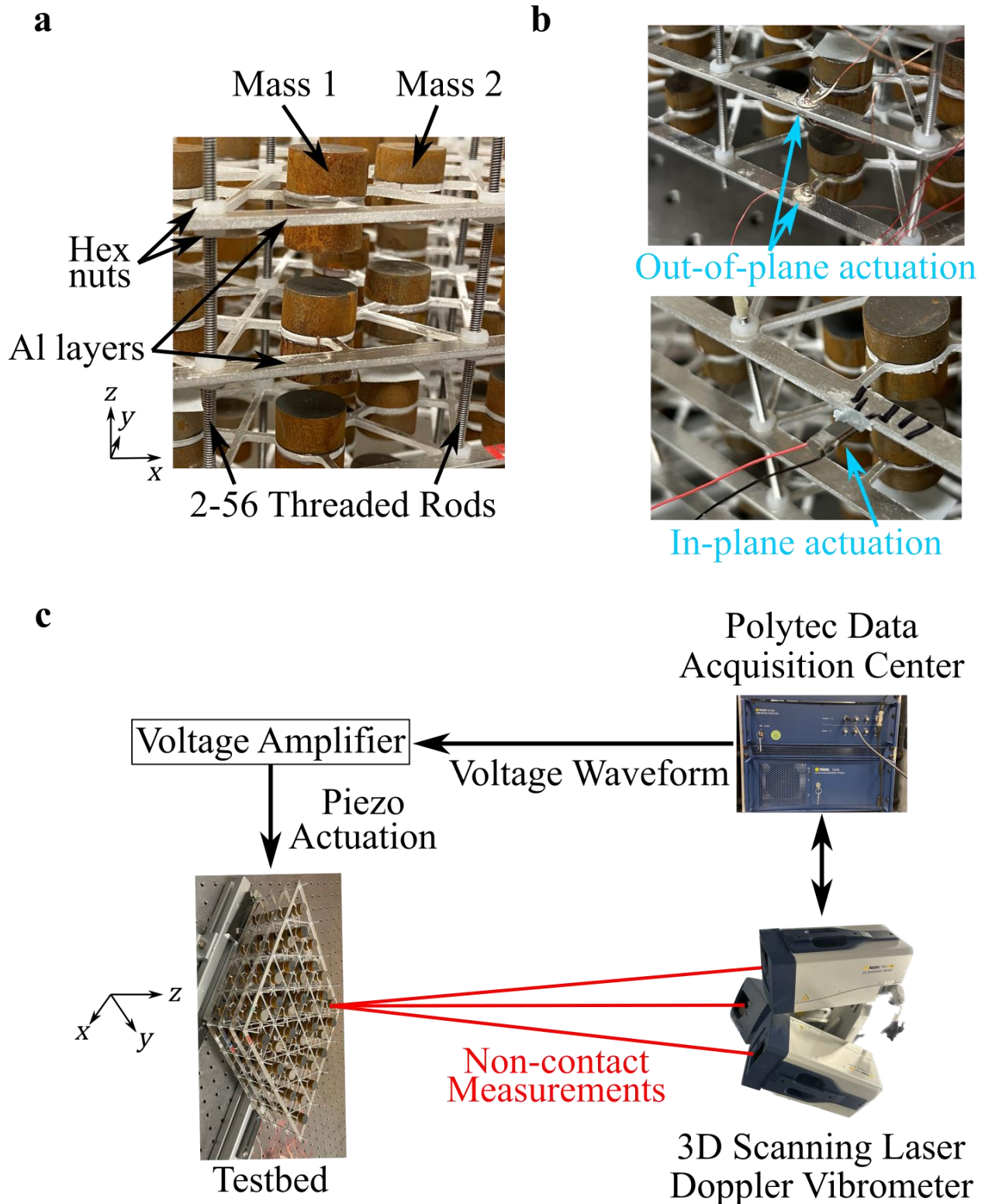


Appendix Figure C.20. Experimental investigation of wave control in the 2D topological metamaterial. (a) A schematic of the experimental setup. (b) Experimentally measured out-of-plane velocity magnitudes (v_{op}) for the frequency range of the hybrid torsional 2 topological waveguide. (c) Experimentally measured out-of-plane transmission ratio for the hybrid torsional 2 topological waveguide, where the input location is treated as the reference. (d) Steady-state wave fields illustrating topological waveguiding achieved by activating the hybrid torsional 1 and hybrid torsional 2 topological states illustrated in Appendix Figure C.19b. The experimental results reveal successful confinement of the dynamic response into the designated waveguide and agree with the theoretical predictions displayed in Appendix Figure C.19c.

Appendix C.8: Fabrication and experimental testing

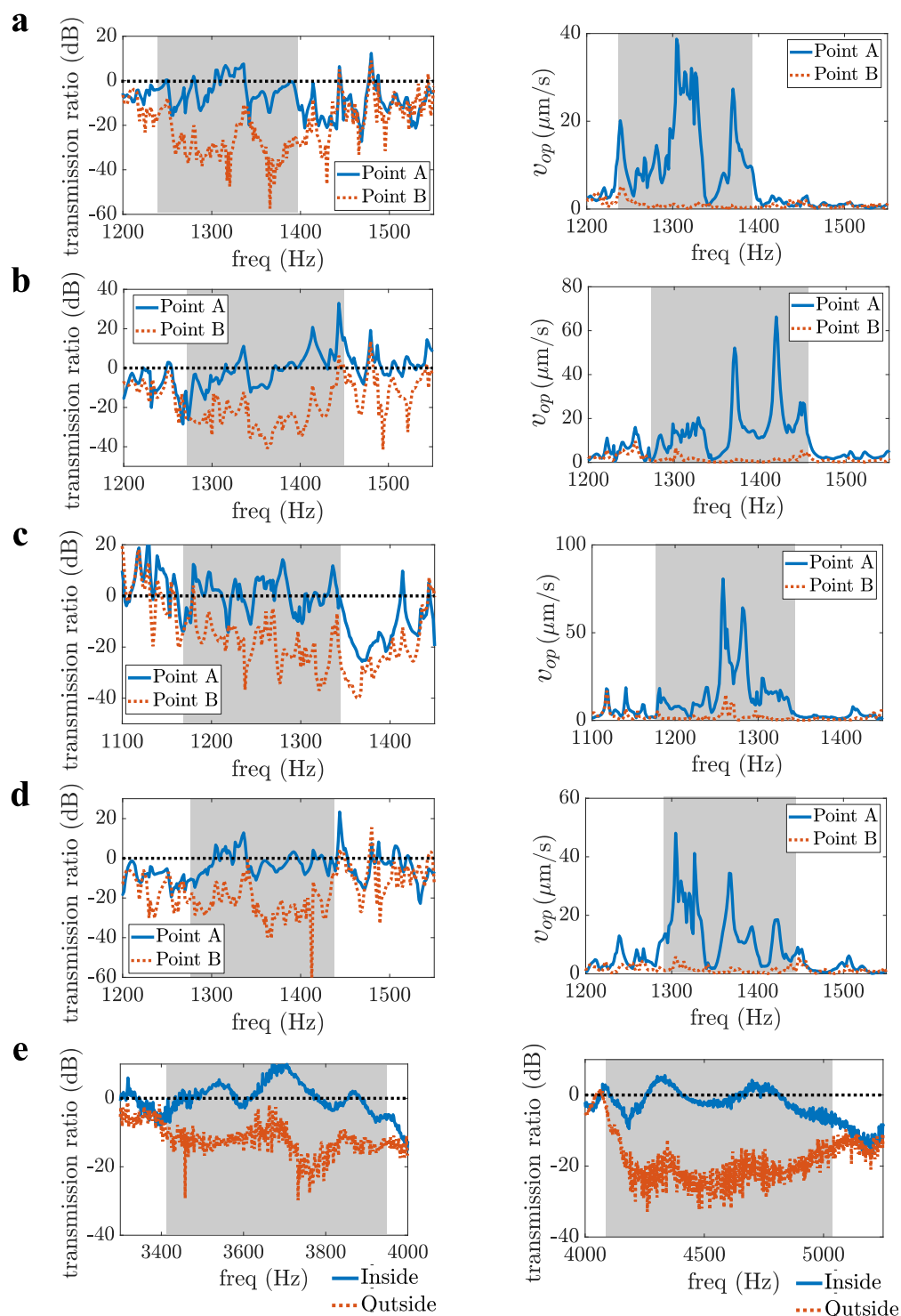
Fabrication: The experimental testbed was constructed as an assembly of multiple components (Appendix Figure C.21a). The hexagonal pattern was waterjet (OMAX) cut into four separate 1.5 mm thick aluminum (6061 alloy) sheets to create substrate layers with spring ligaments (i.e., to create the resonator springs). To form the resonator masses, cylinders with a diameter of 7 mm and two distinct height dimensions (7.9 mm for Mass 1 and 6.4 mm for Mass 2 in Appendix Figure C.21a) were waterjet cut from low-carbon (1018 cold-finished) steel bars. The masses were glued to the aluminum substrate using steel-reinforced epoxy (Permatex® Steel Weld Epoxy). Aluminum threaded interconnecting rods (2-56 threads, 102 mm length) and nylon 6/6 hex nuts were used to connect the four aluminum layers and form the 3D metastructure. To maintain the correct spacing between layers, rectangular spacers were 3D printed using the Formlabs Form 3 photopolymer printer and used to align the layers during assembly. For testing, the four outermost (i.e., farthest from the center) interconnecting rods were fastened to a base fixture (Fig 4.5 in Chapter 4).

Experimental testing: STEMiNC piezoelectric ceramic (lead zirconate titanate, PZT) disc transducers (with a radius of 5 mm and a thickness of 0.4 mm) were glued (MG Chemicals 8331-14G Silver Conductive Epoxy) to the metastructure in a bimorph configuration to provide a flexural (z direction, out-of-plane) excitation (Appendix Figure C.21b). For the in-plane actuation, piezoelectric stack actuators (PICMA® P-882.11) were attached to the structure using Endevco Accelerometer Mounting Wax (Appendix Figure C.21b). A schematic of the entire experimental setup is given in Appendix Figure C.21c. A Polytec PSV-500 scanning laser Doppler vibrometer (SLDV) was used to acquire the out-of-plane measurements. Since only one laser was required for out-of-plane velocity (\dot{w}) measurements, the laser was guided through the gaps in the layers closest to the vibrometer head to reach all four layers, such that a full wave field could be acquired for the entire 3D structure. For the out-of-plane testing, a 90V (using a voltage amplifier) periodic chirp with a bandwidth of 0 to 5 kHz was sent to the PZT transducers. For the in-plane measurements, a 4V periodic chirp with a bandwidth of 0 to 10 kHz was sent as an input to the piezoelectric stack actuator and the Polytec PSV QTec 3D SLDV was used to measure all three velocity components ($\dot{u}, \dot{v}, \dot{w}$). Since three lasers were required in this case, the only layer available for measurements was the top layer, L4. All measurement data was post-processed using the Polytec Data Acquisition Center and MATLAB.



Appendix Figure C.21. (a) Components of the 3D metastructure assembly. (b) The out-of-plane and in-plane piezo-actuators. (c) A schematic of the experimental setup. In-plane measurements require the use of all three lasers, out-of-plane measurements only require the use of one laser.

Appendix C.9: Experimental frequency response



Appendix Figure C.22. Experimentally measured transmission ratio (left column) and out-of-plane velocity magnitude v_{op} (right column) for (a) L4, (b) L3, (c) L2, and (d) L1 of the 3D metastructure. (e) Transmission ratio for the in-plane twisting (left) and in-plane translational (right) experimental measurements. All transmission ratios are defined using the relevant PZT input location as the reference. The frequency ranges where the wave field is trapped in the designated waveguide are indicated by gray shading.

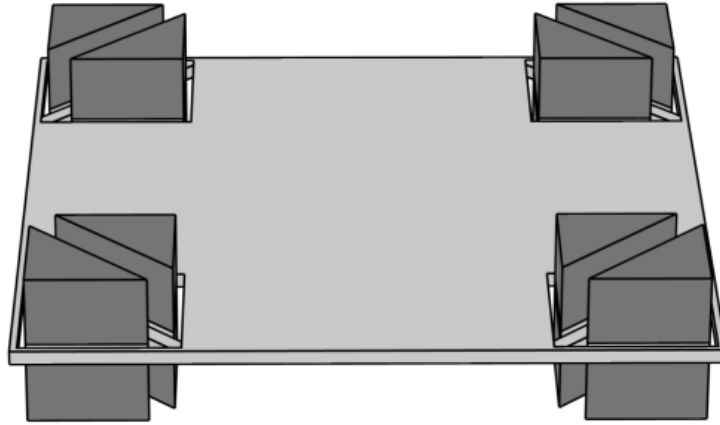
Appendix D: Supplemental Information for Chapter 5

Appendix D.1: Description of finite element simulation methods

All band structure and dynamic response calculations are conducted with the COMSOL Multiphysics Solid Mechanics Module. The unit cell used for numerical simulations is shown in Appendix Figure D.23. The governing equations for wave motion in a linear medium are [25]:

$$\rho(r)\ddot{u}_i = \sum_{j=1}^3 \left\{ \frac{\partial}{\partial x_i} \left(\lambda(r) \frac{\partial u_j}{\partial x_j} \right) + \frac{\partial}{\partial x_j} \left[\mu(r) \left(\frac{\partial u_i}{\partial x_j} + \frac{\partial u_j}{\partial x_i} \right) \right] \right\} \text{ for } i = 1,2,3 \quad (D.1)$$

where $r = (x, y, z)$ is a position vector, $\rho(r)$ is material density, $u(r) = [u, v, w]^T$ is the displacement vector, $\mu(r)$ and $\lambda(r)$ are elastic constants, and $i, j = 1, 2, 3$ correspond to the coordinates x, y, z . To calculate the band structure, Floquet-Bloch periodic boundary conditions are applied to the four unit cell boundaries and a harmonic plane wave solution of the form $u(r; t) = \tilde{u}(r) e^{i(k \cdot r)} e^{i\omega t}$ is assumed, where $k = \{k_x, k_y, k_z\}$ is the Bloch wave vector, $\tilde{u}(r)$ is the Bloch displacement vector, t is time, and ω is the temporal frequency. The band structure is produced by calculating the eigenfrequencies for k that is swept along the boundaries of the IBZ ($\Gamma \rightarrow X \rightarrow M \rightarrow \Gamma$), which is shaded in light blue in Fig 5.1a.



Appendix Figure D.23: COMSOL model of the 2D HOTM for FE calculations.

Appendix D.2: Higher-order topological index calculations and the band inversion

Eqs. 5.1-5.3 in Section 5.3 require the calculation of C_n rotation eigenvalues $\Pi_p^{(n)} = e^{2\pi i(p-1)/n}$ ($p = 1, \dots, n$) at the high-symmetry points. For a lattice with C_4 symmetry, the pertinent C_n rotation eigenvalues are [196]:

$$\Pi_1^{(2)} = e^0 = 1 \rightarrow \Delta\phi = 0 \quad (D.2)$$

$$\Pi_1^{(4)} = e^0 = 1 \rightarrow \Delta\phi = 0 \quad (D.3)$$

$$\Pi_2^{(4)} = e^{\frac{\pi}{2}i} = i \rightarrow \Delta\phi = \frac{\pi}{2} \quad (D.4)$$

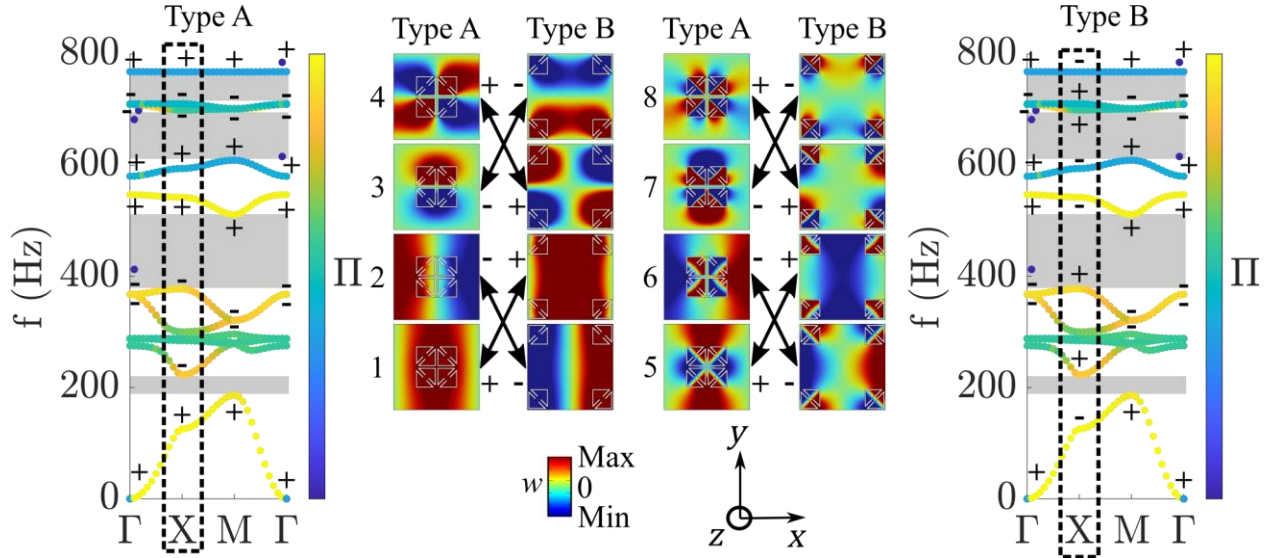
where the phase difference is defined as $\Delta\phi = \phi_{P^*} - \phi_P$, P is any point in the unit cell, and P^* is the point that overlays point P after a $2\pi/n$ rotation. The phase difference for each band is obtained from the eigenmode phase profiles, which are displayed in Fig 5.2 for the bending (bands 1-4 in Fig 5.2) and torsional (centered on the connector ligaments, bands 5-8 in Fig 5.2) bands. The phase profiles for the torsional modes centered on the spring ligaments (bands exist over ~260-300 Hz) are omitted from Fig 5.2, but are also required and accounted for in the C_n rotation eigenvalue calculations for bandgaps II, III, and IV. The C_n rotation eigenvalues obtained for each of the four bandgaps (I-IV) are shown in Appendix Table D.1. The resulting topological indices, bulk polarizations, and corner charges are found in Appendix Table D.2.

Appendix Table D.1: C_n rotation eigenvalues at high-symmetry points of Type A and Type B lattice configurations for the 2D HOTM

C_n Rot. Eigenvalue	<u>Bandgap I</u>		<u>Bandgap II</u>		<u>Bandgap III</u>		<u>Bandgap IV</u>	
	Type A	Type B	Type A	Type B	Type A	Type B	Type A	Type B
$\#\Gamma_1^{(2)}$	1	1	3	3	5	5	5	5
$\#\Gamma_1^{(4)}$	1	1	2	2	2	2	2	2
$\#\Gamma_2^{(4)}$	0	0	2	2	2	2	3	3
$\#\chi_1^{(2)}$	1	0	3	4	5	4	5	6
$\#M_1^{(4)}$	1	0	2	1	2	3	2	3
$\#M_2^{(4)}$	0	0	2	2	2	2	3	3

Appendix Table D.2: The topological indices, bulk polarizations, and corner charges for the 2D HOTM.

Bandgap	Type A ($\beta = 0.25$)			Type B ($\beta = 0.75$)		
	$\chi^{(4)}$	$P_x = P_y$	Q	$\chi^{(4)}$	$P_x = P_y$	Q
I	(0,0,0)	0	0	(-1,-1,0)	$\frac{1}{2}$	$\frac{1}{4}$
II	(0,0,0)	0	0	(1,-1,0)	$\frac{1}{2}$	$\frac{3}{4}$
III	(0,0,0)	0	0	(-1,1,0)	$\frac{1}{2}$	$\frac{1}{4}$
IV	(0,0,0)	0	0	(1,1,0)	$\frac{1}{2}$	$\frac{3}{4}$



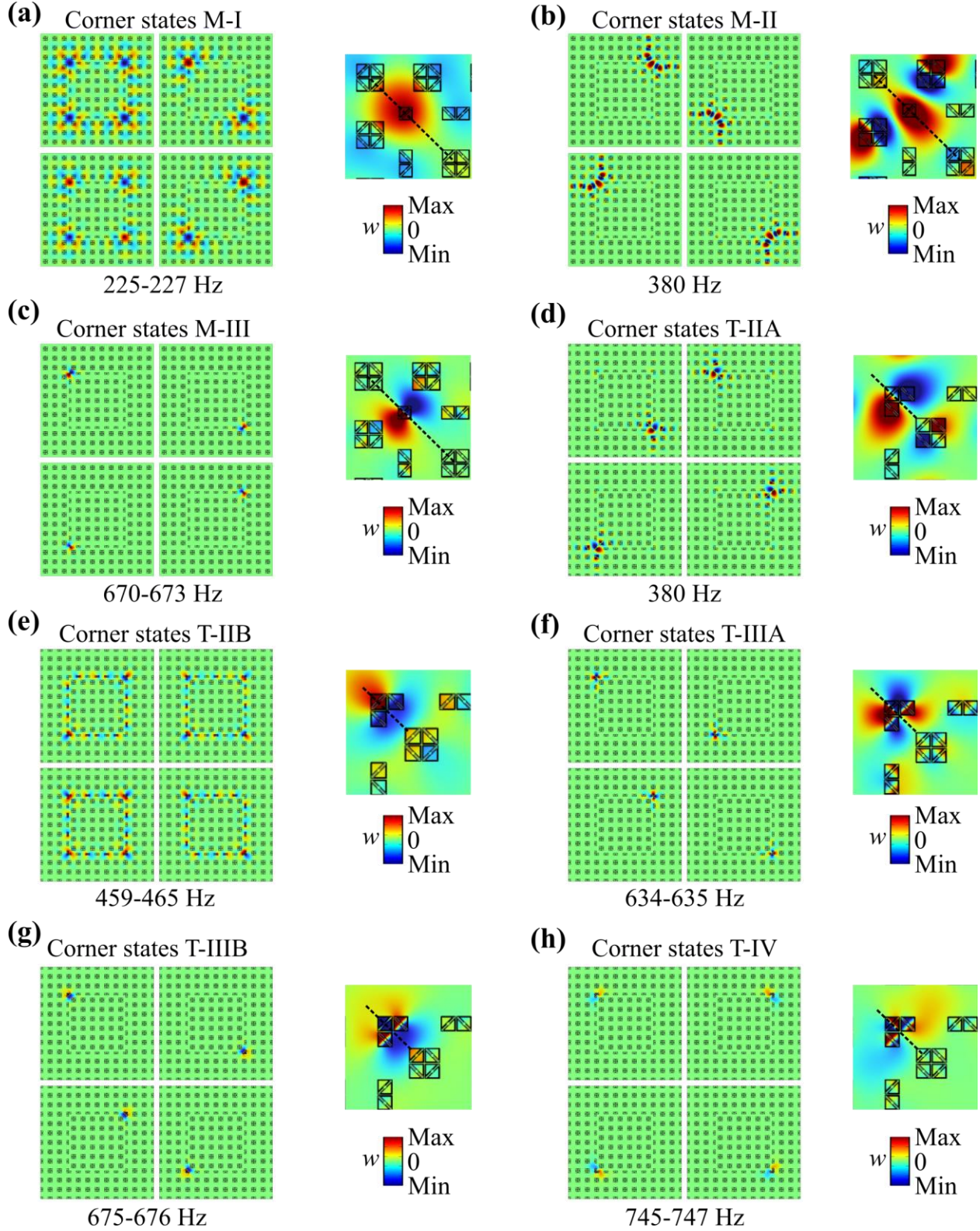
Appendix Figure D.24. A description of the band inversion that occurs between the Type A and Type B domains. The left and right panels contain the band structures for the Type A and Type B lattices, with the “+” and “-” labels representing positive and negative eigenmode parities, respectively. The parity exchange at X for both sets of bands (1-4: bending and bands 5-8: torsional) is displayed in the middle panel.

The band inversion between Type A and Type B lattices can be visualized by analyzing the parity symmetries of the eigenmodes. While the Type A and Type B lattices may have identical band structures, a parity exchange occurs at the X point of high-symmetry for bands 1-8, as illustrated in the middle panel of Appendix Figure D.24. This parity exchange is an indicator of a topological transition between trivial (Type A lattice) and nontrivial (Type B lattice) topological phases.

Appendix D.3: Coupling and symmetries of multiband topological corner states

The corner states from Fig 5.4 and Fig 5.5 have an assortment of displacement field characteristics. These characteristics are elucidated through an analysis of the out-of-plane (w) wave fields for each eigenmode (Appendix Figure D.25). The wave fields for the monomer corner states (Appendix Figure D.25a,b,c) and the trimer corner states (Appendix Figure D.25d,e,f,g,h) are evaluated for (1) their symmetry about an angular bisector, (2) the number of active resonant sites, (3) the level of wave localization at the corner, and (4) the presence of multipolar coupling. The attribution of these features to each of the eight corner states identified in Chapter 5.5 is tabulated in Appendix Table D.3.

The results listed in Appendix Table D.3 indicate that there are four symmetric and four asymmetric corner states in the 2D HOTM, where symmetry is judged about the bisecting black dashed line superimposed onto each eigenmode in Appendix Figure D.25. For the five trimer corner states, there are three that involve activation of all three resonators (T-IIB, T-IIIA, and T-IV) and two that involve the activation of two resonators (T-IIA and T-IIIB). Furthermore, inspection of the two trimer corner states with asymmetric displacements and all three resonators active reveals distinctive wave fields (T-IIIA and T-IV, Appendix Figure D.25f,h). The localization of the corner states is quantified by the parameter γ_{corner} (Eqs. 5.4 and 5.5 in Section 5.5). The γ_{corner} values in Appendix Table D.3 vary over a range of 0.05 to 0.68, quantifying the diverse localization characteristics that are qualitatively recognizable upon inspection of the eight corner states in Appendix Figure D.25, Fig 5.4, and Fig 5.5. In general, the torsional corner states M-III, T-IIIA, T-IIIB, and T-IV exhibit higher localization than the bending corner states M-II, T-IIA, and T-IIB. This is due to the torsional resonant mode being more decoupled from the plate substrate (and thus, more decoupled from other resonators), when compared to the bending resonant mode (see Fig 5.1c in Chapter 5). It is also noted that the low localization of Corner state M-I and the influence of the coexisting Edge state II for Corner state T-IIB facilitate multipolar coupling in those corner state displacement profiles. For Corner state M-I, a monopolar mode (top left in Appendix Figure D.25a), two dipolar modes (top right and bottom right in Appendix Figure D.25), and one quadrupolar mode (bottom left in Appendix Figure D.25) emerge due to the interactions between the evanescent wave fields emanating from the four corners of the lattice [276]. For Corner state T-IIB, the multipolar phenomenon is a result of the coexisting Edge state II, which creates a coupling between the four corners of the lattice. All other corner states do not



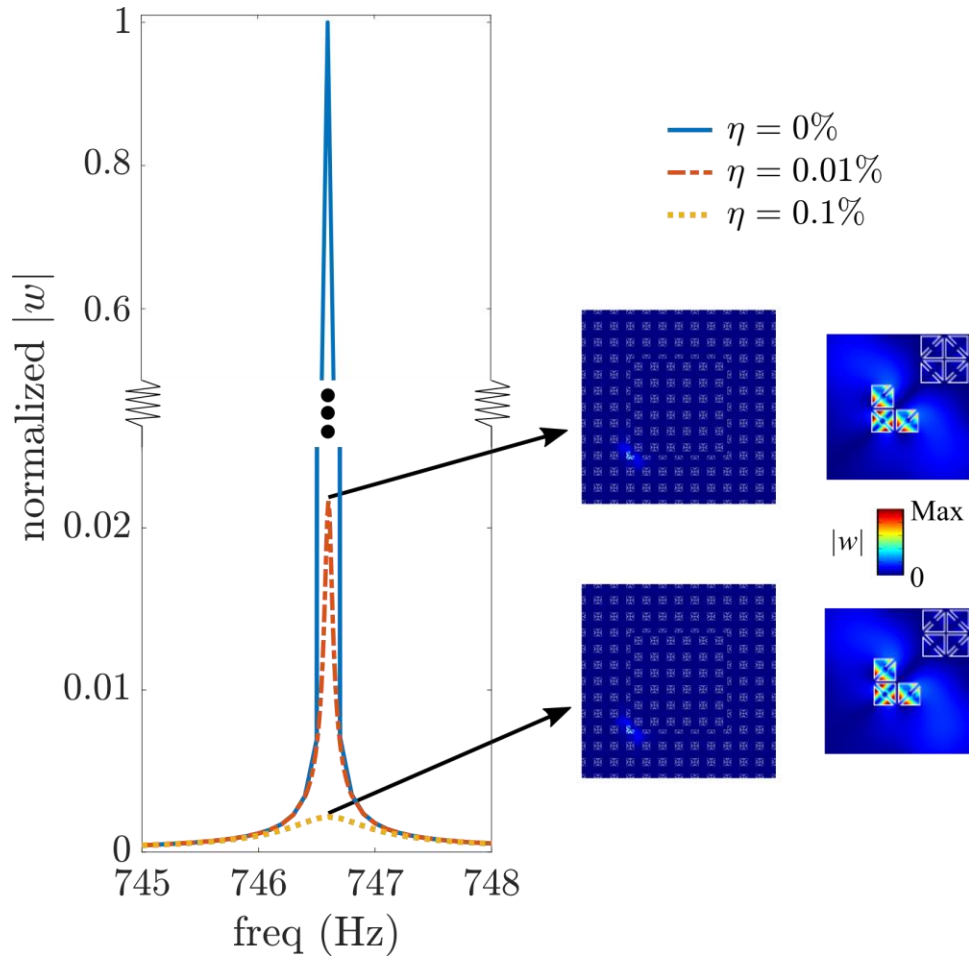
Appendix Figure D.25. Corner state out-of-plane (w) wave fields calculated in the eigenfrequency study. (a)-(c) Eigenmodes for the monomer corner lattice configuration. (d)-(h) Eigenmodes for the trimer corner lattice configuration. The inset shows a zoomed-in view of the displacement field for the corner state. The black dashed line in the inset is the angular bisector for the corner that is used for symmetry evaluations.

Appendix Table D.3: Summary of the corner state eigenmode characteristics

Corner State	Symmetry (about bisector)	# of active resonators/ # of total resonators	γ_{corner}	Multipolar coupling
M-I	Symmetric	1/1	0.05	Yes
M-II	Symmetric	1/1	0.06	No
M-III	Asymmetric	1/1	0.39	No
T-IIA	Asymmetric	2/3	0.18	No
T-IIB	Symmetric	3/3	0.21	Yes
T-IIIA	Asymmetric	3/3	0.46	No
T-IIIB	Symmetric	2/3	0.61	No
T-IV	Asymmetric	3/3	0.68	No

have multipolar behavior or inter-corner coupling present. As shown in [271], the inter-corner coupling and obtainment of multipolar behaviors can be adjusted by modulating the distance between the corners in the lattice; e.g., by making the inner domain larger or smaller.

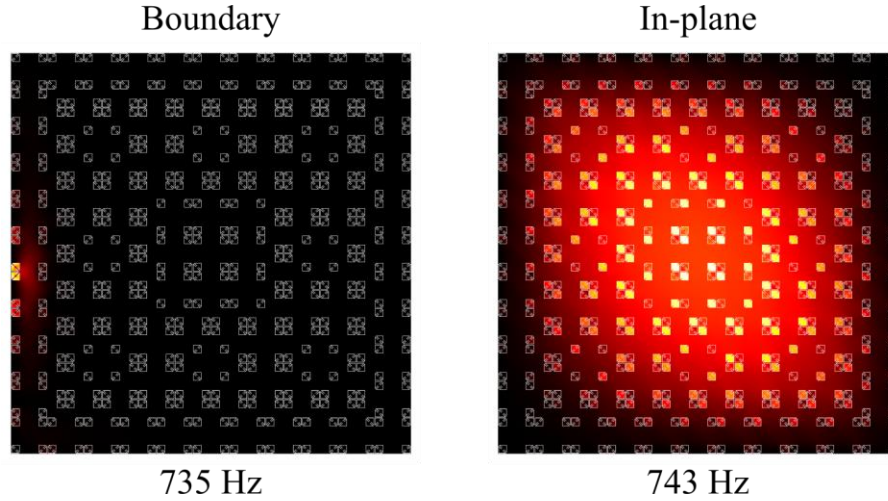
Appendix D.3: Damping in the 2D HOTM



Appendix Figure D.26. An investigation of the effect of damping on the frequency response of the 2D HOTM. The out-of-plane displacement amplitude $|w|$ is normalized according to the maximum value calculated at resonance (746.6 Hz) for the T-IV Corner state in the no damping case ($\eta = 0\%$). Insets show the displacement fields with successful wave confinement for the cases of $\eta = 0.1\%$ and $\eta = 0.01\%$.

A case study is used to illustrate the effect of damping on the corner state response. For Corner State T-IV, the dynamic response tends to infinity at $f = 746.6$ Hz when there is no damping present in the system (Appendix Figure D.26). An isotropic loss factor η is introduced to incorporate damping into the system. When damping is present, the peak response is predictably and dramatically reduced ($\eta = 0.01\%$ and $\eta = 0.1\%$ in the plot on the left side of Appendix Figure D.26). However, the corner state retains wave localization at the corner site (see insets in Appendix Figure D.26). These results suggest that damping, which is unavoidable in a practical setting, does not destroy the topological corner state. An experimental investigation will be needed to further characterize damping and its effects on the 2D HOTM.

Appendix D.4: Boundary and in-plane bulk modes of the fractal HOTM



Appendix Figure D.27. An exemplar boundary mode (735 Hz) and an exemplar in-plane bulk mode (743 Hz) for the fractal HOTM in Configuration 1. These modes do not couple with or inhibit the emergence of topological edge and corner states. The boundary states (left panel, 735 Hz) do not strongly interfere with topological states because they exist in a frequency range (734-740 Hz) with separation from all topological states. The in-plane ($\Gamma \approx 0$) bulk state (right panel, 743 Hz) arises because, as mentioned in Section 5.3, in-plane bands do cross through topological bandgaps III and IV. However, these purely in-plane modes not directly interact with the torsional topological states.

Bibliography

- [1] M. Kadic, G.W. Milton, M. van Hecke, M. Wegener, 3D metamaterials, *Nat. Rev. Phys.* 1 (2019) 198–210. doi:10.1038/s42254-018-0018-y.
- [2] M.I. Hussein, M.J. Leamy, M. Ruzzene, Dynamics of phononic materials and structures: historical origins, recent progress, and future outlook, *Appl. Mech. Rev.* 66 (2014) 040802. doi:10.1115/1.4026911.
- [3] Y.F. Wang, Y.Z. Wang, B. Wu, W. Chen, Y.S. Wang, Tunable and active phononic crystals and metamaterials, *Appl. Mech. Rev.* 72 (2020) 040801. doi:10.1115/1.4046222.
- [4] T. Vasileiadis, J. Varghese, V. Babacic, J. Gomis-Bresco, D.N. Urrios, B. Graczykowski, Progress and perspectives on phononic crystals, *J. Appl. Phys.* 129 (2021) 160901. doi:10.1063/5.0042337.
- [5] R.M. Walser, *Metamaterials : An Introduction*, in: W.S. Lakhtakia, W. Akhlesh (Eds.), *Introd. to Complex Mediu. Opt. Electromagn.*, SPIE—The International Society for Optical Engineering, 2003: pp. 295–316. doi:10.1117/3.504610.
- [6] G. Ma, P. Sheng, Acoustic metamaterials: From local resonances to broad horizons, *Sci. Adv.* 2 (2016) e1501595. doi:10.1126/sciadv.1501595.
- [7] Muhammad, C.W. Lim, From photonic crystals to seismic metamaterials: A review via phononic crystals and acoustic metamaterials, *Arch. Comput. Methods Eng.* 29 (2022) 1137–1198. doi:10.1007/s11831-021-09612-8.
- [8] S.A. Cummer, J. Christensen, A. Alù, Controlling sound with acoustic metamaterials, *Nat. Rev. Mater.* 1 (2016) 16001. doi:10.1038/natrevmats.2016.1.
- [9] B.I. Popa, S.A. Cummer, Non-reciprocal and highly nonlinear active acoustic metamaterials, *Nat. Commun.* 5 (2014) 3398. doi:10.1038/ncomms4398.
- [10] M. Hathcock, B.I. Popa, K.W. Wang, Origami inspired phononic structure with metamaterial inclusions for tunable angular wave steering, *J. Appl. Phys.* 129 (2021) 145103. doi:10.1063/5.0041503.

- [11] Y. Zhai, H. Kwon, B. Popa, Active Willis metamaterials for ultra-compact non-reciprocal linear acoustic devices, *Phys. Rev. B.* 99 (2019) 220301(R).
- [12] M. Pishvar, R.L. Harne, Foundations for soft, smart matter by active mechanical metamaterials, *Adv. Sci.* 7 (2020) 2001384. doi:10.1002/advs.202001384.
- [13] B.I. Popa, S.A. Cummer, Design and characterization of broadband acoustic composite metamaterials, *Phys. Rev. B.* 80 (2009) 174303. doi:10.1103/PhysRevB.80.174303.
- [14] D.Z. Rocklin, S. Zhou, K. Sun, X. Mao, Transformable topological mechanical metamaterials, *Nat. Commun.* 8 (2017) 14201. doi:10.1038/ncomms14201.
- [15] H. Zuo, K. Bi, H. Hao, A state-of-the-art review on the vibration mitigation of wind turbines, *Renew. Sustain. Energy Rev.* 121 (2020) 109710. doi:10.1016/j.rser.2020.109710.
- [16] X.A. Vasanth, P.S. Paul, G. Lawrance, A.S. Varadarajan, Vibration control techniques during turning process: a review, *Aust. J. Mech. Eng.* 19 (2021) 221–241. doi:10.1080/14484846.2019.1585224.
- [17] I.E. Gunduz, M.S. McClain, P. Cattani, G.T.C. Chiu, J.F. Rhoads, S.F. Son, 3D printing of extremely viscous materials using ultrasonic vibrations, *Addit. Manuf.* 22 (2018) 98–103. doi:10.1016/j.addma.2018.04.029.
- [18] Y. Qin, X. Tang, T. Jia, Z. Duan, J. Zhang, Y. Li, L. Zheng, Noise and vibration suppression in hybrid electric vehicles: State of the art and challenges, *Renew. Sustain. Energy Rev.* 124 (2020) 109782. doi:10.1016/j.rser.2020.109782.
- [19] J.M.W. Brownjohn, A. de Stefano, Y.L. Xu, H. Wenzel, A.E. Aktan, Vibration-based monitoring of civil infrastructure: Challenges and successes, *J. Civ. Struct. Heal. Monit.* 1 (2011) 79–95. doi:10.1007/s13349-011-0009-5.
- [20] G.P. Warn, K.L. Ryan, A review of seismic isolation for buildings: Historical development and research needs, *Buildings.* 2 (2012) 300–325. doi:10.3390/buildings2030300.
- [21] C. Dennehy, O.S. Alvarez-Salazar, *Spacecraft Micro-Vibration: A Survey of Problems, Experiences, Potential Solutions, and Some Lessons Learned*, 2018. <https://ntrs.nasa.gov/search.jsp?R=20180006315>.
- [22] W.A. Gill, I. Howard, I. Mazhar, K. McKee, A Review of MEMS Vibrating Gyroscopes and Their Reliability Issues in Harsh Environments, *Sensors.* 22 (2022). doi:10.3390/s22197405.
- [23] M. Wagg, D., Bond, I., Weaver, P. and Friswell, *Adaptive structures: engineering applications*, John Wiley & Sons, 2008.

- [24] D.J. Inman, *Engineering Vibration*, 5th ed., Pearson, 2022.
- [25] K. Graff, *Wave Motion in Elastic Solids*, Dover Publications, New York, NY, United States, 1991.
- [26] Y.-T. Wang, Y.-W. Tsai, Multiple Weyl and double-Weyl points in an elastic chiral lattice, *New J. Phys.* 20 (2018) 083031. doi:10.1088/1367-2630/aada55.
- [27] S.Y. Yu, C. He, Z. Wang, F.K. Liu, X.C. Sun, Z. Li, H.Z. Lu, M.H. Lu, X.P. Liu, Y.F. Chen, Elastic pseudospin transport for integratable topological phononic circuits, *Nat. Commun.* 9 (2018) 3072. doi:10.1038/s41467-018-05461-5.
- [28] Z. Chen, B. Guo, Y. Yang, C. Cheng, Metamaterials-based enhanced energy harvesting: A review, *Phys. B Condens. Matter.* 438 (2014) 1–8. doi:10.1016/j.physb.2013.12.040.
- [29] Y. Jia, Review of nonlinear vibration energy harvesting: Duffing, bistability, parametric, stochastic and others, *J. Intell. Mater. Syst. Struct.* 31 (2020) 921–944. doi:10.1177/1045389X20905989.
- [30] R.L. Harne, K.W. Wang, A review of the recent research on vibration energy harvesting via bistable systems, *Smart Mater. Struct.* 22 (2013) 023001. doi:10.1088/0964-1726/22/2/023001.
- [31] C. Sugino, A. Erturk, Analysis of multifunctional piezoelectric metastructures for low-frequency bandgap formation and energy harvesting, *J. Phys. D: Appl. Phys.* 51 (2018) 215103. doi:10.1088/1361-6463/aab97e.
- [32] S. Tol, F.L. Degertekin, A. Erturk, Gradient-index phononic crystal lens-based enhancement of elastic wave energy harvesting, *Appl. Phys. Lett.* 109 (2016). doi:10.1063/1.4960792.
- [33] Z. Lin, H. Al Ba'ba'a, S. Tol, Piezoelectric metastructures for simultaneous broadband energy harvesting and vibration suppression of traveling waves, *Smart Mater. Struct.* 30 (2021). doi:10.1088/1361-665X/ac04c3.
- [34] H.K. Maheshwari, P. Rajagopal, Novel locally resonant and widely scalable seismic metamaterials for broadband mitigation of disturbances in the very low frequency range of 0 – 33 Hz, *Soil Dyn. Earthq. Eng.* 161 (2022) 107409. doi:10.1016/j.soildyn.2022.107409.
- [35] A.A. Yakovleva, I.B. Movchan, D. Misseroni, N.M. Pugno, A.B. Movchan, Multi-Physics of Dynamic Elastic Metamaterials and Earthquake Systems, *Front. Mater.* 7 (2021) 620701. doi:10.3389/fmats.2020.620701.

- [36] C. Sugino, S. Leadenham, M. Ruzzene, A. Erturk, An investigation of electroelastic bandgap formation in locally resonant piezoelectric metastructures, *Smart Mater. Struct.* 26 (2017) 055029. doi:10.1088/1361-665X/aa6671.
- [37] L. D'Alessandro, V. Zega, R. Ardito, A. Corigliano, 3D auxetic single material periodic structure with ultra-wide tunable bandgap, *Sci. Rep.* 8 (2018) 2262. doi:10.1038/s41598-018-19963-1.
- [38] L. D'Alessandro, R. Ardito, F. Braghin, A. Corigliano, Low frequency 3D ultra-wide vibration attenuation via elastic metamaterial, *Sci. Rep.* 9 (2019) 8039. doi:10.1038/s41598-019-44507-6.
- [39] K.T. Tan, H.H. Huang, C.T. Sun, Optimizing the band gap of effective mass negativity in acoustic metamaterials, *Appl. Phys. Lett.* 101 (2012). doi:10.1063/1.4770370.
- [40] H. Al Ba'Ba'A, Z. Lin, S. Tol, Metadamping enhancement and tunability via scissor-like electromechanical metamaterials, *J. Appl. Phys.* 130 (2021). doi:10.1063/5.0058086.
- [41] O. Abdeljaber, O. Avci, S. Kiranyaz, D.J. Inman, Optimization of linear zigzag insert metastructures for low-frequency vibration attenuation using genetic algorithms, *Mech. Syst. Signal Process.* 84 (2017) 625–641. doi:10.1016/j.ymssp.2016.07.011.
- [42] T. Yang, S. Zhou, S. Fang, W. Qin, D.J. Inman, Nonlinear vibration energy harvesting and vibration suppression technologies: Designs, analysis, and applications, *Appl. Phys. Rev.* 8 (2021) 031317. doi:10.1063/5.0051432.
- [43] K.H. Matlack, A. Bauhofer, S. Krödel, A. Palermo, C. Daraio, Composite 3D-printed metastructures for low-frequency and broadband vibration absorption, *Proc. Natl. Acad. Sci.* 113 (2016) 8386–8390. doi:10.1073/pnas.1600171113.
- [44] T. Jiang, C. Li, Q. He, Z.K. Peng, Randomized resonant metamaterials for single-sensor identification of elastic vibrations, *Nat. Commun.* 11 (2020) 2353. doi:10.1038/s41467-020-15950-1.
- [45] H. Danawe, S. Tol, Experimental realization of negative refraction and subwavelength imaging for flexural waves in phononic crystal plates, *J. Sound Vib.* 518 (2022) 116552. doi:10.1016/j.jsv.2021.116552.
- [46] J. Gong, O. Seow, C. Honnet, J. Forman, S. Mueller, MetaSense : Integrating Sensing Capabilities into Mechanical Metamaterial, in: *34th Annu. ACM Symp. User Interface Softw. Technol.*, 2021: pp. 1063–1073.

- [47] C. He, X. Ni, H. Ge, X.C. Sun, Y.B. Chen, M.H. Lu, X.P. Liu, Y.F. Chen, Acoustic topological insulator and robust one-way sound transport, *Nat. Phys.* 12 (2016) 1124–1129. doi:10.1038/nphys3867.
- [48] B. Deng, M. Zanaty, A.E. Forte, K. Bertoldi, Topological Solitons Make Metamaterials Crawl, *Phys. Rev. Appl.* 17 (2022) 1. doi:10.1103/PhysRevApplied.17.014004.
- [49] A. Pal, V. Restrepo, D. Goswami, R. V. Martinez, Exploiting Mechanical Instabilities in Soft Robotics: Control, Sensing, and Actuation, *Adv. Mater.* 2006939 (2021) 2006939. doi:10.1002/adma.202006939.
- [50] H. Yasuda, P.R. Buskohl, A. Gillman, T.D. Murphey, S. Stepney, R.A. Vaia, J.R. Raney, Mechanical computing, *Nature*. 598 (2021) 39–48. doi:10.1038/s41586-021-03623-y.
- [51] T. Mei, Z. Meng, K. Zhao, C.Q. Chen, A mechanical metamaterial with reprogrammable logical functions, *Nat. Commun.* 12 (2021) 7234. doi:10.1038/s41467-021-27608-7.
- [52] C. El Helou, P.R. Buskohl, C.E. Tabor, R.L. Harne, Digital logic gates in soft, conductive mechanical metamaterials, *Nat. Commun.* 12 (2021) 1633. doi:10.1038/s41467-021-21920-y.
- [53] U. Waheed, C.W. Myant, S.N. Dobson, Boolean AND/OR mechanical logic using multi-plane mechanical metamaterials, *Extrem. Mech. Lett.* 40 (2020) 100865. doi:10.1016/j.eml.2020.100865.
- [54] Z. Liu, H. Fang, J. Xu, K.-W. Wang, Discriminative Transition Sequences of Origami Metamaterials for Mechanologic, *Adv. Intell. Syst.* 5 (2023) 2200146. doi:10.1002/aisy.202200146.
- [55] Z. Liu, X. Zhang, Y. Mao, Y.Y. Zhu, Z. Yang, C.T. Chan, P. Sheng, Locally resonant sonic materials, *Science*. 289 (2000) 1734–1736. doi:10.1126/science.289.5485.1734.
- [56] V. Laude, *Phononic Crystals: Artificial Crystals for Sonic, Acoustic, and Elastic Waves*, De Gruyter, Berlin, München, Boston, 2015. doi:https://doi.org/10.1515/9783110302660.
- [57] S. Yao, X. Zhou, G. Hu, Experimental study on negative effective mass in a 1D mass-spring system, *New J. Phys.* 10 (2008) 043020. doi:10.1088/1367-2630/10/4/043020.
- [58] Y. Xiao, J. Wen, X. Wen, Flexural wave band gaps in locally resonant thin plates with periodically attached spring-mass resonators, *J. Phys. D. Appl. Phys.* 45 (2012) 195401. doi:10.1088/0022-3727/45/19/195401.

- [59] Y. Pennec, B. Djafari-Rouhani, H. Larabi, J.O. Vasseur, A.C. Hladky-Hennion, Low-frequency gaps in a phononic crystal constituted of cylindrical dots deposited on a thin homogeneous plate, *Phys. Rev. B.* 78 (2008) 104105. doi:10.1103/PhysRevB.78.104105.
- [60] H.H. Huang, C.T. Sun, Wave attenuation mechanism in an acoustic metamaterial with negative effective mass density, *New J. Phys.* 11 (2009) 013003. doi:10.1088/1367-2630/11/1/013003.
- [61] C. Sugino, S. Leadenham, M. Ruzzene, A. Erturk, On the mechanism of bandgap formation in locally resonant finite elastic metamaterials, *J. Appl. Phys.* 120 (2016). doi:10.1063/1.4963648.
- [62] L. Liu, M.I. Hussein, Wave motion in periodic flexural beams and characterization of the transition between bragg scattering and local resonance, *J. Appl. Mech.* 79 (2012) 011003. doi:10.1115/1.4004592.
- [63] L. Raghavan, A.S. Phani, Local resonance bandgaps in periodic media: Theory and experiment, *J. Acoust. Soc. Am.* 134 (2013) 1950–1959. doi:10.1121/1.4817894.
- [64] L. Brillouin, *Wave Propagation in Periodic Structures: Electric Filters and Crystal Lattices*, (1946).
- [65] C. Sugino, Y. Xia, S. Leadenham, M. Ruzzene, A. Erturk, A general theory for bandgap estimation in locally resonant metastructures, *J. Sound Vib.* 406 (2017) 104–123. doi:10.1016/j.jsv.2017.06.004.
- [66] R. Chaunsali, C.W. Chen, J. Yang, Experimental demonstration of topological waveguiding in elastic plates with local resonators, *New J. Phys.* 20 (2018) 113036. doi:10.1088/1367-2630/aeb61.
- [67] M. Alshaqqaq, A. Erturk, Graded multifunctional piezoelectric metastructures for wideband vibration attenuation and energy harvesting, *Smart Mater. Struct.* 30 (2020) 015029. doi:10.1088/1361-665X/abc7fa.
- [68] M.S. Kushwaha, P. Halevi, L. Dobrzynski, B. Djafari-Rouhani, Acoustic band structure of periodic elastic composites, *Phys. Rev. Lett.* 75 (1995) 2022. doi:10.1103/PhysRevLett.75.3580.
- [69] R. Martínez-Sala, J. Sancho, J. V. Sánchez, V. Gómez, J. Llinares, F. Meseguer, Sound attenuation by sculpture, *Nature.* 378 (1995) 241. doi:10.1038/378241a0.
- [70] O.R. Bilal, M.I. Hussein, Ultrawide phononic band gap for combined in-plane and out-of-plane waves, *Phys. Rev. E.* 84 (2011) 065701(R). doi:10.1103/PhysRevE.84.065701.

- [71] M.S. Kushwaha, P. Halevi, Band-gap engineering in periodic elastic composites, *Appl. Phys. Lett.* 64 (1994) 1085–1087. doi:10.1063/1.110940.
- [72] F.R. Montero de Espinosa, E. Jimenez, M. Torres, Ultrasonic Band Gap in a Periodic Two-Dimensional Composite, *Phys. Rev. Lett.* 80 (1997) 1208. doi:10.1103/PhysRevLett.80.1208.
- [73] G. Wang, X. Wen, J. Wen, L. Shao, Y. Liu, Two-dimensional locally resonant phononic crystals with binary structures, *Phys. Rev. Lett.* 93 (2004) 154302. doi:10.1103/PhysRevLett.93.154302.
- [74] M. Oudich, M.B. Assouar, Z. Hou, Propagation of acoustic waves and waveguiding in a two-dimensional locally resonant phononic crystal plate, *Appl. Phys. Lett.* 97 (2010) 193503. doi:10.1063/1.3513218.
- [75] S.S. Ganti, T.W. Liu, F. Semperlotti, Weyl points and topological surface states in a three-dimensional sandwich-type elastic lattice, *New J. Phys.* 22 (2020) 083001. doi:10.1088/1367-2630/ab9e31.
- [76] S. Benchabane, A. Khelif, A. Choujaa, B. Djafari-Rouhani, V. Laude, Interaction of waveguide and localized modes in a phononic crystal, *Europhys. Lett.* 71 (2005) 570–575. doi:10.1209/epl/i2005-10131-2.
- [77] F. Casadei, T. Delpero, A. Bergamini, P. Ermanni, M. Ruzzene, Piezoelectric resonator arrays for tunable acoustic waveguides and metamaterials, *J. Appl. Phys.* 112 (2012) 064902. doi:10.1063/1.4752468.
- [78] M. Kafesaki, M.M. Sigalas, N. García, Frequency modulation in the transmittivity of waveguides in elastic-wave band-gap materials, *Phys. Rev. Lett.* 85 (2000) 4044–4047. doi:10.1103/PhysRevLett.85.4044.
- [79] A. Khelif, A. Choujaa, S. Benchabane, B. Djafari-Rouhani, V. Laude, Guiding and bending of acoustic waves in highly confined phononic crystal waveguides, *Appl. Phys. Lett.* 84 (2004) 4400–4402. doi:10.1063/1.1757642.
- [80] X. Liu, G. Cai, K.W. Wang, Synthesizing and reconfiguring metastable modular metamaterials for adaptive wave propagation control, *J. Sound Vib.* 468 (2020) 115114. doi:10.1016/j.jsv.2019.115114.
- [81] J.D. Joannopoulos, P.R. Villeneuve, S. Fan, Photonic crystals: putting a new twist on light, *Nature.* 386 (1997) 6621.

- [82] A. Mekis, J.C. Chen, I. Kurland, S. Fan, P.R. Villeneuve, J.D. Joannopoulos, High transmission through sharp bends in photonic crystal waveguides, *Phys. Rev. Lett.* 77 (1996) 3787–3790. doi:10.1103/PhysRevLett.77.3787.
- [83] R.K. Pal, M. Ruzzene, Edge waves in plates with resonators: an elastic analogue of the quantum valley Hall effect, *New J. Phys.* 19 (2017) 025001. doi:https://doi.org/10.1088/1367-2630/aa56a2.
- [84] J.H. Sun, T.T. Wu, Propagation of surface acoustic waves through sharply bent two-dimensional phononic crystal waveguides using a finite-difference time-domain method, *Phys. Rev. B.* 74 (2006) 174305. doi:10.1103/PhysRevB.74.174305.
- [85] Y. Jin, D. Torrent, B. Djafari-Rouhani, Robustness of conventional and topologically protected edge states in phononic crystal plates, *Phys. Rev. B.* 98 (2018) 054307. doi:10.1103/PhysRevB.98.054307.
- [86] M.Z. Hasan, C.L. Kane, Colloquium: topological insulators, *Rev. Mod. Phys.* 82 (2010) 3045–3067. doi:10.1103/RevModPhys.82.3045.
- [87] X.L. Qi, S.C. Zhang, Topological insulators and superconductors, *Rev. Mod. Phys.* 83 (2011) 1057–1110. doi:10.1103/RevModPhys.83.1057.
- [88] B. Xie, H.X. Wang, X. Zhang, P. Zhan, J.H. Jiang, M. Lu, Y. Chen, Higher-order band topology, *Nat. Rev. Phys.* 3 (2021) 520–532.
- [89] C.L. Kane, Topological band theory and the \mathbb{Z}_2 invariant, in: *Contemp. Concepts Condens. Matter Sci.*, Elsevier, 2013: pp. 3–34. doi:10.1016/B978-0-444-63314-9.00001-9.
- [90] S.D. Huber, Topological mechanics, *Nat. Phys.* 12 (2016) 621–623. doi:10.1038/nphys3801.
- [91] G. Ma, M. Xiao, C.T. Chan, Topological phases in acoustic and mechanical systems, *Nat. Rev. Phys.* 1 (2019) 281–294. doi:10.1038/s42254-019-0030-x.
- [92] L. Xin, Y. Siyuan, L. Harry, L. Minghui, C. Yanfeng, Topological mechanical metamaterials: A brief review, *Curr. Opin. Solid State Mater. Sci.* 24 (2020) 100853. doi:10.1016/j.cossms.2020.100853.
- [93] H. Huang, J. Chen, S. Huo, Recent advances in topological elastic metamaterials, *J. Phys. Condens. Matter.* 33 (2021) 503002. doi:10.1088/1361-648x/ac27d8.
- [94] M. Miniaci, R.K. Pal, Design of topological elastic waveguides, *J. Appl. Phys.* 130 (2021) 141101. doi:10.1063/5.0057288.

- [95] S. Zheng, G. Duan, B. Xia, Progress in Topological Mechanics, Appl. Sci. 12 (2022) 1987. doi:10.3390/app12041987.
- [96] F. Zangeneh-Nejada, A. Alù, R. Fleury, Topological wave insulators: a review, Comptes Rendus Phys. 21 (2020) 467–499. <https://doi.org/10.1016/j.crhy.2018.10.007>.
- [97] Z. Yang, F. Gao, X. Shi, X. Lin, Z. Gao, Y. Chong, B. Zhang, Topological Acoustics, Phys. Rev. Lett. 114 (2015) 114301. doi:10.1103/PhysRevLett.114.114301.
- [98] X. Zhang, M. Xiao, Y. Cheng, M.H. Lu, J. Christensen, Topological sound, Commun. Phys. 1 (2018) 97. doi:10.1038/s42005-018-0094-4.
- [99] L. Lu, J.D. Joannopoulos, M. Soljačić, Topological photonics, Nat. Photonics. 8 (2014) 821–829. doi:10.1038/nphoton.2014.248.
- [100] M. Kim, Z. Jacob, J. Rho, Recent advances in 2D, 3D and higher-order topological photonics, Light Sci. Appl. 9 (2020) 130. doi:10.1038/s41377-020-0331-y.
- [101] M. Segev, M.A. Bandres, Topological photonics: Where do we go from here?, Front. Opt. Photonics. 10 (2021) 437–446. doi:10.1515/9783110710687-032.
- [102] Z. Chen, M. Segev, Highlighting photonics: looking into the next decade, ELight. 1 (2021) 2. doi:10.1186/s43593-021-00002-y.
- [103] P.M. Chaikin, T.C. Lubensky, Principles of Condensed Matter Physics, Cambridge: Cambridge University Press, 2000. doi:10.1017/cbo9780511813467.008.
- [104] X. Wu, Y. Jin, A. Khelif, X. Zhuang, T. Rabczuk, B. Djafari-Rouhani, Topological surface wave metamaterials for robust vibration attenuation and energy harvesting, Mech. Adv. Mater. Struct. 29 (2022) 4759–4767. doi:10.1080/15376494.2021.1937758.
- [105] Z. Wen, Y. Jin, P. Gao, X. Zhuang, T. Rabczuk, B. Djafari-Rouhani, Topological cavities in phononic plates for robust energy harvesting, Mech. Syst. Signal Process. 162 (2022) 108047. doi:10.1016/j.ymsp.2021.108047.
- [106] C. Lan, G. Hu, L. Tang, Y. Yang, Energy localization and topological protection of a locally resonant topological metamaterial for robust vibration energy harvesting, J. Appl. Phys. 129 (2021) 184502. doi:10.1063/5.0047965.
- [107] G.J. Chaplain, J.M. De Ponti, G. Aguzzi, A. Colombi, R. V. Craster, Topological Rainbow Trapping for Elastic Energy Harvesting in Graded Su-Schrieffer-Heeger Systems, Phys. Rev. Appl. 14 (2020) 054035. doi:10.1103/PhysRevApplied.14.054035.

- [108] T.X. Ma, Q.S. Fan, C. Zhang, Y.S. Wang, Flexural wave energy harvesting by the topological interface state of a phononic crystal beam, *Extrem. Mech. Lett.* 50 (2022) 101578. doi:10.1016/j.eml.2021.101578.
- [109] M. Yan, J. Lu, F. Li, W. Deng, X. Huang, J. Ma, Z. Liu, On-chip valley topological materials for elastic wave manipulation, *Nat. Mater.* 17 (2018) 993–998. doi:10.1038/s41563-018-0191-5.
- [110] Y. Wu, M. Yan, Z.K. Lin, H.X. Wang, F. Li, J.H. Jiang, On-chip higher-order topological micromechanical metamaterials, *Sci. Bull.* 66 (2021) 1959–1966. doi:10.1016/j.scib.2021.06.024.
- [111] M. Yan, W. Deng, X. Huang, Y. Wu, Y. Yang, J. Lu, F. Li, Z. Liu, Pseudomagnetic fields enabled manipulation of on-chip elastic waves, *Phys. Rev. Lett.* 127 (2021) 136401. doi:10.1103/PhysRevLett.127.136401.
- [112] J. Zhao, Q. Wang, X. Wang, W. Yuan, Y. Huang, S. Chen, A. Riaud, J. Zhou, On-chip valley phononic crystal plates with graded topological interface, *Int. J. Mech. Sci.* 227 (2022) 107460. doi:10.1016/j.ijmecsci.2022.107460.
- [113] H. Huang, Z. Tan, S. Huo, L. Feng, J. Chen, X. Han, Topologically protected zero refraction of elastic waves in pseudospin-Hall phononic crystals, *Commun. Phys.* 3 (2020) 46. doi:10.1038/s42005-020-0314-6.
- [114] F. Zangeneh-Nejad, R. Fleury, Topological analog signal processing, *Nat. Commun.* 10 (2019) 2058. doi:10.1038/s41467-019-10086-3.
- [115] M.P. Makwana, R. V. Craster, Designing multidirectional energy splitters and topological valley supernetworks, *Phys. Rev. B.* 98 (2018) 235125. doi:10.1103/PhysRevB.98.235125.
- [116] N. Gao, S. Qu, L. Si, J. Wang, W. Chen, Broadband topological valley transport of elastic wave in reconfigurable phononic crystal plate, *Appl. Phys. Lett.* 118 (2021) 063502. doi:10.1063/5.0036840.
- [117] M. Fatemi, J.F. Greenleaf, Ultrasound-Stimulated Vibro-Acoustic Spectrography, *Science.* 280 (1998) 82–85. doi:10.1126/science.280.5360.82.
- [118] Y. Deng, M. Oudich, N.J. Gerard, J. Ji, M. Lu, Y. Jing, Magic-angle Bilayer Phononic Graphene, *Phys. Rev. B.* 102 (2020) 180304(R). doi:10.1103/PhysRevB.102.180304.
- [119] H. Huang, S. Huo, J. Chen, Subwavelength elastic topological negative refraction in ternary locally resonant phononic crystals, *Int. J. Mech. Sci.* 198 (2021) 106391. doi:10.1016/j.ijmecsci.2021.106391.

- [120] Z. Zhang, Y. Tian, Y. Cheng, Q. Wei, X. Liu, J. Christensen, Topological Acoustic Delay Line, *Phys. Rev. Appl.* 9 (2018) 034032. doi:10.1103/PhysRevApplied.9.034032.
- [121] X. Wu, Z. Li, J. Chen, X. Li, J. Tian, Y. Huang, S. Wang, W. Lu, B. Hou, C.T. Chan, W. Wen, Interlayer Topological Transport and Devices Based on Layer Pseudospins in Photonic Valley-Hall Phases, *Adv. Opt. Mater.* 7 (2019) 1900872. doi:10.1002/adom.201900872.
- [122] T. Fujita, M.B.A. Jalil, S.G. Tan, Topological insulator cell for memory and magnetic sensor applications, *Appl. Phys. Express.* 4 (2011) 094201. doi:10.1143/APEX.4.094201.
- [123] M.A. Bandres, S. Wittek, G. Harari, M. Parto, J. Ren, M. Segev, D.N. Christodoulides, M. Khajavikhan, Topological insulator laser: Experiments, *Science* (80-.). 359 (2018). doi:10.1126/science.aar4005.
- [124] G. Harari, M.A. Bandres, Y. Lumer, M.C. Rechtsman, Y.D. Chong, M. Khajavikhan, D.N. Christodoulides, M. Segev, Topological insulator laser: Theory, *Science* (80-.). 359 (2018). doi:10.1126/science.aar4003.
- [125] Y. Zeng, U. Chattopadhyay, B. Zhu, B. Qiang, J. Li, Y. Jin, L. Li, A.G. Davies, E.H. Linfield, B. Zhang, Y. Chong, Q.J. Wang, Electrically pumped topological laser with valley edge modes, *Nature.* 578 (2020) 246–250. doi:10.1038/s41586-020-1981-x.
- [126] Q. Wang, C.C. Liu, Y.M. Lu, F. Zhang, High-Temperature Majorana Corner States, *Phys. Rev. Lett.* 121 (2018) 186801. doi:10.1103/PhysRevLett.121.186801.
- [127] O. You, S. Liang, B. Xie, W. Gao, W. Ye, J. Zhu, S. Zhang, Observation of Non-Abelian Thouless Pump, *Phys. Rev. Lett.* 128 (2022) 244302. doi:10.1103/physrevlett.128.244302.
- [128] G. Jin, E. Greplova, Topological Entanglement Stabilization in Superconducting Quantum Circuits, *Phys. Rev. Res.* 5 (2023) 023088. doi:10.1103/PhysRevResearch.5.023088.
- [129] P. Liu, H. Li, Z. Zhou, Y. Pei, Topological acoustic tweezer and pseudo-spin states of acoustic topological insulators, *Appl. Phys. Lett.* 120 (2022). doi:10.1063/5.0091755.
- [130] J. Yin, M. Ruzzene, J. Wen, D. Yu, L. Cai, L. Yue, Band transition and topological interface modes in 1D elastic phononic crystals, *Sci. Rep.* 8 (2018) 6806. doi:10.1038/s41598-018-24952-5.
- [131] S.Y. Huo, J.J. Chen, H.B. Huang, Y.J. Wei, Z.H. Tan, L.Y. Feng, X.P. Xie, Experimental demonstration of valley-protected backscattering suppression and interlayer topological transport for elastic wave in three-dimensional phononic crystals, *Mech. Syst. Signal Process.* 154 (2021) 107543. doi:10.1016/j.ymssp.2020.107543.

- [132] R. Chaunsali, E. Kim, A. Thakkar, P.G. Kevrekidis, J. Yang, Demonstrating an in situ topological band transition in cylindrical granular chains, *Phys. Rev. Lett.* 119 (2017) 024301. doi:10.1103/PhysRevLett.119.024301.
- [133] H. Chen, H. Nassar, G.L. Huang, A study of topological effects in 1D and 2D mechanical lattices, *J. Mech. Phys. Solids.* 117 (2018) 22–36. doi:10.1016/j.jmps.2018.04.013.
- [134] W. Zhou, B. Wu, Z. Chen, W. Chen, C.W. Lim, J.N. Reddy, Actively controllable topological phase transition in homogeneous piezoelectric rod system, *J. Mech. Phys. Solids.* 137 (2020) 103824. doi:10.1016/j.jmps.2019.103824.
- [135] W. Zhou, W. Chen, M. Destrade, C.W. Lim, Actively controllable topological phase transition in phononic beam systems, *Int. J. Mech. Sci.* 180 (2020) 105668. doi:10.1016/j.ijmecsci.2020.105668.
- [136] S. Li, D. Zhao, H. Niu, X. Zhu, J. Zang, Observation of elastic topological states in soft materials, *Nat. Commun.* 9 (2018) 1370. doi:10.1038/s41467-018-03830-8.
- [137] H. Niu, S. Li, J. Zang, Interface-dependent tunable elastic interface states in soft metamaterials, *J. Appl. Phys.* 129 (2021) 065305. doi:10.1063/5.0037592.
- [138] J. Zak, Berrys phase for energy bands in solids, *Phys. Rev. Lett.* 62 (1989) 2747–2750. doi:10.1103/PhysRevLett.62.2747.
- [139] M. Xiao, Z.Q. Zhang, C.T. Chan, Surface impedance and bulk band geometric phases in one-dimensional systems, *Phys. Rev. X.* 4 (2014) 021017. doi:10.1103/PhysRevX.4.021017.
- [140] L.M. Nash, D. Kleckner, A. Read, V. Vitelli, A.M. Turner, W.T.M. Irvine, Topological mechanics of gyroscopic metamaterials, *Proc. Natl. Acad. Sci.* 112 (2015) 14495–14500. doi:10.1073/pnas.1507413112.
- [141] K. von Klitzing, The quantized Hall effect, *Rev. Mod. Phys.* 58 (1986) 519. doi:10.1016/0378-4363(84)90170-0.
- [142] P. Wang, L. Lu, K. Bertoldi, Topological phononic crystals with one-way elastic edge waves, *Phys. Rev. Lett.* 115 (2015) 104302. doi:10.1103/PhysRevLett.115.104302.
- [143] Y.T. Wang, P.G. Luan, S. Zhang, Coriolis force induced topological order for classical mechanical vibrations, *New J. Phys.* 17 (2015) 073031. doi:10.1088/1367-2630/17/7/073031.
- [144] R. Chaunsali, C.W. Chen, J. Yang, Subwavelength and directional control of flexural waves in zone-folding induced topological plates, *Phys. Rev. B.* 97 (2018) 054307. doi:10.1103/PhysRevB.97.054307.

- [145] C.L. Kane, E.J. Mele, Quantum spin Hall effect in graphene, *Phys. Rev. Lett.* 95 (2005) 226801. doi:10.1103/PhysRevLett.95.226801.
- [146] M. Miniaci, R.K. Pal, B. Morvan, M. Ruzzene, Experimental observation of topologically protected helical edge modes in patterned elastic plates, *Phys. Rev. X.* 8 (2018) 031074. doi:10.1103/PhysRevX.8.031074.
- [147] S.H. Mousavi, A.B. Khanikaev, Z. Wang, Topologically protected elastic waves in phononic metamaterials, *Nat. Commun.* 6 (2015) 8682. doi:10.1038/ncomms9682.
- [148] R. Süsstrunk, S.D. Huber, Observation of phononic helical edge states in a mechanical topological insulator, *Science.* 349 (2015) 47–50. doi:10.1126/science.aab0239.
- [149] L.H. Wu, X. Hu, Scheme for achieving a topological photonic crystal by using dielectric material, *Phys. Rev. Lett.* 114 (2015) 223901. doi:10.1103/PhysRevLett.114.223901.
- [150] K. Nakada, M. Fujita, G. Dresselhaus, M.S. Dresselhaus, Edge state in graphene ribbons: Nanometer size effect and edge shape dependence, *Phys. Rev. B.* 54 (1996) 17954.
- [151] N.M.R. Peres, Colloquium: The transport properties of graphene: An introduction, *Rev. Mod. Phys.* 82 (2010) 2673–2700. doi:10.1103/RevModPhys.82.2673.
- [152] A. Rycerz, J. Tworzydło, C.W.J. Beenakker, Valley filter and valley valve in graphene, *Nat. Phys.* 3 (2007) 172–175. doi:10.1038/nphys547.
- [153] D. Xiao, W. Yao, Q. Niu, Valley-contrasting physics in graphene: magnetic moment and topological transport, *Phys. Rev. Lett.* 99 (2007) 236809. doi:10.1103/PhysRevLett.99.236809.
- [154] T.W. Liu, F. Semperlotti, Experimental evidence of robust acoustic valley Hall edge states in a nonresonant topological elastic waveguide, *Phys. Rev. Appl.* 11 (2019) 014040. doi:10.1103/PhysRevApplied.11.014040.
- [155] M. Miniaci, R.K. Pal, R. Manna, M. Ruzzene, Valley-based splitting of topologically protected helical waves in elastic plates, *Phys. Rev. B.* 100 (2019) 024304. doi:10.1103/PhysRevB.100.024304.
- [156] J. Vila, R.K. Pal, M. Ruzzene, Observation of topological valley modes in an elastic hexagonal lattice, *Phys. Rev. B.* 96 (2017) 134307. doi:10.1103/PhysRevB.96.134307.
- [157] H. Zhu, T.W. Liu, F. Semperlotti, Design and experimental observation of valley-Hall edge states in diatomic-graphene-like elastic waveguides, *Phys. Rev. B.* 97 (2018) 174301. doi:10.1103/PhysRevB.97.174301.

- [158] J.J. Chen, S.Y. Huo, Z.G. Geng, H.B. Huang, X.F. Zhu, Topological valley transport of plate-mode waves in a homogenous thin plate with periodic stubbed surface, *AIP Adv.* 7 (2017) 115215. doi:10.1063/1.5006010.
- [159] Z. Du, H. Chen, G. Huang, Optimal quantum valley Hall insulators by rationally engineering Berry curvature and band structure, *J. Mech. Phys. Solids.* 135 (2020) 103784. doi:10.1016/j.jmps.2019.103784.
- [160] N. Lera, D. Torrent, P. San-Jose, J. Christensen, J. V. Alvarez, Valley Hall phases in kagome lattices, *Phys. Rev. B.* 99 (2019) 134102. doi:10.1103/PhysRevB.99.134102.
- [161] S.S. Ganti, T.W. Liu, F. Semperlotti, Topological edge states in phononic plates with embedded acoustic black holes, *J. Sound Vib.* 466 (2020) 115060. doi:10.1016/j.jsv.2019.115060.
- [162] Q. Zhang, Y. Chen, K. Zhang, G. Hu, Dirac degeneracy and elastic topological valley modes induced by local resonant states, *Phys. Rev. B.* 101 (2020) 014101. doi:10.1103/PhysRevB.101.014101.
- [163] D. Torrent, D. Mayou, J. Sánchez-Dehesa, Elastic analog of graphene: Dirac cones and edge states for flexural waves in thin plates, *Phys. Rev. B.* 87 (2013) 115143. doi:10.1103/PhysRevB.87.115143.
- [164] W. Wang, B. Bonello, B. Djafari-Rouhani, Y. Pennec, Topological valley, pseudospin, and pseudospin-valley protected edge states in symmetric pillared phononic crystals, *Phys. Rev. B.* 100 (2019) 140101. doi:10.1103/PhysRevB.100.140101.
- [165] H. Danawe, H. Li, K. Sun, S. Tol, Finite-Frequency Topological Maxwell Modes in Mechanical Self-Dual Kagome Lattices, *Phys. Rev. Lett.* 129 (2022) 204302. doi:10.1103/physrevlett.129.204302.
- [166] Q. Zhang, Y. Chen, K. Zhang, G. Hu, Programmable elastic valley Hall insulator with tunable interface propagation routes, *Extrem. Mech. Lett.* 28 (2019) 76–80. doi:10.1016/j.eml.2019.03.002.
- [167] A. Darabi, M.J. Leamy, Reconfigurable topological insulator for elastic waves, *J. Acoust. Soc. Am.* 146 (2019) 773–781. doi:10.1121/1.5114920.
- [168] K. Tang, M. Makwana, R. V. Craster, P. Sebbah, Observations of symmetry induced topological mode steering in a reconfigurable elastic plate, *Phys. Rev. B.* 102 (2020) 214103. doi:10.1103/PhysRevB.102.214103.

- [169] H. Al Ba'ba'a, K. Yu, Q. Wang, Elastically-supported lattices for tunable mechanical topological insulators, *Extrem. Mech. Lett.* 38 (2020) 100758. doi:10.1016/j.eml.2020.100758.
- [170] A. Darabi, M. Collet, M.J. Leamy, Experimental realization of a reconfigurable electroacoustic topological insulator, *Proc. Natl. Acad. Sci.* 117 (2020) 16138–16142. doi:10.1073/pnas.1920549117.
- [171] E. Riva, D.E. Quadrelli, G. Cazzulani, F. Braghin, Tunable in-plane topologically protected edge waves in continuum Kagome lattices, *J. Appl. Phys.* 124 (2018) 164903. doi:10.1063/1.5045837.
- [172] Y. Wu, R. Chaunsali, H. Yasuda, K. Yu, J. Yang, Dial-in topological metamaterials based on bistable stewart platform, *Sci. Rep.* 8 (2018) 112. doi:10.1038/s41598-017-18410-x.
- [173] T.W. Liu, F. Semperlotti, Tunable acoustic valley–Hall edge states in reconfigurable phononic elastic waveguides, *Phys. Rev. Appl.* 9 (2018) 014001. doi:10.1103/PhysRevApplied.9.014001.
- [174] H. Liu, S.Y. Huo, L.Y. Feng, H.B. Huang, J.J. Chen, Thermally tunable topological edge states for in-plane bulk waves in solid phononic crystals, *Ultrasonics.* 94 (2019) 227–234. doi:10.1016/j.ultras.2018.09.006.
- [175] B.H. Nguyen, X. Zhuang, H.S. Park, T. Rabczuk, Tunable topological bandgaps and frequencies in a pre-stressed soft phononic crystal, *J. Appl. Phys.* 125 (2019) 095106. doi:10.1063/1.5066088.
- [176] W. Zhou, Y. Su, Muhammad, W. Chen, C.W. Lim, Voltage-controlled quantum valley Hall effect in dielectric membrane-type acoustic metamaterials, *Int. J. Mech. Sci.* 172 (2020) 105368. doi:10.1016/j.ijmecsci.2019.105368.
- [177] X. An, C. Lai, W. He, H. Fan, Three-dimensional meta-truss lattice composite structures with vibration isolation performance, *Extrem. Mech. Lett.* 33 (2019) 100577. doi:10.1016/j.eml.2019.100577.
- [178] Y. Lu, Y. Yang, J.K. Guest, A. Srivastava, 3-D phononic crystals with ultra-wide band gaps, *Sci. Rep.* 7 (2017) 43407. doi:10.1038/srep43407.
- [179] S. Babaei, P. Wang, K. Bertoldi, Three-dimensional adaptive soft phononic crystals, *J. Appl. Phys.* 117 (2015) 244903. doi:10.1063/1.4923032.
- [180] O. McGee, H. Jiang, F. Qian, Z. Jia, L. Wang, H. Meng, D. Chronopoulos, Y. Chen, L. Zuo, 3D printed architected hollow sphere foams with low-frequency phononic band gaps, *Addit. Manuf.* 30 (2019) 100842. doi:10.1016/j.addma.2019.100842.

- [181] O.R. Bilal, D. Ballagi, C. Daraio, Architected Lattices for Simultaneous Broadband Attenuation of Airborne Sound and Mechanical Vibrations in All Directions, *Phys. Rev. Appl.* 10 (2018) 054060. doi:10.1103/PhysRevApplied.10.054060.
- [182] H. Meng, N. Bailey, Y. Chen, L. Wang, F. Ciampa, A. Fabro, D. Chronopoulos, W. Elmadih, 3D rainbow phononic crystals for extended vibration attenuation bands, *Sci. Rep.* 10 (2020) 18989. doi:10.1038/s41598-020-75977-8.
- [183] M.J. Choi, M.H. Oh, B. Koo, S. Cho, Optimal design of lattice structures for controllable extremal band gaps, *Sci. Rep.* 9 (2019) 9976. doi:10.1038/s41598-019-46089-9.
- [184] X. Shi, R. Chaunsali, F. Li, J. Yang, Elastic weyl points and surface arc states in three-dimensional structures, *Phys. Rev. Appl.* 12 (2019) 024058. doi:10.1103/PhysRevApplied.12.024058.
- [185] M. Fruchart, S.Y. Jeon, K. Hur, V. Cheianov, U. Wiesner, V. Vitelli, Soft self-assembly of Weyl materials for light and sound, *Proc. Natl. Acad. Sci.* 115 (2018) E3655–E3664. doi:10.1073/pnas.1720828115.
- [186] Y. Takahashi, T. Kariyado, Y. Hatsugai, Weyl points of mechanical diamond, *Phys. Rev. B.* 99 (2019) 024102. doi:10.1103/PhysRevB.99.024102.
- [187] S.Y. Huo, H.B. Huang, C.M. Fu, J.J. Chen, Ideal type-II Weyl phases and surface states for elastic waves in three-dimensional solid phononic crystals, *Phys. Scr.* 96 (2021) 125714. doi:10.1088/1402-4896/ac2c22.
- [188] G. Zhang, Y. Gao, A three-dimensional magnetoelastic valley Hall insulator with tunable elastic wave route and frequency, *J. Appl. Phys.* 132 (2022) 224108. doi:10.1063/5.0127638.
- [189] B. Yan, C. Felser, Topological materials: Weyl semimetals, *Annu. Rev. Condens. Matter Phys.* 8 (2017) 337–354. doi:10.1146/annurev-conmatphys-031016-025458.
- [190] S.Y. Xu, I. Belopolski, N. Alidoust, M. Neupane, G. Bian, C. Zhang, R. Sankar, G. Chang, Z. Yuan, C.C. Lee, S.M. Huang, H. Zheng, J. Ma, D.S. Sanchez, B.K. Wang, A. Bansil, F. Chou, P.P. Shibayev, H. Lin, S. Jia, M.Z. Hasan, Discovery of a Weyl fermion semimetal and topological Fermi arcs, *Science.* 349 (2015) 613–617. doi:10.1126/science.aaa9297.
- [191] S.A. Parameswaran, Y. Wan, Topological Insulators Turn a Corner, *Physics (College Park, Md.)* 10 (2017) 132. doi:10.1103/physics.10.132.
- [192] F. Schindler, A.M. Cook, M.G. Vergniory, Z. Wang, S.S.P. Parkin, B.A. Bernevig, T. Neupert, Higher-order topological insulators, *Sci. Adv.* 4 (2018) eaat0346. doi:10.1126/sciadv.aat0346.

- [193] W.A. Benalcazar, B.A. Bernevig, T.L. Hughes, Quantized electric multipole insulators, *Science*. 357 (2017) 61–66. doi:10.1126/science.aah6442.
- [194] Z. Song, Z. Fang, C. Fang, (d-2)-Dimensional Edge States of Rotation Symmetry Protected Topological States, *Phys. Rev. Lett.* 119 (2017) 246402. doi:10.1103/PhysRevLett.119.246402.
- [195] M. Ezawa, Minimal models for Wannier-type higher-order topological insulators and phosphorene, *Phys. Rev. B*. 98 (2018) 045125. doi:10.1103/PhysRevB.98.045125.
- [196] W.A. Benalcazar, T. Li, T.L. Hughes, Quantization of fractional corner charge in Cn-symmetric higher-order topological crystalline insulators, *Phys. Rev. B*. 99 (2019) 245151. doi:10.1103/PhysRevB.99.245151.
- [197] M. Ezawa, Higher-Order Topological Insulators and Semimetals on the Breathing Kagome and Pyrochlore Lattices, *Phys. Rev. Lett.* 120 (2018) 26801. doi:10.1103/PhysRevLett.120.026801.
- [198] M. Serra-Garcia, V. Peri, R. Süsstrunk, O.R. Bilal, T. Larsen, L.G. Villanueva, S.D. Huber, Observation of a phononic quadrupole topological insulator, *Nature*. 555 (2018) 342–345. doi:10.1038/nature25156.
- [199] Q. Wu, H. Chen, X. Li, G. Huang, In-Plane Second-Order Topologically Protected States in Elastic Kagome Lattices, *Phys. Rev. Appl.* 14 (2020) 014084. doi:10.1103/PhysRevApplied.14.014084.
- [200] S.Y. Huo, H.N. Huang, L.Y. Feng, J.J. Chen, Edge states and corner modes in second-order topological phononic crystal plates, *Appl. Phys. Express*. 12 (2019) 094003.
- [201] Z. Zheng, J. Yin, J. Wen, D. Yu, Higher-order topological states in locally resonant elastic metamaterials, *Appl. Phys. Lett.* 120 (2022) 144101. doi:10.1063/5.0074463.
- [202] Z. Wang, Q. Wei, An elastic higher-order topological insulator based on kagome phononic crystals, *J. Appl. Phys.* 129 (2021) 035102. doi:10.1063/5.0031377.
- [203] Z. Wang, Q. Wei, H.Y. Xu, D.J. Wu, A higher-order topological insulator with wide bandgaps in Lamb-wave systems, *J. Appl. Phys.* 127 (2020) 075105. doi:10.1063/1.5140553.
- [204] S. An, T. Liu, H. Fan, H. Gao, Z. Gu, S. Liang, S. Huang, Y. Zheng, Y. Chen, L. Cheng, J. Zhu, Second-order elastic topological insulator with valley-selective corner states, *Int. J. Mech. Sci.* 224 (2022) 107337. doi:10.1016/j.ijmecsci.2022.107337.

- [205] H. Fan, B. Xia, S. Zheng, L. Tong, Elastic phononic topological plate with edge and corner states based on pseudospin-valley-coupling, *J. Phys. D: Appl. Phys.* 53 (2020) 395304. doi:10.1088/1361-6463/ab94e2.
- [206] C.-W. Chen, R. Chaunsali, J. Christensen, G. Theocharis, J. Yang, Corner states in a second-order mechanical topological insulator, *Commun. Mater.* 2 (2021) 62. doi:10.1038/s43246-021-00170-x.
- [207] Y. Chen, J. Li, J. Zhu, Topology optimization of quantum spin Hall effect-based second-order phononic topological insulator, *Mech. Syst. Signal Process.* 164 (2022) 108243. doi:10.1016/j.ymsp.2021.108243.
- [208] H. Danawe, H. Li, H. Al Ba'ba'a, S. Tol, Existence of corner modes in elastic twisted kagome lattices, *Phys. Rev. B.* 104 (2021) L241107. doi:10.1103/PhysRevB.104.L241107.
- [209] K. Guesmi, L. Abdeladim, S. Tozer, P. Mahou, T. Kumamoto, K. Jurkus, P. Rigaud, K. Loulier, N. Dray, P. Georges, M. Hanna, J. Livet, W. Supatto, E. Beaurepaire, F. Druon, Dual-color deep-tissue three-photon microscopy with a multiband infrared laser, *Light Sci. Appl.* 7 (2018) 12. doi:10.1038/s41377-018-0012-2.
- [210] G. Shambat, M.S. Mirotznik, G.W. Euliss, V. Smolski, E.G. Johnson, R.A. Athale, Photonic crystal filters for multi-band optical filtering on a monolithic substrate, *J. Nanophotonics.* 3 (2009) 031506. doi:10.1117/1.3110223.
- [211] O. Turkmen, E. Ekmekci, G. Turhan-Sayan, Nested U-ring resonators: A novel multi-band metamaterial design in microwave region, *IET Microwaves, Antennas Propag.* 6 (2012) 1102–1108. doi:10.1049/iet-map.2012.0037.
- [212] Y. Chen, Z. Lan, J. Zhu, Inversely Designed Second-Order Photonic Topological Insulator With Multiband Corner States, *Phys. Rev. Appl.* 17 (2022) 054003. doi:10.1103/PhysRevApplied.17.054003.
- [213] Y. Chen, F. Qian, L. Zuo, F. Scarpa, L. Wang, Broadband and multiband vibration mitigation in lattice metamaterials with sinusoidally-shaped ligaments, *Extrem. Mech. Lett.* 17 (2017) 24–32. doi:10.1016/j.eml.2017.09.012.
- [214] V. Gorshkov, P. Sareh, N. Navadeh, V. Tereshchuk, A.S. Fallah, Multi-resonator metamaterials as multi-band metastructures, *Mater. Des.* 202 (2021) 109522. doi:10.1016/j.matdes.2021.109522.
- [215] Z. Wu, R.L. Harne, K.W. Wang, Exploring a modular adaptive metastructure concept inspired by muscle's cross-bridge, *J. Intell. Mater. Syst. Struct.* 27 (2016) 1189–1202. doi:10.1177/1045389X15586451.

- [216] Y. Zheng, Z. Wu, X. Zhang, K.W. Wang, A piezo-metastructure with bistable circuit shunts for adaptive nonreciprocal wave transmission, *Smart Mater. Struct.* 28 (2019) 045005. <https://doi.org/10.1088/1361-665X/ab083c>.
- [217] D.J. Inman, A. Erturk, *Piezoelectric energy harvesting*, John Wiley & Sons, Chichester, West Sussex, United Kingdom, 2011.
- [218] H.F. Tiersten, *Linear Piezoelectric Plate Vibrations: Elements of the Linear Theory of Piezoelectricity and the Vibrations of Piezoelectric Plates*, Springer, New York, NY, United States, 2013. doi:10.1007/978-1-4899-6453-3.
- [219] L. Meirovitch, *Analytical Methods in Vibrations*, MacMillan, New York, NY, United States, 1967.
- [220] N.W. Hagood, A. von Flotow, Damping of structural vibrations with piezoelectric materials and passive electrical networks, *J. Sound Vib.* 146 (1991) 243–268. doi:10.1016/0022-460X(91)90762-9.
- [221] J. Tang, K.W. Wang, Active-passive hybrid piezoelectric networks for vibration control: comparisons and improvement, *Smart Mater. Struct.* 10 (2001) 794–806.
- [222] K.W. Wang, J. Tang, *Adaptive Structural Systems with Piezoelectric Transducer Circuitry*, Springer, 2008.
- [223] M. Berardengo, O. Thomas, C. Giraud-Audine, S. Manzoni, Improved resistive shunt by means of negative capacitance: new circuit, performances and multi-mode control, *Smart Mater. Struct.* 25 (2016) 075033. doi:10.1088/0964-1726/25/7/075033.
- [224] G. Hu, J. Xu, L. Tang, C. Lan, R. Das, Tunable metamaterial beam using negative capacitor for local resonators coupling, *J. Intell. Mater. Syst. Struct.* 31 (2020) 389–407. doi:10.1177/1045389X19891575.
- [225] U. Kumar, S.K. Shukla, Analytical study of inductor simulation circuits, *Act. Passiv. Electron. Components.* 13 (1989) 211–227. doi:10.1155/1989/39762.
- [226] B. Lossouarn, M. Aucejo, J.F. Deü, B. Multon, Design of inductors with high inductance values for resonant piezoelectric damping, *Sensors Actuators A Phys.* 259 (2017) 68–76. doi:10.1016/j.sna.2017.03.030.
- [227] M.V. Berry, Quantal phase factors accompanying adiabatic changes, *Proc. R. Soc. London. A. Math. Phys. Sci.* 392 (1984) 45–57. doi:10.1142/9789813221215_0006.

- [228] W. Yao, S.A. Yang, Q. Niu, Edge states in graphene: From gapped flat-band to gapless chiral modes, *Phys. Rev. Lett.* 102 (2009) 096801. doi:10.1103/PhysRevLett.102.096801.
- [229] K. Qian, D.J. Apigo, C. Prodan, Y. Barlas, E. Prodan, Topology of the valley-Chern effect, *Phys. Rev. B.* 98 (2018) 155138. doi:10.1103/PhysRevB.98.155138.
- [230] M. Thota, S. Li, K.W. Wang, Lattice reconfiguration and phononic band-gap adaptation via origami folding, *Phys. Rev. B.* 95 (2017) 064307. doi:10.1103/PhysRevB.95.064307.
- [231] M. Thota, K.W. Wang, Tunable waveguiding in origami phononic structures, *J. Sound Vib.* 430 (2018) 93–100. doi:10.1016/j.jsv.2018.05.031.
- [232] N.Y. Kim, K. Kusudo, A. Löffler, S. Höfling, A. Forchel, Y. Yamamoto, Exciton-polariton condensates near the Dirac point in a triangular lattice, *New J. Phys.* 15 (2013) 035032. doi:10.1088/1367-2630/15/3/035032.
- [233] M. Plihal, A.A. Maradudin, Photonic band structure of two-dimensional systems: The triangular lattice, *Phys. Rev. B.* 44 (1991) 8565–8571. doi:10.1103/PhysRevB.44.8565.
- [234] X. Zhang, Observing Zitterbewegung for photons near the Dirac point of a two-dimensional photonic crystal, *Phys. Rev. Lett.* 100 (2008) 113903. doi:10.1103/PhysRevLett.100.113903.
- [235] P. Dorin, K.W. Wang, Broadband frequency and spatial on-demand tailoring of topological wave propagation harnessing piezoelectric metamaterials, *Front. Mater.* 7 (2021) 602996. doi:10.3389/fmats.2020.602996.
- [236] X. Liu, G. Cai, K.W. Wang, Reconfigurable topologically protected wave propagation in metastable structure, *J. Sound Vib.* 492 (2021) 115819. doi:10.1016/j.jsv.2020.115819.
- [237] L. Yang, K. Yu, B. Bonello, B. Djafari-Rouhani, W. Wang, Y. Wu, Abnormal topological refraction into free medium at subwavelength scale in valley phononic crystal plates, *Phys. Rev. B.* 103 (2021) 184303. doi:https://doi.org/10.1103/PhysRevB.103.184303.
- [238] T.W. Liu, F. Semperlotti, Nonconventional topological band properties and gapless helical edge states in elastic phononic waveguides with Kekulé distortion, *Phys. Rev. B.* 100 (2019) 214110. doi:10.1103/PhysRevB.100.214110.
- [239] S. Li, J. Yang, Topological transition in spiral elastic valley metamaterials, *Phys. Rev. Appl.* 15 (2021) 014058. doi:10.1103/PhysRevApplied.15.014058.
- [240] Y. Jin, W. Wang, Z. Wen, D. Torrent, B. Djafari-Rouhani, Topological states in twisted pillared phononic plates, *Extrem. Mech. Lett.* 39 (2020) 100777. doi:10.1016/j.eml.2020.100777.

- [241] J. Mei, J. Wang, X. Zhang, S. Yu, Z. Wang, M.H. Lu, Robust and High-Capacity Phononic Communications through Topological Edge States by Discrete Degree-of-Freedom Multiplexing, *Phys. Rev. Appl.* 12 (2019) 054041. doi:10.1103/PhysRevApplied.12.054041.
- [242] J. Qiu, An electrothermally-actuated bistable MEMS relay for power applications, 2003.
- [243] J. Qiu, J.H. Lang, A.H. Slocum, A curved-beam bistable mechanism, *J. Microelectromechanical Syst.* 13 (2004) 137–146.
- [244] H. Liu, Q. Zhang, K. Zhang, G. Hu, H. Duan, Designing 3D digital metamaterial for elastic waves: from elastic wave polarizer to vibration control, *Adv. Sci.* 6 (2019) 1900401. doi:10.1002/advs.201900401.
- [245] Z. Wu, Y. Zheng, K.W. Wang, Metastable modular metastructures for on-demand reconfiguration of band structures and nonreciprocal wave propagation, *Phys. Rev. E.* 97 (2018) 022209. doi:10.1103/PhysRevE.97.022209.
- [246] J. Lu, C. Qiu, W. Deng, X. Huang, F. Li, F. Zhang, S. Chen, Z. Liu, Valley topological phases in bilayer sonic crystals, *Phys. Rev. Lett.* 120 (2018) 116802. doi:10.1103/PhysRevLett.120.116802.
- [247] C. He, S.Y. Yu, H. Ge, H. Wang, Y. Tian, H. Zhang, X.C. Sun, Y.B. Chen, J. Zhou, M.H. Lu, Y.F. Chen, Three-dimensional topological acoustic crystals with pseudospin-valley coupled saddle surface states, *Nat. Commun.* 9 (2018) 4555. doi:10.1038/s41467-018-07030-2.
- [248] M. Ezawa, Topological Kirchhoff law and bulk-edge correspondence for valley Chern and spin-valley Chern numbers, *Phys. Rev. B - Condens. Matter Mater. Phys.* 88 (2013) 161406(R). doi:10.1103/PhysRevB.88.161406.
- [249] C. Kaspar, B.J. Ravoo, W.G. van der Wiel, S. V. Wegner, W.H.P. Pernice, The rise of intelligent matter, *Nature.* 594 (2021) 345–355. doi:10.1038/s41586-021-03453-y.
- [250] M.A. McEvoy, N. Correll, Materials that couple sensing, actuation, computation, and communication, *Science.* 347 (2015) 1261689. doi:10.1126/science.1261689.
- [251] J. Ma, K. Sun, S. Gonella, Valley Hall in-plane edge states as building blocks for elastodynamic logic circuits, *Phys. Rev. Appl.* 12 (2019) 044015. doi:10.1103/PhysRevApplied.12.044015.
- [252] J. Cha, K.W. Kim, C. Daraio, Experimental realization of on-chip topological nanoelectromechanical metamaterials, *Nature.* 564 (2018) 229–233. doi:10.1038/s41586-018-0764-0.

- [253] P. Dorin, X. Liu, K.W. Wang, Emergence of bilayer-locked states and synthesis of elastic wave networks in a programmable 3D topological metamaterial, *Appl. Phys. Lett.* 120 (2022) 221703. doi:10.1063/5.0094184.
- [254] H. Liu, Multiband topologically protected states realized by elastic honeycomb structures based on fundamental mechanical elements, *Eur. J. Mech. A/Solids.* 97 (2023) 104803. doi:10.1016/j.euromechsol.2022.104803.
- [255] Z.D. Zhang, S.Y. Yu, M.H. Lu, Y.F. Chen, Dual-Band Helical Edge States and Discrete Dirac Vortices in Solid-State Elastic Waves, *Phys. Rev. Appl.* 17 (2022) 034029. doi:10.1103/PhysRevApplied.17.034029.
- [256] W. Yuan, J. Zhao, Y. Long, J. Ren, Z. Zhong, Multi-branch valley-chiral edge states of antisymmetric plate wave in phononic crystal plates with double-sided symmetric pillars, *Int. J. Mech. Sci.* 197 (2021) 106347. doi:10.1016/j.ijmecsci.2021.106347.
- [257] S.Y. Huo, J.J. Chen, H.B. Huang, G. Huang, Simultaneous multi-band valley-protected topological edge states of shear vertical wave in two-dimensional phononic crystals with veins, *Sci. Rep.* 7 (2017) 10335. doi:10.1038/s41598-017-10857-2.
- [258] G.-G. Xu, X.-W. Sun, X.-D. Wen, X.-X. Liu, T. Song, Z.-J. Liu, Valley transport via dual-band elastic topological edge states in local-resonant phononic crystal plate, *J. Appl. Phys.* 133 (2023) 095110. doi:10.1063/5.0136890.
- [259] J. Ma, X. Xi, X. Sun, Experimental Demonstration of Dual-Band Nano-Electromechanical Valley-Hall Topological Metamaterials, *Adv. Mater.* 33 (2021) 2006521. doi:10.1002/adma.202006521.
- [260] J. Chen, K.F. Tong, A. Al-Armaghany, J. Wang, A Dual-Band Dual-Polarization Slot Patch Antenna for GPS and Wi-Fi Applications, *IEEE Antennas Wirel. Propag. Lett.* 15 (2016) 406–409. doi:10.1109/LAWP.2015.2448536.
- [261] A. Ni, Z. Shi, Topological metamaterial plates: numerical investigation, experimental validation and applications, *Eng. Struct.* 275 (2023) 115288. doi:10.1016/j.engstruct.2022.115288.
- [262] M. Murer, S.K. Guruva, G. Formica, W. Lacarbonara, A multi-bandgap metamaterial with multi-frequency resonators, *J. Compos. Mater.* 57 (2023) 783–804. doi:10.1177/00219983231151578.
- [263] D. Giannini, M. Schevenels, E.P.B. Reynders, Rotational and multimodal local resonators for broadband sound insulation of orthotropic metamaterial plates, *J. Sound Vib.* 547 (2023) 117453. doi:10.1016/j.jsv.2022.117453.

- [264] M.F. Ashby, H. Shercliff, D. Cebon, *Materials: Engineering, Science, Processing and Design*, 4th ed., Butterworth-Heinemann, 2019.
- [265] A. Nazir, O. Gokcekaya, K. Md Masum Billah, O. Ertugrul, J. Jiang, J. Sun, S. Hussain, Multi-material additive manufacturing: A systematic review of design, properties, applications, challenges, and 3D printing of materials and cellular metamaterials, *Mater. Des.* 226 (2023) 111661. doi:10.1016/j.matdes.2023.111661.
- [266] P. Dorin, M. Khan, K.W. Wang, Uncovering and experimental realization of multimodal 3D topological metamaterials for low-frequency and multiband elastic wave control, *Adv. Sci.* (2023) 2304793. doi:10.1002/advs.202304793.
- [267] W.P. Su, J.R. Schrieffer, A.J. Heeger, Solitons in polyacetylene, *Phys. Rev. Lett.* 42 (1979) 1698–1701. doi:10.1103/PhysRevLett.42.1698.
- [268] F. Liu, K. Wakabayashi, Novel Topological Phase with a Zero Berry Curvature, *Phys. Rev. Lett.* 118 (2017) 076803. doi:10.1103/PhysRevLett.118.076803.
- [269] B.Y. Xie, G.X. Su, H.F. Wang, H. Su, X.P. Shen, P. Zhan, M.H. Lu, Z.L. Wang, Y.F. Chen, Visualization of Higher-Order Topological Insulating Phases in Two-Dimensional Dielectric Photonic Crystals, *Phys. Rev. Lett.* 122 (2019) 233903. doi:10.1103/PhysRevLett.122.233903.
- [270] M. Kim, J. Rho, Topological edge and corner states in a two-dimensional photonic Su-Schrieffer-Heeger lattice, *Nanophotonics*. 9 (2020) 3227–3234. doi:10.1515/nanoph-2019-0451.
- [271] M. Li, Y. Wang, T. Sang, H. Chu, Y. Lai, G. Yang, Experimental observation of multiple edge and corner states in photonic slabs heterostructures, *Photonics Res.* 10 (2022) 197–204. doi:10.1364/prj.440640.
- [272] Z. Zheng, J. Yin, J. Wen, D. Yu, X. Chen, Switchable corner states in phononic crystals realized by inverse design, *Int. J. Mech. Sci.* 243 (2023) 108035. doi:10.1016/j.ijmecsci.2022.108035.
- [273] G. Duan, S. Zheng, Z. Lin, J. Jiao, J. Liu, Numerical and experimental investigation of second-order mechanical topological insulators, *J. Mech. Phys. Solids*. 174 (2023) 105251. doi:10.1016/j.jmps.2023.105251.
- [274] S. Liu, W. Gao, Q. Zhang, S. Ma, L. Zhang, C. Liu, Y.J. Xiang, T.J. Cui, S. Zhang, Topologically Protected Edge State in Two-Dimensional Su–Schrieffer–Heeger Circuit, *Research*. 2019 (2019) 8609875. doi:10.34133/2019/8609875.

- [275] B.Y. Xie, H.F. Wang, H.X. Wang, X.Y. Zhu, J.H. Jiang, M.H. Lu, Y.F. Chen, Second-order photonic topological insulator with corner states, *Phys. Rev. B.* 98 (2018) 205147. doi:10.1103/PhysRevB.98.205147.
- [276] H.R. Kim, M.S. Hwang, D. Smirnova, K.Y. Jeong, Y. Kivshar, H.G. Park, Multipolar lasing modes from topological corner states, *Nat. Commun.* 11 (2020) 5758. doi:10.1038/s41467-020-19609-9.
- [277] O.R. Bilal, A. Foehr, C. Daraio, Bistable metamaterial for switching and cascading elastic vibrations, *Proc. Natl. Acad. Sci.* 114 (2017) 4603–4606. doi:10.1073/pnas.1618314114.
- [278] K. Chen, X. Dong, P. Gao, J. Zhang, Y. Sun, G. Tu, Z. Peng, Multifunctional applications of topological valley-locked elastic waves, *Int. J. Mech. Sci.* 259 (2023) 108589. doi:10.1016/j.ijmecsci.2023.108589.
- [279] H. Pirie, S. Sadhuka, J. Wang, R. Andrei, J.E. Hoffman, Topological Phononic Logic, *Phys. Rev. Lett.* 128 (2022) 015501. doi:10.1103/PhysRevLett.128.015501.
- [280] S. Jia, R. Huang, J. Hu, Y. Jiang, H. Huang, B. Xie, M. Lu, P. Zhan, Y. Chen, Z. Wang, Phase-Engineering Strategy for Multidimensional Light Steering in a Photonic Higher-Order Topological Insulator, *Laser Photon. Rev.* 17 (2023) 2200949. doi:10.1002/lpor.202200949.
- [281] T.L. Floyd, *Digital Fundamentals*, Pearson, 2015.
- [282] Z.G. Song, Y.Y. Zhang, S.S. Li, The topological insulator in a fractal space, *Appl. Phys. Lett.* 104 (2014) 233106. doi:10.1063/1.4882166.
- [283] M.N. Ivaki, I. Sahlberg, K. Pöyhönen, T. Ojanen, Topological Random Fractals, *Commun. Phys.* 5 (2022) 327. doi:10.1038/s42005-022-01101-z.
- [284] S. Fischer, M. Van Hooft, T. Van Der Meijden, C.M. Smith, L. Fritz, M. Fremling, Robustness of chiral edge modes in fractal-like lattices below two dimensions: A case study, *Phys. Rev. Res.* 3 (2021) 043103. doi:10.1103/PhysRevResearch.3.043103.
- [285] M. Fremling, M. Van Hooft, C.M. Smith, L. Fritz, Existence of robust edge currents in Sierpiński fractals, *Phys. Rev. Res.* 2 (2020) 013044. doi:10.1103/PhysRevResearch.2.013044.
- [286] A.A. Iliasov, M.I. Katsnelson, S. Yuan, Hall conductivity of a Sierpiński carpet, *Phys. Rev. B.* 101 (2020) 045413. doi:10.1103/PhysRevB.101.045413.
- [287] S. Sarangi, A.E.B. Nielsen, Effect of coordination on topological phases on self-similar structures, *Phys. Rev. B.* 104 (2021) 045147. doi:10.1103/PhysRevB.104.045147.

- [288] S. Pai, A. Prem, Topological states on fractal lattices, *Phys. Rev. B.* 100 (2019) 155135. doi:10.1103/PhysRevB.100.155135.
- [289] S.N. Kempkes, M.R. Slot, S.E. Freeney, S.J.M. Zevenhuizen, D. Vanmaekelbergh, I. Swart, C.M. Smith, Design and characterization of electrons in a fractal geometry, *Nat. Phys.* 15 (2019) 127–131. doi:10.1038/s41567-018-0328-0.
- [290] S. Manna, C.W. Duncan, C.A. Weidner, J.F. Sherson, A.E.B. Nielsen, Anyon braiding on a fractal lattice with a local Hamiltonian, *Phys. Rev. A.* 105 (2022) L021302. doi:10.1103/PhysRevA.105.L021302.
- [291] S. Manna, S. Nandy, B. Roy, Higher-order topological phases on fractal lattices, *Phys. Rev. B.* 105 (2022) L201301. doi:10.1103/physrevb.105.l201301.
- [292] B.B. Mandelbrot, J.A. Wheeler, The Fractal Geometry of Nature, *Am. J. Phys.* 51 (1983) 286–287. doi:10.1119/1.13295.
- [293] B.B. Mandelbrot, How long is the coast of Britain? Statistical self-similarity and fractional dimension, *Science.* 156 (1967) 636–638. doi:10.1126/science.156.3775.636.
- [294] C. McMullen, The Hausdorff dimension of general Sierpinski carpets, *Nagoya Math. J.* 96 (1984) 1–9.
- [295] Z. Yang, E. Lustig, Y. Lumer, M. Segev, Photonic Floquet topological insulators in a fractal lattice, *Light Sci. Appl.* 9 (2020) 128. doi:10.1038/s41377-020-00354-z.
- [296] T. Biesenthal, L.J. Maczewsky, Z. Yang, M. Kremer, M. Segev, A. Szameit, M. Heinrich, Fractal photonic topological insulators, *Science.* 376 (2022) 1114–1119. doi:10.1126/science.abm2842.
- [297] S. Zheng, X. Man, Z.L. Kong, Z.K. Lin, G. Duan, N. Chen, D. Yu, J.H. Jiang, B. Xia, Observation of fractal higher-order topological states in acoustic metamaterials, *Sci. Bull.* 67 (2022) 2069–2075. doi:10.1016/j.scib.2022.09.020.
- [298] J. Li, Y. Sun, Q. Mo, Z. Ruan, Z. Yang, Fractality-induced topological phase squeezing and devil’s staircase, *Phys. Rev. Res.* 5 (2023) 023189. doi:10.1103/physrevresearch.5.023189.
- [299] J. Li, Q. Mo, J.H. Jiang, Z. Yang, Higher-order topological phase in an acoustic fractal lattice, *Sci. Bull.* 67 (2022) 2040–2044. doi:10.1016/j.scib.2022.09.024.
- [300] S. Shankar, A. Souslov, M.J. Bowick, M.C. Marchetti, V. Vitelli, Topological active matter, *Nat. Rev. Phys.* 4 (2022) 380–398. doi:10.1038/s42254-022-00445-3.

- [301] M. Al Rifaie, H. Abdulhadi, A. Mian, Advances in mechanical metamaterials for vibration isolation: A review, *Adv. Mech. Eng.* 14 (2022). doi:10.1177/16878132221082872.
- [302] M.F. Daqaq, R. Masana, A. Erturk, D.D. Quinn, On the role of nonlinearities in vibratory energy harvesting: a critical review and discussion, *Appl. Mech. Rev.* 66 (2014) 040801. doi:10.1115/1.4026278.
- [303] D. Balageas, C.P. Fritzen, A. Güemes, *Structural health monitoring*, John Wiley & Sons, 2010.
- [304] Z. Su, L. Ye, *Identification of Damage Using Lamb Waves: From Fundamentals to Applications*, Springer London, 2009. doi:10.1007/978-84882-784-4.
- [305] V. Giurgiutiu, *Structural Health Monitoring With Piezoelectric Wafer Active Sensors*, 2nd ed., Academic Press, 2014.
- [306] C. Zhang, A.A. Mousavi, S.F. Masri, G. Gholipour, K. Yan, X. Li, Vibration feature extraction using signal processing techniques for structural health monitoring: A review, *Mech. Syst. Signal Process.* 177 (2022) 109175. doi:10.1016/j.ymsp.2022.109175.
- [307] S. Li, L. Da Xu, S. Zhao, The internet of things: a survey, *Inf. Syst. Front.* 17 (2015) 243–259. doi:10.1007/s10796-014-9492-7.
- [308] L. Da Xu, W. He, S. Li, Internet of things in industries: A survey, *IEEE Trans. Ind. Informatics.* 10 (2014) 2233–2243. doi:10.1109/TII.2014.2300753.
- [309] L. Atzori, A. Iera, G. Morabito, The Internet of Things: A survey, *Comput. Networks.* 54 (2010) 2787–2805. doi:10.1016/j.comnet.2010.05.010.
- [310] H. Yoo, H. Park, S. Yoo, S. On, H. Seong, S.G. Im, J.J. Kim, Highly stacked 3D organic integrated circuits with via-hole-less multilevel metal interconnects, *Nat. Commun.* 10 (2019) 2424. doi:10.1038/s41467-019-10412-9.
- [311] K.S. Novoselov, V.I. Fal'Ko, L. Colombo, P.R. Gellert, M.G. Schwab, K. Kim, A roadmap for graphene, *Nature.* 490 (2012) 192–200. doi:10.1038/nature11458.
- [312] A. Slobozhanyuk, S.H. Mousavi, X. Ni, D. Smirnova, Y.S. Kivshar, A.B. Khanikaev, Three-dimensional all-dielectric photonic topological insulator, *Nat. Photonics.* 11 (2017) 130–136. doi:10.1038/nphoton.2016.253.
- [313] S. Wong, A. El-Gamal, P. Griffin, T. Nishi, F. Pease, J. Plummer, Monolithic 3D integrated circuits, in: *Int. Symp. VLSI Technol. Syst. Appl.*, Hsinchu, Taiwan, 2007. doi:10.1109/VTSA.2007.378923.

- [314] S. Wang, M.B. Tahoori, Electromigration-Aware Local-Via Allocation in Power/Ground TSVs of 3-D ICs, in: *IEEE Trans. Very Large Scale Integr. Syst.*, 2017: pp. 2881–2892. doi:10.1109/TVLSI.2017.2716821.
- [315] S. Sinha, X. Xu, M. Bhargava, S. Das, B. Cline, G. Yeric, Stack up your chips: Betting on 3D integration to augment Moore’s Law scaling, in: *Proc. IEEE S3S*, 2019. <http://arxiv.org/abs/2005.10866>.
- [316] T. Zhang, Y. Jiang, Z. Song, H. Huang, Y. He, Z. Fang, H. Weng, C. Fang, Catalogue of topological electronic materials, *Nature*. 566 (2019) 475–479. doi:10.1038/s41586-019-0944-6.
- [317] A. Kitaev, Periodic table for topological insulators and superconductors, *AIP Conf. Proc.* 1134 (2009) 22–30. doi:10.1063/1.3149495.
- [318] A.P. Schnyder, S. Ryu, A. Furusaki, A.W.W. Ludwig, Classification of topological insulators and superconductors in three spatial dimensions, *Phys. Rev. B*. 78 (2008) 195125. doi:10.1103/PhysRevB.78.195125.
- [319] Y. Barlas, E. Prodan, Topological classification table implemented with classical passive metamaterials, *Phys. Rev. B*. 98 (2018) 094310. doi:10.1103/PhysRevB.98.094310.
- [320] W. Cheng, E. Prodan, C. Prodan, Topological D-Class Physics with Passive Acoustic Elements, *ArXiv Prepr.* (2022). <http://arxiv.org/abs/2204.03613>.
- [321] Y. Jin, L. He, Z. Wen, B. Mortazavi, H. Guo, D. Torrent, B. Djafari-Rouhani, T. Rabczuk, X. Zhuang, Y. Li, Intelligent on-demand design of phononic metamaterials, *Nanophotonics*. 11 (2022) 439–460. doi:10.1515/nanoph-2021-0639.
- [322] Y. Zhai, H.S. Kwon, Y. Choi, D. Kovacevich, B.I. Popa, Learning the dynamics of metamaterials from diffracted waves with convolutional neural networks, *Commun. Mater.* 3 (2022) 53. doi:10.1038/s43246-022-00276-w.
- [323] Muhammad, J. Kennedy, C.W. Lim, Machine learning and deep learning in phononic crystals and metamaterials – A review, *Mater. Today Commun.* 33 (2022) 104606. doi:10.1016/j.mtcomm.2022.104606.
- [324] S. Kriegman, D. Blackiston, M. Levin, J. Bongard, A scalable pipeline for designing reconfigurable organisms, *Proc. Natl. Acad. Sci.* 117 (2020) 1853–1859. doi:10.1073/pnas.1910837117.

- [325] H. Xue, Z. Wang, Y.X. Huang, Z. Cheng, L. Yu, Y.X. Foo, Y.X. Zhao, S.A. Yang, B. Zhang, Projectively Enriched Symmetry and Topology in Acoustic Crystals, *Phys. Rev. Lett.* 128 (2022) 116802. doi:10.1103/PhysRevLett.128.116802.
- [326] Y. Deng, Y. Jing, Acoustic Crystals with a Möbius Twist, *Physics (College. Park. Md)*. 15,36 (2022). doi:10.1103/physics.15.36.
- [327] T. Li, J. Du, Q. Zhang, Y. Li, X. Fan, F. Zhang, C. Qiu, Acoustic Möbius Insulators from Projective Symmetry, *Phys. Rev. Lett.* 128 (2022) 116803. doi:10.1103/PhysRevLett.128.116803.
- [328] M. Sitti, Physical intelligence as a new paradigm, *Extrem. Mech. Lett.* 46 (2021) 101340. doi:10.1016/j.eml.2021.101340.
- [329] P. Bhowad, S. Li, Physical reservoir computing with origami and its application to robotic crawling, *Sci. Rep.* 11 (2021) 13002. doi:10.1038/s41598-021-92257-1.
- [330] Y. Zhang, K.W. Wang, Enabling mechano-intelligence in adaptive structures utilizing physical computing, in: *SPIE Smart Struct. + Nondestruct. Eval. Act. Passiv. Smart Struct. Integr. Syst.* XVI, 2022: p. 1204317. doi:10.1117/12.2614439.
- [331] K. Nakajima, Physical reservoir computing-an introductory perspective, *Jpn. J. Appl. Phys.* 59 (2020) 060501. doi:10.35848/1347-4065/ab8d4f.
- [332] Y. Jiang, L.M. Korpas, J.R. Raney, Bifurcation-based embodied logic and autonomous actuation, *Nat. Commun.* 10 (2019) 128. doi:10.1038/s41467-018-08055-3.
- [333] D. Drotman, S. Jadhav, D. Sharp, C. Chan, M.T. Tolley, Electronics-free pneumatic circuits for controlling soft-legged robots, *Sci. Robot.* 6 (2021) eaay2627. doi:10.1126/scirobotics.aay2627.
- [334] K. Nakajima, H. Hauser, T. Li, R. Pfeifer, Information processing via physical soft body, *Sci. Rep.* 5 (2015) 10487. doi:10.1038/srep10487.
- [335] C. Li, T. Jiang, Q. He, Z. Peng, Smart metasurface shaft for vibration source identification with a single sensor, *J. Sound Vib.* 493 (2021) 115836. doi:10.1016/j.jsv.2020.115836.
- [336] N.M. Estakhri, B. Edwards, N. Engheta, Inverse-designed metastructures that solve equations, *Science.* 363 (2019) 1333–1338. doi:10.1126/science.aaw2498.
- [337] T. Chen, M. Pauly, P.M. Reis, A reprogrammable mechanical metamaterial with stable memory, *Nature.* 589 (2021) 386–390. doi:10.1038/s41586-020-03123-5.

- [338] F. Zangeneh-Nejad, D.L. Sounas, A. Alù, R. Fleury, Analogue computing with metamaterials, *Nat. Rev. Mater.* 6 (2021) 207–225. doi:10.1038/s41578-020-00243-2.
- [339] Y. Zhang, A. Deshmukh, K.W. Wang, Uncovering multifunctional mechano-intelligence in and through phononic metastructures harnessing physical reservoir computing, *Adv Sci.* (2023) 2305074.
- [340] COMSOL Multiphysics Reference Manual, version 6.0, (2023).
- [341] T.-W. Liu, F. Semperlotti, Nonconventional topological band properties and gapless helical edge states in elastic phononic waveguides with Kekulé distortion, *Phys. Rev. B.* 100 (2019) 214110. doi:10.1103/PhysRevB.100.214110.
- [342] T.-W. Liu, F. Semperlotti, Synthetic Kramers Pair in Phononic Elastic Plates and Helical Edge States on a Dislocation Interface, *Adv. Mater.* 33 (2021) 2005160. doi:10.1002/adma.202005160.